

GEOMETRIC PHASE AND ITS APPLICATIONS: TOPOLOGICAL PHASES, QUANTUM WALKS AND NON-INERTIAL QUANTUM SYSTEMS

VIKASH MITTAL

*A thesis submitted for the partial fulfillment of
the degree of Doctor of Philosophy*



DEPARTMENT OF PHYSICAL SCIENCES

INDIAN INSTITUTE OF SCIENCE EDUCATION & RESEARCH (IISER) MOHALI,
SECTOR 81 SAS NAGAR, MANAULI PO 140306 PUNJAB, INDIA

AUGUST 2022

*dedicated to my family and
to all the people
to whom I owe more than I can express . . .*

Abstract

Geometric phase plays a fundamental role in quantum theory and accounts for wide phenomena ranging from the Aharonov-Bohm effect, the integer and fractional quantum hall effects, and topological phases of matter, including topological insulators, to name a few. In this thesis, we have proposed a fresh perspective of geodesics and null phase curves, which are key ingredients in understanding the geometric phase. We have also looked at a number of applications of geometric phases in topological phases, quantum walks, and non-inertial quantum systems.

The shortest curve between any two points on a given surface is a (minimal) geodesic. They are also the curves along which a system does not acquire any geometric phase. In the same context, we can generalize geodesics to define a larger class of curves, known as null phase curves (NPCs), along which also the acquired geometric phase is zero; however, they need not be the shortest curves between the two points. We have proposed a geometrical decomposition of geodesics and null phase curves on the Bloch sphere, which is crucial in improving our understanding of the geometry of the state space and the intrinsic symmetries of geodesics and NPCs.

We have also investigated the persistence of topological phases in quantum walks in the presence of an external (lossy) environment. We show that the topological order in one and two-dimensional quantum walks persist against moderate losses. Further, we use the geometric phase to detect the non-inertial modifications to the field correlators perceived by a circularly rotating two-level atom placed inside a cavity.

List of Figures

2.1	Structure of Hilbert space \mathcal{H} and ray or projective space \mathcal{R}	12
2.2	The Bargmann Invariant and the geometric phase.	14
2.3	Schematic for cyclic geometric phase in Samuel and Bhandari's setting.	17
2.4	Schematic for non-cyclic geometric phase in Samuel and Bhandari's setting.	19
2.5	A geodesic on the surface of a sphere.	25
2.6	Bargmann invariant	29
2.7	Continuous limit of Bargmann invariant	31
2.8	Sjöqvist interferometric setup.	40
2.9	Bloch sphere representation of a qubit.	49
2.10	Schematic of the experimental setup in Ericsson et al [1].	52
2.11	The solid angle Ω , shown by shaded region, by one of the eigenvector of the density matrix ρ . The other eigenvector traces the same path, except in the clockwise direction.	54
2.12	Comparison of Berry's phase for pure states and Uhlmann phase for mixed states.	54
3.1	Schematic of the protocol of two steps of 1D DTQW. The system consists of 1D lattice where site index runs from $-n$ to $+n$ and spin degrees of freedom. We can see the interference at $n = 0$ after the second step.	76

3.2	The probability distribution of walker after 150 time steps for different values of (ξ, θ, ζ)	78
3.3	Probability distribution of a walker after 200 time steps for different initial states. (a) $ \psi(0)\rangle = 0\rangle \otimes \downarrow\rangle$, (b) $ \psi(0)\rangle = 0\rangle \otimes \uparrow\rangle$, (c) $ \psi(0)\rangle = 0\rangle \otimes (\uparrow\rangle + i \downarrow\rangle)/\sqrt{2}$ in contrast to classical walk (red). Only the points with non-zero probability are plotted. (d) The variance, $\sigma^2(t)$ for quantum and classical walks with time steps t . The axes are chosen on logarithmic scale.	82
3.4	The quasi-energy spectrum of the effective Hamiltonian $H(\theta)$ for (a) $\theta = 0$, (b) $\theta = \pi/2$ and (c) $\theta = \pi$	84
3.5	The dispersion relation of the 1D SSQW given in Eq. (3.34) as function of rotation angle θ_2 and the quasi-momentum k for (a) $\theta_1 = 0$, (a) $\theta_1 = \pi/2$, and (a) $\theta_1 = \pi$	85
3.6	Probability distribution of a walker after 200 time steps for (a) $(\theta_1, \theta_2) = (\pi/2, \pi/3)$, (b) $(\theta_1, \theta_2) = (\pi/3, \pi/3)$, (c) $(\theta_1, \theta_2) = (-\pi/2, 3\pi/4)$, (c) $(\theta_1, \theta_2) = (\pi/2, 0)$. All the plots are symmetric due to the choice of symmetric initial state $ \psi(0)\rangle = 0\rangle \otimes (\uparrow\rangle + i \downarrow\rangle)/\sqrt{2}$. In (d) we recovered the probability distribution of 1D DTQW by putting $\theta_2 = 0$	86
3.7	Schematic of the protocol of 2D DTQW. The system consists of 2D lattice and site index runs from $-n$ to $+n$ in both the directions.	87
3.8	(Color online) 2D DTQW with nontrivial topology on a triangular lattice and its equivalent square lattice.	89
3.9	The quasi-energy band structure of the effective Hamiltonian $H_{2D}(\theta_1, \theta_2)$ for (a) $\theta_1 = \pi/2 = \theta_2$, (b) $\theta_1 = 7\pi/6 = \theta_2$ and (c) $\theta_1 = 3\pi/2 = \theta_2$	90
3.10	The probability distribution of the 2D DTQW given in Eq. (3.40) after 100 number of time steps for different values of θ_1 and θ_2 . In (a) $\theta_1 = \pi/2 = \theta_2$, (b) $\theta_1 = 7\pi/6 = \theta_2$, (c) $\theta_1 = 3\pi/4 = \theta_2$ and (d) $\theta_1 = -\pi/5, \theta_2 = 3\pi/7$. The system size is taken to be 201×201	91
3.11	Probability distribution for (a) Hadamard, (c) Grover, and (e) Fourier coin. The lattice size is taken to be 201×201 for all the plots.	94

3.12	Probability distribution of the walker initially localized at the origin and with the symmetric state of the coin for $\theta_1 = \pi/4, \theta_2 = \pi/7$ after 200 steps. We took the system size to be $N = 400$. with unitary given by (3.32) and in the inset with unitary given by (3.59).	96
3.13	The evolution of probability density on the lattice with number of time steps with lattice size, $N = 101$. (a) $\theta_2 = \pi/2$, and (b) $\theta_2 = \pi/4$. Here we chose $\phi = 2\pi/60$	97
3.14	The plot of the returning probability $P(x_0, x_M)$ after M number of steps and the variance as a function of time steps for (a) $\theta_2 = \pi/2$, (b) $\theta_2 = \pi/4$	98
4.1	Block diagonalization of \hat{H} as the consequence of a unitary symmetry.	103
4.2	Dispersion relation of a system that exhibits all three, time-reversal, charge-conjugation and chiral symmetry. The arrows represent the relation between the states $ \psi(\mathbf{k})\rangle$ and $\mathcal{T} \psi(\mathbf{k})\rangle, \mathcal{C} \psi(\mathbf{k})\rangle, \Gamma \psi(\mathbf{k})\rangle$ which is discussed in the text.	111
4.3	1D lattice with lattice spacing a and the hopping amplitude between nearest neighbors t	112
4.4	The plot of the dispersion relation derived in Eq. (4.44).	114
4.5	The geometry of SSH with lattice spacing a . One unit cell consists of two sites A and B , which is shown with shaded part. A chain consists of N unit cells.	114
4.6	Dispersion relation of the SSH model $E_{\pm}(k)$ given in Eq. (4.54) for different settings of v and w . (a) $v = 1, w = 0$, (b) $v = 1, w = 0.5$, (c) $v = 1, w = 1$, (d) $v = 0.5, w = 1$, (e) $v = 0, w = 1$. In the bottom row, the endpoints of the vectors $\mathbf{d}(k)$ [given in Eq. (4.53)] in the d_x - d_y plane as k takes values form 0 to 2π in first Brillouin zone.	117

4.7	A schematic to illustrate the winding of the wavefunction $ \psi(k)\rangle$, as k goes around in the Brillouin zone, for the trivial (top) and the topological phase (bottom). Note, that the two phases shown above cannot be smoothly connected due to the presence of a twist in the topologically non-trivial phase (bottom).	118
4.8	The two extreme cases of open chain of SSH in the dimerized limit.	119
4.9	(Energy spectrum of the finite chain with $N = 100$ unit cells and for (a) fixed $w = 1$ and varying v , (b) fixed $v = 1$ and varying w . (a) shows that $v > w$ and $v < w$ corresponds to trivial and topological phases respectively.	121
4.10	(a), (b) The plot of the wavefunction corresponding to zero-energy edge states. The blue and orange bars represent the components on the sublattice A and B respectively. (c) shows any bulk state for the reference which is delocalized all over the chain.	121
4.11	The calculation of the Berry curvature using the $U(1)$ -link on a discretized two-dimensional Brillouin zone. The two momenta k_x, k_y goes from 0 to $2\pi/q_x$ and 0 to $2\pi/q_y$ in a discrete step of $2\pi/q_x N_x$ and $2\pi/q_y N_y$ respectively. N_x, N_y being the total number of points in respective directions.	125
4.12	(Color online) (a) Different topological phases realized in 1D SSQW as a function of θ_1 and θ_2 . We observe two topological phases here corresponding to $W = 0$ and 1. Here, black and red lines represent closing of energy band at $k = 0$ and $k = \pi$, respectively, and solid and dotted lines demonstrate the closing at $E = 0$ and $E = \pi$, respectively. (b) Topological phases which exist in 2D DTQW for different values of θ_1 and θ_2 . Here, blue and black lines show the closing of energy gap at $E = 0$ and $E = \pi$, respectively. The yellow, violet and white regions correspond to $C = +1, -1$ and 0, respectively.	127
4.13	Plot of the average displacement of the walker, initially localized at $ -\rangle \otimes 0\rangle$, as a function of θ_1 after $M = 200$ steps for two different values of θ_2 . The number of sites L are taken to be 51.	131
4.14	Gaussian curvature.	132

4.15	Explaining Gaussian curvature.	132
5.1	The quasienergy for $\theta_1 = \pi/4, \theta_2 = -\pi/6$, and $\phi = 0$. In top row, the blue (red) corresponds to real (imaginary) part of the quasienergy, whereas in the bottom row we have eigenvalues of the unitary operator Eq. (5.19) on a unit circle. (a) $e^\gamma = 1$, (b) $e^\gamma = 1.1$, (c) $e^\gamma = e^{\gamma_c}$, (d) $e^\gamma = 1.4$	141
5.2	Probability distribution of the walker initially localized at the origin and with the symmetric state of the coin for $\theta_1 = \pi/4, \theta_2 = -\pi/6$ after 200 steps in top row. In bottom row we plot the time evolution of the norm for different settings of γ . (a) $e^\gamma = 1$, (c), $e^\gamma = 1.1$ $e^\gamma = e^{\gamma_c}$, (d) $e^\gamma = 1.4$. The system size is taken to be $N = 400$	141
5.3	Real (a) and imaginary (b) part of the eigenvalues are plotted with the parameter β . The blue and red corresponds to E_+ and E_- respectively.	143
6.1	(Color online) Winding of the Bloch vector around the origin with the lattice size, $N = 201$ (a) $\theta_1 = -3\pi/8, \theta_2 = \pi/8, \gamma = 0.25$ (b) $\theta_1 = -3\pi/8, \theta_2 = 5\pi/8, \gamma = 0.25$ (c) $\theta_1 = -3\pi/8, \theta_2 = \pi/8, \gamma = 1.8$ (d) $\theta_1 = -3\pi/8, \theta_2 = \pi/8, \gamma = 3.0$	148
6.2	(Color online) Plot for W_- for lower energy band as a function of γ and θ_2 , and (a) $\theta_1 = -\pi/2$ (b) $\theta_1 = -3\pi/4$ (c) $\theta_1 = -\pi$. The system size is taken to be $N = 201$. The red and black lines in all of the panels represent γ_c for $(k, E) = (0, 0)$ and $(k, E) = (\pi, 0)$, respectively.	149
6.3	(Color online) Effect of γ_x on Chern number is plotted with varying θ_2 for $\gamma_y = 0$ (a) $\theta_1 = \pi/4$ (b) $\theta_1 = 3\pi/8$ (c) $\theta_1 = 3\pi/2$. In the bottom row, (d) $\gamma_y = 0.1$, (e) $\gamma_y = 0.5$, (f) $\gamma_y = 1.0$, respectively. The lattice size is taken to be 201×201	150

- 6.4 (Color online) The bulk boundary correspondence is studied by dividing the lattice in two parts which are characterized by distinct topological phases locally. (a) 1D lattice is divided in two equal parts with two boundaries at $\pm L_B$ with $L_B = 50$ and system size $N = 201$. (b) A two dimensional periodic lattice is divided into two equal parts where the partition is made in the y -direction while retaining the periodicity in the x -direction. The boundary on the y -axis is chosen at $\pm L_B$ with a lattice size 201×201 152
- 6.5 (Color online) The eigenvalues, λ of the time evolution operator in Eq. (5.17) are plotted for $(\theta_1^1, \theta_2^1) = (-3\pi/8, \pi/4)$ and $(\theta_1^0, \theta_2^0) = (-3\pi/8, 5\pi/8)$ and different values of γ . In (a) $\gamma = 0$, (b) $\gamma = 0.2$, (c) $\gamma = \min(\gamma^1, \gamma^2) = 0.2110$, and (d) $\gamma = 0.25$ 154
- 6.6 (Color online) Energy bands for the 2D DTQW are plotted for inhomogeneous lattice with lattice size 201×201 . We have chosen $(\theta_1^0, \theta_2^0) = (3\pi/2, 2\pi/2)$ and $(\theta_1^{+1}, \theta_2^{+1}) = (7\pi/6, 7\pi/6)$ which correspond to $C = 0$ and $C = +1$, respectively, for the two parts of the lattice. The scaling parameters are chosen to be $\gamma_x = \gamma_y = 0, 0.2, 0.3$ for (a), (b) and (c), respectively. In all these figures we can see the edge states appearing on the boundaries of the two parts of the lattice. For larger values of the scaling parameter, i.e., $\gamma_x = \gamma_y = 0.47$ in Fig. (d) we see a large number of states between the two bands, which is due to the losses. 155
- 7.1 (Color online) Here we plot the geometric decomposition of a geodesic between two states given in Eq. (7.23) where we have chosen (a) $\theta = \pi/3$, (b) $\theta = \pi/5$. The blue and orange curve correspond to $\{\mathbf{n}_+\}$ and $\{\mathbf{n}_-\}$ respectively, given in Eq. (7.28). 166
- 7.2 (Color online) Geometric decomposition of geodesics in (a) 4- (b) 5- (c) 6- (d) 7- (e) 8-dimensional state space for $\theta = \pi/3$. We can see that we obtain $n-1$ number of curves for n -dimensional system which is consistent with our decomposition. 170

- 7.3 (Color online) Here we plot the Bloch geometric decomposition of NPCs in three-dimensional state space between the two states given in Eq. (7.52). In (a) $\theta = \pi/3$, (b) $\theta = \pi/6$ we plot the NPCs which are constructed by considering dual pairs of curves. Whereas, in (c) and (d) we plot the NPCs which are constructed by geometric decomposition of the curve in Eq. (7.57). We have chosen $\chi = \pi/3$ and the same values of θ as in (a) and (b). 176
- 8.1 (Color online) The plot for Γ_{\downarrow} vs. ω_c and the non-unitary GP versus the number of quasi-cycles (n) in the two regimes discussed in the paper. We plot the inertial (φ_{in}) and the non-inertial contributions (φ_{n-in}) to the non-unitary GP here. (a),(b) $\omega \gg \bar{\Omega}_0$ with $\omega = 5$ GHz, $\Omega_0 = 10$ MHz, $V = 10^{-7}$ m³, and $R = 10^{-6}$ m which correspond to an average acceleration $a = \omega^2 R \sim 2.5 \times 10^{13}$ m/s². For this set of parameters, $\pi n A / \Omega_0 \sim 10^{-16} n$. (c),(d) $\omega \ll \bar{\Omega}_0$ with $\omega = 0.1$ MHz, $\Omega_0 = 10$ MHz, $V = 10^{-3}$ m³, and $R = 10^{-3}$ m which correspond to an average acceleration $a = \omega^2 R \sim 10^7$ m/s². The plots are for $\theta = \pi/2$ in Eq. (8.10). The vertical black dashed lines in Figs. (a), (c) mark the normal frequencies at which the cavity is tuned to obtain the GP versus n plots in Figs. (b),(d). 185

Contents

1	Introduction	1
2	Geometric Phase	3
2.1	Berry's derivation of Geometric phase	4
2.2	An example of a spin - 1/2 particle in an external magnetic field	7
2.3	Non-adiabatic, cyclic phase by Aharanov & Anandan	9
2.4	Mathematical interlude	11
2.5	Non-adiabatic, non-cyclic geometric phase	13
2.5.1	Pancharatnam phase	13
2.5.2	Parallel transport	15
2.5.3	Cyclic evolution	17
2.5.4	Non-cyclic evolution	19
2.6	Kinematic Approach to geometric phase	21
2.6.1	Geometric phase for smooth parametrized curve	22
2.6.2	24
2.6.3	Bargmann invariant and geometric phase	29

2.6.4	Continuous limit of Bargmann invariant	31
2.7	Null phase curves	32
2.8	Geometric phase for mixed states	33
2.8.1	Mixed state geometric phase in interferometry	35
2.8.2	Parallel transport	38
2.8.3	Gauge invariance	40
2.8.4	Explicit example of a 2-level (spin -1/2) system	42
2.9	Non-unitary evolution	43
2.10	Measurement of Mixed state Geometric Phase in Interferometry	49
2.10.1	Experimental setup	52
2.11	Uhlmann Holonomies	54
2.11.1	Uhlmann's amplitudes	55
2.11.2	Parallel amplitudes	57
2.11.3	Uhlmann's phase for a two-level system	60
2.11.4	A comment on the importance of the two approaches, interferometric and Uhlmann's approach, for mixed geometric phases in the topological characterization	66
2.12	Weak Measurement Approach to Measure GP	66
2.12.1	Weak value measurements with qubits	69
2.13	Qubit as A Measurement Device	71
3	Quantum Walks	75

3.1	1D Discrete Time Quantum Walk (DTQW)	76
3.1.1	Unitary equivalence of quantum walks	78
3.1.2	Effective Hamiltonian	81
3.2	1D Split-Step Quantum Walk (SSQW)	84
3.3	2D DTQW	87
3.3.1	2D DTQW with 4D Coin	90
3.3.2	Decomposition of SSQW	95
3.3.3	Electric Quantum Walk	97
4	Symmetries and Topology	99
4.1	Classification of topological phases	101
4.2	Symmetries	102
4.2.1	Unitary symmetries	102
4.2.2	Non-unitary/Anti-unitary symmetries	104
4.2.3	Particle-hole or Charge conjugation symmetry (PHS)	109
4.2.4	Chiral or Sub-lattice symmetry (CS)	109
4.3	Tenfold Way by AZ	110
4.4	1D Tight-Binding Model	112
4.5	Su-Schrieffer-Heeger (SSH) model	114
4.5.1	Edge states	119
4.5.2	Symmetries of SSH model	122
4.5.3	Winding number	122

4.5.4	Bulk-edge correspondence	123
4.6	Topological characterization in 2D systems	124
4.7	Topological Phases in Quantum Walk	126
4.8	Real-space representation of Winding number	127
4.9	Gauss-Bonnet theorem	131
5	Non-Hermitian Systems	135
5.1	Symmetry ramification and unification in non-Hermitian systems	136
5.2	Non-unitary/Non-hermitian Quantum Walk	137
5.2.1	Homogeneous system	138
5.3	Physics of degenerate and exceptional points	142
6	Persistence of Topological Phases in Non-Hermitian Quantum Walk	145
6.1	Symmetries of the Hamiltonian	145
6.2	Results	147
6.2.1	Topological phases in 1D non-unitary quantum walk	147
6.2.2	Topological phases in 2D non-unitary quantum walk	149
6.2.3	Bulk-boundary correspondence	152
7	Bloch decomposition of geodesics and null phase curves (NPCs)	157
7.1	MS representation	159
7.1.1	Bargmann invariant (BI) and geometric phase	161
7.1.2	Geodesic curves	162

7.1.3	NPCs	163
7.2	Bloch sphere decomposition of geodesics	164
7.2.1	Geodesics in three-dimensional state space	164
7.2.2	Geodesics in higher-dimensional state space	168
7.3	Bloch Sphere decomposition of NPCs	171
8	Geometric Phase and non-inertial Effect	179
8.1	Open quantum system description of the rotating atom and the Geometric phase	180
8.2	GP response of the circularly rotating detector	183
8.2.1	Transition rates in the atom's frame	184
9	Conclusion and Future Outlook	189

Chapter 1

Introduction

Berry showed that a quantum system that is taken around a closed path by varying the parameters \mathbf{R} of its Hamiltonian $H(\mathbf{R})$ would acquire an additional phase factor in addition to the standard dynamical phase [2]. This extra phase factor, known as *geometric phase* is purely geometric in nature and depends only on the geometry of the path traversed by the system in the parameter space. The geometric phase accounts for wide phenomena in physics, such as the Aharonov-Bohm effect [3], the integer and fractional hall effect [4, 5], the topological phases of matter [6] and is instrumental in quantum information processing [7, 8]. In this thesis, we focus on the fundamental structure of the geometric phase and study its applications.

In this thesis, we introduce a Bloch sphere decomposition of geodesics and null phases curves, which are the key ingredients to understand the fundamental structure of the geometric phases [9, 10]. The shortest curve between any two points on a given surface is a (minimal) geodesic. Geodesics in the state space of quantum systems play an important role in the theory of geometric phases, as these are also the curves along which the acquired geometric phase is zero. Null phase curves (NPCs) are the generalization of the geodesics, which are defined as the curves along which the acquired geometric phase is zero even though they need not be the shortest curves between two points. We proposed a geometrical way to construct geodesics and a class of null phase curves in n -dimensional systems using Majorana star (MS) representation [11]. This work might be useful in improving the understanding of the state-space structure of higher-dimensional systems. We have further looked at several applications of geometric phases.

One direct application of geometric phase is to define topological invariants which are used to characterize different topological phases of matter [12, 13]. The geometric phases originated due to the underlying topology of the system are robust against local perturbations. Quantum walks are the quantum analog of classical random walks and are known to exhibit exotic topological phases [14, 15]. We have investigated the behavior of topological phases in quantum walks in the presence of a lossy environment. We show that the topological phases of the quantum walks are robust against moderate losses. The topological order in one-dimensional (1D) split-step quantum walk persists as long as the Hamiltonian respects exact \mathcal{PT} -symmetry. We also observe that the topological nature persists in two-dimensional (2D) quantum walks as well; however, the \mathcal{PT} -symmetry has little role to play there.

We further use the geometric phase to detect the effects of the non-inertial motion of a rotating atom placed inside an electromagnetic cavity. The cavity enables the isolation or strengthening of the non-inertial response relative to the inertial one. The accumulative nature of the geometric phase may facilitate the experimental observation of the resulting, otherwise feeble, non-inertial contribution to the modified field correlations. We have also indicated the possibility of an experimental observation of the modified vacuum fluctuations using the geometric phase acquired by a circularly accelerated atom interacting with the field vacuum inside an electromagnetic cavity. We have shown that the atom acquires an experimental observable phase at accelerations as low as 10^7m/s^2 .

Chapter 2

Geometric Phase

A quantum system taken around a closed path by varying the parameters \mathbf{R} of its Hamiltonian $H(\mathbf{R})$ acquires a geometrical phase. This phase is different from the standard dynamical phase of quantum systems in the sense that it depends only on the geometry of the path traversed by the system in the parameter space [2, 16–19]. Aharonov-Bohm effect [3] and Pancharatnam's phase [20] are the few manifestations of this phase. In the same year, immediately after Berry's paper, Barry Simon interpreted the geometric phase as the holonomy of the fiber bundle [21]. This geometric phase has wide applicability in the fields of quantum computation [22], condensed matter-physics [12], optics [23] and high-energy physics [24]. Berry's derivation of the geometric phase (also known as the Berry phase) requires the assumption of quantum adiabatic approximation and cyclic evolution. It further made use of the eigenstates of the Hamiltonian of the quantum system under consideration. In the following, the geometric phase was introduced for general unitary cyclic evolutions by Aharonov and Anandan [25] in 1987 and subsequently generalized to arbitrary (not necessarily unitary or cyclic) evolutions by Samuel and Bhandari [26]. The final generalization was introduced by Mukunda *et al.* [9] using a kinematical approach. In this approach, the connection between the geometric phase and the Bargmann invariant [27] was established which proved to be very important in order to find the geometric phase for a given set of discrete states. The definition of geometric phase in terms of Bargmann invariant can be taken very well as the fundamental definition of Berry's phase.

In this chapter we will first talk about geometric phase in the context of pure states start-

ing with the original derivation due to Berry and then discuss its subsequent generalizations by Aharanov and Anandan [25], Samuel and Bhandari [28] and finally by Simon and Mukunda [29]. We will further extend the definition of the geometric phase for more general states, referred to as mixed states, which was developed by Uhlmann [30] first in the context of parallel transport and then by Sjoqvist *et. al* [31] in the context of interferometry. We discuss the most general form of the geometric phase by Tong *et. al* [32]. We look at the idea of geometric phase from the perspective of weak measurements and finally conclude the chapter by looking at some applications of geometric phase in characterizing topological phases of matter.

2.1 Berry's derivation of Geometric phase

Consider a quantum mechanical system whose Hamiltonian $H(\mathbf{R})$ depends on real parameters $\mathbf{R} = (X, Y, \dots)$. The time evolution of the system (in the parameter space) is generated by slowly changing the parameters over time. The time dependence in Hamiltonian comes indirectly from $\mathbf{R}(t)$ such that $H(\mathbf{R}) \rightarrow H(\mathbf{R}(t))$. The parameters are changed slowly enough to stay within the limits of the adiabatic theorem. The *adiabatic theorem* in quantum mechanics [33] (or [34]) states that if the Hamiltonian $H(\mathbf{R}(t))$ is slowly varying, then at any instant of time, the system will be in an eigenstate of the instantaneous $H(\mathbf{R}(t))$.

$$\mathbf{R} \rightarrow \mathbf{R}(t) = (X(t), Y(t), \dots) \in \text{multidimensional parameter space}$$

The system evolves between times $t = 0$ and $t = T$ which can be seen as a transport around a closed path $\mathbf{R}(t)$ in the parameter space such that $\mathbf{R}(T) = \mathbf{R}(0)$. This closed path is denoted by \mathcal{C} . Here, T is the time it takes the system to return to the initial state (with an overall phase factor). For the applicability of the adiabatic theorem, the time scale T over which $H(\mathbf{R}(t))$ varies must be large. For a given time-dependent Hamiltonian $H(\mathbf{R}(t))$, the state vector $|\psi(t)\rangle$ of the system evolves according to the time dependent Schrödinger equation,

$$i\hbar \frac{d}{dt} |\psi(t)\rangle = H(\mathbf{R}(t)) |\psi(t)\rangle \quad (2.1)$$

At a given instant of time t for $\mathbf{R} = \mathbf{R}(t)$, we have an orthonormal set of eigenstates $\{|n; \mathbf{R}(t)\rangle\}$ and the corresponding eigenvalues $E_n(\mathbf{R}(t))$ of $H(\mathbf{R}(t))$ such that

$$H(\mathbf{R}(t)) |n; \mathbf{R}(t)\rangle = E_n(\mathbf{R}(t)) |n; \mathbf{R}(t)\rangle \quad (2.2)$$

Initially, the system is prepared in one of the eigenstate of $H(\mathbf{R}(0))$, $|\psi(t=0)\rangle = |n; \mathbf{R}(0)\rangle$ which will evolve adiabatically with $H(\mathbf{R}(t))$. The state at time t is written as

$$|\psi(t)\rangle = \exp \left\{ -\frac{i}{\hbar} \int_0^t dt' E_n(\mathbf{R}(t')) \right\} \exp(i\gamma_n(t)) |n; \mathbf{R}(t)\rangle \quad (2.3)$$

NOTE: This is the form of $|\psi(t)\rangle$ which Berry assumed and wanted to derive an explicit expression for the extra phase factor $\gamma_n(t)$.

The first exponential phase factor $\exp \left(-\frac{i}{\hbar} \int_0^t dt' E_n(\mathbf{R}(t')) \right)$ is well known in the theory of quantum mechanics. The other phase factor $\exp(i\gamma_n(t))$ is the subject of interest here.

This extra phase factor $\exp(i\gamma_n(t))$ is non-integrable (because all the contribution from dynamics is embedded in the first phase factor). The expression for $\gamma_n(t)$ is written by substituting $|\psi(t)\rangle$ given by Eq. (2.3) in Eq. (2.1) which gives

$$\dot{\gamma}_n(t) = i \langle n; \mathbf{R}(t) | \frac{d}{dt} |n; \mathbf{R}(t)\rangle \quad (2.4)$$

which can also be expressed in terms of gradient in parameter space,

$$\dot{\gamma}_n(t) = i \langle n; \mathbf{R}(t) | \nabla_{\mathbf{R}} |n; \mathbf{R}(t)\rangle \cdot \dot{\mathbf{R}}(t). \quad (2.5)$$

So, the state at the end of the closed loop \mathcal{C} when $t = T$, reads

$$|\psi(T)\rangle = \exp \left\{ -\frac{i}{\hbar} \int_0^T dt' E_n(\mathbf{R}(t')) \right\} \exp(i\gamma_n(T)) |\psi(0)\rangle \quad (2.6)$$

where

$$\gamma_n(T) \equiv \gamma_n(\mathcal{C}) = i \oint_{\mathcal{C}} \langle n; \mathbf{R}(t) | \nabla_{\mathbf{R}} |n; \mathbf{R}(t)\rangle \cdot \dot{\mathbf{R}}(t). \quad (2.7)$$

The integrand in the above integral is pure imaginary, which makes $\gamma_n(\mathcal{C})$ real and a physically observable quantity. It is very straightforward to see it using the fact that $|n; \mathbf{R}(t)\rangle$ are

normalized. The Eq. (2.7) can be written further as

$$\gamma_n(\mathcal{C}) = -\text{Im} \oint_{\mathcal{C}} \langle n; \mathbf{R}(t) | \nabla_{\mathbf{R}} | n; \mathbf{R}(t) \rangle \cdot d\mathbf{R}(t) \quad \text{mod } 2\pi. \quad (2.8)$$

If we consider the parameter space $\mathbf{R}(t)$ to be three-dimensional, then we can easily transform the line integral in the last equation to a surface integral using Stokes' theorem, which leads to

$$\begin{aligned} \gamma_n(\mathcal{C}) &= -\text{Im} \iint_{\mathcal{S}} d\mathbf{S} \cdot \nabla \times \langle n; \mathbf{R}(t) | \nabla_{\mathbf{R}} | n; \mathbf{R}(t) \rangle, \quad \nabla \equiv \nabla_{\mathbf{R}} \\ &= -\text{Im} \iint_{\mathcal{S}} d\mathbf{S} \cdot (\nabla \langle n; \mathbf{R}(t) |) \times (\nabla | n; \mathbf{R}(t) \rangle) \\ &= -\text{Im} \iint_{\mathcal{S}} d\mathbf{S} \cdot \sum_{m \neq n} (\nabla \langle n; \mathbf{R}(t) |) | m; \mathbf{R}(t) \rangle \langle m; \mathbf{R}(t) | (\nabla | n; \mathbf{R}(t) \rangle) \quad \text{mod } 2\pi \end{aligned} \quad (2.9)$$

where \mathcal{S} is the surface bounded by the curve \mathcal{C} and $d\mathbf{S}$ is the surface element. In deriving the last expression, we have made use of the complete set of eigenstates

$$\sum_m | m; \mathbf{R}(t) \rangle \langle m; \mathbf{R}(t) | = \mathbb{1} \quad (2.10)$$

and the vector identity [35]

$$\nabla \times [f(x) \nabla g(x)] = (\nabla f(x)) \times (\nabla g(x)). \quad (2.11)$$

Note that the expression in Eq. (2.9) does not depend on the choice of the surface \mathcal{S} . We note that terms for which $m = n$ does not contribute in Eq. (2.9) by virtue of the fact that $\langle n; \mathbf{R}(t) | \nabla_{\mathbf{R}} | n; \mathbf{R}(t) \rangle$ is a pure imaginary. For $m \neq n$, from Eq. (2.2) we can deduce

$$\langle m; \mathbf{R}(t) | \nabla | n; \mathbf{R}(t) \rangle = \frac{\langle m; \mathbf{R}(t) | \nabla H(\mathbf{R}(t)) | n; \mathbf{R}(t) \rangle}{E_n(\mathbf{R}(t)) - E_m(\mathbf{R}(t))}. \quad (2.12)$$

By substituting this back in Eq. (2.9), we have

$$\gamma_n(\mathcal{C}) = -\text{Im} \iint_{\mathcal{S}} d\mathbf{S} \cdot \sum_{m \neq n} \frac{\langle n; \mathbf{R}(t) | \nabla H(\mathbf{R}(t)) | m; \mathbf{R}(t) \rangle \times \langle m; \mathbf{R}(t) | \nabla H(\mathbf{R}(t)) | n; \mathbf{R}(t) \rangle}{(E_n(\mathbf{R}(t)) - E_m(\mathbf{R}(t)))^2}. \quad (2.13)$$

and hence $\gamma_n(\mathcal{C})$ can be expressed in a more compact notation as,

$$\gamma_n(\mathcal{C}) = - \iint_{\mathcal{S}} d\mathbf{S} \cdot \mathbf{V}_n(\mathbf{R}) \quad (2.14)$$

with

$$\mathbf{V}_n(\mathbf{R}) = \text{Im} \sum_{m \neq n} \frac{\langle n; \mathbf{R}(t) | \nabla H(\mathbf{R}(t)) | m; \mathbf{R}(t) \rangle \times \langle m; \mathbf{R}(t) | \nabla H(\mathbf{R}(t)) | n; \mathbf{R}(t) \rangle}{(E_n(\mathbf{R}(t)) - E_m(\mathbf{R}(t)))^2}. \quad (2.15)$$

We make a few observations here. The $\mathbf{V}_n(\mathbf{R})$ is the curl of $\langle n; \mathbf{R}(t) | \nabla_{\mathbf{R}} | n; \mathbf{R}(t) \rangle$ [from Eq. (2.9)] which makes it invariant under gauge transformations of the type

$$|n; \mathbf{R}(t)\rangle \rightarrow \exp(i\phi(\mathbf{R})) |n; \mathbf{R}(t)\rangle. \quad (2.16)$$

In the later chapter [Chapter 4], where we will discuss topological phases, we will identify $\mathbf{V}_n(\mathbf{R})$ with the Berry curvature and the quantity $i \langle n; \mathbf{R}(t) | \nabla_{\mathbf{R}} | n; \mathbf{R}(t) \rangle$ is called Berry connection.

2.2 An example of a spin - 1/2 particle in an external magnetic field

Let's consider a spin - 1/2 particle in an external magnetic field with Hamiltonian,

$$H(\mathbf{R}(t)) = -\frac{\mu}{2} \boldsymbol{\sigma} \cdot \mathbf{R}(t) \quad (2.17)$$

where $\mathbf{R}(t) = (X(t), Y(t), Z(t))$ is the external magnetic field and $\boldsymbol{\sigma}$ is the vector operator whose components are Pauli operators,

$$\sigma_X = \begin{pmatrix} 0 & 1 \\ 1 & 0 \end{pmatrix}, \quad \sigma_Y = \begin{pmatrix} 0 & -i \\ i & 0 \end{pmatrix}, \quad \sigma_Z = \begin{pmatrix} 1 & 0 \\ 0 & -1 \end{pmatrix}. \quad (2.18)$$

Thus,

$$H(\mathbf{R}(t)) = -\frac{\mu}{2} \begin{pmatrix} Z(t) & X(t) - iY(t) \\ X(t) + iY(t) & Z(t) \end{pmatrix} \quad (2.19)$$

By diagonalizing $H(\mathbf{R}(t))$ we will have eigenstates $|+; \mathbf{R}(t)\rangle, |-; \mathbf{R}(t)\rangle$ with corresponding eigenvalues,

$$E_{\pm}(\mathbf{R}(t)) = \pm \frac{\mu}{2} \sqrt{X^2(t) + Y^2(t) + Z^2(t)} = \pm \frac{\mu}{2} R(t). \quad (2.20)$$

where $R(t) = |\mathbf{R}(t)| = \sqrt{X^2(t) + Y^2(t) + Z^2(t)}$. Also,

$$\nabla H(\mathbf{R}(t)) = -\frac{\mu}{2}\boldsymbol{\sigma} \quad (2.21)$$

Now, if we choose $\mathbf{R}(t)$ to be along the z -axis, i.e. $\mathbf{R}(t) = R(t)\hat{\mathbf{k}}$, without any loss of generality and by using Eq. (2.15), we get

$$\begin{aligned} \mathbf{V}_+(R(t)\hat{\mathbf{k}}) &= \frac{1}{4R^2(t)} \text{Im} \langle +|\boldsymbol{\sigma}|- \rangle \times \langle -|\boldsymbol{\sigma}|+ \rangle \\ &= \left[\frac{\hat{\mathbf{k}}}{4R^2(t)} \right] \text{Im} (\langle +|\sigma_X|- \rangle \langle -|\sigma_Y|+ \rangle - \langle +|\sigma_Y|- \rangle \langle -|\sigma_X|+ \rangle) \end{aligned} \quad (2.22)$$

From Pauli's algebra, we have the following relations;

$$\sigma_X |\pm\rangle = |\mp\rangle, \quad \sigma_Y |\pm\rangle = \pm i |\mp\rangle, \quad \sigma_Z |\pm\rangle = \pm |\pm\rangle \quad (2.23)$$

where $|\pm\rangle$ are the eigenstates of σ_Z . Using these relations in Eq. (2.22) we will get the following

$$\mathbf{V}_+(R(t)\hat{\mathbf{k}}) = \frac{\hat{\mathbf{k}}}{2R^2(t)} \quad (2.24)$$

or, generally,

$$\mathbf{V}_n(\mathbf{R}) = \frac{\hat{\mathbf{R}}}{2R^2(t)} = \frac{\mathbf{R}}{2R^3(t)}. \quad (2.25)$$

Therefore, the Berry phase will be

$$\begin{aligned} \gamma_{\pm}(\mathcal{C}) &= \mp \iint_{\mathcal{S}} d\mathbf{S} \cdot \frac{\mathbf{R}}{2R^3(t)}, \\ &= \mp \frac{1}{2} \iint_{\mathcal{S}} d\mathbf{S} \cdot \frac{\mathbf{R}}{R^3(t)}, \\ &= \mp \frac{1}{2} \Omega(\mathcal{C}) \end{aligned} \quad (2.26)$$

where $\Omega(\mathcal{C})$ is the solid angle subtended by the closed path \mathcal{C} at the origin.

The solid angle is defined as

$$\Omega = \iint_{\mathcal{S}} \frac{\hat{\mathbf{r}} \cdot \hat{\mathbf{n}}}{r^2} dS = \iint_{\mathcal{S}} \sin \theta d\theta d\varphi \quad (2.27)$$

Here we have a cone for which we have

$$\Omega = \int_0^\theta \int_0^{2\pi} \sin \theta d\theta d\varphi = 2\pi(1 - \cos \theta) \quad (2.28)$$

2.3 Non-adiabatic, cyclic phase by Aharonov & Anandan

The first generalization of the Berry phase was given by Aharonov & Anandan [25] for nonadiabatic evolution under the assumption of a cyclic state. They used *projective space*, \mathcal{P} to derive the geometric phase expression. In this space, all normalized states in the Hilbert space \mathcal{H} , which differ only by a phase factor, are projected onto one point (state) in \mathcal{P} . Let us consider a normalized state $|\psi(t)\rangle \in \mathcal{H}$ that evolves according to the Schrödinger equation

$$i\hbar \frac{d|\psi(t)\rangle}{dt} = H(t) |\psi(t)\rangle \implies |\dot{\psi}(t)\rangle = -\frac{i}{\hbar} H(t) |\psi(t)\rangle. \quad (2.29)$$

Since we are considering a cyclic evolution, the initial and final states can be related by a phase factor such that

$$|\psi(\tau)\rangle = e^{i\phi} |\psi(0)\rangle. \quad (2.30)$$

Now, we define a map $\Pi : \mathcal{H} \rightarrow \mathcal{P}$ as

$$\Pi(|\psi(t)\rangle) = \{ |\psi'(t)\rangle = e^{i\alpha} |\psi(t)\rangle \mid \alpha \in [0, 2\pi) \} \quad (2.31)$$

which takes all states that differ only by a phase factor to a single point in \mathcal{P} . Then $|\psi(t)\rangle$ defines a curve

$$\mathcal{C} : [0, \tau] \rightarrow \mathcal{H} \quad (2.32)$$

such that $C \equiv \Pi(\mathcal{C})$ is the projection of \mathcal{C} and is a closed curve in \mathcal{P} . Now, define

$$|\tilde{\psi}(t)\rangle = e^{-if(t)} |\psi(t)\rangle \quad (2.33)$$

such that $f(\tau) - f(0) = \phi$. The state $|\tilde{\psi}(t)\rangle$ belongs to \mathcal{P} where it forms a closed loop $C : [0, \tau]$ which is evident by the fact that

$$\begin{aligned} |\tilde{\psi}(\tau)\rangle &= e^{-if(\tau)} |\psi(\tau)\rangle = e^{-if(\tau)} e^{i\phi} |\psi(0)\rangle \\ &= e^{-i(f(\tau)-\phi)} |\psi(0)\rangle = e^{-if(0)} |\psi(0)\rangle \\ &= |\tilde{\psi}(0)\rangle \end{aligned} \quad (2.34)$$

Further, by solving Schrödinger equation for $|\tilde{\psi}(t)\rangle$ we get

$$i\hbar \langle \tilde{\psi}(t) | \frac{d}{dt} |\tilde{\psi}(t)\rangle = \hbar \dot{f}(t) + \langle \psi(t) | H(t) | \psi(t)\rangle \quad (2.35)$$

By rearranging the last expression, we get

$$-\frac{df(t)}{dt} = \frac{1}{\hbar} \langle \psi(t) | H(t) | \psi(t)\rangle - i \langle \tilde{\psi}(t) | \frac{d}{dt} |\tilde{\psi}(t)\rangle$$

and by integrating the above equation over an interval $t \in [0, \tau]$ we have

$$\phi = \int_0^\tau \frac{df(t)}{dt} dt = -\frac{1}{\hbar} \int_0^\tau dt \langle \psi(t) | H(t) | \psi(t)\rangle + \int_0^\tau dt \langle \tilde{\psi}(t) | i \frac{d}{dt} |\tilde{\psi}(t)\rangle \quad (2.36)$$

Here, we note that the total phase is naturally decomposed into two parts, one which depends on $H(t)$ and is the same in \mathcal{H} and \mathcal{P} . Identifying the first part of LHS of Eq. (2.36) as the dynamical phase

$$\Phi_{dyn} = -\frac{1}{\hbar} \int_0^\tau dt \langle \psi(t) | H(t) | \psi(t)\rangle \quad (2.37)$$

leaves the other part to be *geometric phase* given by

$$\Phi_g \equiv \int_0^\tau dt \langle \tilde{\psi}(t) | i \frac{d}{dt} |\tilde{\psi}(t)\rangle = \phi + \frac{1}{\hbar} \int_0^\tau dt \langle \psi(t) | H(t) | \psi(t)\rangle \quad (2.38)$$

Since we can find many curves \mathcal{C} in \mathcal{H} such that they all have the same projection in \mathcal{P} and these different curves are generated by different Hamiltonians H . We can find the same $|\tilde{\psi}(t)\rangle$ for each H by an appropriate choice of $f(t)$, the phase factor Φ_g is independent of H for a given closed curve C . Thus, the *geometric phase* defined in this manner does not depend on $H(t)$ and is purely a property of the projective space \mathcal{P} . We also note that Φ_g is uniquely defined up to $2\pi n$ with n being an integer. Another difference to note in the Aharonov Anandan phase is that $|\psi(t)\rangle$ need not to be an eigenstate of $H(t)$ unlike in the case of Berry.

2.4 Mathematical interlude

Before moving on to talk about the next generalization, we set up some mathematical definitions and notation and explain the necessary concepts which will help to grasp the subtlety of the topic. Consider a complex Hilbert space \mathcal{H} representing a quantum system with complex dimension N . The states in the system are written as $\{|\phi\rangle, |\psi\rangle, \dots\}$ with an inner product structure $\langle\psi|\phi\rangle$. The unit sphere \mathcal{B} corresponding to the complex Hilbert space \mathcal{H} is defined as

$$\mathcal{B} = \{|\psi\rangle \in \mathcal{H} \mid \langle\psi|\psi\rangle = 1\} \subset \mathcal{H} \quad (2.39)$$

and has a real dimension $2N - 1$. The group $U(1)$ acts on \mathcal{B} as

$$|\psi\rangle \in \mathcal{B} \implies |\psi'\rangle = e^{i\alpha} |\psi\rangle \in \mathcal{B}, \quad 0 \leq \alpha \leq 2\pi. \quad (2.40)$$

Now, we define the space of unit rays \mathcal{R} as

$$\mathcal{R} = \{\rho(\psi) = |\psi\rangle\langle\psi| \mid |\psi\rangle \in \mathcal{B}\} \quad (2.41)$$

which is the quotient of unit sphere \mathcal{B} over $U(1)$ actions. We can define a projection map $\pi : \mathcal{B} \rightarrow \mathcal{R}$ between \mathcal{B} and \mathcal{R} that takes $|\psi\rangle \in \mathcal{B}$ to a point $\rho(\psi) = |\psi\rangle\langle\psi| \in \mathcal{R}$ in the ray space, as illustrated in Fig. 2.1(a). Since \mathcal{R} contains all the projections, it is also referred to as the projective space of \mathcal{H} . \mathcal{R} is not a linear vector space, and it has a real dimension $2(N - 1)$ and it is CP^{N-1} complex manifold. Note, that the dimension of the ray space \mathcal{R} is always even. The ray space for pure quantum states is very special mathematical object and it happen to be Riemannian manifold that carries a natural Riemannian metric—the Fubini-Study metric [36] and a natural symplectic structure [37]. The projection map π is defined as

$$\pi : \mathcal{B} \rightarrow \mathcal{R} : |\psi\rangle \in \mathcal{B} \rightarrow \rho(\psi) = |\psi\rangle\langle\psi| \text{ or } \psi\psi^\dagger \in \mathcal{R}. \quad (2.42)$$

The one-dimensional $U(1)$ fibre sitting on top of $\rho(\psi) \in \mathcal{R}$ is an entire equivalence class of state vectors which are related by one another just by a phase factor and all project down to a single point in \mathcal{R} i.e.

$$\rho(\psi) \in \mathcal{R} \rightarrow \pi^{-1}(\rho(\psi)) = \{|\psi'\rangle = e^{i\alpha} |\psi\rangle \in \mathcal{B} \mid 0 \leq \alpha < 2\pi\} \subset \mathcal{B} \quad (2.43)$$

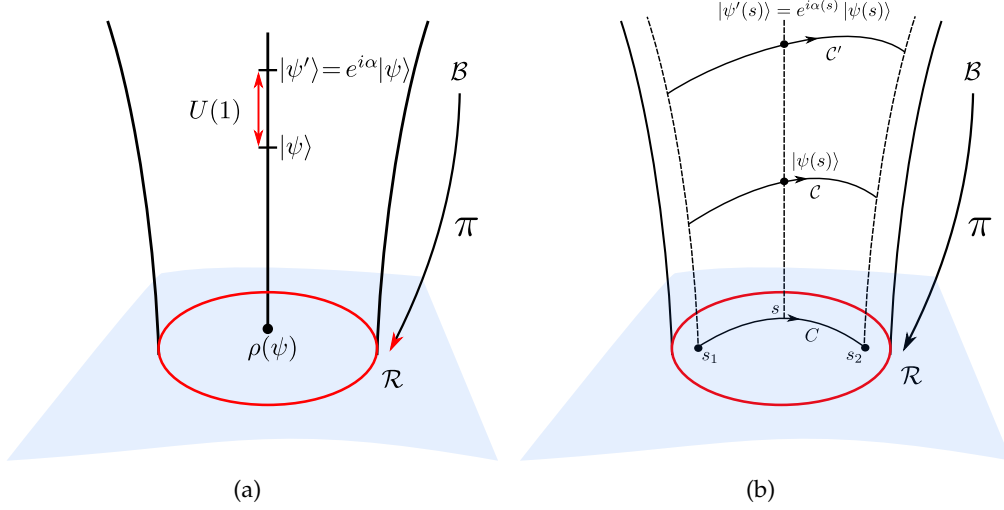


FIGURE 2.1: Structure of Hilbert space \mathcal{H} and ray or projective space \mathcal{R} .

Now, we define a smooth curve \mathcal{C} of unit vectors in \mathcal{B} as

$$\mathcal{C} = \{|\psi(s)\rangle \in \mathcal{B} \mid s_1 \leq s \leq s_2\} \subset \mathcal{B} \quad (2.44)$$

parameterized by a real variable s . The action of the map π on \mathcal{C} results in a curve $C \in \mathcal{R}$ that reads

$$C = \pi[\mathcal{C}] = \{\rho(\psi(s)) = |\psi(s)\rangle\langle\psi(s)| \in \mathcal{R} \mid s_1 \leq s \leq s_2\} \subset \mathcal{R} \quad (2.45)$$

Every parameterized curve $\mathcal{C} \subset \mathcal{R}$ as shown in Fig. 2.1(b) projecting onto the same curve $C \subset \mathcal{R}$ is called a *lift* of C from the ray space \mathcal{R} to \mathcal{B} . Any other lift \mathcal{C}' is related to \mathcal{C} by a smooth pointwise phase shift known as *gauge transformation* and is written as

$$\mathcal{C}' = \{|\psi'(s)\rangle = e^{i\alpha(s)} |\psi(s)\rangle \mid |\psi(s)\rangle \in \mathcal{C}, s_1 \leq s \leq s_2\} \subset \mathcal{B} \quad (2.46)$$

and

$$\pi[\mathcal{C}] = \pi[\mathcal{C}'] = C \subset \mathcal{R}. \quad (2.47)$$

This is all we need for the time being and we will discuss another mathematical interlude when we discuss the kinematic approach to the geometric phase.

2.5 Non-adiabatic, non-cyclic geometric phase

The next development in generalization is due to Samuel and Bhandari [28]. They generalized the definition for the cases when the curve is open in the projective Hilbert space \mathcal{P} and the initial and final state does not belong to the same ray. They make use of the early work of Pancharatnam [38] on the interference of polarized light beams and some concepts of differential geometry. We thus first go through Pancharatnam's phase and then move on to Samuel and Bhandari's work.

2.5.1 Pancharatnam phase

If we have a pair of vectors (or states) $|\psi_1\rangle$ and $|\psi_2\rangle$ such that $|\psi_2\rangle = e^{i\Phi} |\psi_1\rangle$ then they are the same quantum states and represent the same quantum system due to the fact that they belong to the same *ray*. A ray is defined as an equivalence class of states differing only by a phase factor. Furthermore, the two states $|\psi_1\rangle$ and $|\psi_2\rangle$ map to one point in the projective Hilbert space \mathcal{R} , that is, $\pi(|\psi_1\rangle) = |\psi_1\rangle\langle\psi_1| = |\psi_2\rangle\langle\psi_2| = \pi(|\psi_2\rangle)$. In this case, the relative phase between $|\psi_1\rangle$ and $|\psi_2\rangle$ is naturally Φ . However, when $|\psi_1\rangle$ and $|\psi_2\rangle$ represent two different quantum states, it is not trivial to define a relative phase between two and this question was first addressed by Pancharatnam. He gave a geometrical/physical interpretation of the relative phase between distinct polarization states of light. It is as follows: Given two non-orthogonal vectors / states $|\psi_1\rangle$ and $|\psi_2\rangle$, the relative phase difference Φ between them is given by

$$\langle\psi_1|\psi_2\rangle = |\langle\psi_1|\psi_2\rangle|e^{i\Phi} \quad (2.48)$$

i.e. Φ is the phase of their inner product $\arg \langle\psi_1|\psi_2\rangle$. The $|\psi_1\rangle$ and $|\psi_2\rangle$ are said to be *in phase* when

$$\langle\psi_1|\psi_2\rangle \text{ is real and positive.} \quad (2.49)$$

In the literature, it is commonly referred to as $|\psi_1\rangle$ and $|\psi_2\rangle$ are *in phase* in Pancharatnam sense and is known as *Pancharatnam connection*. An interesting point to note here is that this relation is not transitive, that is, if $|\psi_1\rangle$ is in phase with $|\psi_2\rangle$, and $|\psi_2\rangle$ is in phase with another state $|\psi_3\rangle$, then $|\psi_3\rangle$ need not to be in phase with $|\psi_1\rangle$. It can be illustrated by considering three

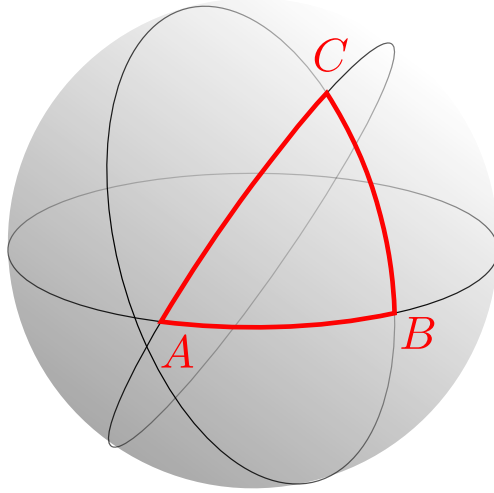


FIGURE 2.2: The Bargmann Invariant and the geometric phase.

normalized vectors

$$|\psi_1\rangle = \frac{1}{\sqrt{2}} \begin{pmatrix} 1 \\ 1 \end{pmatrix}, \quad |\psi_2\rangle = \begin{pmatrix} 1 \\ 0 \end{pmatrix}, \quad |\psi_3\rangle = \frac{1}{\sqrt{2}} \begin{pmatrix} 1 \\ i \end{pmatrix} \quad (2.50)$$

which are the eigenvectors of Pauli matrices. We can clearly see that

$$\langle \psi_1 | \psi_2 \rangle = \frac{1}{\sqrt{2}} \implies \text{real and positive} \implies |\psi_1\rangle \text{ is in phase with } |\psi_2\rangle$$

$$\langle \psi_2 | \psi_3 \rangle = \frac{1}{\sqrt{2}} \implies \text{real and positive} \implies |\psi_2\rangle \text{ is in phase with } |\psi_3\rangle$$

$$\langle \psi_3 | \psi_1 \rangle = \frac{1+i}{2} \implies \text{not real} \implies |\psi_3\rangle \text{ is not in phase with } |\psi_1\rangle$$

The Pancharatnam phase Φ depends on the geometry of the state space. For two-level systems, let us take three states $\{|A\rangle, |B\rangle, |C\rangle\}$ such that $|A\rangle$ is in phase with $|B\rangle$, $|B\rangle$ is with $|C\rangle$, then, in general, $|C\rangle$ is not in phase with $|A\rangle$. Let $|A'\rangle = e^{i\Phi} |A\rangle$ be a state vector such that $|C\rangle$ is in phase with $|A'\rangle$, then this “excess” phase is expressed as

$$\Phi = -\frac{1}{2}\Omega_{ABC} \quad (2.51)$$

where Ω_{ABC} is the solid angle of triangle ABC subtended at the center as shown in Fig. 2.2. Pancharatnam arrives at this result by considering two polarization states $|A\rangle$ and $|C\rangle$ which are in phase with each other. Now, projecting both states onto a third state $|B\rangle$, that is, $|A\rangle \rightarrow |\tilde{A}\rangle = (|B\rangle\langle B|) |A\rangle$ and $|C\rangle \rightarrow |\tilde{C}\rangle = (|B\rangle\langle B|) |C\rangle$ so that the relative phase between $|\tilde{A}\rangle$ and

$|\tilde{C}\rangle$ becomes

$$\begin{aligned}\arg \langle \tilde{A} | \tilde{C} \rangle &= \arg \langle A | B \rangle \langle B | B \rangle \langle B | C \rangle \\ &= \arg \langle A | B \rangle \langle B | C \rangle \langle C | A \rangle \quad \because \arg \langle C | A \rangle = 0 \\ &= \Delta(A, B, C).\end{aligned}$$

The quantity $\Delta(A, B, C)$ is invariant under gauge transformations of the kind $|A\rangle \rightarrow e^{i\beta} |A\rangle$ and therefore is a characteristic of a projective Hilbert space \mathcal{R} . Considering $\{|A\rangle, |B\rangle, |C\rangle\}$ to be polarization states of the light beam that are represented by a point on the *Poincare* sphere, we find

$$\Delta(A, B, C) = \frac{1}{2} \Omega_{ABC}. \quad (2.52)$$

The quantity $\Delta(A, B, C)$ is closely related to the geometric phase and is identified as *Bargmann invariant*. This connection was made by Simon and Mukunda [29] which is the topic for the next section. We will come again to the Pancharatnam phase when we discuss the geometric phase for mixed states.

2.5.2 Parallel transport

In the previous section, we identified Φ_{dyn} which is given by

$$\Phi_{dyn} = -\frac{1}{\hbar} \int_0^\tau dt \langle \psi(t) | H(t) | \psi(t) \rangle \quad (2.53)$$

and talked about the lifts of a closed curve C in the projective Hilbert space \mathcal{P} to \mathcal{C} in the normalized Hilbert space \mathcal{H} . There exist special lifts of C in Hilbert space, along which the dynamical phase vanishes and the whatever phase is accumulated during an evolution is purely geometrical. To achieve that, the integrand in Eq. (2.53) has to vanish i.e.,

$$\langle \psi(t) | H(t) | \psi(t) \rangle = 0 \quad (2.54)$$

for all time t . Further, using the Schrödinger equation, we can write

$$\langle \psi(t) | \frac{d}{dt} | \psi(t) \rangle = 0 \quad (2.55)$$

and this is precisely the condition for *parallel transport*. The parallel transport refers to an evolution in which the state vector $|\psi(t)\rangle$ at time t remains *in phase* with the adjacent state vector $|\psi(t + dt)\rangle$.

With the definition of Pancharatnam phase Φ and parallel transport at our disposal, we move to the results of Samuel and Bhandari. Consider a quantum system with Hilbert space \mathcal{H} . A state vector $|\psi(t)\rangle \in \mathcal{H}$ evolves according to the Schrödinger equation as

$$i\hbar \frac{d|\psi(t)\rangle}{dt} = H(t) |\psi(t)\rangle. \quad (2.56)$$

Here, H is a linear operator and does not need to be Hermitian. We choose a lift, known as *horizontal lift* of the curve C in projective space \mathcal{P} in such a way that the dynamical phase vanishes. That can be done by defining a new state vector $|\phi(t)\rangle$

$$|\phi(t)\rangle = e^{\frac{i}{\hbar} \int_0^t h(t') dt'} |\psi(t)\rangle \quad (2.57)$$

with

$$h(t') = \frac{\text{Re} \langle \psi(t') | H(t') | \psi(t') \rangle}{\langle \psi(t') | \psi(t') \rangle}. \quad (2.58)$$

The difference between $|\phi(t)\rangle$ and $|\psi(t)\rangle$ is that we have removed the dynamical phase factor from $|\psi(t)\rangle$ and left with only the geometric contribution. By substituting $|\phi(t)\rangle$ into the Schrödinger equation, we get

$$\begin{aligned} i\hbar \frac{d|\phi(t)\rangle}{dt} &= i\hbar \left(\frac{i}{\hbar} h(t) |\phi(t)\rangle + e^{i \int_0^t h(t') dt'} \frac{d|\psi(t)\rangle}{dt} \right) \\ &= i \left(ih(t) |\phi(t)\rangle - \frac{i}{\hbar} e^{\frac{i}{\hbar} \int_0^t h(t') dt'} H(t) \psi(t) \right) \\ &= (H(t) - h(t)) |\phi(t)\rangle. \end{aligned}$$

Further, taking the inner product with $|\phi(t)\rangle$ from left, we get

$$\begin{aligned} i\hbar \langle \phi(t) | \frac{d}{dt} |\phi(t)\rangle &= \langle \phi(t) | H(t) - h(t) | \phi(t)\rangle \\ &= \langle \phi(t) | H(t) | \phi(t)\rangle - \langle \phi(t) | h(t) | \phi(t)\rangle \\ &= \langle \psi(t) | H(t) | \psi(t)\rangle - \text{Re} \langle \psi(t) | H(t) | \psi(t)\rangle \\ &= \text{Im} \langle \psi(t) | H(t) | \psi(t)\rangle \end{aligned}$$

We now consider the cyclic evolution and derive the geometric phase with this setting. Let $\mathcal{C} = \{|\phi(s)\rangle \mid s \in [s_1, s_2]\}$ be a curve in the Hilbert space of unit vectors \mathcal{B} . When $|\phi(s_2)\rangle = e^{i\phi} |\phi(s_1)\rangle$ for real ϕ as shown in Fig. 2.3, then its projection $C \in \mathcal{R}$ will be a closed curve. For this curve in \mathcal{B} the tangent vector is given by

$$|u(s)\rangle = \frac{d}{ds} |\phi(s)\rangle \quad (2.62)$$

and we define a quantity $A_s = \text{Im} \langle \phi(s) | u(s) \rangle$. This quantity A_s resembles the vector potential in electrodynamics because, under gauge transformations of the kind $|\phi(s)\rangle \rightarrow e^{i\alpha(s)} |\phi(s)\rangle$ it transforms like $A_s \rightarrow A_s + d\alpha/ds$. The motivation to define this quantity will become clear in a moment.

Let's consider our original state vector $|\psi(s)\rangle$ and a curve traced by it in \mathcal{B} . Now, if $|\psi(s)\rangle$ is a cyclic solution of the Schrödinger equation i.e. it returns to the same *ray* after a time period τ (red curve \mathcal{C} in Fig. 2.3), then the projection of this curve (under the projection map π) is a closed curve in \mathcal{R} . However, we are not actually interested in $|\psi(s)\rangle$ because it also has a dynamical contribution in the total phase after evolving for time τ . So, given a closed curve $C \in \mathcal{R}$, we need to find a lift $\mathcal{C} = \{|\phi(s)\rangle \mid s \in [0, \tau]\} \in \mathcal{B}$ which is traced by a state vector with the removed dynamical phase. Such lifts are called "horizontal" lifts and are determined by the parallel-transport law Eq. (2.59) which implies $A_s = 0$ along the curve. Consider the integral

$$\phi_g = \oint A_s ds \quad (2.63)$$

along the curve $\mathcal{C} \in \mathcal{B}$, which is closed by a vertical line that joins $|\phi(s_1)\rangle$ and $|\phi(s_2)\rangle$ as shown in Fig. 2.3. The part $|\phi(s)\rangle$ shows the true evolution of the system, and A_s vanishes along this curve. The only contribution to the integral Eq. (2.63) is due to the vertical line, and consequently ϕ_g is given by the Pancharatnam phase between $|\phi(s_1)\rangle$ and $|\phi(s_2)\rangle$ i.e. $\phi_g = \arg \langle \phi(s_1) | \phi(s_2) \rangle$. From this we see that the Pancharatnam phase is, in fact, an early example of Berry phase [39].

Given a closed curve in $C \in \mathcal{R}$, we can lift this curve so that A_s vanishes along that lift, i.e. a horizontal lift. However, the horizontal lift of a closed curve in \mathcal{R} need not to be closed in \mathcal{B} . This is called holonomy of the connection [40]. Furthermore, in the language of the fibre bundles, A_s is referred to as *one-form* which defines a horizontal lift.

By using the gauge invariance of Eq. (2.63), this integral can be identified as a characteristic of the projective Hilbert space \mathcal{R} . We can further use Stokes' theorem to write ϕ_g as

$$\phi_g = \int_S \mathcal{F} \quad (2.64)$$

where S denotes the surface bounded by a closed curve C in \mathcal{R} and \mathcal{F} is the gauge-invariant *two-form*. It denotes the exterior derivative of A_s that is equivalent to $\nabla \times A_s$ in three dimensions. Hence, ϕ_g depends only on the curve $C \in \mathcal{R}$ and not on the rate at which it is transversed in the parameter space.

2.5.4 Non-cyclic evolution

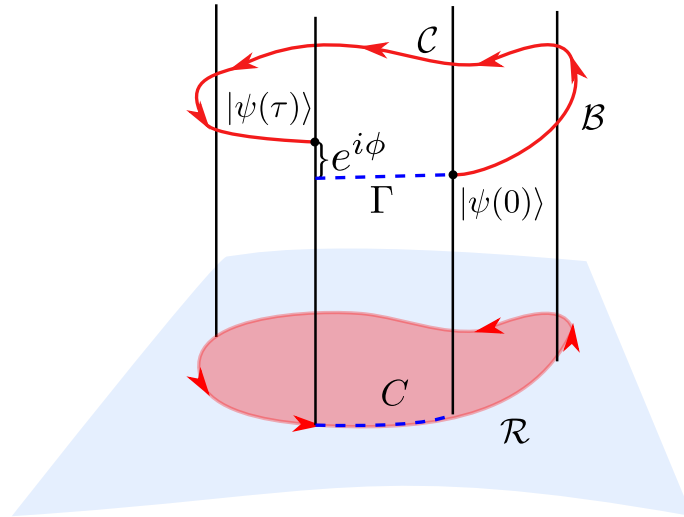


FIGURE 2.4: Schematic for non-cyclic geometric phase in Samuel and Bhandari's setting.

Now, we come to the main results of Samuel & Bhandari. Let us consider a quantum system undergoing a non-cyclic evolution and the initial $|\psi(0)\rangle$ and final state vector $|\psi(\tau)\rangle$ does not belong to the same ray. Also, the curve $C \in \mathcal{R}$ is not a closed curve. At this point Pancharatnam

comes to our rescue and shows us a way to proceed.

The most important result proved by Samuel and Bhandari is that the Pancharatnam phase difference β between any two nonorthogonal states $|\phi_1\rangle$ and $|\phi_2\rangle$ is written as the integral of one-form A_s along a *geodesic* i.e.

$$\beta = \arg \langle \phi_1 | \phi_2 \rangle = \int_{\Gamma} A_s ds \quad (2.65)$$

where Γ is the geodesic curve $|\phi(s)\rangle$ that connects $|\phi_1\rangle$ and $|\phi_2\rangle$. We are not going through the proof here, although we will discuss geodesics in great detail in the next section. The structure of geodesics is very important for one of our problem that we dealt with in this thesis.

Therefore, the geometric phase acquired by a state vector $|\phi(s)\rangle$ as it evolves from $|\phi(0)\rangle$ to $|\phi(\tau)\rangle$ (they are not orthogonal) is expressed as

$$\phi_g = \int_{\mathcal{C}+\Gamma} A_s ds = \int_{\mathcal{C}} A_s ds + \int_{\Gamma} A_s ds \quad (2.66)$$

where \mathcal{C} is the horizontal curve along which A_s and hence the first integral vanishes. Thus, the geometric phase between $|\phi(0)\rangle$ and $|\phi(\tau)\rangle$ is given by the integral Eq. (2.63) where the curve \mathcal{C} is given by the actual evolution of the system from $|\phi(0)\rangle$ to $|\phi(\tau)\rangle$ and *back along a geodesic curve* connecting $|\phi(\tau)\rangle$ and $|\phi(0)\rangle$. This can also be expressed as a surface integral of two-form \mathcal{F} over a surface bounded by the curve $\pi(\mathcal{C})$ in the projective Hilbert space \mathcal{R} . This geodesic rule proposition for the non-cyclic geometric phase has recently been experimentally tested by Folman *et al.* [41]. They also discussed the possible applications of geodesic rule in general relativity to obtain the red-shifts. This might be the first step towards probing/measuring gravitational effects using a quantum system.

In the original paper of Samuel & Bhandari, they worked with a subset of Hilbert space \mathcal{H} with non-zero state vectors i.e. $\langle \psi | \psi \rangle \neq 0$ and not with unit vectors.

2.6 Kinematic Approach to geometric phase

The final generalization for the geometric phase has been proposed by Simon & Mukunda [29] based entirely on the kinematic approach. In this approach, there is no need for dynamics (or Hamiltonian), and the whole idea is based on the characteristics of curves connecting two states in projective Hilbert space \mathcal{R} .

For any given two state vectors $|\psi_1\rangle, |\psi_2\rangle \in \mathcal{B}$, we start by looking for the invariant under the $U(1)$ phase transformation given by

$$|\psi'_1\rangle = e^{i\alpha_1} |\psi_1\rangle, \quad |\psi'_2\rangle = e^{i\alpha_2} |\psi_2\rangle. \quad (2.67)$$

The one possible nontrivial invariant can be modulus of the inner product of the two vectors, which reads

$$|\langle \psi_1 | \psi_2 \rangle| = |\langle \psi'_1 | \psi'_2 \rangle| \quad (2.68)$$

that is $U(1) \times U(1)$ -invariant. We can extend it to three given states $\{|\psi_1\rangle, |\psi_2\rangle, |\psi_3\rangle\} \in \mathcal{B}$ using *Bargmann invariants* [27] of the form

$$\langle \psi_1 | \psi_2 \rangle \langle \psi_2 | \psi_3 \rangle \langle \psi_3 | \psi_1 \rangle \quad (2.69)$$

that are $U(1) \times U(1) \times U(1)$ -invariant and subsequently for $\{|\psi_1\rangle, |\psi_2\rangle, \dots, |\psi_N\rangle\} \in \mathcal{B}$ we can write a cyclic quantity as

$$\langle \psi_1 | \psi_2 \rangle \langle \psi_2 | \psi_3 \rangle \dots \langle \psi_N | \psi_1 \rangle \quad (2.70)$$

that is $U(1) \times U(1) \times \dots \times U(1)$ -invariant (there are N numbers of $U(1)$'s). The modulus of the inner product of the two vectors is the simplest example of a Bargmann invariant

$$|\langle \psi_1 | \psi_2 \rangle|^2 = \langle \psi_1 | \psi_2 \rangle \langle \psi_2 | \psi_1 \rangle. \quad (2.71)$$

The expression Eq. (2.69) is a *complex* invariant in contrast with the expression Eq. (2.67) which are limited to real and positive values. We will soon explore the importance of Bargmann invariants in the study of geometric phases.

2.6.1 Geometric phase for smooth parametrized curve

Consider a one-parameter smooth curve $\mathcal{C} \in \mathcal{B}$ that consists of state vectors $|\psi(s)\rangle$ and reads

$$\mathcal{C} = \{|\psi(s)\rangle \in \mathcal{B} \mid s \in [s_1, s_2] \subset \mathbb{R}\}. \quad (2.72)$$

By invoking the normalization of $|\psi(s)\rangle$, it is easy to show that the quantity $\langle \psi(s) | \dot{\psi}(s) \rangle$ is pure imaginary i.e.

$$\langle \psi(s) | \dot{\psi}(s) \rangle = i \operatorname{Im} \langle \psi(s) | \dot{\psi}(s) \rangle \quad (2.73)$$

where the dot represents the derivative with respect to s . Now, we perform phase changes on $|\psi(s)\rangle$ at each value of s , i.e., local phase transformation which we call *gauge transformation*. These transformations are characterized by a smooth parameter $\alpha(s)$, which takes \mathcal{C} to \mathcal{C}' as

$$\mathcal{C} \rightarrow \mathcal{C}' = \{|\psi'(s)\rangle = e^{i\alpha(s)} |\psi(s)\rangle \mid s \in [s_1, s_2]\}. \quad (2.74)$$

Under this gauge transformation, the quantity in Eq. (2.73) transforms as

$$\langle \psi(s) | \frac{d}{ds} |\psi(s)\rangle \rightarrow \langle \psi'(s) | \frac{d}{ds} |\psi'(s)\rangle = \langle \psi(s) | \frac{d}{ds} |\psi(s)\rangle + i\dot{\alpha}(s) \quad (2.75)$$

and

$$\operatorname{Im} \langle \psi'(s) | \dot{\psi}'(s) \rangle = \langle \psi(s) | \dot{\psi}(s) \rangle + \dot{\alpha}(s). \quad (2.76)$$

Note that the quantity in Eq. (2.73) is invariant under *global transformation* of the kind $|\psi(s)\rangle \rightarrow |\psi'(s)\rangle = e^{i\alpha} |\psi(s)\rangle$. Now, our goal is to construct a functional of \mathcal{C} that is invariant under the gauge transformation given in Eq. (2.74) i.e. which should be same for \mathcal{C} and \mathcal{C}' . Such a functional is given by

$$\begin{aligned} \phi_g[\mathcal{C}] &= \arg \langle \psi(s_1) | \psi(s_2) \rangle - \operatorname{Im} \int_{s_1}^{s_2} ds \langle \psi(s) | \dot{\psi}(s) \rangle \\ &= \arg \langle \psi'(s_1) | \psi'(s_2) \rangle - \operatorname{Im} \int_{s_1}^{s_2} ds \langle \psi'(s) | \dot{\psi}'(s) \rangle \\ &= \text{gauge invariant.} \end{aligned} \quad (2.77)$$

Choosing different curves \mathcal{C} or \mathcal{C}' corresponds to choosing different Hamiltonians, and the invariance of the functional under the gauge transformations means that this is a functional of the image $C \in \mathcal{R}$ of \mathcal{C} in the projective Hilbert space. In addition to the invariance under gauge

transformation, the function $\phi_g[\mathcal{C}]$ is also *reparametrisation* invariant. The reparametrisation transformations are defined as

$$\mathcal{C} \rightarrow \mathcal{C}' = \{|\psi'(s')\rangle \in \mathcal{B} \mid s' = f(s), \frac{df(s)}{ds} \geq 0\} \quad (2.78)$$

Under such a transformation, we have $ds = \frac{ds}{df} df$

$$\begin{aligned} & \arg \langle \psi'(f(s_1)) | \psi'(f(s_2)) \rangle - \text{Im} \int_{f(s_1)}^{f(s_2)} \langle \psi'(f(s)) | \frac{d}{df} \frac{df}{ds} | \psi'(f(s)) \rangle \frac{ds}{df} df \\ &= \arg \langle \psi'(f(s_1)) | \psi'(f(s_2)) \rangle - \text{Im} \int_{f(s_1)}^{f(s_2)} \langle \psi'(f(s)) | \frac{d}{df} | \psi'(f(s)) \rangle df \end{aligned}$$

and

$$|\psi[f(s)]\rangle = |\psi(s)\rangle \implies |\psi'[f(s_1)]\rangle = |\psi(s_1)\rangle, \quad |\psi'[f(s_2)]\rangle = |\psi(s_2)\rangle \quad (2.79)$$

for $f(s_1) = s_1$ and $f(s_2) = s_2$. The reparameterization transformation takes a curve $\mathcal{C} \in \mathcal{B}$ to $\mathcal{C}' \in \mathcal{B}$ that is transversed at a different rate. Thus, the functional $\phi_g[\mathcal{C}]$ gives the geometric phase associated with a smooth curve $\mathcal{C} \in \mathcal{R}$. The individual terms in the functional depend on a particular lift $\mathcal{C} \in \mathcal{B}$ of the smooth curve $\mathcal{C} \in \mathcal{R}$, whereas the functional itself depends only on the smooth curve $\mathcal{C} = \pi[\mathcal{C}] = \pi[\mathcal{C}']$ in the projective Hilbert space \mathcal{R} . This implies the possibility that the geometric phase is the property of the projective Hilbert space \mathcal{R} and we write it as

$$\phi_g[\mathcal{C}] \equiv \arg \langle \psi(s_1) | \psi(s_2) \rangle - \text{Im} \int_{s_1}^{s_2} ds \langle \psi(s) | \dot{\psi}(s) \rangle. \quad (2.80)$$

Also, this definition is only valid when $|\psi(s_1)\rangle$ and $|\psi(s_2)\rangle$ are *non-orthogonal* because the first inner product between the initial and final states vanishes, and hence $\arg \langle \psi(s_1) | \psi(s_2) \rangle$ is not defined in case two states are orthogonal. The two terms on the RHS of the above equation are identified as

$$\arg \langle \psi(s_1) | \psi(s_2) \rangle \equiv \phi_t[\mathcal{C}] = \text{total phase of } \mathcal{C}, \quad (2.81)$$

$$\text{Im} \int_{s_1}^{s_2} ds \langle \psi(s) | \dot{\psi}(s) \rangle \equiv \phi_{\text{dyn}}[\mathcal{C}] = \text{dynamical phase of } \mathcal{C} \quad (2.82)$$

It is very important to note that these two functionals depend on \mathcal{C} individually and it is only their difference that is a functional of \mathcal{C} .

Now, for a given smooth curve \mathcal{C} in the projective Hilbert space \mathcal{R} . There are several options

to choose a lift $\mathcal{C} \in \mathcal{B}$ to calculate $\phi_g[\mathcal{C}]$. We point out two such lifts, which are interesting:

- (i) we can choose a lift such that the total phase $\phi_t[\mathcal{C}] = \arg \langle \psi(s_1) | \psi(s_2) \rangle$ vanishes along the curve and the two state vectors $|\psi(s_1)\rangle$ and $|\psi(s_2)\rangle$ are said to be *in phase* i.e

$$\phi_t[\mathcal{C}] = 0 \implies \phi_g[\mathcal{C}] = -\phi_{\text{dyn}}[\mathcal{C}].$$

- (ii) or we can choose a lift such that the dynamical phase $\phi_{\text{dyn}}[\mathcal{C}]$ vanishes. This lift is called a *horizontal lift* and it hold the parallel-transport law i.e

$$\mathcal{C} \text{ horizontal} \implies \langle \psi(s) | \dot{\psi}(s) \rangle = 0 \implies \phi_{\text{dyn}}[\mathcal{C}] = 0 \implies \phi_g[\mathcal{C}] = \phi_t[\mathcal{C}].$$

2.6.2

Geodesics in ray space \mathcal{R} We started by constructing gauge invariant quantities with a given finite set of vectors and then showed how can one approach to define a gauge invariant, reparametrization invariant functional to define the geometric phase. We will now derive an expression for geometric phase in terms of the gauge invariant quantities, very well known as Bargmann invariants. To do that, we first need to introduce the notion of a "geodesic". The shortest curve between any given two points on a surface is a geodesic¹. For example, a geodesic between two points on a sphere is a curve along the great circle passing through the two points, as shown in Fig. 2.5. In this section we will introduce the *geodesics* and how they are important in the context of geometric phase. We will first derive a differential equation by minimizing the distance and using the variational approach. Let us start by considering a smooth parametrized curve $\mathcal{C} = \{|\psi(s)\rangle\} \subset \mathcal{B}$. The tangent at the point $|\psi(s)\rangle$ on \mathcal{C} , gives the velocity that we write as

$$|u(s)\rangle = \frac{d}{ds} |\psi(s)\rangle \quad (2.83)$$

and the component of $|u(s)\rangle$ that is orthogonal to $|\psi(s)\rangle$ reads

$$|u_{\perp}(s)\rangle = |u(s)\rangle - (\langle \psi(s) | u(s) \rangle) |\psi(s)\rangle \quad (2.84)$$

¹Geodesics are locally shortest paths. The minimal length path between two points is referred to as minimal geodesic connecting those points. Here, it is essential to note that a curve being locally the shortest does not necessarily imply it is globally the shortest [42, 43]. We will frequently use the term geodesic; by this, we shall always mean minimal geodesic, which is unique provided that the given pair of points correspond to nonorthogonal states.

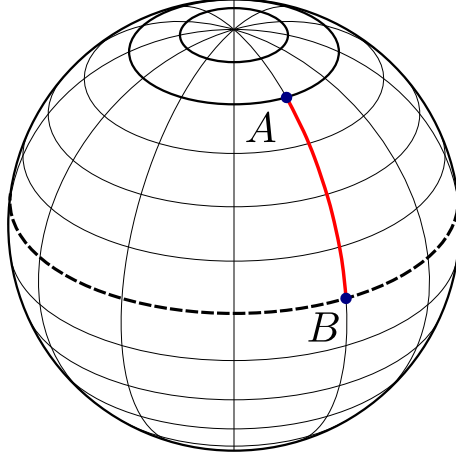


FIGURE 2.5: A geodesic on the surface of a sphere.

The motivation to choose the orthogonal component of the tangent vector $|u_{\perp}(s)\rangle$ is because under gauge transformation of the kind $|\psi(s)\rangle \rightarrow |\psi'(s)\rangle = e^{i\alpha(s)} |\psi(s)\rangle$ it is $|u_{\perp}(s)\rangle$ that transforms linearly and homogeneously as same as $|\psi(s)\rangle$ i.e. $|u'_{\perp}(s)\rangle = e^{i\alpha(s)} |u_{\perp}(s)\rangle$ [9, 44]. We can now define a functional that is a ray space quantity called length as

$$\mathcal{L}[C] = \int_{s_1}^{s_2} ds \langle u_{\perp}(s) | u_{\perp}(s) \rangle^{1/2}. \quad (2.85)$$

which is gauge and reparametrization invariant. The quantity

$$\|u_{\perp}\| = \langle u_{\perp}(s) | u_{\perp}(s) \rangle^{1/2} = (\langle u(s) | u(s) \rangle - \langle u(s) | \psi(s) \rangle \langle \psi(s) | u(s) \rangle) \quad (2.86)$$

is the norm of the tangent vector $|u(s)\rangle$. A class of curves in \mathcal{R} for which this length is stationary ($\delta\mathcal{L} = 0$) is called *geodesic curves*. The differential equation for the geodesic curves can be obtained using the variational principle. By making an infinitesimal change in $|\psi(s)\rangle$ we obtain

the following

$$\begin{aligned}
\delta\mathcal{L}[C] &= \frac{1}{2} \int_{s_1}^{s_2} ds \frac{1}{\|u_\perp\|} \delta (\langle u|u \rangle - \langle u|\psi \rangle \langle \psi|u \rangle), \\
&= \frac{1}{2} \int_{s_1}^{s_2} ds \frac{1}{\|u_\perp\|} (\langle \delta u|u \rangle + \langle u|\delta u \rangle - \langle \delta u|\psi \rangle \langle \psi|u \rangle - \langle u|\delta \psi \rangle \langle \psi|u \rangle \\
&\quad - \langle u|\psi \rangle \langle \delta \psi|u \rangle - \langle u|\psi \rangle \langle \psi|\delta u \rangle), \\
&= \int_{s_1}^{s_2} ds \frac{1}{\|u_\perp\|} \text{Re} (\langle \delta u|u \rangle - \langle \delta u|\psi \rangle \langle \psi|u \rangle - \langle \delta \psi|u \rangle \langle u|\psi \rangle), \\
&= \int_{s_1}^{s_2} ds \frac{1}{\|u_\perp\|} \text{Re} (\langle \delta u|u_\perp \rangle - \langle \delta \psi|u \rangle \langle u|\psi \rangle) \tag{2.87}
\end{aligned}$$

where in the third step we collected (1) and (2), (3) and (6), (4) and (5) terms from inside the brackets which are complex conjugates of each other. If we look at the term,

$$\begin{aligned}
\langle \delta \psi|u \rangle \langle u_\perp|\psi \rangle &= \langle \delta \psi|u_\perp \rangle \langle u|\psi \rangle \\
&= \langle \delta \psi|(u - \langle \psi|u \rangle \psi) \rangle \langle u|\psi \rangle \\
&= \langle \delta \psi|u \rangle \langle u|\psi \rangle - \langle \delta \psi|\psi \rangle |\langle u|\psi \rangle|^2 \\
\implies \text{Re} \langle \delta \psi|u \rangle \langle u_\perp|\psi \rangle &= \text{Re} \langle \delta \psi|u \rangle \langle u|\psi \rangle
\end{aligned}$$

where we used the fact that $\langle u|\psi \rangle$ and $\langle \delta \psi|\psi \rangle$, both are pure imaginary. Therefore,, we can write

$$\delta\mathcal{L}[C] = \int_{s_1}^{s_2} ds \frac{1}{\|u_\perp\|} \text{Re} (\langle \delta u|u_\perp \rangle + \langle \delta \psi|u_\perp \rangle \langle \psi|u \rangle)$$

Now, by integrating the first term with δu by parts, we get

$$\int_{s_1}^{s_2} ds \text{Re} \left\langle \frac{d}{ds} \delta \psi \left| \frac{u_\perp}{\|u_\perp\|} \right. \right\rangle = \left\langle \delta \psi \left| \frac{u_\perp}{\|u_\perp\|} \right. \right\rangle \Big|_{s_1}^{s_2} - \int ds \left\langle \delta \psi \left| \frac{d}{ds} \frac{u_\perp}{\|u_\perp\|} \right. \right\rangle$$

and by discarding the boundary terms, we finally have

$$\delta\mathcal{L}[C] = - \int_{s_1}^{s_2} ds \text{Re} \left\langle \delta \psi \left| \left(\frac{d}{ds} \frac{u_\perp}{\|u_\perp\|} - \langle \psi|u \rangle \frac{u_\perp}{\|u_\perp\|} \right) \right. \right\rangle \tag{2.88}$$

By demanding that this integral vanishes for any arbitrary variations $\delta \psi$ and subjected to the

condition $\langle \delta\psi | \psi \rangle$ is pure imaginary, we get a differential equation for a geodesic which reads

$$\left(\frac{d}{ds} - \langle \psi(s) | u(s) \rangle \right) \frac{|u_{\perp}(s)\rangle}{\|u_{\perp}(s)\|} = f(s) |\psi(s)\rangle \quad (2.89)$$

where $f(s)$ is some real function. We note that since $\mathcal{L}[C]$ is gauge and reparametrization invariant, the differential equation for a geodesic is gauge and reparametrization covariant and yields the same result for any lift of a given smooth curve $C \in \mathcal{R}$. Also, if C is a geodesic in \mathcal{R} , then any lift of C in \mathcal{B} will also be a geodesic. One such lift is the horizontal one along which $\langle \psi(s) | u(s) \rangle$ vanishes and Eq. (2.89) reduces to a simpler form

$$\frac{d}{ds} \frac{|u(s)\rangle}{\|u(s)\|} = f(s) |\psi(s)\rangle \quad (2.90)$$

with some real $f(s)$. Further, we can exploit the reparameterization freedom to demand $\|u(s)\|$ to be constant. This freedom makes our life easy and we can further write Eq. (2.90) as

$$\frac{d^2}{ds^2} |\psi(s)\rangle = f(s) |\psi(s)\rangle \quad (2.91)$$

with

$$\langle \psi(s) | \psi(s) \rangle = 1, \quad \langle \psi(s) | u(s) \rangle = 0, \quad \langle u(s) | u(s) \rangle = \text{constant}. \quad (2.92)$$

Using the conditions given in the above expression, we can evaluate the real function $f(s)$ as

$$\begin{aligned} \langle \psi(s) | \psi(s) \rangle = 1 &\implies \langle \psi(s) | \dot{\psi}(s) \rangle + \langle \dot{\psi}(s) | \psi(s) \rangle = 0 \\ \langle \psi(s) | \ddot{\psi}(s) \rangle + \langle \ddot{\psi}(s) | \psi(s) \rangle + 2 \langle \dot{\psi}(s) | \dot{\psi}(s) \rangle &= 0 \\ \implies f(s) &= - \langle \dot{\psi}(s) | \dot{\psi}(s) \rangle \end{aligned} \quad (2.93)$$

which further reduces Eq. (2.91) to

$$\frac{d^2}{ds^2} |\psi(s)\rangle = - \langle \dot{\psi}(s) | \dot{\psi}(s) \rangle |\psi(s)\rangle \quad (2.94)$$

Since the above differential equation resembles the simple harmonic motion. The general solution of the reads

$$|\psi(s)\rangle = |\psi(0)\rangle \cos(\omega s) + |\dot{\psi}(0)\rangle \frac{\sin(\omega s)}{\omega} \quad (2.95)$$

with

$$\langle \psi(0) | \psi(0) \rangle = 1, \quad \langle \psi(0) | \dot{\psi}(0) \rangle = 0, \quad \langle \dot{\psi}(0) | \dot{\psi}(0) \rangle = \omega^2 \quad (2.96)$$

We note that everything is reduced to the real domain here. For a horizontal lift, we have $\phi_g[C] = \arg \langle \psi(s_1) | \psi(s_2) \rangle$ which will be identically zero. Therefore, we have a very important result here, which becomes handy at many places in which the geometric phase vanishes along a geodesic curve.

$$C = \text{geodesic} \implies \phi_g[C] = 0. \quad (2.97)$$

Given any two non-orthogonal vectors in \mathcal{B} , we can connect them by a unique geodesic curve. We consider two nonorthogonal vectors $|\psi_1\rangle, |\psi_2\rangle$ such that the inner product is

$$\langle \psi_1 | \psi_2 \rangle = \cos(\theta) e^{i\beta}. \quad (2.98)$$

The geodesic curve connecting $|\psi_1\rangle$ and $|\psi_2\rangle$ which is a unique solution of Eq. (7.14) reads [29]

$$\begin{aligned} |\psi(s)\rangle &= e^{i\beta s/\theta} \left[\cos(s) |\psi_1\rangle + \left(\frac{e^{-i\beta} |\psi_2\rangle - |\psi_1\rangle \cos \theta}{\sin \theta} \right) \sin(s) \right], \\ &= e^{i\beta s/\theta} (\sin(\theta - s) |\psi_1\rangle + e^{-i\beta} \sin(s) |\psi_2\rangle) / \sin \theta \end{aligned} \quad (2.99)$$

where s varies from 0 to θ . In this way, one can construct a unique geodesic between any given two nonorthogonal states [9]. Here we note that, a geodesic connecting the two orthogonal states may not be unique. For example, there exist infinite choices to connect two antipodal points, on the Bloch sphere, via a geodesic.

2.6.3 Bargmann invariant and geometric phase

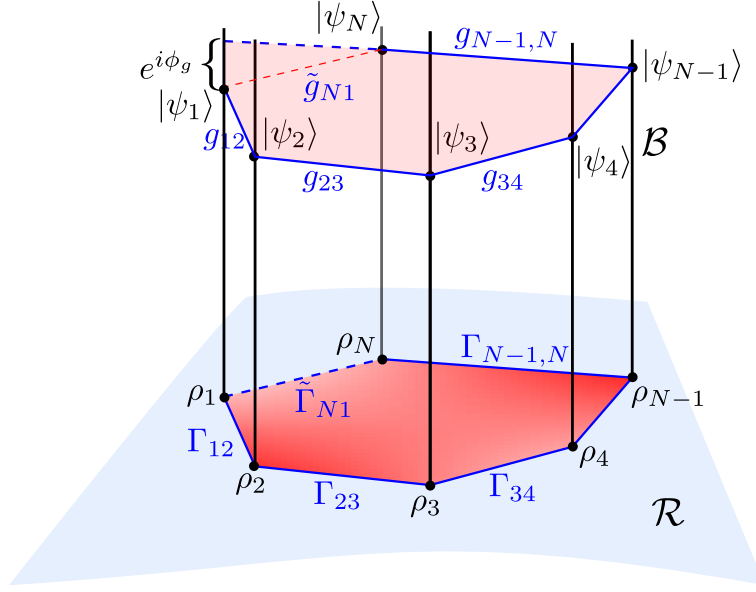


FIGURE 2.6: Bargmann invariant

We now move on to second part of their result, which is about the Bargmann invariant and its connection with the geometric phase. Let us consider as open polygonal curve C in projective Hilbert space \mathcal{R} which consists of $N-1$ geodesics ($\Gamma_{12}, \Gamma_{23}, \dots$) connecting ρ_1 to ρ_2 , ρ_2 to ρ_3 , \dots , ρ_{N-1} to ρ_N as shown in Fig. 2.6. The $\rho_1, \rho_2, \dots, \rho_N$ are the given N points on the curve $C \in \mathcal{R}$. Now, we construct a lift $\mathcal{C} \in \mathcal{B}$ of the curve C such that the state vectors $|\psi_1\rangle, |\psi_2\rangle, |\psi_3\rangle, \dots, |\psi_N\rangle$ are mutually nonorthogonal. We connect the successive pair of state vectors with a geodesic $g_{12}, g_{23}, \dots, g_{N-1,N}$ as shown in Fig. 2.6. Then, the geometric phase for the open curve C is given by

$$\begin{aligned} \phi_g[C] &= \phi_t[C] - \phi_{\text{dyn}}[C] \\ &= \arg \langle \psi_1 | \psi_N \rangle - \sum_{i=1}^{N-1} \phi_{\text{dyn}}[\text{geodesic}(g_{i,i+1}) | \psi_i \rangle \text{ to } | \psi_{i+1} \rangle] \end{aligned} \quad (2.100)$$

By making use of the result in Eq. (2.97) and the dynamical part in the above expression can be further written as

$$\sum_{i=1}^{N-1} \phi_{\text{dyn}}[\text{geodesic}(g_{i,i+1}) | \psi_i \rangle \text{ to } | \psi_{i+1} \rangle] = \sum_{i=1}^{N-1} \{ \phi_t[g_{i,i+1}] - \phi_g[\Gamma_{i,i+1}] \} = \sum_{i=1}^{N-1} \phi_t[g_{i,i+1}]. \quad (2.101)$$

Therefore, $\phi_g[C]$ becomes

$$\begin{aligned}
\phi_g[C] &= \arg \langle \psi_1 | \psi_N \rangle - \sum_{i=1}^{N-1} \phi_t[g_{i,i+1}] \\
&= \arg \langle \psi_1 | \psi_N \rangle - \sum_{i=1}^{N-1} \arg \langle \psi_i | \psi_{i+1} \rangle \\
&= - \arg \langle \psi_1 | \psi_2 \rangle \langle \psi_2 | \psi_3 \rangle \dots \langle \psi_{N-1} | \psi_N \rangle \langle \psi_N | \psi_1 \rangle.
\end{aligned} \tag{2.102}$$

Here, we see how beautifully Bargmann invariants appear in the discussion of geometric phase and finally the geometric phase is expressed as the negative of the argument of Bargmann invariant associated with a polygonal (discrete) path C . Just for completeness, we can go one step further to close the curve C by connecting ρ_N to ρ_1 with a geodesic as shown by the blue dotted line in Fig. 2.6 and call the new curve \tilde{C} . The same thing we do with the lift and connect $|\psi_N\rangle$ to $|\psi_1\rangle$ with a geodesic and close the curve as shown by the dotted red line in Fig. 2.6. With these considerations, we shall have

$$\begin{aligned}
\phi_g[\tilde{C}] &= \phi_t[\tilde{C}] - \phi_{\text{dyn}}[\tilde{C}] \\
&= - \sum_{i=1}^N \phi_{\text{dyn}}[g_{i,i+1}] \\
&= - \sum_{i=1}^N \{ \phi_t[g_{i,i+1}] - \phi_g[\Gamma_{i,i+1}] \} \\
&= - \sum_{i=1}^N \phi_t[g_{i,i+1}] = \sum_{i=1}^N \arg \langle \psi_i | \psi_{i+1} \rangle \\
&= - \arg \langle \psi_1 | \psi_2 \rangle \langle \psi_2 | \psi_3 \rangle \dots \langle \psi_{N-1} | \psi_N \rangle \langle \psi_N | \psi_1 \rangle \\
&= \phi_g[C]
\end{aligned} \tag{2.103}$$

with $|\psi_{N+1}\rangle \equiv |\psi_1\rangle$. Here, we see that the geometric for both curves is identical. This is one of the results of Samuel and Bhandari and it works perfectly fine in the general setting. The geodesic connecting ρ_N to ρ_1 does not contribute to any geometric phase due to the very basic construction of a geodesic.

2.6.4 Continuous limit of Bargmann invariant

In this section, we will retrieve the main expression of the geometric phase Eq. (2.80) starting from the Bargmann invariant. We take a smooth parameterized curve $\mathcal{C} \in \mathcal{B}$ (with projection $C \in \mathcal{R}$) with parameter $s \in [s_1, s_2]$ and divide it into N bins of size Δs as shown in Fig. 2.7.

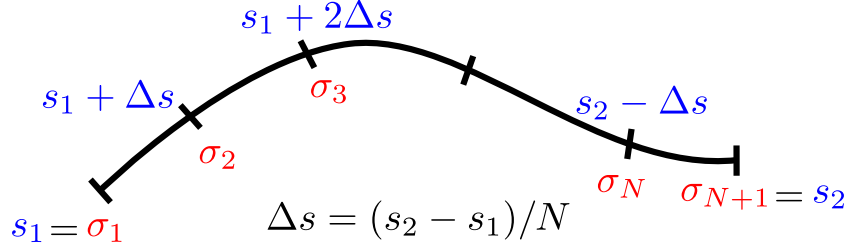


FIGURE 2.7: Continuous limit of Bargmann invariant

The corresponding points on \mathcal{C} are given by

$$|\psi(s_1)\rangle \equiv |\psi(\sigma_1)\rangle = |\psi_1\rangle, \quad |\psi(\sigma_2)\rangle = |\psi_2\rangle, \dots, \quad |\psi(\sigma_N)\rangle = |\psi_N\rangle, \quad |\psi(s_2)\rangle \equiv |\psi(\sigma_{N+1})\rangle = |\psi_{N+1}\rangle$$

and connect the successive pair of state vectors $|\psi_j\rangle$ and $|\psi_{j+1}\rangle$ by a geodesic arc such that the geometric phase is written in terms of the Bargmann invariant as

$$\begin{aligned} \phi_g[C] &= \lim_{N \rightarrow \infty} \left\{ -\arg \langle \psi_1 | \psi_2 \rangle \langle \psi_2 | \psi_3 \rangle \dots \langle \psi_N | \psi_{N+1} \rangle \langle \psi_{N+1} | \psi_1 \rangle \right\} \\ &= \lim_{N \rightarrow \infty} \left\{ \arg \langle \psi(s_1) | \psi(s_2) \rangle - \arg \prod_{j=1}^N \langle \psi(\sigma_j) | \psi(\sigma_{j+1}) \rangle \right\} \\ &= \lim_{N \rightarrow \infty} \left\{ \arg \langle \psi(s_1) | \psi(s_2) \rangle - \arg \prod_{j=1}^N \left(\langle \psi(\sigma_j) | \psi(\sigma_j) + \Delta s \dot{\psi}(\sigma_j) + \mathcal{O}(\Delta s^2) \rangle \right) \right\} \\ &\approx \lim_{N \rightarrow \infty} \left\{ \arg \langle \psi(s_1) | \psi(s_2) \rangle - \arg \prod_{j=1}^N \left(1 + \Delta s \langle \psi(\sigma_j) | \dot{\psi}(\sigma_j) \rangle \right) \right\} \\ &\approx \lim_{N \rightarrow \infty} \left\{ \arg \langle \psi(s_1) | \psi(s_2) \rangle - \arg \exp \left(\sum_{j=1}^N \Delta s \langle \psi(\sigma_j) | \dot{\psi}(\sigma_j) \rangle \right) \right\} \\ &= \arg \langle \psi(s_1) | \psi(s_2) \rangle - \arg \exp \left(\int_{s_1}^{s_2} ds \langle \psi(s) | \dot{\psi}(s) \rangle \right) \end{aligned}$$

which is the same as Eq. (2.80). The expression of geometric phase in terms of Bargmann invariant is instrumental in processes where we have measurements, which results in a discrete set of states [45–47]. With this we end the discussion on the geometric phase for pure states.

The geometric phase for mixed states has been experimentally verified in several systems such as photons [48], NMR [49], neutrons [50], sodium trimer [51], and in graphene [52], Mach-Zehnder interferometer [53] and polarimetry [54, 55]. There also exists a method where the geometric phase has been measured without interferometry [56].

2.7 Null phase curves

We have seen that geodesics play an integral role in establishing a relation between the geometric phase and the Bargmann invariants because the system does not acquire any geometric phase when evolves along a geodesic. We connect two consecutive state vectors (nonorthogonal) by a geodesic. This notion can be extended to define a broader class of ray space curves with the property that the geometric phase vanishes for any connected stretch of any of these curves [10]. These are known as "null phase curves", and these provide an alternative way to connect geometric phase with Bargmann invariants by replacing geodesics with null phase curves. Null phase curves (NPCs) are the larger class of curves and geodesics are the subset of them. We recall Eq. (2.102),

$$\begin{aligned}\phi_g[C] &= -\arg \langle \psi_1 | \psi_2 \rangle \langle \psi_2 | \psi_3 \rangle \dots \langle \psi_{N-1} | \psi_N \rangle \langle \psi_N | \psi_1 \rangle \\ &= -\arg \Delta_N(\psi_1, \psi_2, \dots, \psi_N)\end{aligned}\tag{2.104}$$

where C is the N -vertex polygon in the projective Hilbert space \mathcal{R} connecting ρ_1 to ρ_2 , ρ_2 to ρ_3 , \dots , ρ_N to ρ_1 by geodesics with $\rho_1, \rho_2, \dots, \rho_N$ being projections of $|\psi_1\rangle, |\psi_2\rangle, \dots, |\psi_N\rangle$, respectively in \mathcal{R} . Here, we note that the LHS of Eq. (2.102) gives the geometric phase which depends on a discrete set of state vectors, whereas, to evaluate RHS we need an additional element, a curve that connects consecutive state vectors without contributing any extra geometric phase. Mathematically, a smooth parametrized curve $\mathcal{C} = \{|\psi(s)\rangle \in \mathcal{B} \mid s \in [s_1, s_2]\} \in \mathcal{B}$, with

$$\langle \psi(s) | \psi(s') \rangle \neq 0, \quad \forall s, s' \in [s_1, s_2]\tag{2.105}$$

and $|\psi(s)\rangle, \rho(s)$ continuous once differentiable will be an NPC, if for any three mutually nonorthogonal consecutive vectors on it, the third-order Bargmann invariant is real and posi-

tive [57] i.e.,

$$\Delta_3(\psi(s), \psi(s'), \psi(s'')) = \text{Tr}(\rho(s)\rho(s')\rho(s'')) > 0, \quad s, s', s'' \in [s_1, s_2]. \quad (2.106)$$

We leave NPCs with this remark to maintain the continuity of the discussion on the geometric phase for mixed states. We will discuss NPCs in detail in Chapter 7.

2.8 Geometric phase for mixed states

So far, we have only considered pure quantum states, which are projectors of rank one and represent only a very limited class of quantum states. For example, the dynamics of a quantum system interacting with another system (an external environment) cannot be fully captured by a pure state. These are the so-called open quantum systems. Even if we start initially in a pure state of the form $|\psi\rangle = |\phi_1\rangle \otimes |\phi_2\rangle \in \mathcal{H}_{SE} = \mathcal{H}_S \otimes \mathcal{H}_E$, the system evolves to a state (entangled state) that cannot be written anymore as the tensor product of the states of individual systems. However, in such cases, a quantum state can be represented by the statistical average (or the ensemble) of the pure states. These statistical averages are called *mixed* quantum states and are represented by *density operators* (or *density matrix*). Suppose that a quantum system is in either one of the states $|\psi_i\rangle$ with respective probabilities p_i where $i = 1, 2, 3, \dots, N$. The density operator for this system is defined as

$$\rho \equiv \sum_i p_i |\psi_i\rangle\langle\psi_i|. \quad (2.107)$$

with $\sum_i p_i = 1$. An important point to appreciate here is that statistical averages are different from quantum superposition. If we have a system that is in the pure states $|\psi_1\rangle$ and $|\psi_2\rangle$ with respective probabilities p_1 and p_2 , then the superposed state will look like

$$|\Psi\rangle = \sqrt{p_1} |\psi_1\rangle + e^{i\phi} \sqrt{p_2} |\psi_2\rangle \quad (2.108)$$

with an arbitrary and unknown phase $\phi \in \mathbb{R}$ and the corresponding density matrix will be

$$\rho = p_1 |\psi_1\rangle\langle\psi_1| + p_2 |\psi_2\rangle\langle\psi_2| \quad (2.109)$$

which are not the same. A rank-one projector, representing a pure state, is a special case of a density operator. However, a general density operator can have a rank greater than 1. The density operator of a statistical average of a number of pure states is a convex sum of the density operators of the individual states. A density operator ρ is represented by a positive operator with unit trace, i.e.

$$\langle \phi | \rho | \phi \rangle \geq 0 \quad \forall \quad |\phi\rangle \in \mathcal{H}, \quad \text{Tr } \rho = 1. \quad (2.110)$$

For a given distribution of states $\{p_i, |\psi_i\rangle\}$, we have a unique density operator given by Eq. (2.107), however, the reverse is not true. The given density operator ρ can be decomposed into infinite ways representing distinct ensembles. To illustrate this, let us take ρ and write its spectral decomposition as

$$\rho = \sum_i \lambda_i |\psi_i\rangle\langle\psi_i|, \quad \lambda_i \geq 0, \quad \sum_i \lambda_i = 1 \quad (2.111)$$

where $\{|\psi_i\rangle\}$ forms an orthonormal set of basis. Now we define a new set of vectors $|\phi_k\rangle$ using a unitary operator W as

$$|\phi_k\rangle = \sum_i W_{ki} \sqrt{\lambda_i} |\psi_i\rangle \quad (2.112)$$

and we see

$$\begin{aligned} \sum_k |\phi_k\rangle\langle\phi_k| &= \sum_k \left(\sum_i W_{ki} \sqrt{\lambda_i} |\psi_i\rangle \right) \left(\sum_j W_{jk}^* \sqrt{\lambda_j} \langle\psi_j| \right) \\ &= \sum_{ij} \sqrt{\lambda_i \lambda_j} \left(\sum_k W_{ki} W_{jk}^* \right) |\psi_i\rangle\langle\psi_j| \\ &= \sum_{ij} \delta_{ij} \sqrt{\lambda_i \lambda_j} |\psi_i\rangle\langle\psi_j| \\ &= \sum_i \lambda_i |\psi_i\rangle\langle\psi_i| = \rho \end{aligned}$$

which results in the same density operator. Therefore, we get a distinct decomposition by choosing a distinct unitary W , and therefore infinitely many decompositions exist for a given ρ .

In this section, we extend the definition of a geometric phase for *mixed* quantum states. The fundamental criterion like gauge invariance and reparametrization invariance will remain the same. We also have a parallel-transport law for mixed states. Due to the complex structure of

mixed states, there have been many attempts to settle the definition of geometric phase for the mixed state, and the literature is vast on the same. As a result, we have several possibilities to define the geometric phase that are not consistent, in general, with each other (we will cover some examples to illustrate this). We will try our best to cover critical results in the development of the field. We begin our discussion on the geometric phase for mixed states, starting with the interferometric approach by Sjoqvist et al. [31]. It has been generalized to include non-degenerate states [58] but still for unitary evolution. It was further generalized to provide a consistent definition for geometric phase for the mixed states that undergo a non-unitary evolution by a kinematic approach [59]. There are number of articles where the geometric phase has been calculated in open quantum system settings [60–65] We will also discuss the first experimental measurement of the mixed state geometric phase using photon interferometry [66].

Apart from this, there is another approach to define the geometric phase for mixed state by Uhlmann [30, 67]. A key idea used by Uhlmann in his analysis is to lift the given density operator ρ for a system, acting on the Hilbert space \mathcal{H} , to an extended Hilbert space $\mathcal{H}^{\text{ext}} = \mathcal{H} \otimes \mathcal{H}'$ where \mathcal{H}' is another Hilbert space. This process is known as purification. Uhlmann was probably the first to address the issue of mixed state holonomy, but as a purely mathematical problem. We will discuss a work by Ericsson et al. [68] that presents more information on this approach. There were several studies in which topological classification has been shown using the Uhlmann phase [69–71]. The definition by Uhlmann works for both unitary and non-unitary processes. This approach is not usually preferred because of its complex mathematics and lack of experimental observations. There are several theoretical and experimental studies that talk about the compatibility of two approaches [72–76]. A differential geometric approach was also given by Chaturvedi et al. [77] for the mixed state geometric phase.

2.8.1 Mixed state geometric phase in interferometry

For the pure states, we define a relative phase (Pancharatnam) between two non-orthogonal state vectors $|A\rangle$ and $|B\rangle$ as

$$\phi = \arg \langle A|B \rangle. \quad (2.113)$$

In the context of interferometry this phase difference can be measured by shifting the phase of $|A\rangle$ by χ i.e. $|A\rangle \rightarrow e^{i\chi} |A\rangle$ and making it interfere with $|B\rangle$ which results in the following

intensity

$$\begin{aligned}\mathcal{I} &= |e^{i\chi} |A\rangle + |B\rangle|^2 \\ &= 2 + 2|\langle A|B\rangle| \cos[\chi - \arg \langle A|B\rangle].\end{aligned}\quad (2.114)$$

The intensity attains the maximum value precisely at the Pancharatnam phase $\phi = \arg \langle A|B\rangle$. By following the same argument for a mixed state ρ_0 that is undergoing a unitary evolution such that $\rho_0 \rightarrow \rho(t) = U(t)\rho_0 U^\dagger(t)$. We now write a spectral decomposition for ρ_0 and $\rho(t)$ as

$$\rho_0 = \sum_k w_k |k\rangle\langle k|, \quad \rho(t) = \sum_k w_k |k(t)\rangle\langle k(t)| \quad (2.115)$$

where $\{|k\rangle\}, \{|k(t)\rangle\}$ form a set orthonormal basis and are related by $|k(t)\rangle = U(t) |k\rangle$.

Now, we introduce a phase shift in $|k\rangle \mapsto e^{i\chi} |k\rangle$ in a similar fashion to that we did before, and see the total interference profile,

$$\begin{aligned}\mathcal{I} &= \sum_k \mathcal{I}_k \\ &= \sum_k w_k |e^{i\chi} |k\rangle + |k(t)\rangle|^2 \\ &= \sum_k w_k (\langle k|k\rangle + \langle k(t)|k(t)\rangle + e^{-i\chi} \langle k|k(t)\rangle + e^{i\chi} \langle k(t)|k\rangle) \\ &= 2 + 2 \sum_k w_k |\langle k|k(t)\rangle| \cos(\chi - \arg \langle k|k(t)\rangle) \quad \because \sum_k w_k = 1\end{aligned}\quad (2.116)$$

Here we note that the total intensity \mathcal{I} is an incoherent average of the interference profiles \mathcal{I}_k of individual pure states. Now, we will present the above expression in a form similar to Eq. (2.114) which will provide physical insights into the picture. In order to do that, we define

$$\langle k(t)|k(t)\rangle = \langle k|U(t)|k\rangle \equiv v_k e^{i\varphi_k} \quad (2.117)$$

such that $\varphi_k = \arg \langle k|U(t)|k\rangle$ which is the relative phase between $|k\rangle$ and $|k(t)\rangle$ and $v_k =$

$|\langle k|U(t)|k\rangle|$ is defined as *visibility factor*. Using these notation, we get

$$\begin{aligned}
\mathcal{I} &= 2 + 2 \sum_k w_k v_k \cos(\chi - \varphi_k), \\
&= 2 + 2 \left[\cos \chi \left(\sum_k w_k v_k \cos \varphi_k \right) + \sin \chi \left(\sum_k w_k v_k \sin \varphi_k \right) \right], \\
&= 2 + 2 \left[\cos \chi \left| \sum_k w_k v_k e^{i\varphi_k} \right| \cos \left(\arg \sum_k w_k v_k e^{i\varphi_k} \right) \right. \\
&\quad \left. + \sin \chi \left| \sum_k w_k v_k e^{i\varphi_k} \right| \sin \left(\arg \sum_k w_k v_k e^{i\varphi_k} \right) \right].
\end{aligned} \tag{2.118}$$

by defining

$$\varphi \equiv \arg \left(\sum_k w_k v_k e^{i\varphi_k} \right), \quad \text{and} \quad v \equiv \left| \sum_k w_k v_k e^{i\varphi_k} \right| \tag{2.119}$$

the expression for intensity reduces to

$$\mathcal{I} = 2 + 2v \cos(\chi - \varphi) \tag{2.120}$$

which is very similar to Eq. (2.114). On further inspection, one finds

$$\varphi = \arg \left(\sum_k w_k \langle k|U(t)|k\rangle \right) = \arg \text{Tr} [U(t)\rho_0] \tag{2.121}$$

and

$$v = \left| \sum_k w_k \langle k|U(t)|k\rangle \right| = |\text{Tr} [U(t)\rho_0]| \tag{2.122}$$

that is

$$\text{Tr} (U(t)\rho_0) = v e^{i\varphi} \tag{2.123}$$

So, for a continuous evolution of ρ_0 , given by $\rho(t) = U(t)\rho_0 U^\dagger(t)$, we see that the final state $\rho(t)$ acquires a phase with respect to the initial state ρ_0 when

$$\text{Tr} (U(t)\rho_0) \neq 0.$$

2.8.2 Parallel transport

To interpret the total phase acquired by the state $\varphi = \arg \text{Tr} [U(t)\rho_0]$ as the geometric phase, we need to ensure that the state is parallel transported. In extension of the notion of parallel transport for pure states, here we demand that at each time the $\rho(t)$ must be *in phase* with the state $\rho(t + dt)$ at an infinitesimal time apart from $\rho(t)$. The state $\rho(t + dt)$ is related to $\rho(t)$ as

$$\rho(t + dt) = U(t + dt)\rho_0U^\dagger(t + dt) = U(t + dt)U^\dagger(t)\rho(t)U(t)U^\dagger(t + dt). \quad (2.124)$$

From this we can see the phase difference between $\rho(t + dt)$ and $\rho(t)$ as

$$d\varphi = \arg \left[\text{Tr} \left(U(t + dt)U^\dagger(t)\rho(t) \right) \right] \quad (2.125)$$

and to get rid of this phase $d\varphi$, $\text{Tr} (U(t + dt)U^\dagger(t)\rho(t))$ must be real and positive. This is one of the generalizations of Pancharatnam's connection for pure states. We can further write

$$\text{Tr} \left[U(t + dt)U^\dagger(t)\rho(t) \right] = 1 + \text{Tr} \left[\dot{U}(t)U^\dagger(t)\rho(t) \right] dt + \mathcal{O}(dt^2) \quad (2.126)$$

and by using the normalization and hermiticity of $\rho(t)$, we can deduce

$$\text{Tr} \left[\rho(t)\dot{U}(t)U^\dagger(t) \right] = \text{pure imaginary}. \quad (2.127)$$

From here, the parallel transport condition for mixed states evolving unitarily reads

$$\text{Tr} \left[\rho(t)\dot{U}(t)U^\dagger(t) \right] = 0. \quad (2.128)$$

The above condition together with a $\rho(t)$ determines the $N \times N$ unitary, up to N phase factors, where N is the $\dim[\rho(t)]$. These N factors can be fixed by demanding a condition that is more strong than the condition in Eq. (2.128) which is stated as

$$\langle k(t) | \dot{U}(t)U^\dagger(t) | k(t) \rangle = 0, \quad k = 1, 2, 3, \dots, N. \quad (2.129)$$

where $\{|k(t)\rangle\}$ are defined in Eq. (2.115). The above condition basically demands the parallel transport of individual eigenstates of $\rho(t)$ independently. These two conditions together are sufficient to find the parallel transport operator $U(t)$ for a given non-degenerate density matrix

$\rho(t)$.

The last component in this part is the dynamical phase. The dynamical phase is given by the time integral of the average Hamiltonian H of the system, which reads

$$\phi_{\text{dyn}} = -\frac{1}{\hbar} \int_0^T dt \text{Tr}[\rho(t)H(t)]. \quad (2.130)$$

Using Eq. (2.125), we can further write it as

$$\phi_{\text{dyn}} = \int_0^T d\varphi = -i \int_0^T dt \text{Tr} [\rho_0 U^\dagger(t) \dot{U}(t)] \quad (2.131)$$

which vanishes identically if the state ρ_0 is undergoing parallel transport. Therefore, for a state that traced a curve $C : t \in [0, T] \rightarrow \rho(t) = U(t)\rho_0 U^\dagger(t)$ where $U(t)$ satisfies the parallel-transport condition, the geometric phase is expressed as

$$\phi_g[C] = \varphi = \arg \text{Tr} [U(T)\rho_0] = \arg \left(\sum_k w_k v_k e^{i\varphi_k} \right) \quad (2.132)$$

The geometric phase defined above satisfies the following properties:

1. For pure states $\rho_0 = |\psi_0\rangle\langle\psi_0|$, the phase difference φ reduces to Pancharatnam (or relative) phase between $|\psi\rangle$ and $U(T)|\psi\rangle$.
2. For a pure state density operator $\rho(t) = |\psi(t)\rangle\langle\psi(t)|$, the parallel transport condition Eq. (2.128) reduces to

$$\langle\psi(t)|\dot{\psi}(t)\rangle = 0 \quad (2.133)$$

which was discussed in the context of pure state geometric phase.

$$\text{Tr} [\rho(t)\dot{U}(t)U^\dagger(t)] = \text{Tr} [|\psi(t)\rangle\langle\psi(t)|\dot{U}(t)U^\dagger(t)] \quad (2.134)$$

The Mach-Zehnder interferometer as shown in Fig. 2.8 was used by Sjöqvist *et al* [31] to arrive at the intensity interference pattern which reads

$$\mathcal{I} = 2 + 2|\text{Tr} [U_i\rho_0]| \cos [\chi - \arg \text{Tr} (U_i\rho_0)]. \quad (2.135)$$

for a mixed state undergoing a unitary evolution,

$$\rho_0 \rightarrow \rho(t) = U(t)\rho_0 U^\dagger(t) \quad (2.136)$$

with χ being a relative $U(1)$ phase as shown in Fig. 2.8.

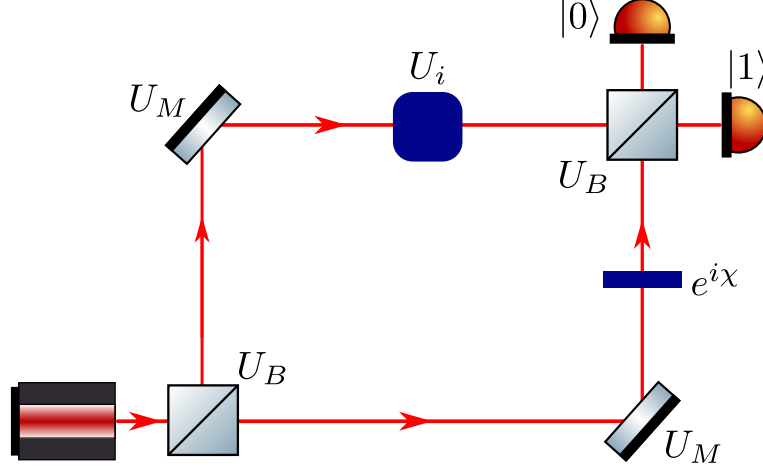


FIGURE 2.8: Sjöqvist interferometric setup.

2.8.3 Gauge invariance

The expression of $\phi_g[C]$ given in Eq. (2.132) defines the geometric phase for a mixed state evolving unitarily and the unitary is completely specified by the condition of parallel transport (2.128). However, if $U(t)$ does not satisfy the parallel transport condition, we have an additional contribution to the dynamical phase and $\phi_g[C] = \arg \text{Tr} [U(t)\rho_0]$ is no longer a purely geometrical quantity (or not gauge invariant). For example, consider a group element G (which is $U(N)$) given by

$$G = \underbrace{U(1) \times U(1) \times \cdots \times U(1)}_{N \text{ times}} \equiv \sum_{n=1}^N e^{i\theta_n} |n\rangle\langle n| \quad (2.137)$$

where $\{\theta_k\}$ are arbitrary phases and $\{|n\rangle\}$ are the orthonormal bases of $\rho(0)$. Now, under such a transformation

$$U(t) \in U(N) \longrightarrow U'(t) = U(t) \sum_{n=1}^N e^{i\theta_n(t)} |n\rangle\langle n|. \quad (2.138)$$

leaves the evolution of the density matrix unaffected [58]

$$\rho_0 \longrightarrow \rho'(t) = U'(t)\rho_0U'^{\dagger}(t) = U(t)\rho_0U^{\dagger}(t) = \rho(t). \quad (2.139)$$

where we make use of the spectral decomposition for $\rho(0)$. Therefore, depending on the choice of parameters θ_n 's, we have an infinite number of transformations that correspond to the same evolution of $\rho(t)$. As we have observed in the case of pure state, we get a gauge invariant quantity by subtracting the dynamical phase from the total. However, under the transformation given by Eq. (2.138), the total phase transforms as

$$\phi_t \longrightarrow \phi'_t = \arg\{\text{Tr} [\rho_0U'(T)]\} = \arg \left[\sum_k w_k e^{i\theta_k(T)} \langle k|U(T)|k\rangle \right], \quad (2.140)$$

whereas dynamical phase transforms as

$$\phi_{\text{dyn}} \longrightarrow \phi'_{\text{dyn}} = -i \int_0^T dt \text{Tr} [\rho_0U'^{\dagger}(t)\dot{U}'(t)] = -i \int_0^T dt \text{Tr} [\rho_0U^{\dagger}(t)\dot{U}(t)] + \sum_k w_k \theta_k(T). \quad (2.141)$$

It is very clear from the expressions of the total and dynamical phases that we cannot get rid of the $\theta_k(t)$ dependence in the total phase just by subtracting the dynamical. In order to resolve this problem, a gauge invariant functional [58] can be defined that reads

$$\phi_g[U] = \arg \left[\sum_k w_k \langle k|U(T)|k\rangle \exp \left\{ - \int_0^T dt \langle k|U^{\dagger}(t)\dot{U}(t)|k\rangle \right\} \right]. \quad (2.142)$$

The above expression is gauge invariant, and we can very easily verify that

$$\phi_g[U'] = \arg \left[\sum_k w_k \langle k|U'(T)|k\rangle \exp \left\{ - \int_0^T dt \langle k|U'^{\dagger}(t)\dot{U}'(t)|k\rangle \right\} \right] = \phi_g[U].$$

In addition to that, for the unitary $U(t)$ which satisfies the parallel-transport condition, this expression reduces to one derived in [31]. Further for pure states (density matrix of rank 1), it reduces to the existing results in [29].

2.8.4 Explicit example of a 2-level (spin -1/2) system

Consider a case of a 2-level (spin -1/2) system with density matrix

$$\rho_0 = \frac{1}{2}(\mathbb{1} + \mathbf{r} \cdot \boldsymbol{\sigma}) \quad (2.143)$$

With the choice of $\mathbf{r} = (r \sin \theta, 0, r \cos \theta)$, we get

$$\rho_0 = \frac{1}{2} \begin{pmatrix} 1 + r \cos \theta & r \sin \theta \\ r \sin \theta & 1 - r \cos \theta \end{pmatrix}. \quad (2.144)$$

The above density matrix can be diagonalized as

$$\rho_0 = \frac{1}{2} \begin{pmatrix} 1 + r & 0 \\ 0 & 1 - r \end{pmatrix} \quad (2.145)$$

with the following eigenvectors

$$|k+\rangle = \begin{pmatrix} \cos(\theta/2) \\ \sin(\theta/2) \end{pmatrix}, \quad \text{and} \quad |k-\rangle = \begin{pmatrix} \sin(\theta/2) \\ -\cos(\theta/2) \end{pmatrix}. \quad (2.146)$$

The geometric phase can be obtained using Eq. (2.142) as

$$\begin{aligned} \phi_g[U] &= \arg \left[-\frac{1+r}{2} e^{i\pi \cos \theta} - \frac{1-r}{2} e^{-i\pi \cos \theta} \right], \\ &= \arg [-(\cos(\pi \cos \theta) + ir \sin(\pi \cos \theta))], \\ &= \tan^{-1} [r \tan(\pi \cos \theta)]. \end{aligned} \quad (2.147)$$

which can be further simplified as

$$\begin{aligned} \phi_g[U] &= \tan^{-1} [r \tan(\pi \cos \theta)], \\ &= \tan^{-1} [-r \tan(\pi - \pi \cos \theta)], \\ &= \tan^{-1} [-r \tan(\pi(1 - \cos \theta))], \\ &= -\tan^{-1} \left[-r \tan \frac{\Omega}{2} \right], \end{aligned} \quad (2.148)$$

with $\Omega = 2\pi(1 - \cos \theta)$ being the solid angle subtended by the Bloch vector at the origin. This is the same expression obtained by Sjöqvist *et al.* [31], however, by imposing the condition

of parallel transport, unlike here. The above result reduces to the usual expression for the geometric phase of the pure state, $\phi_g[U] = -\Omega/2$, in the limit $r \rightarrow 1$. Note, the expression of $\phi_g[U]$ in Eqs. (2.147), (2.148) is ill defined in the limit of $r \rightarrow 0$.

2.9 Non-unitary evolution

The definition of geometric phase was first generalized for the nonunitary evolution using operator sum representation or *Kraus decomposition* [68, 78], but it was found that in this approach, the geometric phase depends explicitly on the choice of Kraus operators, which are not unique. Also, in [79] the geometric phase of a system subjected to decoherence has been proposed through a quantum jump approach that discusses only a particular system. This ambiguity was resolved by Tong *et al.*[59] by giving a formalism to evaluate geometric phases in nonunitary evolution by taking a kinematic approach. In this section, we will elucidate the main results in [59].

Let us start by consider a N dimensional quantum system S described by a Hilbert space \mathcal{H}_S such that the initial state is written as

$$\rho(0) = \sum_k \omega_k(0) |\phi_k(0)\rangle\langle\phi_k(0)|. \quad (2.149)$$

An evolution of this state can be written as

$$\mathcal{P} : t \in [0, \tau] \rightarrow \rho(t) = \sum_k \omega_k(t) |\phi_k(t)\rangle\langle\phi_k(t)| \quad (2.150)$$

where $\omega_k(t) \geq 0$ and $\{|\phi_k(t)\rangle\}$ are the eigenvalues and eigenvectors of ρ at time t . Now, we write purification for $\rho(t)$ by introducing an ancilla A such that we get a tensor product structure $\mathcal{H}_S \otimes \mathcal{H}_A$ and the lifted pure state in extended Hilbert space can be written as

$$|\Psi(t)\rangle = \sum_k \sqrt{\omega_k(t)} |\phi_k(t)\rangle \otimes |a_k\rangle \in \mathcal{H}_s \otimes \mathcal{H}_A \quad (2.151)$$

with $t \in [0, \tau]$. It is very straightforward to check that

$$\rho(t) = \text{Tr}_A |\Psi(t)\rangle\langle\Psi(t)|. \quad (2.152)$$

Now, we can define the Pancharatnam relative phase between $|\Psi(\tau)\rangle$ and $|\Psi(0)\rangle$ as

$$\alpha(\tau) = \arg \langle \Psi(0) | \Psi(\tau) \rangle = \arg \left(\sum_k \sqrt{\omega_k(0)\omega_k(\tau)} \langle \phi_k(0) | \phi_k(\tau) \rangle \right) \quad (2.153)$$

Since $\{|\phi_k(0)\rangle\}$ and $\{|\phi_k(t)\rangle\}$ are orthonormal basis from the same Hilbert space \mathcal{H}_S , there must exist a unitary operator $V(t)$ for $t \in [0, \tau]$ such that

$$|\phi_k(t)\rangle = V(t) |\phi_k(0)\rangle \quad (2.154)$$

with $V(0) = \mathbb{1}$, $\mathbb{1}$ being the identity operator in \mathcal{H}_S . We can also write $V(t)$ explicitly as

$$V(t) = |\phi_1(t)\rangle\langle\phi_1(0)| + |\phi_2(t)\rangle\langle\phi_2(0)| + \cdots + |\phi_N(t)\rangle\langle\phi_N(0)|. \quad (2.155)$$

With this expression of $V(t)$ we can rewrite $\alpha(\tau)$ as

$$\alpha(\tau) = \arg \langle \Psi(0) | \Psi(\tau) \rangle = \arg \left(\sum_k \sqrt{\omega_k(0)\omega_k(\tau)} \langle \phi_k(0) | V(\tau) | \phi_k(0) \rangle \right) \quad (2.156)$$

This is the relative phase between the final and initial state, not the geometric phase. In order to interpret this as the geometric phase, we need to ensure that the evolution satisfies the parallel transport condition, i.e.

$$\langle \Psi(t) | \dot{\Psi}(t) \rangle = 0. \quad (2.157)$$

There is only one condition or constraint that is sufficient only for a pure state. However, in case of mixed state we require N conditions to fix the arbitrary phases of $V(t)$ and to ensure that the geometric phase is independent of purification. We note that there exists a set of unitaries $\tilde{V}(t)$ for $t \in [0, \tau]$ that realize the same evolution. These are nothing but the one with includes gauge transformation and written as

$$\tilde{V}(t) = V(t) \sum_{k=1}^N e^{i\theta_k(t)} |\phi_k(0)\rangle\langle\phi_k(0)| \quad (2.158)$$

for real time-dependent parameters $\theta_k(t)$ such that $\theta_k(0) = 0$. We can particularly choose one unitary $V^{\parallel}(t)$ from the whole set such that it satisfies the parallel transport condition

$$\langle \phi_k(0) | V^{\parallel\dagger} \dot{V}^{\parallel}(t) | \phi_k(0) \rangle = 0, \quad k = 1, 2, \dots, N. \quad (2.159)$$

in which case $\alpha(\tau)$ can be interpreted as the geometric phase for \mathcal{P} of the mixed state. By substituting, $V^{\parallel}(t) = \tilde{V}(t)$ we have

$$V^{\parallel}(t) = V(t) \sum_k e^{i\theta_k(t)} |\phi_k(0)\rangle\langle\phi_k(0)|$$

$$\dot{V}^{\parallel}(t) = \dot{V}(t) \sum_k e^{i\theta_k(t)} |\phi_k(0)\rangle\langle\phi_k(0)| + i\dot{\theta}_k(t)V(t) \sum_k e^{i\theta_k(t)} |\phi_k(0)\rangle\langle\phi_k(0)|$$

and by substituting in (2.159), we get

$$\begin{aligned} V^{\parallel\dagger}(t)\dot{V}^{\parallel}(t) &= \sum_{l,m} e^{-i(\theta_l(t)-\theta_m(t))} |\phi_l(0)\rangle\langle\phi_l(0)| V^{\dagger}(t)\dot{V}(t) |\phi_m(0)\rangle\langle\phi_m(0)| + i\dot{\theta}_l(t) \\ \langle\phi_k(0)|V^{\parallel\dagger}(t)\dot{V}^{\parallel}(t)|\phi_k(0)\rangle &= \langle\phi_k(0)|V^{\dagger}(t)\dot{V}(t)|\phi_k(0)\rangle + i\dot{\theta}_k(t) = 0 \end{aligned} \quad (2.160)$$

which gives us

$$\theta_k(t) = i \int_0^t ds \langle\phi_k(0)|V^{\dagger}(s)\dot{V}(s)|\phi_k(0)\rangle \quad (2.161)$$

Finally, taking all the above expressions into account, we can write the geometric phase $\gamma[\mathcal{P}]$ for the path \mathcal{P} as

$$\begin{aligned} \gamma[\mathcal{P}] &= \arg \left(\sum_k \sqrt{\omega_k(0)\omega_k(\tau)} \langle\phi_k(0)|V^{\parallel}(\tau)|\phi_k(0)\rangle \right) \\ &= \arg \left(\sum_k \sqrt{\omega_k(0)\omega_k(\tau)} \langle\phi_k(0)|V(\tau)|\phi_k(0)\rangle e^{-\int_0^\tau dt \langle\phi_k(0)|V^{\dagger}(t)\dot{V}(t)|\phi_k(0)\rangle} \right) \\ &= \arg \left(\sum_k \sqrt{\omega_k(0)\omega_k(\tau)} \langle\phi_k(0)|\phi_k(\tau)\rangle e^{-\int_0^\tau dt \langle\phi_k(t)|\dot{\phi}_k(t)\rangle} \right) \end{aligned} \quad (2.162)$$

There are certain basic requirements which an expression of geometric phase must satisfy. These are

- (a) it must be invariant under gauge transformation,
- (b) it should be reduced to the already existing results in the limit of unitary evolution and pure state, and
- (c) it should be feasible to get it tested experimentally.

The geometric phase in (2.162) is gauge invariant, i.e.

$$\begin{aligned}
\gamma[\mathcal{P}]|_{\tilde{V}(t)} &= \arg \left(\sum_k \sqrt{\omega_k(0)\omega_k(\tau)} \langle \phi_k(0) | \tilde{V}(\tau) | \phi_k(0) \rangle e^{-\int_0^\tau dt \langle \phi_k(0) | \tilde{V}^\dagger(t) \dot{\tilde{V}}(t) | \phi_k(0) \rangle} \right) \\
&= \arg \left(\sum_k \sqrt{\omega_k(0)\omega_k(\tau)} \langle \phi_k(0) | V(\tau) | \phi_k(0) \rangle e^{i\theta_k(\tau)} e^{-\int_0^\tau dt \langle \phi_k(0) | V^\dagger(t) \dot{V}(t) | \phi_k(0) \rangle} e^{-\int_0^\tau i\dot{\theta}_k(t)} \right) \\
&= \arg \left(\sum_k \sqrt{\omega_k(0)\omega_k(\tau)} \langle \phi_k(0) | V(\tau) | \phi_k(0) \rangle e^{-\int_0^\tau dt \langle \phi_k(0) | V^\dagger(t) \dot{V}(t) | \phi_k(0) \rangle} \right) \\
&= \gamma[\mathcal{P}]|_{V(t)}
\end{aligned}$$

where we used $\theta_k(0) = 0$ and

$$\langle \phi_k(0) | \tilde{V}^\dagger(t) \dot{\tilde{V}}(t) | \phi_k(0) \rangle = \langle \phi_k(0) | V^\dagger(t) \dot{V}(t) | \phi_k(0) \rangle + i\dot{\theta}_k(t)$$

Second, when the evolution is unitary, which corresponds to the case where ω_k are time independent and the operator $V(t)$ is identified with the time evolution operator of the system, the geometric phase Eq. (2.162) reduces to the well-known results [58]. This phase is experimentally testable by lifting the given state $\rho(t)$ to a higher dimensional state $|\Psi(t)\rangle$ using purification techniques [59]. We now illustrate the method described above by considering an explicit example.

Let us consider a two-level system with a free Hamiltonian $H = (\eta/2)\sigma_z$, interacting with an environment represented by the Lindblad operator $\Gamma = (\sqrt{\Lambda/2})\sigma_z$. It is a kind of pure dephasing environment (bosonic bath). We can solve the Lindblad equation like

$$\begin{aligned}
\frac{d}{dt}\rho &= -i[H, \rho] + \frac{1}{2} \sum_k \left(2\Gamma_k \rho \Gamma_k^\dagger - \Gamma_k \Gamma_k^\dagger \rho - \rho \Gamma_k \Gamma_k^\dagger \right) \\
&= -i\frac{\eta}{2}[\sigma_z, \rho] + \frac{\Lambda}{4} (2\sigma_z \rho \sigma_z - \rho - \rho) \\
&= -i\frac{\eta}{2}[\sigma_z, \rho] + \frac{\Lambda}{2} (\sigma_z \rho \sigma_z - \rho) \\
&= \begin{bmatrix} 0 & (-i\eta - \Lambda)\rho_{01} \\ (i\eta - \Lambda)\rho_{10} & 0 \end{bmatrix}
\end{aligned}$$

For an initial state given by

$$\rho(0) = \frac{1}{2} (\mathbb{1} + \mathbf{r} \cdot \boldsymbol{\sigma}) \quad (2.163)$$

with $\mathbf{r} = (\sin \theta_0, 0, \cos \theta_0)$, we can solve for $\rho(t)$ and will get

$$\begin{aligned}\rho_{00}(t) &= \rho_{00}(0) = \frac{1}{2}(1 + \cos \theta_0) \\ \rho_{01}(t) &= \rho_{00}(0)e^{-i\eta t - \Lambda t} = \frac{1}{2} \sin \theta_0 e^{-i\eta t - \Lambda t} \\ \rho_{10}(t) &= \rho_{10}(0)e^{i\eta t - \Lambda t} = \frac{1}{2} \sin \theta_0 e^{i\eta t - \Lambda t} \\ \rho_{11}(t) &= \rho_{11}(0) = \frac{1}{2}(1 - \cos \theta_0)\end{aligned}$$

which results in

$$\rho(t) = \frac{1}{2} \begin{bmatrix} 1 + \cos \theta_0 & \sin \theta_0 e^{-i\eta t - \Lambda t} \\ \sin \theta_0 e^{i\eta t - \Lambda t} & 1 - \cos \theta_0 \end{bmatrix}. \quad (2.164)$$

It is characterized by the following eigenvalues

$$\lambda_{1,2}(t) = \frac{1}{2} \left(1 \pm \sqrt{\cos^2 \theta_0 + e^{-2\Lambda t} \sin^2 \theta_0} \right)$$

and we can also write

$$\rho(t) = \frac{1}{2} (\mathbb{1} + \mathbf{r}(t) \cdot \boldsymbol{\sigma}) \quad (2.165)$$

where

$$\mathbf{r} = (\sin \theta_0 \cos(\eta t) e^{-\Lambda t}, \sin \theta_0 \sin(\eta t) e^{-\Lambda t}, \cos \theta_0).$$

Therefore, we will have

$$\tan \phi(t) = \tan(\eta t), \quad \tan \theta_t = e^{-\Lambda t} \tan \theta_0, \quad (2.166)$$

and the corresponding eigenstates are

$$\begin{aligned}|\phi_1(t)\rangle &= \cos(\theta_t/2) |0\rangle + e^{i\eta t} \sin(\theta_t/2) |1\rangle, \\ |\phi_2(t)\rangle &= -e^{-i\eta t} \sin(\theta_t/2) |0\rangle + \cos(\theta_t/2) |1\rangle\end{aligned} \quad (2.167)$$

where $\{|0\rangle, |1\rangle\}$ are the standard computational basis. Since $\lambda_2(0) = 0$, the only contribution comes from the $|\phi_1(t)\rangle$ in geometric phase. We have

$$\langle \phi_1(t) | \dot{\phi}_1(t) \rangle = i\eta \sin^2(\theta_t/2) = \frac{i\eta}{2} \left[1 - \frac{1}{\sqrt{1 + e^{-2\Lambda t} \tan^2 \theta_0}} \right]$$

By using all these relations in Eq. (2.162) we get

$$\gamma[\mathcal{P}] = -\pi + \frac{\eta}{4\Lambda} \ln \left[\frac{(\cos \theta_0 - 1)(\cos \theta_0 + \sqrt{\cos^2 \theta_0 + e^{-4\pi\Lambda/\eta} \sin^2 \theta_0})}{(\cos \theta_0 + 1)(\cos \theta_0 - \sqrt{\cos^2 \theta_0 + e^{-4\pi\Lambda/\eta} \sin^2 \theta_0})} \right] \quad (2.168)$$

where we made use of a trigonometric identity $\tanh^{-1} x = \frac{1}{2} \ln \left(\frac{1+x}{1-x} \right)$ for $-1 \leq x \leq 1$. For small dephasing, i.e., for $\Lambda/\eta \ll 1$, we can use the Taylor expansion for the second term and obtain the geometric phase up to a first order as

$$\gamma[\mathcal{P}] \approx -\pi(1 - \cos \theta_0) + \pi^2 \cos \theta_0 \sin^2 \theta_0 \left(\frac{\Lambda}{\eta} \right). \quad (2.169)$$

The effect of dephasing on the geometric phase has been analyzed in [79] using the quantum jump approach. However, in quantum-jump approach, we effectively have a pure state at all the time. The robust nature of the geometric phase has been explicitly shown in [79] against dephasing. The geometric phase calculated using mixed state, results in first order correction Eq.(2.169) due to dephasing which reduces to the results of [79] for $\theta_0 = \pi/2$ which corresponds to the precession in the equatorial plane of the Bloch sphere.

NOTE: A general state for a two-level system in computational basis is written as

$$|\psi\rangle = \cos(\theta/2) |0\rangle + e^{i\phi} \sin(\theta/2) |1\rangle = \begin{bmatrix} \cos(\theta/2) \\ e^{i\phi} \sin(\theta/2) \end{bmatrix}$$

where θ and ϕ define a point on the unit three-dimensional sphere, known as "Bloch sphere" as shown in Fig. 2.9. We can further write the state $|\psi\rangle$ in the Bloch sphere representation as

$$\rho = |\psi\rangle\langle\psi| = \frac{1}{2}(\mathbb{1} + \mathbf{r} \cdot \boldsymbol{\sigma})$$

where $\mathbf{r} \in \mathbb{R}^3$ such that $|\mathbf{r}| \leq 1$. This vector is known as the Bloch sphere and is given by

$$\mathbf{r} = (r_x, r_y, r_z) = (\sin \theta \cos \phi, \sin \theta \sin \phi, \cos \theta).$$

with

$$\tan \phi = \frac{r_y}{r_x}, \quad \tan \theta = \frac{\sqrt{r_x^2 + r_y^2}}{r_z}.$$

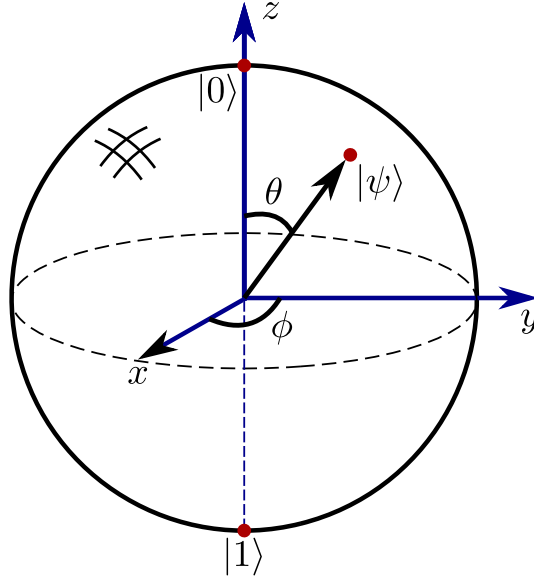


FIGURE 2.9: Bloch sphere representation of a qubit.

2.10 Measurement of Mixed state Geometric Phase in Interferometry

The first experimental verification of the mixed state geometric phase was given in [1] based on Single Photon Interferometry. We briefly discuss the experimental setup here. The composite Hilbert space of the system is given by the tensor product of Hilbert spaces corresponding to spatial (\mathcal{H}_s) and internal modes (\mathcal{H}_i) i.e. we have

$$\mathcal{H} = \mathcal{H}_s \otimes \mathcal{H}_i \quad (2.170)$$

Here, we start with

$$\begin{aligned} \rho_{in} &= |a\rangle\langle a| \otimes |\psi_0\rangle\langle\psi_0| = |a\rangle\langle a| \otimes \rho_0 \\ &= \left[\begin{array}{c|c} \rho_0 & 0 \\ \hline 0 & 0 \end{array} \right] \end{aligned} \quad (2.171)$$

Then it gets split by BS1 whose action can be written as

$$\begin{aligned}
U_{BS} &= \frac{1}{\sqrt{2}} \begin{pmatrix} 1 & i \\ i & 1 \end{pmatrix} \otimes \mathbb{1} \\
&= \frac{1}{\sqrt{2}} \left[\begin{array}{c|c} \mathbb{1} & i \\ \hline i & \mathbb{1} \end{array} \right]
\end{aligned} \tag{2.172}$$

$$\begin{aligned}
\rho_{in} \mapsto U_{BS} \rho_{in} U_{BS}^\dagger = \rho_1 &= \frac{1}{2} \left[\begin{array}{c|c} \mathbb{1} & i \\ \hline i & \mathbb{1} \end{array} \right] \left[\begin{array}{c|c} \rho_0 & 0 \\ \hline 0 & 0 \end{array} \right] \left[\begin{array}{c|c} \mathbb{1} & -i \\ \hline -i & \mathbb{1} \end{array} \right] \\
&= \frac{1}{2} \left[\begin{array}{c|c} \mathbb{1} & i \\ \hline i & \mathbb{1} \end{array} \right] \left[\begin{array}{c|c} \rho_0 & -i\rho_0 \\ \hline 0 & 0 \end{array} \right] \\
&= \frac{1}{2} \left[\begin{array}{c|c} \rho_0 & -i\rho_0 \\ \hline i\rho_0 & \rho_0 \end{array} \right]
\end{aligned} \tag{2.173}$$

Then we have two half-wave plates (HWP) in mode b and a phase shift, χ in mode a ,

$$\rho_1 \mapsto U \rho_1 U^\dagger = \rho_2 \tag{2.174}$$

where

$$U = \{ |a\rangle\langle a| \otimes H + |b\rangle\langle b| \otimes e^{i\chi} \} \tag{2.175}$$

with $H = HWP_{\theta_2} \times HWP_{\theta_1}$. Therefore

$$\begin{aligned}
\rho_2 &= \frac{1}{2} \left[\begin{array}{c|c} H & 0 \\ \hline 0 & e^{i\chi} \end{array} \right] \left[\begin{array}{c|c} \rho_0 & -i\rho_0 \\ \hline i\rho_0 & \rho_0 \end{array} \right] \left[\begin{array}{c|c} H^\dagger & 0 \\ \hline 0 & e^{-i\chi} \end{array} \right] \\
&= \frac{1}{2} \left[\begin{array}{c|c} H & 0 \\ \hline 0 & e^{i\chi} \end{array} \right] \left[\begin{array}{c|c} \rho_0 H^\dagger & -i\rho_0 e^{-i\chi} \\ \hline i\rho_0 H^\dagger & \rho_0 e^{-i\chi} \end{array} \right] \\
&= \frac{1}{2} \left[\begin{array}{c|c} H\rho_0 H^\dagger & -iH\rho_0 e^{-i\chi} \\ \hline i\rho_0 H^\dagger e^{i\chi} & \rho_0 \end{array} \right]
\end{aligned} \tag{2.176}$$

Then we have two mirrors M_1 & M_2 and their action would be

$$M = \begin{pmatrix} 0 & 1 \\ 1 & 0 \end{pmatrix} \otimes \mathbb{1} = \left[\begin{array}{c|c} 0 & \mathbb{1} \\ \hline \mathbb{1} & 0 \end{array} \right] \quad (2.177)$$

$$\begin{aligned} \rho_3 &\mapsto M\rho_3M^\dagger \\ &= \frac{1}{2} \left[\begin{array}{c|c} 0 & \mathbb{1} \\ \hline \mathbb{1} & 0 \end{array} \right] \left[\begin{array}{c|c} H\rho_0H^\dagger & -iH\rho_0e^{-i\chi} \\ \hline i\rho_0H^\dagger e^{i\chi} & \rho_0 \end{array} \right] \left[\begin{array}{c|c} 0 & \mathbb{1} \\ \hline \mathbb{1} & 0 \end{array} \right] \\ &= \frac{1}{2} \left[\begin{array}{c|c} 0 & \mathbb{1} \\ \hline \mathbb{1} & 0 \end{array} \right] \left[\begin{array}{c|c} -iH\rho_0e^{-i\chi} & H\rho_0H^\dagger \\ \hline \rho_0 & i\rho_0H^\dagger e^{i\chi} \end{array} \right] \\ &= \frac{1}{2} \left[\begin{array}{c|c} \rho_0 & i\rho_0H^\dagger e^{i\chi} \\ \hline -iH\rho_0e^{-i\chi} & H\rho_0H^\dagger \end{array} \right] \end{aligned} \quad (2.178)$$

And finally BS2

$$\begin{aligned} \rho_{op} &= \frac{1}{4} \left[\begin{array}{c|c} \mathbb{1} & i \\ \hline i & \mathbb{1} \end{array} \right] \left[\begin{array}{c|c} \rho_0 & i\rho_0H^\dagger e^{i\chi} \\ \hline -iH\rho_0e^{-i\chi} & H\rho_0H^\dagger \end{array} \right] \left[\begin{array}{c|c} \mathbb{1} & -i \\ \hline -i & \mathbb{1} \end{array} \right] \\ &= \frac{1}{4} \left[\begin{array}{c|c} \mathbb{1} & i \\ \hline i & \mathbb{1} \end{array} \right] \left[\begin{array}{c|c} \rho_0 + \rho_0H^\dagger e^{i\chi} & -i\rho_0 + i\rho_0H^\dagger e^{i\chi} \\ \hline -iH\rho_0e^{-i\chi} - iH\rho_0H^\dagger & -H\rho_0e^{-i\chi} + H\rho_0H^\dagger \end{array} \right] \\ &= \frac{1}{4} \text{diag} \left[\rho_0 + H\rho_0H^\dagger + \rho_0H^\dagger e^{i\chi} + H\rho_0e^{-i\chi}, \right. \\ &\quad \left. \rho_0 + H\rho_0H^\dagger - \rho_0H^\dagger e^{i\chi} - H\rho_0e^{-i\chi} \right] \end{aligned} \quad (2.179)$$

So, the intensity along $|a\rangle\langle a|$ or D1 is

$$\begin{aligned} \mathcal{I}_a &= \frac{1}{4} \text{Tr} \left[\rho_0 + H\rho_0H^\dagger + \rho_0H^\dagger e^{i\chi} + H\rho_0e^{-i\chi} \right] \\ &= \frac{1}{4} \left(2 \text{Tr}[\rho_0] + \text{Tr}[\rho_0H^\dagger] e^{i\chi} + \text{Tr}[H\rho_0] e^{-i\chi} \right). \end{aligned} \quad (2.180)$$

Using

$$\text{Tr}[\rho_0H^\dagger] = (\text{Tr}[H\rho_0])^* = z^* = re^{-i\phi} \quad (2.181)$$

and assuming $\text{Tr}[\rho_0] = 1$ we can write

$$\begin{aligned}\mathcal{J}_a &= \frac{1}{4} [2 + z^* e^{i\chi} + z e^{-i\chi}] \\ &= \frac{1}{4} [2 + r e^{i(\chi-\phi)} + r e^{-i(\chi-\phi)}] \\ &\propto 1 + r \cos(\chi - \phi).\end{aligned}\tag{2.182}$$

and similarly along $|b\rangle\langle b|$ or D2, will be

$$\mathcal{J}_b = \frac{1}{4} \text{Tr} [\rho_0 + H\rho_0 H^\dagger - \rho_0 H^\dagger e^{i\chi} - H\rho_0 e^{-i\chi}] \propto 1 - r \cos(\chi - \phi).\tag{2.183}$$

where

$$\phi = \arg(\text{Tr}[H\rho_0]).\tag{2.184}$$

2.10.1 Experimental setup

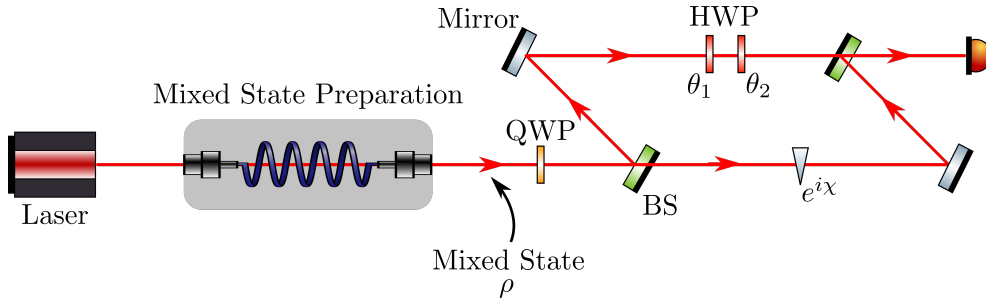


FIGURE 2.10: Schematic of the experimental setup in Ericsson et al [1].

The system is prepared in a mixed state given by

$$\rho = \cos^2 \theta_p |H\rangle\langle H| + \sin^2 \theta_p |V\rangle\langle V| = \begin{bmatrix} \cos^2 \theta_p & 0 \\ 0 & \sin^2 \theta_p \end{bmatrix}\tag{2.185}$$

with purity, $r = |\cos 2\theta_p|$. It is sent to a QWP to create a mixture of $|R\rangle$ and $|L\rangle$ polarization states (it is just a change of basis),

$$\rho \mapsto \rho_0 = Q\rho Q^{-1} = \cos^2 \theta_p |R\rangle\langle R| + \sin^2 \theta_p |L\rangle\langle L|,\tag{2.186}$$

with

$$Q = \begin{bmatrix} e^{i\pi/4} & 0 \\ 0 & e^{-i\pi/4} \end{bmatrix} = e^{i\pi/4} \begin{bmatrix} 1 & 0 \\ 0 & -i \end{bmatrix} \quad (2.187)$$

such that

$$Q |H\rangle = Q \begin{bmatrix} 1 \\ 0 \end{bmatrix} = |R\rangle = \frac{e^{i\pi/4}}{\sqrt{2}} \begin{bmatrix} 1 \\ -i \end{bmatrix} \quad (2.188)$$

and

$$Q |V\rangle = Q \begin{bmatrix} 0 \\ 1 \end{bmatrix} = |L\rangle = \frac{e^{i\pi/4}}{\sqrt{2}} \begin{bmatrix} 1 \\ i \end{bmatrix}. \quad (2.189)$$

Therefore, the ρ_0 in $\{|H\rangle, |V\rangle\}$ (it is necessary because Q is written in the same) basis can be written as

$$\begin{aligned} \rho_0 &= |H\rangle\langle H| + i \cos 2\theta_p |H\rangle\langle V| - i \cos 2\theta_p |V\rangle\langle H| + |V\rangle\langle V| \\ &= \frac{1}{2} \begin{bmatrix} 1 & i \cos 2\theta_p \\ -i \cos 2\theta_p & 1 \end{bmatrix} = \frac{1}{2} \begin{bmatrix} 1 & ir \\ -ir & 1 \end{bmatrix} = \frac{1}{2} (\mathbb{1} - r\sigma_z). \end{aligned} \quad (2.190)$$

In one mode, we have two HWP at angles θ_1 and θ_2

$$H_\theta = R(\theta)H_0R(\theta)^{-1} = R(\theta)i\sigma_zR(\theta)^{-1} = i \begin{bmatrix} \cos 2\theta & \sin 2\theta \\ \sin 2\theta & -\cos 2\theta \end{bmatrix} \quad (2.191)$$

with

$$R(\theta) = \begin{bmatrix} \cos \theta & -\sin \theta \\ \sin \theta & \cos \theta \end{bmatrix} \quad (2.192)$$

which gives us

$$U \equiv H_{\theta_2}H_{\theta_1} = - \begin{bmatrix} \cos 2(\theta_1 - \theta_2) & \sin 2(\theta_1 - \theta_2) \\ \sin 2(\theta_1 - \theta_2) & \cos 2(\theta_1 - \theta_2) \end{bmatrix} \quad (2.193)$$

In this case, the dynamical phase vanishes because of the fact that both components of ρ are parallel-transported, as shown in Fig. 2.11. So, the total phase has contribution only from the geometric phase which is given by

$$\begin{aligned} \gamma_g &= \arg(\text{Tr}[H\rho_0]), \\ &= \arg(-\cos 2(\theta_1 - \theta_2) + ir \sin 2(\theta_1 - \theta_2)), \\ &= -\arctan(r \tan 2(\theta_1 - \theta_2)). \end{aligned} \quad (2.194)$$

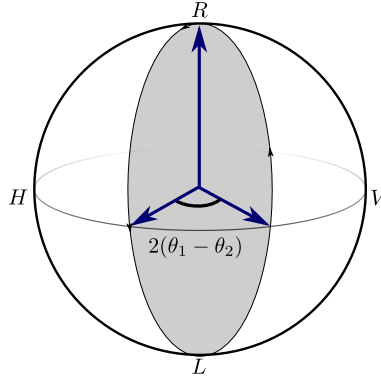


FIGURE 2.11: The solid angle Ω , shown by shaded region, by one of the eigenvector of the density matrix ρ . The other eigenvector traces the same path, except in the clockwise direction.

2.11 Uhlmann Holonomies

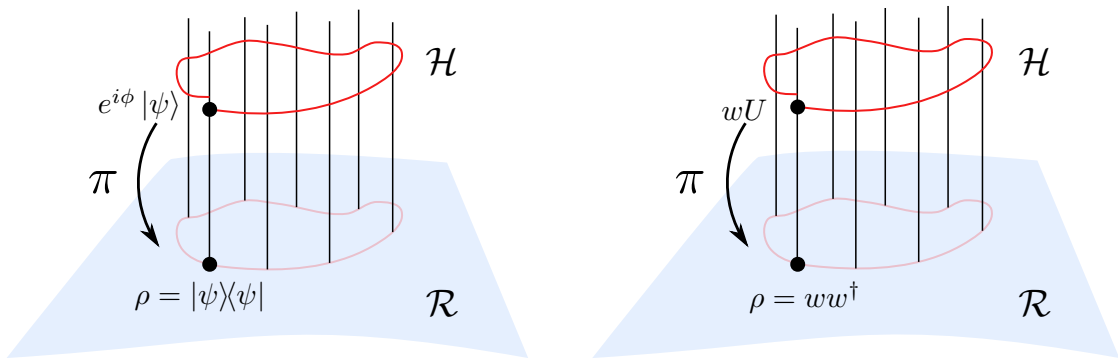


FIGURE 2.12: Comparison of Berry's phase for pure states and Uhlmann phase for mixed states.

The extension of geometric phase for pure states to mixed states is not trivial and straightforward. We have already discussed the interferometric approach [31] in previous sections which is more appealing from a physical perspective. However, Uhlmann was the first to address the issue of geometric phase for mixed states using a rigorous mathematical framework [30, 67, 80–82] and provided a satisfactory solution. The two key elements in Uhlmann's approach were the purification of states in an extended Hilbert space and the parallel transport of states. The purification of mixed states in Uhlmann's sense can be understood in analogy with the case of pure state, which we developed in Sect. 2.4 and also shown in Fig. 2.12. The purification of states can be represented by an operator (Hilbert-Schmidt) in the extended space and is referred to as an amplitude. For a given path of the density operator, a corresponding path of the

amplitude can be constructed, which projects down to the original path. There exists a certain special path of amplitudes which obeys the parallel transport condition and leads to a unique path in the extended Hilbert space. Such a choice of amplitude is a property only of the path of the states and defines a holonomy invariant. One advantage of Uhlmann's approach is that it does not distinguish between unitary or nonunitary evolution. The main aim of this part is to discuss the compatibility of the two approaches for the mixed state geometric phase. We start with a discussion on the construction of the amplitudes and the parallel transport law.

2.11.1 Uhlmann's amplitudes

As we have seen, in the case of pure states, we can define a projective Hilbert space \mathcal{R} that consists of physical states $\rho = |\psi\rangle\langle\psi|$. By physical, we mean that the states $|\psi\rangle$ and $e^{i\phi}|\psi\rangle$ describe the same state of the system ρ . However, this concept cannot be trivially extended for the mixed states. The fundamental problem which arises while extending the idea of a geometric phase for the mixed state is, for a given set of real numbers $\{p_i\}$ and density matrices $\{\rho_i\}$, the linear combination $\sum_i p_i \rho_i$ is not a valid density matrix until and unless $p_i \leq 0 \forall i$ and $\sum_i p_i = 1$. Our aim is to find such an analogous construction for a mixed state represented by a density matrix ρ . To achieve that, we consider a density matrix ρ and define an *amplitude* as a matrix $w \in \mathcal{H}_w$ such that

$$\rho = ww^\dagger \quad (2.195)$$

These amplitudes form another Hilbert space \mathcal{H}_w (space of Hilbert-Schmidt operators) with an inner product or a Hilbert-Schmidt product defined as

$$(w_1, w_2) = \text{Tr}(w_1^\dagger w_2) \quad (2.196)$$

We can clearly see from the last expression that there is a $U(n)$ gauge freedom to choose because w and wU , U being a unitary operator corresponds to the same state. We note here that, as in the case of pure states, we had a gauge freedom of $U(1)$ in the states, here we have a $U(n)$ -gauge freedom for the amplitudes as shown in Fig. 2.12. Furthermore, the projection map, π , is defined as [see Fig. 2.12]

$$\pi : \mathcal{H}_w \rightarrow \mathcal{R}, \quad \pi(w) = ww^\dagger = \rho. \quad (2.197)$$

In the case of pure states, the projective space \mathcal{R} consists of projection operators, $P(\psi) = |\psi\rangle\langle\psi|$ which corresponds to all states $e^{i\phi} |\psi\rangle \in \mathcal{H}$ with $\phi \in \mathbb{R}$. We can extend this idea to mixed states by writing ρ as a linear combination of $P(\psi_i)$'s

$$\rho = \sum_i p_i P(\psi_i) = \sum_i p_i |\psi_i\rangle\langle\psi_i| \quad (2.198)$$

The amplitude w is written as

$$w = \sqrt{\rho}U = \sum_i \sqrt{p_i} |\psi_i\rangle\langle\psi_i| U, \quad (2.199)$$

which is nothing but the polar decomposition of w and is known as the 'square root' section of the Uhlmann fibre bundle [71]. It can be seen as

$$w = \sum_i \sqrt{p_i} |\psi_i\rangle \otimes \langle\phi_i| U, \quad (2.200)$$

which corresponds to an operator in extended Hilbert space \mathcal{H}_w which is a tensor product of the systems Hilbert space \mathcal{H}_S and an ancilla (of dimension at least equal to the dimension of the system) \mathcal{H}_A i.e. $\mathcal{H}_w = \mathcal{H}_S \otimes \mathcal{H}_A$, $\{\langle\phi_i|\} \in \mathcal{H}_A$ is the set of orthonormal basis vectors. This process is known as *purification*. The main difference between this and the standard one is that the density matrices are further purified by operators instead of vectors. This is how Uhlmann defined purification [30]. We can easily verify that

$$\begin{aligned} ww^\dagger &= \left(\sum_i \sqrt{p_i} |\psi_i\rangle \otimes \langle\phi_i| U \right) \left(\sum_j \sqrt{p_j} \langle\psi_j| \otimes U^\dagger |\phi_j\rangle \right) \\ &= \sum_{ij} \sqrt{p_i p_j} |\psi_i\rangle\langle\psi_j| \otimes \langle\phi_i| U U^\dagger |\phi_j\rangle \\ &= \sum_i p_i |\psi_i\rangle\langle\psi_i| \quad \langle\phi_i|\phi_j\rangle = \delta_{ij}. \end{aligned} \quad (2.201)$$

But later, an isomorphism was defined [71] between the operator $w \in \mathcal{H}_w$ and the vectors $|w\rangle \in \mathcal{H}_S \otimes \mathcal{H}_A$ as

$$w = \sum_i \sqrt{p_i} |\psi_i\rangle \otimes \langle\psi_i| U \longleftrightarrow |w\rangle = \sum_i \sqrt{p_i} |\psi_i\rangle \otimes U^T |\psi_i\rangle \quad (2.202)$$

where U^T denotes the complex transposition of U with respect to the eigenbasis of ρ . Using

$$U^T |\psi_i\rangle \equiv |\phi_i\rangle \implies \langle \psi_i|U = \langle \phi_i|$$

again we can show that

$$\begin{aligned} \rho &= \text{Tr}_A |w\rangle\langle w| \\ &= \text{Tr}_A \left(\sum_i \sqrt{p_i} |\psi_i\rangle \otimes U^T |\psi_i\rangle \right) \left(\sum_j \sqrt{p_j} \langle \psi_j| \otimes \langle \psi_j|U \right) \\ &= \text{Tr}_A \left(\sum_i \sqrt{p_i} |\psi_i\rangle \otimes |\phi_i\rangle \right) \left(\sum_j \sqrt{p_j} \langle \psi_j| \otimes \langle \phi_j| \right) \\ &= \sum_k \sum_i \sum_j \sqrt{p_i p_j} |\psi_i\rangle\langle \psi_j| \otimes \langle \phi_k|\phi_i\rangle \langle \phi_j|\phi_k\rangle, \\ &= \sum_i p_i |\psi_i\rangle\langle \psi_i|. \end{aligned} \tag{2.203}$$

where Tr_A represents the partial trace over the ancilla in $\mathcal{H}_S \otimes \mathcal{H}_A$. Therefore, any amplitude w can be seen as a pure state $|w\rangle$ in an extended Hilbert space $\mathcal{H}_S \otimes \mathcal{H}_A$ such that the partial trace over the ancilla gives us ρ .

2.11.2 Parallel amplitudes

In order to understand the parallel transport condition by Uhlmann and the holonomy, we need the concept of parallel amplitudes. For two given pairs of density matrices, ρ_1 and ρ_2 , there are two corresponding amplitudes w_1 and w_2 , respectively. They are parallel if they minimize the Hilbert space distance in \mathcal{H}_w which is given by

$$\|w_1 - w_2\|^2 = \min_{w'_1, w'_2} \|w'_1 - w'_2\|^2 \tag{2.204}$$

with $\rho_1 = w'_1 w'_1{}^\dagger$ and $\rho_2 = w'_2 w'_2{}^\dagger$.

$$\begin{aligned}
\min_{w'_1, w'_2} \|w'_1 - w'_2\|^2 &= \min_{w'_1, w'_2} (w'_1 - w'_2, w'_1 - w'_2), \\
&= \min_{w'_1, w'_2} \text{Tr} \left[(w'_1 - w'_2)^\dagger (w'_1 - w'_2) \right], \\
&= \min_{w'_1, w'_2} \text{Tr} \left[w'_1{}^\dagger w'_1 - w'_1{}^\dagger w'_2 - w'_2{}^\dagger w'_1 + w'_2{}^\dagger w'_2 \right], \\
&= \text{Tr} \rho_1 + \text{Tr} \rho_2 - \max_{w'_1, w'_2} \text{Tr} \left[w'_1{}^\dagger w'_2 + w'_2{}^\dagger w'_1 \right], \\
&= 2 - 2 \max_{w'_1, w'_2} \text{Re} \text{Tr} \left[w'_1{}^\dagger w'_2 \right] \tag{2.205}
\end{aligned}$$

Since we know $\text{Re}(x) \leq |x|$, therefore, the expression inside the parentheses can be maximized by choosing w'_1 and w'_2 in such a way that

$$w'_1{}^\dagger w'_2 = w'_2{}^\dagger w'_1 > 0 \tag{2.206}$$

i.e. $w'_1{}^\dagger w'_2$ is self-adjoint and positive definite, which ensures that diagonal entries are real. According to the polar decomposition theorem, any operator A can be decomposed into a hermitian $|A|$ and a unitary factor U_A as

$$A = |A|U_A \tag{2.207}$$

where $|A| = \sqrt{AA^\dagger}$. It is an extension of the conventional polar decomposition of complex numbers $z = |r|e^{i \arg(r)}$. For a given unitary matrix U , we can write [83, 84]

$$\begin{aligned}
\text{Re}[\text{Tr}(AU)] &\leq |\text{Tr}(AU)|, \\
&= |\text{Tr}(|A|U_A U)|, \\
&= |\text{Tr}(\sqrt{|A|}\sqrt{|A|}U_A U)|, \\
&\leq \sqrt{(\text{Tr} |A|)[\text{Tr}(U^\dagger U_A^\dagger |A| U_A U)]}, \\
&= \text{Tr} |A|. \tag{2.208}
\end{aligned}$$

where we have used the Cauchy-Schwarz inequality;

$$|\text{Tr}(M^\dagger N)|^2 \leq \text{Tr}(M^\dagger M) \text{Tr}(N^\dagger N)$$

with $M = \sqrt{|A|}$ and $N = \sqrt{|A|}U_A U$. We finally have $\text{Re}[\text{Tr}(AU)] \leq \text{Tr}|A|$ and the equality holds when $U = U_A^\dagger$ i.e.

$$\max_U \text{Re}[\text{Tr}(AU)] = \text{Tr}|A| \quad (2.209)$$

Now, we write the polar decomposition for the amplitudes as follows

$$w'_1 = \sqrt{\rho_1}U_1, \quad w'_2 = \sqrt{\rho_2}U_2 \quad (2.210)$$

and

$$\begin{aligned} \max_{w'_1, w'_2} \text{Re}[\text{Tr}(w_1^\dagger w'_2)] &= \max_{U_1, U_2} \text{Re}[\text{Tr}(U_1^\dagger \sqrt{\rho_1} \sqrt{\rho_2} U_2)], \\ &= \max_U \text{Re}[\text{Tr}(\sqrt{\rho_1} \sqrt{\rho_2} U)], \quad U = U_2 U_1^\dagger \\ &= \text{Tr}|\sqrt{\rho_1} \sqrt{\rho_2}|, \\ &= \text{Tr} \sqrt{\sqrt{\rho_1} \rho_2 \sqrt{\rho_1}} \end{aligned} \quad (2.211)$$

where we have used the following polar decomposition $\sqrt{\rho_1} \sqrt{\rho_2} = |\sqrt{\rho_1} \sqrt{\rho_2}| U_{\sqrt{\rho_1} \sqrt{\rho_2}}$. This is exactly the Bures distance [83, 85] between two states ρ_1 and ρ_2 . Therefore, the final condition on w_1 and w_2 to achieve parallelity can be written as

$$\begin{aligned} \|w_1 - w_2\|^2 &= \min_{w'_1, w'_2} \|w'_1 - w'_2\|^2, \\ &= 2 - 2 \max_{w'_1, w'_2} \text{Re}[\text{Tr}(w_1^\dagger w'_2)], \\ &= 2 - 2 \text{Tr} \sqrt{\sqrt{\rho_1} \rho_2 \sqrt{\rho_1}}. \end{aligned} \quad (2.212)$$

As stated earlier, equality holds when

$$U = U_2 U_1^\dagger = U_{\sqrt{\rho_1} \sqrt{\rho_2}}^\dagger. \quad (2.213)$$

This unitary is defined only when ρ_1 and ρ_2 are full-rank operators. In that scenario

$$U_{\sqrt{\rho_1} \sqrt{\rho_2}} = |\sqrt{\rho_1} \sqrt{\rho_2}|^{-1} \sqrt{\rho_1} \sqrt{\rho_2} \quad (2.214)$$

and

$$\begin{aligned}
U_{\sqrt{\rho_1}\sqrt{\rho_2}}U_{\sqrt{\rho_1}\sqrt{\rho_2}}^\dagger &= \mathbb{1} \\
(|\sqrt{\rho_1}\sqrt{\rho_2}|^{-1}\sqrt{\rho_1}\sqrt{\rho_2})U_{\sqrt{\rho_1}\sqrt{\rho_2}}^\dagger &= \mathbb{1} \\
\implies U_{\sqrt{\rho_1}\sqrt{\rho_2}}^\dagger &= \sqrt{\rho_2^{-1}}\sqrt{\rho_1^{-1}}|\sqrt{\rho_1}\sqrt{\rho_2}|
\end{aligned}$$

which gives us

$$U_{\sqrt{\rho_1}\sqrt{\rho_2}}^\dagger = U_2U_1^\dagger = \sqrt{\rho_2^{-1}}\sqrt{\rho_1^{-1}}\sqrt{\sqrt{\rho_1}\rho_2\sqrt{\rho_1}} \quad (2.215)$$

Therefore, the freedom that we have to choose U is used to define a parallel transport condition for given two density states ρ_1 and ρ_2 with amplitudes w_1 and w_2 , respectively.

2.11.3 Uhlmann's phase for a two-level system

In [68], a two-level system undergoing a unitary precession has been studied. It was shown explicitly that the two approaches for the mixed state geometric phase yield two different results in general and converge only in certain limit. We go through the results step by step. We start by considering a path

$$\zeta : t \in [0, \tau] \rightarrow \rho_t$$

which can be lifted or purified with $w_t \in \mathcal{H}$ where \mathcal{H} is Hilbert space of Hilbert-Schmidt operators with scalar product

$$\langle w_t | w_{t'} \rangle = \text{Tr}(w_t^\dagger w_{t'}) \quad \text{such that} \quad \rho_t = w_t w_t^\dagger. \quad (2.216)$$

NOTE: w_t is a matrix not vector and $w_t = \sqrt{\rho_t}x_t$ is a purification of ρ_t for an arbitrary unitary x_t .

Uhlmann phase associated with ζ is defined as

$$\Phi_g = \arg \lim_{N \rightarrow \infty} (\langle w_0 | w_{\tau/N} \rangle \langle w_{\tau/N} | w_{2\tau/N} \rangle \dots \langle w_{(N-1)\tau/N} | w_\tau \rangle \langle w_\tau | w_0 \rangle) \quad (2.217)$$

A parallel transport condition on w_t is imposed by demanding that $w_{t+dt}^\dagger w_t$ must be Hermitian and positive $\forall t$. We can further see that

$$\begin{aligned} w_{t+dt}^\dagger w_t &= (\mathbf{1} + \dot{w}_t dt + \mathcal{O}(dt^2))^\dagger w_t, \\ &= (\mathbf{1} + \dot{w}_t^\dagger dt + \mathcal{O}(dt^2)) w_t, \\ &= w_t + \dot{w}_t^\dagger w_t dt + \mathcal{O}(dt^2). \end{aligned}$$

and

$$w_t^\dagger w_{t+dt} = w_t + w_t^\dagger \dot{w}_t dt + \mathcal{O}(dt^2)$$

which reduces to

$$w_t^\dagger \dot{w}_t = \dot{w}_t^\dagger w_t \quad (2.218)$$

In (2.217) the intermediate terms should be real and positive. It will ensure that the argument for these terms will be zero.

$$\langle w_{t+dt} | w_t \rangle = \text{Tr}(w_{t+dt}^\dagger w_t) > 0 \quad (2.219)$$

For such a parallel lift, (2.217) reduces to

$$\Phi_g = \arg \langle w_\tau | w_0 \rangle = \arg \langle w_0 | w_\tau \rangle \quad (2.220)$$

Now, let us consider a unitary evolution

$$\rho_0 = \sum_k \lambda_k |k\rangle\langle k| \rightarrow \rho_t = u_t \rho_0 u_t^\dagger \quad (2.221)$$

$$w_0 = \sqrt{\rho_0} \rightarrow w_t = \sqrt{\rho_t} x_t = u_t \sqrt{\rho_0} u_t^\dagger x_t = u_t \sqrt{\rho_0} v_t \quad (2.222)$$

$$= \sum_k \sqrt{\lambda_k} u_t |k\rangle\langle k| v_t \quad (2.223)$$

where we used $x_0 = \mathbb{1}$ and $v_t = u_t^\dagger x_t$. Using this and (2.220) we get

$$\begin{aligned}
\Phi_g &= \arg \langle w_0 | w_\tau \rangle \\
&= \arg \left(\text{Tr} \sum_k \sqrt{\lambda_k} |k\rangle\langle k| \sum_l \sqrt{\lambda_l} u_\tau |l\rangle\langle l| v_\tau \right) \\
&= \arg \left(\sum_{k,l} \sqrt{\lambda_k \lambda_l} |k\rangle\langle k| u_\tau |l\rangle\langle l| v_\tau \right) \\
&= \arg \sum_{k,l} \sqrt{\lambda_k \lambda_l} \langle k | u_\tau | l \rangle \langle l | v_\tau | k \rangle
\end{aligned} \tag{2.224}$$

We can establish a one-to-one connection between Uhlmann's purification and the conventional purification by considering a pure state $|\Psi_0\rangle$ belonging to the combined Hilbert space of the system and ancilla, i.e., $|\Psi_0\rangle \in \mathcal{H}_s \otimes \mathcal{H}_a$. The evolution of $|\Psi_0\rangle$ will be governed by a bilocal operator $u_t \otimes y_t$ (where $y_t = v_t^T$) that is,

$$w_t \leftrightarrow |\Psi_t\rangle = \sum_k \sqrt{\lambda_k} u_t |k\rangle \otimes y_t |k\rangle, \tag{2.225}$$

such that

$$\Phi_g = \arg \langle \Psi_0 | \Psi_\tau \rangle \tag{2.226}$$

Here, if we consider a unilocal operation of type $u_t \otimes \mathbb{1}$ instead of a bilocal operator, then

$$|\Psi_t\rangle = \sum_k \sqrt{\lambda_k} u_t |k\rangle \otimes |k\rangle. \tag{2.227}$$

Consequently, the phase difference between the initial and final states will be

$$\arg \langle \Psi_0 | \Psi_\tau \rangle = \arg \sum_k \langle k | u_\tau | k \rangle = \arg[\text{Tr}(\rho_0 u_\tau)]. \tag{2.228}$$

In a situation where u_t satisfies parallel transport, it reduces to the geometric phase for mixed states as defined in [31]

$$\Phi_g = \arg \sum_k \lambda_k \nu_k e^{i\beta_k}, \tag{2.229}$$

where $\langle k | u_\tau | k \rangle = \nu_k e^{i\beta_k}$ and β_k is the pure state geometric phase for $|k\rangle$. Let us go back to the Uhlmann's geometric phase where we have a bilocal operator and u_t and v_t are related via the parallel transport condition given by (2.218). We can solve this further to have an explicit

expression

$$\begin{aligned}
w_t &= u_t \sqrt{\rho_0} v_t, \\
w_t^\dagger &= v_t^\dagger \sqrt{\rho_0} u_t^\dagger, \\
\dot{w}_t &= \dot{u}_t \sqrt{\rho_0} v_t + u_t \sqrt{\rho_0} \dot{v}_t, \\
\dot{w}_t^\dagger &= \dot{v}_t^\dagger \sqrt{\rho_0} u_t^\dagger + v_t^\dagger \sqrt{\rho_0} \dot{u}_t^\dagger,
\end{aligned}$$

$$\begin{aligned}
w_t^\dagger \dot{w}_t &= v_t^\dagger \sqrt{\rho_0} u_t^\dagger (\dot{u}_t \sqrt{\rho_0} v_t + u_t \sqrt{\rho_0} \dot{v}_t) \\
&= v_t^\dagger \sqrt{\rho_0} u_t^\dagger \dot{u}_t \sqrt{\rho_0} v_t + v_t^\dagger \rho_0 \dot{v}_t
\end{aligned}$$

$$\begin{aligned}
\dot{w}_t^\dagger u_t &= (\dot{v}_t^\dagger \sqrt{\rho_0} u_t^\dagger + v_t^\dagger \sqrt{\rho_0} \dot{u}_t^\dagger) u_t \sqrt{\rho_0} v_t \\
&= \dot{v}_t^\dagger \rho_0 v_t + v_t^\dagger \sqrt{\rho_0} \dot{u}_t^\dagger u_t \sqrt{\rho_0} v_t
\end{aligned}$$

Also, let us write

$$u_t = \exp(-iHt), v_t = \exp(i\tilde{H}t) \quad (2.230)$$

$$\begin{aligned}
\dot{u}_t &= -iHu_t, \quad \dot{v}_t = i\tilde{H}v_t, \\
\dot{u}_t^\dagger &= iu_t^\dagger H, \quad \dot{v}_t^\dagger = -iv_t^\dagger \tilde{H}
\end{aligned}$$

Using the above relations and (2.218) we get

$$\begin{aligned}
v_t^\dagger \rho_0 \dot{v}_t + v_t^\dagger \sqrt{\rho_0} u_t^\dagger \dot{u}_t \sqrt{\rho_0} v_t &= \dot{v}_t^\dagger \rho_0 v_t + v_t^\dagger \sqrt{\rho_0} \dot{u}_t^\dagger u_t \sqrt{\rho_0} v_t \\
v_t^\dagger \rho_0 \dot{v}_t - \dot{v}_t^\dagger \rho_0 v_t &= v_t^\dagger \sqrt{\rho_0} (\dot{u}_t^\dagger u_t - u_t^\dagger \dot{u}_t) \sqrt{\rho_0} v_t \\
v_t^\dagger \rho_0 (i\tilde{H}v_t) - (-iv_t^\dagger \tilde{H}) \rho_0 v_t &= v_t^\dagger \sqrt{\rho_0} ((iu_t^\dagger H)u_t - u_t^\dagger (-iHu_t)) \sqrt{\rho_0} v_t, \\
i(v_t^\dagger \rho_0 \tilde{H}v_t + v_t^\dagger \tilde{H} \rho_0 v_t) &= 2iv_t^\dagger \sqrt{\rho_0} H \sqrt{\rho_0} v_t, \\
iv_t^\dagger (\rho_0 \tilde{H} + \tilde{H} \rho_0) v_t &= 2iv_t^\dagger \sqrt{\rho_0} H \sqrt{\rho_0} v_t
\end{aligned}$$

which gives us a relation between H and \tilde{H}

$$\rho_0 \tilde{H} + \tilde{H} \rho_0 = \sqrt{\rho_0} H \sqrt{\rho_0}. \quad (2.231)$$

Now, using the spectral decomposition for $\rho_0 = \sum_k \lambda_k |k\rangle\langle k|$ we can write

$$\begin{aligned} \mathbb{1}(\rho_0 \tilde{H} + \tilde{H} \rho_0) \mathbb{1} &= \sum_{k,l} 2\sqrt{\lambda_k \lambda_l} |k\rangle\langle l| \langle k| H |l\rangle \\ \sum_k |k\rangle\langle k| (\rho_0 \tilde{H} + \tilde{H} \rho_0) \sum_k |l\rangle\langle l| &= \sum_{k,l} 2\sqrt{\lambda_k \lambda_l} |k\rangle\langle l| \langle k| H |l\rangle \\ \sum_{k,l} (\lambda_k + \lambda_l) \langle k| \tilde{H} |l\rangle |k\rangle\langle l| &= \sum_{k,l} 2\sqrt{\lambda_k \lambda_l} |k\rangle\langle l| \langle k| H |l\rangle \end{aligned}$$

implies

$$\tilde{H} = \sum_{k,l} \frac{2\sqrt{\lambda_k \lambda_l}}{\lambda_k + \lambda_l} |k\rangle\langle l| \langle k| H |l\rangle. \quad (2.232)$$

For example, consider a two-level system with the Hamiltonian given by

$$H = \frac{1}{2} \hat{\mathbf{n}} \cdot \boldsymbol{\sigma} = \frac{1}{2} (n_x \sigma_x + n_z \sigma_z), \quad n_x^2 + n_z^2 = 1. \quad (2.233)$$

and initially in the state

$$\rho_0 = \frac{1}{2} (\mathbb{1} + r \sigma_z) = \frac{1+r}{2} |0\rangle\langle 0| + \frac{1-r}{2} |1\rangle\langle 1| \quad (2.234)$$

By substituting H into (2.232) we get

$$\tilde{H} = \frac{1}{2} (\sqrt{1-r^2} n_x \sigma_x + n_z \sigma_z) = \frac{1}{2} \sqrt{1-r^2} n_x^2 (\tilde{n}_x \sigma_x + \tilde{n}_z \sigma_z) = \frac{1}{2} \sqrt{1-r^2} n_x^2 (\tilde{\mathbf{n}} \cdot \boldsymbol{\sigma})$$

where

$$\tilde{\mathbf{n}} = \left(\frac{\sqrt{1-r^2} n_x}{\sqrt{1-r^2} n_x^2}, 0, \frac{n_z}{\sqrt{1-r^2} n_x^2} \right) \quad (2.235)$$

Thus

$$\begin{aligned} \Phi_g &= \arg \sum_{k,l} \sqrt{\lambda_k \lambda_l} \langle k| u_\tau |l\rangle \langle l| v_\tau |k\rangle, \\ &= \arg \sum_{k,l} \sqrt{\lambda_k \lambda_l} \langle k| e^{-i\tau H} |l\rangle \langle l| e^{i\tau \tilde{H}} |k\rangle, \\ &= \arg \sum_{k,l} \sqrt{\lambda_k \lambda_l} \langle k| e^{-i\tau(\hat{\mathbf{n}} \cdot \boldsymbol{\sigma})/2} |l\rangle \langle l| e^{i\tau(\tilde{\mathbf{n}} \cdot \boldsymbol{\sigma})/2} |k\rangle, \end{aligned}$$

Using

$$\begin{aligned}
\langle 0|e^{-i\tau(\hat{\mathbf{n}}\cdot\boldsymbol{\sigma})/2}|0\rangle &= \cos\frac{\tau}{2} - in_z \sin\frac{\tau}{2}, \\
\langle 0|e^{-i\tau(\hat{\mathbf{n}}\cdot\boldsymbol{\sigma})/2}|1\rangle &= -in_x \sin\frac{\tau}{2}, \\
\langle 1|e^{-i\tau(\hat{\mathbf{n}}\cdot\boldsymbol{\sigma})/2}|0\rangle &= -in_x \sin\frac{\tau}{2}, \\
\langle 1|e^{-i\tau(\hat{\mathbf{n}}\cdot\boldsymbol{\sigma})/2}|1\rangle &= \cos\frac{\tau}{2} + in_z \sin\frac{\tau}{2}
\end{aligned}$$

and similarly for $e^{-i\tilde{\tau}(\tilde{\mathbf{n}}\cdot\boldsymbol{\sigma})/2}$ and

$$\tilde{\tau} = \sqrt{1 - r^2 n_x^2} \tau$$

we get the Uhlmann phase as

$$\Phi_g = \tan^{-1} \left[\frac{r \left(\tilde{n}_z \tan \frac{\tilde{\tau}}{2} - n_z \tan \frac{\tau}{2} \right)}{1 + (n_z \tilde{n}_z + \sqrt{1 - r^2 n_x^2} \tilde{n}_x) \tan \frac{\tau}{2} \tan \frac{\tilde{\tau}}{2}} \right] \quad (2.236)$$

First, for the cyclic case, that is, for $\tau = 2\pi$, we have

$$\Phi_g = \tan^{-1} \left[r \tilde{n}_z \tan \pi \sqrt{1 - r^2 n_x^2} \right] = \tan^{-1} \left[\frac{r n_z}{\sqrt{1 - r^2 n_x^2}} \tan \pi \sqrt{1 - r^2 n_x^2} \right] \quad (2.237)$$

Now, if we consider the state to be pure, that is, $r = 1$, we have $\tilde{\mathbf{n}} = (0, 0, 1)$ and $\tilde{\tau} = \sqrt{1 - n_x^2} = n_z$ which yields

$$\Phi_g = -\tan^{-1} \left[n_z \tan \frac{\tau}{2} \right] + n_z \frac{\tau}{2}. \quad (2.238)$$

This is exactly equal to the minus half of the geodesically closed solid angle subtended by the open path on the Bloch sphere. Compared to the results we get using the interferometric approach [31], where the geometric phase for a mixed state ρ with $r \neq 0$, we have $\phi_g = -\tan^{-1} [r \tan(\Omega/2)]$ where Ω is the geodesically closed solid angle on the Bloch sphere. The two approaches converge only in the case of pure state or in a trivial case when both the system and the ancilla are not evolving. This convergence of two approaches has been experimentally verified using NMR in [75].

2.11.4 A comment on the importance of the two approaches, interferometric and Uhlmann's approach, for mixed geometric phases in the topological characterization

Topological characterization [don't worry, we will discuss it in detail in upcoming chapters] using Uhlmann's approach to mixed state geometric phase was proposed [69, 86–88]. It was also pointed out that the topological properties cannot survive above a certain critical temperature using Uhlmann construction [69], in contrast to the interferometric approach where topological properties survive for non-zero temperature and cease to survive only in the limit of infinite temperature. Furthermore, a modified Chern character was also proposed, whose integral gives the thermal Uhlmann Chern number [89]. In Ref. [90], the measurement of Uhlmann's phase has been demonstrated using superconducting qubits. Apart from these, there is something called "ensemble geometric phase" which is used to characterize topology of the system in mixed states [91–93].

2.12 Weak Measurement Approach to Measure GP

The geometric phase can be associated with the complex-valued weak value that arises in certain experiments. In such experiments, we make the system interact with an ancilla in a limited amount in order to preserve the quantum nature of the system, such as coherence. For a system, prepared in a pre-selected state $|\psi_i\rangle$ and subject to a post-selection state $|\psi_f\rangle$, the weak value of an observable A is given by [94–96]

$$A_w = \frac{\langle \psi_f | A | \psi_i \rangle}{\langle \psi_f | \psi_i \rangle}. \quad (2.239)$$

In this section, we will establish a connection between the geometric phase and the complex valued A_w . Let us start by considering a quantum system and a quantum measurement device prepared initially in the product state [97]

$$\rho_0 = \rho_{qs} \otimes \rho_{md} = |a\rangle\langle a| \otimes |M_0\rangle\langle M_0| \quad (2.240)$$

The system and the measurement device are made to interact by an interaction Hamiltonian given by [98, 99]

$$H(t) = g(t)\mathcal{P}^b \otimes Q \quad (2.241)$$

where $\mathcal{P}^b = |b\rangle\langle b|$ is a one-dimensional projector acting on the quantum system, $g(t)$ is the coupling parameter which controls the interaction, and Q is the position operator for the measurement device or pointer. We take the initial state of the measurement device, in the position representation, as Gaussian i.e.,

$$M_0(q) = \langle q|M_0\rangle \sim e^{-q^2/2\sigma^2} \quad (2.242)$$

where $|q\rangle$ is the eigenstate of the position operator Q of the measurement device or the pointer. The unitary evolution is

$$\begin{aligned} U(t) &= e^{-\frac{i}{\hbar} \int g(t)\mathcal{P}^b \otimes Q} \\ &= e^{-i\kappa\mathcal{P}^b \otimes Q} \end{aligned} \quad (2.243)$$

with

$$\kappa = \frac{1}{\hbar} \int g(t) dt \quad (2.244)$$

After the interaction, the state of the combined system is as follows

$$\rho(t) = U(t)\rho_0 U^\dagger(t) = e^{-i\kappa\mathcal{P}^b \otimes Q} |a\rangle\langle a| \otimes |M_0\rangle\langle M_0| e^{i\kappa\mathcal{P}^b \otimes Q} \quad (2.245)$$

and conditioned on the post-selection of the state $|c\rangle\langle c|$, we get

$$\begin{aligned} \rho_{ps} &= |c\rangle\langle c| \otimes \langle c| U(t)\rho_0 U^\dagger(t) |c\rangle \\ &= |c\rangle\langle c| \otimes \langle c| e^{-i\kappa\mathcal{P}^b \otimes Q} |a\rangle |M_0\rangle \langle M_0| \langle a| e^{i\kappa\mathcal{P}^b \otimes Q} |c\rangle \end{aligned} \quad (2.246)$$

In the limit $\kappa \ll 1$,

$$\begin{aligned}
& \langle c | e^{-i\kappa \mathcal{P}^b \otimes Q} | a \rangle \\
&= \langle c | \mathbb{1} - i\kappa \mathcal{P}^b \otimes Q | a \rangle \\
&= \langle c | \mathbb{1} - i\kappa |b\rangle\langle b| \otimes Q | a \rangle \\
&= \langle c | a \rangle - i\kappa \langle c | b \rangle \langle b | a \rangle Q \\
&= \langle c | a \rangle \left(\mathbb{1} - i\kappa \frac{\langle c | b \rangle \langle b | a \rangle}{\langle c | a \rangle} Q \right) \\
&= \langle c | a \rangle \left(\mathbb{1} - i\kappa \mathcal{P}_w^b(a, c) Q \right) \\
&= \langle c | a \rangle e^{-i\kappa \mathcal{P}_w^b(a, c) Q}
\end{aligned} \tag{2.247}$$

where

$$\mathcal{P}_w^b(a, c) = \frac{\langle c | b \rangle \langle b | a \rangle}{\langle c | a \rangle} \tag{2.248}$$

is the weak value of the operator \mathcal{P}^b with pre-selected state $|a\rangle$ and post-selected state $|c\rangle$. Thus,

$$\rho_{ps} = |c\rangle \langle c| \otimes |\langle c | a \rangle|^2 e^{-i\kappa \mathcal{P}_w^b(a, c) Q} |M_0\rangle \langle M_0| e^{i\kappa \mathcal{P}_w^b(c, a) Q} \tag{2.249}$$

The state of the pointer after the post-selection is

$$\begin{aligned}
|M\rangle &= e^{-i\kappa z Q} |M_0\rangle \sim e^{-i\kappa z Q} \left(\sum_i e^{q_i^2/2\sigma^2} |q_i\rangle \right) \\
&= \sum_i e^{q_i^2/2\sigma^2} e^{-i\kappa z q_i} |q_i\rangle
\end{aligned} \tag{2.250}$$

which further results in

$$M(q) = \langle q | M \rangle \sim e^{q^2/2\sigma^2} e^{-i\kappa z q} \tag{2.251}$$

Writing $z = a + ib$ and by completing the square, we will get

$$M(q) \sim \underbrace{\exp\left(-\frac{(q - \kappa\sigma^2 b)^2}{2\sigma^2}\right)}_{\text{shifted Gaussian}} \times \underbrace{\exp(-i\kappa a q)}_{\text{shift in momentum}} \tag{2.252}$$

Therefore, as a result of post-selection, the weak measurement results in a shift in position of the pointer

$$\delta q = \kappa\sigma^2 b = \kappa\sigma^2 \text{Im } \mathcal{P}_w^b(a, c) \tag{2.253}$$

and the momentum of the pointer.

$$\delta p = -\hbar\kappa a = -\hbar\kappa \operatorname{Re} \mathcal{P}_w^b(a, c) \quad (2.254)$$

We have

$$\begin{aligned} \mathcal{P}_w^b(a, c) &= \frac{\langle c|b\rangle \langle b|a\rangle}{\langle c|a\rangle} \\ &= \frac{\langle a|c\rangle \langle c|b\rangle \langle b|a\rangle}{|\langle c|a\rangle|^2} \\ \implies \arg \mathcal{P}_w^b(a, c) &= \arg \langle a|c\rangle \langle c|b\rangle \langle b|a\rangle = \arg \Delta_3(a, b, c) \end{aligned} \quad (2.255)$$

where Δ_3 is the third-order Bargmann invariant (as discussed earlier), the argument of which results in the geometric phase between the three mutually nonorthogonal states $\{|a\rangle, |b\rangle, |c\rangle\}$.

Therefore, we have

$$\begin{aligned} \gamma_g = \arg \Delta_3(a, b, c) &= \tan^{-1} \left(\frac{\operatorname{Im} \mathcal{P}_w^b(a, c)}{\operatorname{Re} \mathcal{P}_w^b(a, c)} \right) \\ &= \tan^{-1} \left(\frac{\delta q / \kappa \sigma^2}{-\delta p / \hbar \kappa} \right) \\ &= -\tan^{-1} \left(\frac{\hbar \delta q}{\sigma^2 \delta p} \right) \end{aligned} \quad (2.256)$$

Therefore, by measuring the shift in position and the momentum of the pointer after turning off the interaction, we can find the geometric phase. The above method can be extended for the case where we have N number of mutually non-orthogonal states $\{|\psi_0\rangle, |\psi_1\rangle, |\psi_2\rangle, \dots, |\psi_{N-1}\rangle\}$. Recently, weak measurement sequence has been shown to lead to the accumulation of the geometric phase, depending on the strength of the measurement [45].

2.12.1 Weak value measurements with qubits

Let's consider a spin-1/2 system pre-selected and post-selected states represented by Bloch vectors $\hat{\mathbf{n}}$ and $\hat{\mathbf{m}}$ respectively and is given by

$$|\psi_i\rangle\langle\psi_i| = \frac{1}{2} (\mathbb{1} + \hat{\mathbf{n}} \cdot \boldsymbol{\sigma}) \quad (2.257)$$

and

$$|\psi_f\rangle\langle\psi_f| = \frac{1}{2} (\mathbb{1} + \hat{\mathbf{m}} \cdot \boldsymbol{\sigma}) \quad (2.258)$$

We now consider the observable Z of the form

$$Z = \frac{1}{2} (\mathbf{1} + \hat{\mathbf{k}} \cdot \boldsymbol{\sigma}) \quad (2.259)$$

and calculate the weak value corresponding to Z as

$$\begin{aligned} Z_w(\psi_i, \psi_f) &= \frac{\langle \psi_f | Z | \psi_i \rangle}{\langle \psi_f | \psi_i \rangle} \\ &= \frac{\langle \psi_f | Z | \psi_i \rangle \langle \psi_i | \psi_f \rangle}{|\langle \psi_f | \psi_i \rangle|^2} \\ &= \frac{\text{Tr} [|\psi_f\rangle \langle \psi_f| Z |\psi_i\rangle \langle \psi_i|]}{\text{Tr} [|\psi_f\rangle \langle \psi_f| \psi_i\rangle \langle \psi_i|]} \\ &= \frac{1}{2} \frac{\text{Tr} [(\mathbf{1} + \hat{\mathbf{n}} \cdot \boldsymbol{\sigma}) (\mathbf{1} + \hat{\mathbf{n}} \cdot \boldsymbol{\sigma}) (\mathbf{1} + \hat{\mathbf{k}} \cdot \boldsymbol{\sigma})]}{\text{Tr} [(\mathbf{1} + \hat{\mathbf{n}} \cdot \boldsymbol{\sigma}) (\mathbf{1} + \hat{\mathbf{n}} \cdot \boldsymbol{\sigma})]} \\ &= \frac{1}{2} \left(\frac{1 + \hat{\mathbf{n}} \cdot \hat{\mathbf{k}} + \hat{\mathbf{k}} \cdot \hat{\mathbf{m}} + \hat{\mathbf{m}} \cdot \hat{\mathbf{n}} + i \hat{\mathbf{k}} \cdot (\hat{\mathbf{n}} \times \hat{\mathbf{m}})}{1 + \hat{\mathbf{m}} \cdot \hat{\mathbf{n}}} \right) \end{aligned} \quad (2.260)$$

Further, if we choose $Z = |\uparrow\rangle\langle\uparrow|$ i.e. $\hat{\mathbf{k}} = (0, 0, 1)$ then

$$Z_w(\psi_i, \psi_f) = \frac{1}{2} \left(\frac{1 + n_z + m_z + \hat{\mathbf{m}} \cdot \hat{\mathbf{n}} + i(\hat{\mathbf{n}} \times \hat{\mathbf{m}})_z}{1 + \hat{\mathbf{m}} \cdot \hat{\mathbf{n}}} \right) \quad (2.261)$$

Since $Z_w(\psi_i, \psi_f)$ is a complex quantity, we can write a polar decomposition for it as

$$Z_w = \frac{\sqrt{(1 + n_z + m_z + \hat{\mathbf{m}} \cdot \hat{\mathbf{n}})^2 + [(\hat{\mathbf{n}} \times \hat{\mathbf{m}})_z]^2}}{2(1 + \hat{\mathbf{m}} \cdot \hat{\mathbf{n}})} e^{-i\phi} \quad (2.262)$$

where

$$\phi = \tan^{-1} \left(\frac{(\hat{\mathbf{n}} \times \hat{\mathbf{m}})_z}{1 + n_z + m_z + \hat{\mathbf{m}} \cdot \hat{\mathbf{n}}} \right) \quad (2.263)$$

Using the expression for the solid angle Ω , subtended by given three vectors $\mathbf{R}_1, \mathbf{R}_2$, and \mathbf{R}_3 on the center [100] as

$$\tan \frac{\Omega}{2} = \frac{\mathbf{R}_1 \cdot (\mathbf{R}_2 \times \mathbf{R}_3)}{R_1 R_2 R_3 + (\mathbf{R}_1 \cdot \mathbf{R}_2) R_3 + (\mathbf{R}_1 \cdot \mathbf{R}_3) R_2 + (\mathbf{R}_2 \cdot \mathbf{R}_3) R_1} \quad (2.264)$$

we conclude from Eq. (2.260) directly, that the phase ϕ is nothing but the half of the solid angle subtended by the Bloch vectors $\hat{\mathbf{m}}, \hat{\mathbf{n}}$ and $\hat{\mathbf{k}}$ at the origin i.e.,

$$\phi = \frac{\Omega}{2}. \quad (2.265)$$

In general, the weak value of the operator of the form $\hat{\mathbf{q}} \cdot \boldsymbol{\sigma}$ can be evaluated using Pauli's algebra as

$$\begin{aligned} \langle \hat{\mathbf{q}} \cdot \boldsymbol{\sigma} \rangle_w &= \frac{\langle \psi_f | \hat{\mathbf{q}} \cdot \boldsymbol{\sigma} | \psi_i \rangle}{\langle \psi_f | \psi_i \rangle} \\ &= \frac{\text{Tr}(|\psi_f\rangle \langle \psi_f| \hat{\mathbf{q}} \cdot \boldsymbol{\sigma} |\psi_i\rangle \langle \psi_i|)}{\text{Tr}(|\psi_f\rangle \langle \psi_f| \langle \psi_i| \langle \psi_i|)} \\ &= \frac{\hat{\mathbf{q}} \cdot \hat{\mathbf{n}} + \hat{\mathbf{q}} \cdot \hat{\mathbf{m}} + i\hat{\mathbf{q}} \cdot (\hat{\mathbf{n}} \times \hat{\mathbf{m}})}{1 + \hat{\mathbf{n}} \cdot \hat{\mathbf{m}}}. \end{aligned} \quad (2.266)$$

Next, we will take qubit as the measurement device or pointer and see how we can measure the real and imaginary parts of the weak value, which are required to calculate the geometric phase.

2.13 Qubit as A Measurement Device

Suppose we consider a qubit as a measurement device in an initial state $|\phi_i\rangle$. We again make the system and the pointer interact and after the post-selection, total state of the system and the measurement qubit will be

$$\rho_{ps} = |\psi_f\rangle \langle \psi_f| \otimes \langle \psi_f | e^{-i\kappa \mathcal{P}^b \otimes Q} | \psi_i \rangle | \phi_i \rangle \langle \phi_i | \langle \phi_i | \langle \psi_i | e^{i\kappa \mathcal{P}^b \otimes Q} | \psi_f \rangle \quad (2.267)$$

Therefore

$$\begin{aligned} |\phi_f\rangle &= \langle \psi_f | e^{-i\kappa \mathcal{P}^b \otimes Q} | \psi_i \rangle | \phi_i \rangle \\ &\sim \langle \psi_f | \psi_i \rangle (\mathbb{1} - i\kappa \langle \mathcal{P}^b \rangle_w Q) | \phi_i \rangle \end{aligned} \quad (2.268)$$

Now, we consider any general operation for a qubit which reads

$$Q = \hat{\mathbf{n}} \cdot \boldsymbol{\sigma} \quad (2.269)$$

where $\hat{\mathbf{n}}$ is a unit vector and let us say $\langle \mathcal{P}^b \rangle_w = z = x + iy$. After the interaction is switched off and the system is subject to post-selection, we are free to measure any operator of the form $\hat{\mathbf{q}} \cdot \boldsymbol{\sigma}$, the expectation value of which is given by [101]

$$\langle \phi_f | \hat{\mathbf{q}} \cdot \boldsymbol{\sigma} | \phi_f \rangle = \frac{\langle \phi_f | \hat{\mathbf{q}} \cdot \boldsymbol{\sigma} | \phi_f \rangle}{\langle \phi_f | \phi_f \rangle} \quad (2.270)$$

Numerator

$$\begin{aligned}
& \langle \phi_f | \hat{\mathbf{q}} \cdot \boldsymbol{\sigma} | \phi_f \rangle \\
&= |\langle \psi_f | \psi_i \rangle|^2 \langle \phi_i | (\mathbb{1} + i\kappa z^* (\hat{\mathbf{q}} \cdot \boldsymbol{\sigma}) \hat{\mathbf{q}} \cdot \boldsymbol{\sigma} (\mathbb{1} - i\kappa z (\hat{\mathbf{n}} \cdot \boldsymbol{\sigma})) | \phi_i \rangle \\
&\simeq |\langle \psi_f | \psi_i \rangle|^2 (\langle \phi_i | \hat{\mathbf{q}} \cdot \boldsymbol{\sigma} | \phi_i \rangle + i\kappa x \langle \phi_i | [\hat{\mathbf{n}} \cdot \boldsymbol{\sigma}, \hat{\mathbf{q}} \cdot \boldsymbol{\sigma}] | \phi_i \rangle + \kappa y \langle \phi_i | \{\hat{\mathbf{n}} \cdot \boldsymbol{\sigma}, \hat{\mathbf{q}} \cdot \boldsymbol{\sigma}\}_+ | \phi_i \rangle) + \mathcal{O}(g^2)
\end{aligned} \tag{2.271}$$

Denominator

$$\begin{aligned}
\langle \phi_f | \phi_f \rangle &= |\langle \psi_f | \psi_i \rangle|^2 \langle \phi_i | (\mathbb{1} + i\kappa z^* (\hat{\mathbf{n}} \cdot \boldsymbol{\sigma})) (\mathbb{1} - i\kappa z (\hat{\mathbf{n}} \cdot \boldsymbol{\sigma})) | \phi_i \rangle \\
&= |\langle \psi_f | \psi_i \rangle|^2 (\mathbb{1} + 2gy \langle \phi_i | \hat{\mathbf{n}} \cdot \boldsymbol{\sigma} | \phi_i \rangle + 2g^2 |z|^2) \\
&\simeq |\langle \psi_f | \psi_i \rangle|^2 (\mathbb{1} + 2gy \langle \phi_i | \hat{\mathbf{n}} \cdot \boldsymbol{\sigma} | \phi_i \rangle) + \mathcal{O}(g^2)
\end{aligned} \tag{2.272}$$

Thus,

$$\frac{\langle \phi_f | \hat{\mathbf{q}} \cdot \boldsymbol{\sigma} | \phi_f \rangle}{\langle \phi_f | \phi_f \rangle} = \frac{\langle \phi_i | \hat{\mathbf{q}} \cdot \boldsymbol{\sigma} | \phi_i \rangle + i\kappa x \langle \phi_i | [\hat{\mathbf{n}} \cdot \boldsymbol{\sigma}, \hat{\mathbf{q}} \cdot \boldsymbol{\sigma}] | \phi_i \rangle + \kappa y \langle \phi_i | \{\hat{\mathbf{n}} \cdot \boldsymbol{\sigma}, \hat{\mathbf{q}} \cdot \boldsymbol{\sigma}\}_+ | \phi_i \rangle}{\mathbb{1} + 2gy \langle \phi_i | \hat{\mathbf{n}} \cdot \boldsymbol{\sigma} | \phi_i \rangle} \tag{2.273}$$

By expanding the denominator in power series up to first order in g , we get

$$\begin{aligned}
\frac{\langle \phi_f | \hat{\mathbf{q}} \cdot \boldsymbol{\sigma} | \phi_f \rangle}{\langle \phi_f | \phi_f \rangle} &= \langle \phi_i | \hat{\mathbf{q}} \cdot \boldsymbol{\sigma} | \phi_i \rangle + i\kappa x \langle \phi_i | [\hat{\mathbf{n}} \cdot \boldsymbol{\sigma}, \hat{\mathbf{q}} \cdot \boldsymbol{\sigma}] | \phi_i \rangle + \kappa y \langle \phi_i | \{\hat{\mathbf{n}} \cdot \boldsymbol{\sigma}, \hat{\mathbf{q}} \cdot \boldsymbol{\sigma}\}_+ | \phi_i \rangle \\
&\quad - 2\kappa y \langle \phi_i | \hat{\mathbf{n}} \cdot \boldsymbol{\sigma} | \phi_i \rangle \langle \phi_i | \hat{\mathbf{q}} \cdot \boldsymbol{\sigma} | \phi_i \rangle
\end{aligned} \tag{2.274}$$

We further take

$$|\phi_i\rangle\langle\phi_i| = \frac{1}{2}(\mathbb{1} + \hat{\mathbf{m}} \cdot \boldsymbol{\sigma}) \tag{2.275}$$

and using the relation [35]

$$(\hat{\mathbf{a}} \cdot \boldsymbol{\sigma})(\hat{\mathbf{b}} \cdot \boldsymbol{\sigma}) = (\mathbf{a} \cdot \mathbf{b})\mathbb{1} + i(\mathbf{a} \times \mathbf{b}) \cdot \boldsymbol{\sigma}. \tag{2.276}$$

we further simplify the expression for the expectation value. The first term would be

$$\begin{aligned}
\langle \phi_i | \hat{\mathbf{q}} \cdot \boldsymbol{\sigma} | \phi_i \rangle &= \text{Tr}(\hat{\mathbf{q}} \cdot \boldsymbol{\sigma} | \phi_i \rangle \langle \psi_i |) \\
&= \frac{1}{2} \text{Tr}(\hat{\mathbf{q}} \cdot \boldsymbol{\sigma} (\mathbb{1} + \hat{\mathbf{m}} \cdot \boldsymbol{\sigma})) \\
&= \frac{1}{2} \text{Tr}(\hat{\mathbf{q}} \cdot \boldsymbol{\sigma} + (\hat{\mathbf{q}} \cdot \boldsymbol{\sigma})(\hat{\mathbf{m}} \cdot \boldsymbol{\sigma})) \\
&= \hat{\mathbf{q}} \cdot \hat{\mathbf{m}}.
\end{aligned} \tag{2.277}$$

Second term

$$\begin{aligned}
& i\kappa x \langle \phi_i | [\hat{\mathbf{n}} \cdot \boldsymbol{\sigma}, \hat{\mathbf{q}} \cdot \boldsymbol{\sigma}] | \phi_i \rangle \\
&= \frac{i\kappa x}{2} \text{Tr}([\hat{\mathbf{n}} \cdot \boldsymbol{\sigma}, \hat{\mathbf{q}} \cdot \boldsymbol{\sigma}] | \phi_i \rangle \langle \phi_i |) \\
&= \frac{i\kappa x}{2} \text{Tr}((\hat{\mathbf{n}} \cdot \boldsymbol{\sigma})(\hat{\mathbf{q}} \cdot \boldsymbol{\sigma}) - (\hat{\mathbf{q}} \cdot \boldsymbol{\sigma})(\hat{\mathbf{n}} \cdot \boldsymbol{\sigma}))(\mathbb{1} + \hat{\mathbf{m}} \cdot \boldsymbol{\sigma})] \\
&= \frac{i\kappa x}{2} \text{Tr}((\hat{\mathbf{n}} \cdot \boldsymbol{\sigma})(\hat{\mathbf{q}} \cdot \boldsymbol{\sigma}) - (\hat{\mathbf{q}} \cdot \boldsymbol{\sigma})(\hat{\mathbf{n}} \cdot \boldsymbol{\sigma}) + (\hat{\mathbf{n}} \cdot \boldsymbol{\sigma})(\hat{\mathbf{q}} \cdot \boldsymbol{\sigma})(\hat{\mathbf{m}} \cdot \boldsymbol{\sigma}) - (\hat{\mathbf{q}} \cdot \boldsymbol{\sigma})(\hat{\mathbf{n}} \cdot \boldsymbol{\sigma})(\hat{\mathbf{m}} \cdot \boldsymbol{\sigma})) \\
&= \frac{i\kappa x}{2} (i(\hat{\mathbf{n}} \times \hat{\mathbf{q}}) \cdot \hat{\mathbf{m}} - i(\hat{\mathbf{q}} \times \hat{\mathbf{n}}) \cdot \hat{\mathbf{m}}) \\
&= 2\kappa x (\hat{\mathbf{q}} \times \hat{\mathbf{n}}) \cdot \hat{\mathbf{m}}
\end{aligned} \tag{2.278}$$

Third term

$$\begin{aligned}
& \kappa y \langle \phi_i | \{\hat{\mathbf{n}} \cdot \boldsymbol{\sigma}, \hat{\mathbf{q}} \cdot \boldsymbol{\sigma}\}_+ | \phi_i \rangle \\
&= \frac{\kappa y}{2} \text{Tr}(\{\hat{\mathbf{n}} \cdot \boldsymbol{\sigma}, \hat{\mathbf{q}} \cdot \boldsymbol{\sigma}\}_+ | \phi_i \rangle \langle \phi_i |) \\
&= \frac{\kappa y}{2} \text{Tr}((\hat{\mathbf{n}} \cdot \boldsymbol{\sigma})(\hat{\mathbf{q}} \cdot \boldsymbol{\sigma}) + (\hat{\mathbf{q}} \cdot \boldsymbol{\sigma})(\hat{\mathbf{n}} \cdot \boldsymbol{\sigma}))(\mathbb{1} + \hat{\mathbf{m}} \cdot \boldsymbol{\sigma})] \\
&= \frac{\kappa y}{2} \text{Tr}((\hat{\mathbf{n}} \cdot \boldsymbol{\sigma})(\hat{\mathbf{q}} \cdot \boldsymbol{\sigma}) + (\hat{\mathbf{q}} \cdot \boldsymbol{\sigma})(\hat{\mathbf{n}} \cdot \boldsymbol{\sigma}) + (\hat{\mathbf{n}} \cdot \boldsymbol{\sigma})(\hat{\mathbf{q}} \cdot \boldsymbol{\sigma})(\hat{\mathbf{m}} \cdot \boldsymbol{\sigma}) + (\hat{\mathbf{q}} \cdot \boldsymbol{\sigma})(\hat{\mathbf{n}} \cdot \boldsymbol{\sigma})(\hat{\mathbf{m}} \cdot \boldsymbol{\sigma})) \\
&= 2\kappa y \hat{\mathbf{q}} \cdot \hat{\mathbf{n}}
\end{aligned} \tag{2.279}$$

Fourth term

$$\begin{aligned}
& -2\kappa y \langle \phi_i | \hat{\mathbf{n}} \cdot \boldsymbol{\sigma} | \phi_i \rangle \langle \phi_i | \hat{\mathbf{q}} \cdot \boldsymbol{\sigma} | \phi_i \rangle \\
&= -2\kappa y \text{Tr}(\hat{\mathbf{n}} \cdot \boldsymbol{\sigma} | \phi_i \rangle \langle \phi_i | \hat{\mathbf{q}} \cdot \boldsymbol{\sigma} | \phi_i \rangle \langle \phi_i |) \\
&= -\frac{\kappa y}{2} \text{Tr}(\hat{\mathbf{n}} \cdot \boldsymbol{\sigma}(\mathbb{1} + \hat{\mathbf{m}} \cdot \boldsymbol{\sigma})\hat{\mathbf{q}} \cdot \boldsymbol{\sigma}(\mathbb{1} + \hat{\mathbf{m}} \cdot \boldsymbol{\sigma})) \\
&= -\frac{\kappa y}{2} \text{Tr}((\hat{\mathbf{n}} \cdot \boldsymbol{\sigma})(\hat{\mathbf{q}} \cdot \boldsymbol{\sigma}) + (\hat{\mathbf{n}} \cdot \boldsymbol{\sigma})(\hat{\mathbf{q}} \cdot \boldsymbol{\sigma})(\hat{\mathbf{m}} \cdot \boldsymbol{\sigma}) + (\hat{\mathbf{n}} \cdot \boldsymbol{\sigma})(\hat{\mathbf{m}} \cdot \boldsymbol{\sigma})(\hat{\mathbf{q}} \cdot \boldsymbol{\sigma}) + (\hat{\mathbf{n}} \cdot \boldsymbol{\sigma})(\hat{\mathbf{m}} \cdot \boldsymbol{\sigma})(\hat{\mathbf{q}} \cdot \boldsymbol{\sigma})(\hat{\mathbf{m}} \cdot \boldsymbol{\sigma})) \\
&= -\kappa y (\hat{\mathbf{n}} \cdot \hat{\mathbf{q}} + i(\hat{\mathbf{n}} \times \hat{\mathbf{q}}) \cdot \hat{\mathbf{m}} + i(\hat{\mathbf{n}} \times \hat{\mathbf{m}}) \cdot \hat{\mathbf{q}} + (\hat{\mathbf{n}} \cdot \hat{\mathbf{m}})(\hat{\mathbf{q}} \cdot \hat{\mathbf{m}})) \\
&= -\kappa y (\hat{\mathbf{q}} \cdot \hat{\mathbf{n}} + (\hat{\mathbf{n}} \cdot \hat{\mathbf{m}})(\hat{\mathbf{q}} \cdot \hat{\mathbf{m}}))
\end{aligned} \tag{2.280}$$

Therefore, Eq. (2.274) becomes

$$\frac{\langle \phi_f | \hat{\mathbf{q}} \cdot \boldsymbol{\sigma} | \phi_f \rangle}{\langle \phi_f | \phi_f \rangle} = \hat{\mathbf{q}} \cdot \hat{\mathbf{m}} + 2\kappa [(\hat{\mathbf{q}} \times \hat{\mathbf{n}}) \cdot \hat{\mathbf{m}}] x + 2\kappa [\hat{\mathbf{q}} \cdot \hat{\mathbf{n}} - (\hat{\mathbf{n}} \cdot \hat{\mathbf{m}})(\hat{\mathbf{q}} \cdot \hat{\mathbf{m}})] y. \tag{2.281}$$

where

$$x = \text{Re} \langle \mathcal{P}_B \rangle_w, \quad y = \text{Im} \langle \mathcal{P}_B \rangle_w \tag{2.282}$$

and $\hat{\mathbf{m}}$ is the Bloch corresponding to the initial state of the pointer. We observe that the expectation value given in Eq. (2.281) depends on the initial state of the pointer. By choosing the appropriate initial state of the meter qubit, we can obtain the real and imaginary parts of the weak value A_w in terms of the expectation value of an observable. For example, if we choose $\hat{\mathbf{m}} \perp \hat{\mathbf{n}}$ and $\hat{\mathbf{q}} = \hat{\mathbf{n}} \times \hat{\mathbf{m}}$, then

$$\frac{\langle \phi_f | \hat{\mathbf{q}} \cdot \boldsymbol{\sigma} | \phi_f \rangle}{\langle \phi_f | \phi_f \rangle} = 2\kappa x \quad (2.283)$$

and if $\hat{\mathbf{m}} \perp \hat{\mathbf{n}}$ and $\hat{\mathbf{q}} = \hat{\mathbf{n}}$

$$\frac{\langle \phi_f | \hat{\mathbf{q}} \cdot \boldsymbol{\sigma} | \phi_f \rangle}{\langle \phi_f | \phi_f \rangle} = 2\kappa y. \quad (2.284)$$

To conclude this chapter, we have reviewed the concept of geometric phases for pure states starting from Berry's derivation in the context of the adiabatic theorem and its subsequent generalizations. We have moved on to geometric phases for mixed states, where we discussed two approaches: the interferometric approach and Uhlmann's approach. The interferometric approach looks convenient from the experimental perspective. We will use it in later chapters to study the geometric response of a rotating two-level atom inside an electromagnetic cavity. Uhlmann's approach to the geometric phase is mathematically rigorous; however, it is used to study topological phase transitions in condensed matter systems [102] and to study the topological indicators at finite-temperature [103]. We have also discussed some experimental studies to measure the geometric phase.

Chapter 3

Quantum Walks

Quantum walks are the quantum analogue of classical random walks [104–108] where a quantum walker propagates on a lattice and the direction of propagation is conditioned over the state of its coin. Due to the quantum nature of the walker and the coin, the position state of the walker is a superposition of multiple lattice sites. This provides a quadratically fast spread of the walker across the lattice compared to its classical counterpart [105]. As opposed to classical random walks, quantum walks are governed by quantum superpositions of amplitudes rather than classical probability distributions. There are two kinds of quantum walks, continuous and discrete. In this thesis, we will consider only discrete-time quantum walks.

Quantum walks, continuous-time as well as discrete-time, are important in various fields including universal quantum computation [109–111], quantum search algorithms [112–116], quantum simulations [117], quantum state transfer [118] and simulation of physical systems [119–121]. Quantum walks have also been used in other branches of science, such as biology, to study energy transfer in photosynthesis [122, 123]. They have also been shown to be a promising candidate to simulate the decoherence [124–126] and for the implementation of generalized measurements, positive operator valued measures (POVM) [127, 128]. The discrete-time quantum walks have been realized on a variety of systems such as NMR [129], trapped ions [130–132], in linear optical systems like linear cavity [133], optical rings [134–137], interferometry [138, 139], optical lattices [140, 141], optical networks [142–145], classical light [146], using superconducting qubits [147], cavity QED [148], quantum optics [149–152], trapped ions [130, 153], neutral atom trap [154], superconducting processors [155, 156], inte-

grated photonics [120, 157], BECs [158, 159].

In this chapter, we will discuss various protocols of discrete-time quantum walk (DTQW) in one (1D) and two dimensions (2D). We discuss the generalization of 1D DTQW to 1D split-step quantum walk (SSQW), and we further show the decomposition of 1D SSQW and 2D DTQW into 1D DTQW.

3.1 1D Discrete Time Quantum Walk (DTQW)

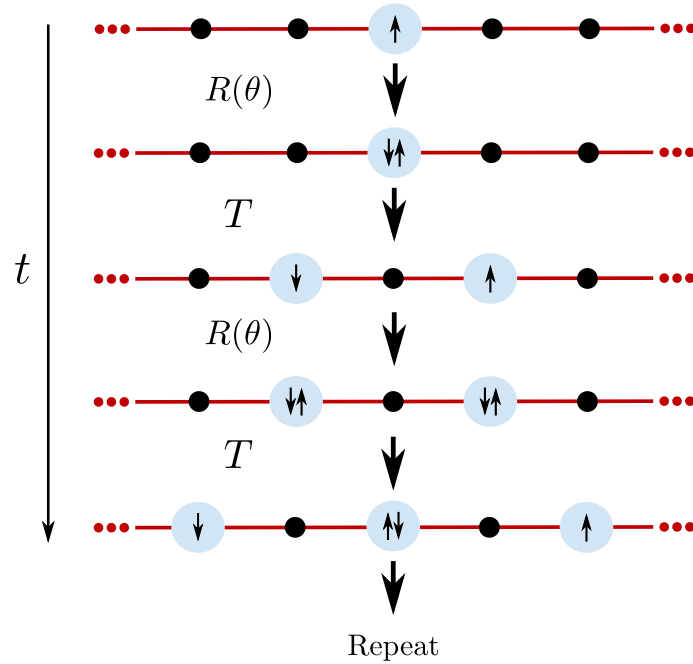


FIGURE 3.1: Schematic of the protocol of two steps of 1D DTQW. The system consists of 1D lattice where site index runs from $-n$ to $+n$ and spin degrees of freedom. We can see the interference at $n = 0$ after the second step.

DTQW protocol is defined for a particle hopping over a 1D lattice with an internal degree of freedom, spin, which is equivalent to the coin in a classical random walk. The particle has two orthogonal spin states which are referred to as spin ‘up’ and ‘down’. DTQW consists of two operations

1. a coin toss or spin flip operation

$$R(\xi, \theta, \zeta, \eta) = \sum_n R_n(\xi, \theta, \zeta, \eta) \otimes |n\rangle\langle n|. \quad (3.1)$$

where $R_n(\xi, \theta, \zeta, \eta)$ is a general U(2) operator given by [160]

$$R_n(\xi, \theta, \zeta, \eta) = e^{i\eta n} \begin{pmatrix} e^{-i\xi n/2} \cos \theta_n/2 & -e^{-i\zeta n/2} \sin \theta_n/2 \\ e^{i\zeta n/2} \sin \theta_n/2 & e^{i\xi n/2} \cos \theta_n/2 \end{pmatrix} \quad (3.2)$$

and the factor n in the subscript represents the dependence on lattice sites.

2. a spin dependent translation operator T which makes the particle move to the right (left) by one lattice site when the spin is up (down) i.e.

$$T(|\uparrow\rangle \otimes |n\rangle) = |\uparrow\rangle \otimes |n+1\rangle,$$

$$T(|\downarrow\rangle \otimes |n\rangle) = |\downarrow\rangle \otimes |n-1\rangle,$$

$$T = \sum_n |\uparrow\rangle\langle\uparrow| \otimes |n+1\rangle\langle n| + |\downarrow\rangle\langle\downarrow| \otimes |n-1\rangle\langle n|. \quad (3.3)$$

In position basis $\{|n\rangle\} \in \mathcal{H}_{\text{pos}}$ and spin basis $\{|\uparrow\rangle, |\downarrow\rangle\} \in \mathcal{H}_{\text{spin}}$, the unitary operator which governs the time evolution of the walker for a unit step time reads

$$\begin{aligned} U(\xi, \theta, \zeta) &= TR(\xi, \theta, \zeta) \\ &= \sum_n |\uparrow\rangle\langle\uparrow| R_n(\xi, \theta, \zeta) \otimes |n+1\rangle\langle n| + |\downarrow\rangle\langle\downarrow| R_n(\xi, \theta, \zeta) \otimes |n-1\rangle\langle n|. \end{aligned} \quad (3.4)$$

For the time being, we consider the case of homogeneous system where the spin flip operator does not depend on the lattice site and $\eta = 0$ which yields

$$R(\xi, \theta, \zeta) = \sum_n R_n(\xi, \theta, \zeta) \otimes |n\rangle\langle n| \mapsto R(\xi, \theta, \zeta) \otimes \mathbb{1} \quad (3.5)$$

and consequently

$$U(\xi, \theta, \zeta) = \sum_n |\uparrow\rangle\langle\uparrow| R(\xi, \theta, \zeta) \otimes |n+1\rangle\langle n| + |\downarrow\rangle\langle\downarrow| R(\xi, \theta, \zeta) \otimes |n-1\rangle\langle n|. \quad (3.6)$$

where $\mathbb{1}$ denotes the identity operation on the lattice. The total Hilbert space \mathcal{H} is the tensor product \mathcal{H}_{pos} and $\mathcal{H}_{\text{spin}}$. Given an initial state $|\psi(0)\rangle$, the wave function after t time steps is written as

$$|\psi(t)\rangle = U^t |\psi(0)\rangle = \sum_n (\psi_{n,\uparrow}(t) |n\rangle \otimes |\uparrow\rangle + \psi_{n,\downarrow}(t) |n\rangle \otimes |\downarrow\rangle) \quad (3.7)$$

where $\psi_{n,\uparrow}(t)$ and $\psi_{n,\downarrow}(t)$ are the normalized probability amplitudes such that $\sum_n (|\psi_{n,\uparrow}(t)|^2 + |\psi_{n,\downarrow}(t)|^2) = 1$. The probability of finding the walker at the n th site after t time steps is given by

$$\begin{aligned} P(n, t) &= |\langle n | \otimes \langle \uparrow | \psi(t) \rangle|^2 + |\langle n | \otimes \langle \downarrow | \psi(t) \rangle|^2 \\ &= |\psi_{n,\uparrow}(t)|^2 + |\psi_{n,\downarrow}(t)|^2. \end{aligned} \quad (3.8)$$

In Fig. (3.2), we plotted the probability distribution of the walker after 150 time steps for different (ξ, θ, ζ) . The walker was initially localized at the origin, and the coin is taken to be in a symmetric state such that

$$|\psi(0)\rangle = |0\rangle \otimes \left(\frac{|\uparrow\rangle + i|\downarrow\rangle}{\sqrt{2}} \right). \quad (3.9)$$

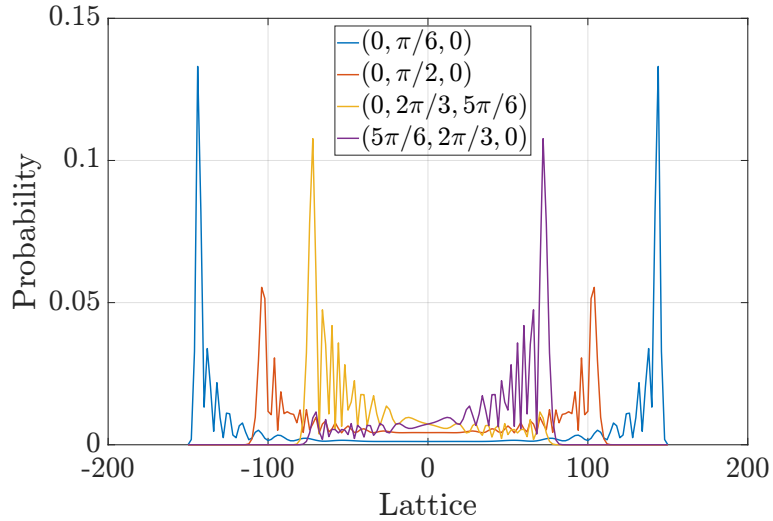


FIGURE 3.2: The probability distribution of walker after 150 time steps for different values of (ξ, θ, ζ) .

We observe that for $\xi = \zeta = 0$, the probability distribution is symmetric. However, the distribution is dominant along one direction for non-zero values of ξ and ζ despite the fact that the initial coin state is symmetric.

3.1.1 Unitary equivalence of quantum walks

In this part, we show that the quantum walk, governed by the time evolution operator in Eq. (3.4), can be reduced to a single-parameter family of quantum walks [161]. We note that

the two time evolution operator of quantum walk, given by

$$U = T(R \otimes \mathbb{1}), \quad U' = T'(R' \otimes \mathbb{1}) \quad (3.10)$$

are unitary equivalent, if

$$U' = VUV^\dagger \quad (3.11)$$

where V is unitary. The state of the quantum walker after t time steps under the evolution of U is written as

$$|\psi(t)\rangle = U^t |\psi(0)\rangle = (V^\dagger U' V)^t |\psi(0)\rangle = V^\dagger (U')^t V |\psi(0)\rangle. \quad (3.12)$$

Therefore, the dynamics of the state $|\psi(0)\rangle$ under the action of U is the same as the dynamics of the initial state $V |\psi(0)\rangle$ under the action of U' . Note that the factor V^\dagger is just a unitary and leaves the underlying physics unaffected. That is, the statistics of any observable O , with the initial state of the system $|\psi(0)\rangle$, governed by U , will be equivalent to the statistics of the observable VOV^\dagger in the system with the initial state $V |\psi(0)\rangle$ and under the action of U' . Now, by demanding the invariance of the entanglement between the coin and the lattice and the translational invariance under the action of V , we can choose it to be of the form

$$V = X \otimes \mathbb{1} \quad (3.13)$$

i.e., V acts only on the coin degree of freedom. The operator R can be taken to any $SU(2)$ of the form

$$R = \exp\left(i\frac{\phi}{2}\mathbf{r} \cdot \boldsymbol{\sigma}\right) \quad (3.14)$$

and X to be of the form

$$X = |\uparrow\rangle\langle\uparrow| + |\downarrow\rangle\langle\downarrow| \quad (3.15)$$

such that

$$\mathbf{r} \cdot \boldsymbol{\sigma} |\uparrow\rangle = |\uparrow\rangle, \quad \mathbf{r} \cdot \boldsymbol{\sigma} |\downarrow\rangle = -|\downarrow\rangle. \quad (3.16)$$

Under the action of this transformation and utilizing Eq. (3.16) we get

$$\begin{aligned}
R \rightarrow R' &= VRV^\dagger = X \exp\left(i\frac{\phi}{2}\mathbf{r} \cdot \boldsymbol{\sigma}\right) X^\dagger \\
&= X \left(\exp\{i\phi/2\} |\uparrow\rangle\langle\uparrow| + \exp\{-i\phi/2\} |\downarrow\rangle\langle\downarrow|\right) X^\dagger \\
&= \exp\{i\phi/2\} |\uparrow\rangle\langle\uparrow| + \exp\{-i\phi/2\} |\downarrow\rangle\langle\downarrow| = \exp(i\phi\sigma_z/2). \tag{3.17}
\end{aligned}$$

Therefore, the time evolution operator U transforms as

$$U \rightarrow U' = VUV^\dagger = \exp(i\phi\sigma_z/2) |\uparrow\rangle\langle\uparrow| \otimes T + \exp(i\phi\sigma_z/2) |\downarrow\rangle\langle\downarrow| \otimes T^\dagger. \tag{3.18}$$

Now, we consider the transformation of the form $V = W \otimes X$ which preserves the coin basis but does not need to be translationally invariant. The propagation operator in Euler parameterization is written as [161]

$$U(\eta, \theta, \xi) = e^{i\frac{\eta}{2}\sigma_z} e^{i\frac{\theta}{2}\sigma_y} e^{i\frac{\xi}{2}} |\uparrow\rangle\langle\uparrow| \otimes T + e^{i\frac{\eta}{2}\sigma_z} e^{i\frac{\theta}{2}\sigma_y} e^{-i\frac{\xi}{2}} |\downarrow\rangle\langle\downarrow| \otimes T^\dagger \tag{3.19}$$

where we utilized the following relations

$$e^{i\frac{\xi}{2}\sigma_z} |\uparrow\rangle = e^{i\frac{\xi}{2}} |\uparrow\rangle, \quad e^{i\frac{\xi}{2}\sigma_z} |\downarrow\rangle = e^{-i\frac{\xi}{2}} |\downarrow\rangle. \tag{3.20}$$

Next, we choose X to be of the form $X = e^{-i\frac{\eta}{2}\sigma_z}$ such that

$$U(\eta, \theta, \xi) \rightarrow (X \otimes \mathbb{1})U(\eta, \theta, \xi)(X^\dagger \otimes \mathbb{1}) = e^{i\frac{\theta}{2}\sigma_y} e^{i\frac{\xi+\eta}{2}} |\uparrow\rangle\langle\uparrow| \otimes T + e^{i\frac{\theta}{2}\sigma_y} e^{-i\frac{\xi+\eta}{2}} |\downarrow\rangle\langle\downarrow| \otimes T^\dagger.$$

Finally, we introduce a phase shift Φ in the quasi-momentum, which results in breaking of the translation invariance and reads

$$E_\Phi R E_\Phi^\dagger = e^{i\Phi} R, \quad E_\Phi = \sum_n e^{i\Phi n} |n\rangle\langle n|. \tag{3.21}$$

We introduced this phase factor to choose $W = E_{-(\eta+\xi)/2}$ so that, together with $X = e^{-i\frac{\eta}{2}\sigma_z}$, it yields

$$(\mathbb{1} \otimes W)U(\eta, \theta, \xi)(\mathbb{1} \otimes W^\dagger) = e^{i\frac{\theta}{2}\sigma_y} |\uparrow\rangle\langle\uparrow| \otimes T + e^{i\frac{\theta}{2}\sigma_y} |\downarrow\rangle\langle\downarrow| \otimes T^\dagger. \tag{3.22}$$

Therefore, the three-parameter quantum walk governed by $U(\eta, \theta, \xi)$ is unitary equivalent to a one-parameter quantum walk with $U(\theta)$. We can also rewrite the above equation as

$$U(\theta) = \sum_n R(\theta) |\uparrow\rangle\langle\uparrow| \otimes |n+1\rangle\langle n| + R(\theta) |\downarrow\rangle\langle\downarrow| \otimes |n-1\rangle\langle n| \quad (3.23)$$

where $R(\theta) = e^{-i\theta\sigma_y/2}$ ($-i$ and $+i$ are equivalent and just a matter of convention) with $\theta \in [-2\pi, 2\pi]$ being a real parameter and σ_y the Pauli matrix along the y -axis. We will continue our discussion with the time evolution operator $U(\theta)$. It has been shown that the angle θ plays a role in characterizing phase and group velocity [162].

We now plot the probability distribution of the walker dynamics, which is governed by Eq. (3.23) in Fig. 3.3(a), 3.3(b), 3.3(c) for 200 time steps and for different initial states. In Fig. 3.3(c) we have compared the probability distribution for the classical and quantum walk. We can see a contrasting behavior between the two. In quantum walk, we let the probability amplitude evolve with time, which leads to constructive and destructive interference. It interferes constructively at the extremes and destructively at the origin. However, classical lack coherence, and thus we do not see any interference effects and get a normal distribution. The variance for DTQW for the same initial state as in Fig. 3.3(c) is proportional to the square of the step number t , i.e. $\sigma^2 \propto t^2$, which is quadratically faster than that of the classical random walk. In Fig. 3.3(d) we plotted the variance for the classical and quantum walk on the logarithmic scale. On the logarithmic scale, the variance for DTQW and the classical random walk will be a straight line; however, the slope in DTQW is twice ($\log(t^2)$) as compared to the classical one ($\log(t)$). Due to this, the DTQW and classical walk processes are referred to as ballistic and diffusive processes, respectively.

3.1.2 Effective Hamiltonian

The unitary evolution of the quantum walk governed by Eq. (3.23) can also be generated by an underlying time independent Hamiltonian $H(\theta)$ [14] over a unit time such that

$$U(\theta) = e^{-iH(\theta)} \quad (3.24)$$

For simplicity, we have assumed $\hbar = 1$ and the periodic boundary condition with N number of lattice sites. Since the unitary operator $U(\theta)$ and the Hamiltonian are translationally invariant,

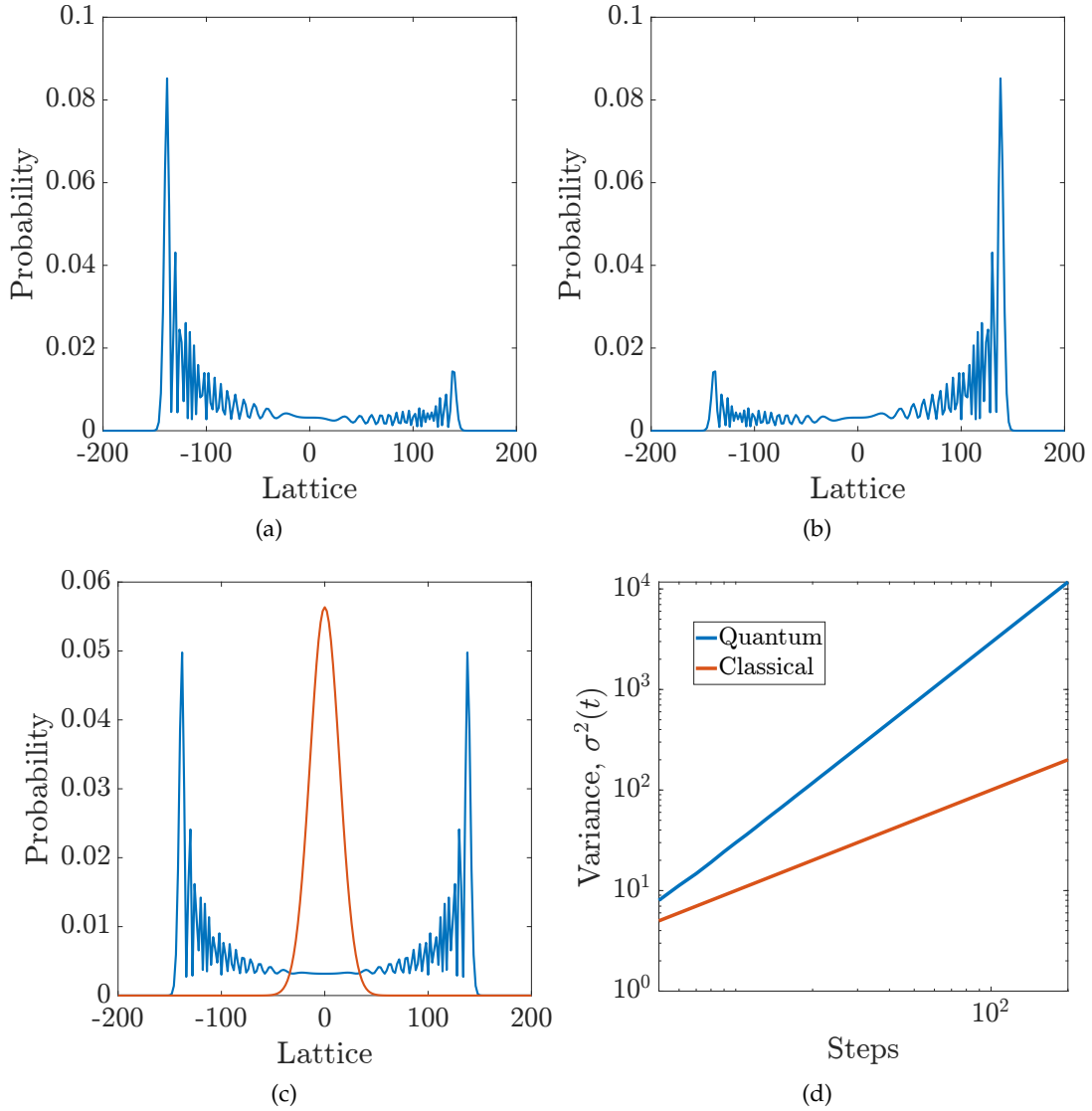


FIGURE 3.3: Probability distribution of a walker after 200 time steps for different initial states. (a) $|\psi(0)\rangle = |0\rangle \otimes |\downarrow\rangle$, (b) $|\psi(0)\rangle = |0\rangle \otimes |\uparrow\rangle$, (c) $|\psi(0)\rangle = |0\rangle \otimes (|\uparrow\rangle + i|\downarrow\rangle)/\sqrt{2}$ in contrast to classical walk (red). Only the points with non-zero probability are plotted. (d) The variance, $\sigma^2(t)$ for quantum and classical walks with time steps t . The axes are chosen on logarithmic scale.

these will be reduced to block diagonal form in (quasi) momentum or Fourier basis $\{|k\rangle\}$ which are defined as

$$|k\rangle = \frac{1}{\sqrt{N}} \sum_n e^{-i2\pi kn/N} |n\rangle, \quad (3.25)$$

with k being the quasi-momentum that can take discrete values between $-\pi$ and π in integer multiples of $2\pi/N$. Hence, in the momentum basis $|k\rangle \otimes |\sigma\rangle = \frac{1}{\sqrt{N}} \sum_n e^{-ikn} |n\rangle \otimes |\sigma\rangle$, translational operator in (3.3) transforms as

$$T(k) = \sum_k e^{ik\sigma_z} \otimes |k\rangle\langle k| \quad (3.26)$$

however $R(\theta)$ remains unchanged. Using these, we can write the evolution operator $U(\theta)$ quasi-momentum basis as

$$\begin{aligned} U(\theta) &= TR(\theta) \\ &= \sum_k e^{ik\sigma_z} R(\theta) \otimes |k\rangle\langle k|, \end{aligned} \quad (3.27)$$

We can find the effective Hamiltonian by comparing (3.27) with the most general unitary for a two-level system given by

$$U = \sum_k e^{-i\mathbf{n}(k)\cdot\boldsymbol{\sigma}} \otimes |k\rangle\langle k| \quad (3.28)$$

which represents the most general Hamiltonian for the two-level system in block-diagonal form. Resultantly, the effective Hamiltonian $H(\theta)$ in the quasi-momentum space reads [14]

$$H(\theta) = \sum_k [E_\theta(k) \mathbf{n}_\theta(k) \cdot \boldsymbol{\sigma}] \otimes |k\rangle\langle k|, \quad (3.29)$$

where the quasienergy $E_\theta(k)$ and the unit Bloch vector $\mathbf{n}_\theta(k)$ read

$$E_\theta(k) = \cos^{-1} [\cos(\theta/2) \cos k] \quad (3.30)$$

and

$$\mathbf{n}_\theta(k) = \frac{1}{\sin E_\theta(k)} (\sin(\theta/2) \sin k, \sin(\theta/2) \cos k, -\cos(\theta/2) \sin k). \quad (3.31)$$

We have plotted the quasi-energy spectrum in Fig. (3.4) for $\theta = 0$, $\theta = \pi/2$ and $\theta = \pi$. There are two bands due to the two internal states, and there exists a gap between them. We see that the gap closes for $\theta = 0$ at $E = 0$ and at $E = \pi$. Note that the quasienergy has a periodicity of 2π . For $\theta = 0, 2\pi$, the quasienergy and the Bloch vector are ill defined, and the spectrum

becomes gapless.

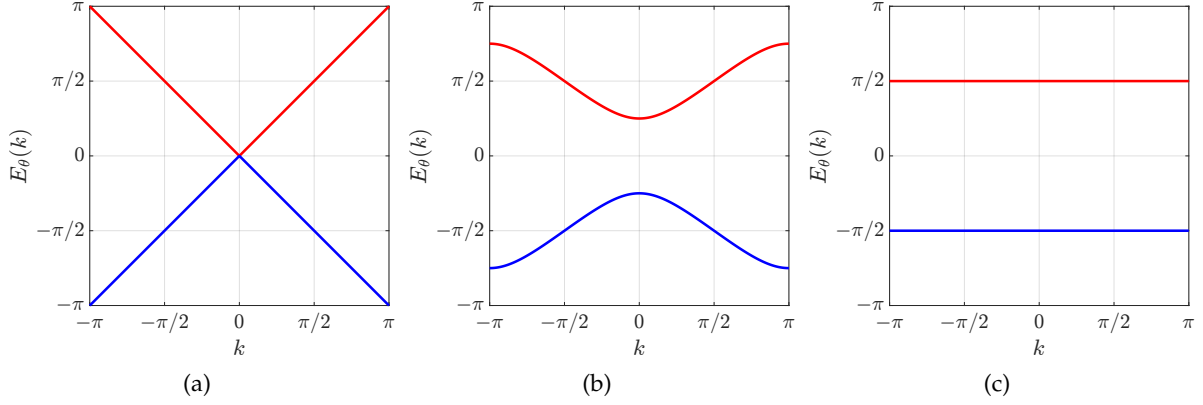


FIGURE 3.4: The quasi-energy spectrum of the effective Hamiltonian $H(\theta)$ for (a) $\theta = 0$, (b) $\theta = \pi/2$ and (c) $\theta = \pi$.

3.2 1D Split-Step Quantum Walk (SSQW)

A more enriched class of 1D DTQW is SSQW, which involves splitting the conditional shift operator T into left-shift (T_\downarrow) and right-shift (T_\uparrow) operators, separated by an additional coin toss $R(\theta_2)$ [14]. The resultant time evolution operator for split-step quantum walks (in one dimension) reads

$$U_{\text{ss}}(\theta_1, \theta_2) = T_\downarrow R(\theta_2) T_\uparrow R(\theta_1), \quad (3.32)$$

where

$$T_\downarrow = \sum_n |\uparrow\rangle \langle \uparrow| \otimes \mathbb{1}_{2j+1} + |\downarrow\rangle \langle \downarrow| \otimes |n-1\rangle \langle n|,$$

$$T_\uparrow = \sum_n |\uparrow\rangle \langle \uparrow| \otimes |n+1\rangle \langle n| + |\downarrow\rangle \langle \downarrow| \otimes \mathbb{1}_{2j+1}.$$

We plot the probability distribution of the walker after 200 steps in Fig. 3.6. It is evident from Fig. 3.6(d) that for $\theta_2 = 0$, SSQW reduces to conventional DTQW which was explained in the previous section. As before, we can go to the Fourier basis using Eq. (3.25) which yields

$$T_\downarrow(k) = \sum_k e^{ik(\sigma_z - \mathbb{1})/2} \otimes |k\rangle \langle k|,$$

$$T_\uparrow(k) = \sum_k e^{ik(\sigma_z + \mathbb{1})/2} \otimes |k\rangle \langle k|.$$

Consequently, in this case, the effective Hamiltonian $H_{\text{SS}}(\theta_1, \theta_2)$ can be written down in quasi-momentum space as

$$H_{\text{SS}}(\theta_1, \theta_2) = \sum_k [E_{\theta_1, \theta_2}(k) \mathbf{n}_{\theta_1, \theta_2}(k) \cdot \boldsymbol{\sigma}] \otimes |k\rangle\langle k|. \quad (3.33)$$

The quasi-energy [see Fig. 3.5] and the components of the Bloch vector are given by

$$\cos E_{\theta_1, \theta_2}(k) = \cos(\theta_1/2) \cos(\theta_2/2) \cos k - \sin(\theta_1/2) \sin(\theta_2/2), \quad (3.34)$$

and $\mathbf{n}_{\theta_1, \theta_2}(k) = n_x(k)\hat{\mathbf{i}} + n_y(k)\hat{\mathbf{j}} + n_z(k)\hat{\mathbf{k}}$ with

$$\begin{aligned} n_x(k) &= \frac{\sin(\theta_1/2) \cos(\theta_2/2) \sin k}{\sin E_{\theta_1, \theta_2}(k)}, \\ n_y(k) &= \frac{\cos(\theta_1/2) \sin(\theta_2/2) + \sin(\theta_1/2) \cos(\theta_2/2) \cos k}{\sin E_{\theta_1, \theta_2}(k)}, \\ n_z(k) &= \frac{-\cos(\theta_1/2) \cos(\theta_2/2) \sin k}{\sin E_{\theta_1, \theta_2}(k)}. \end{aligned} \quad (3.35)$$

1D SSQW possess a rich topological structure depending on the symmetries in the system. We will discuss symmetries and topological characterization in quantum walks in detail in upcoming chapters.

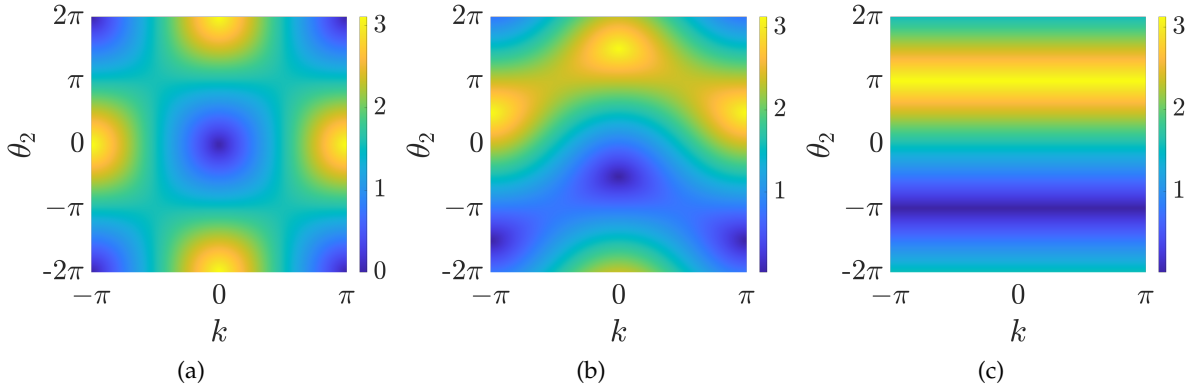


FIGURE 3.5: The dispersion relation of the 1D SSQW given in Eq. (3.34) as function of rotation angle θ_2 and the quasi-momentum k for (a) $\theta_1 = 0$, (a) $\theta_1 = \pi/2$, and (a) $\theta_1 = \pi$.

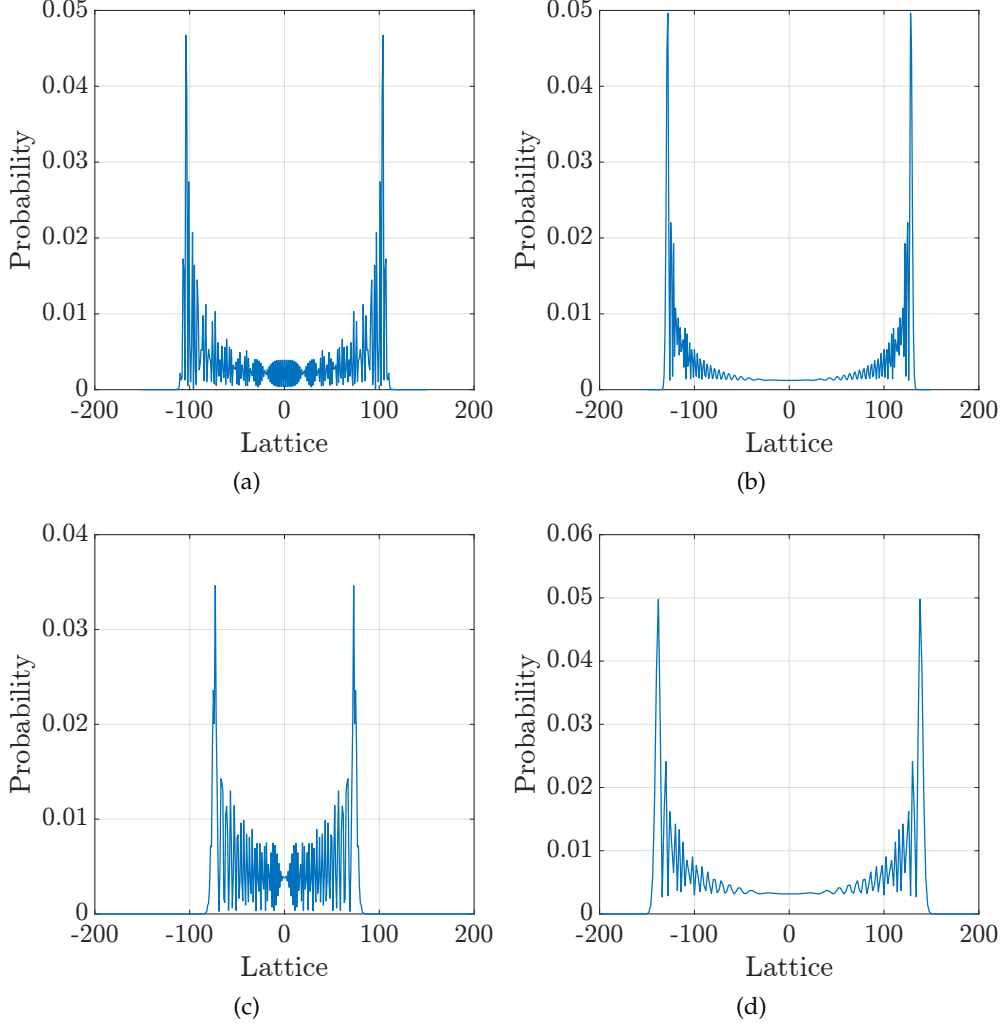


FIGURE 3.6: Probability distribution of a walker after 200 time steps for (a) $(\theta_1, \theta_2) = (\pi/2, \pi/3)$, (b) $(\theta_1, \theta_2) = (\pi/3, \pi/3)$, (c) $(\theta_1, \theta_2) = (-\pi/2, 3\pi/4)$, (d) $(\theta_1, \theta_2) = (\pi/2, 0)$. All the plots are symmetric due to the choice of symmetric initial state $|\psi(0)\rangle = |0\rangle \otimes (|\uparrow\rangle + i|\downarrow\rangle)/\sqrt{2}$. In (d) we recovered the probability distribution of 1D DTQW by putting $\theta_2 = 0$.

3.3 2D DTQW

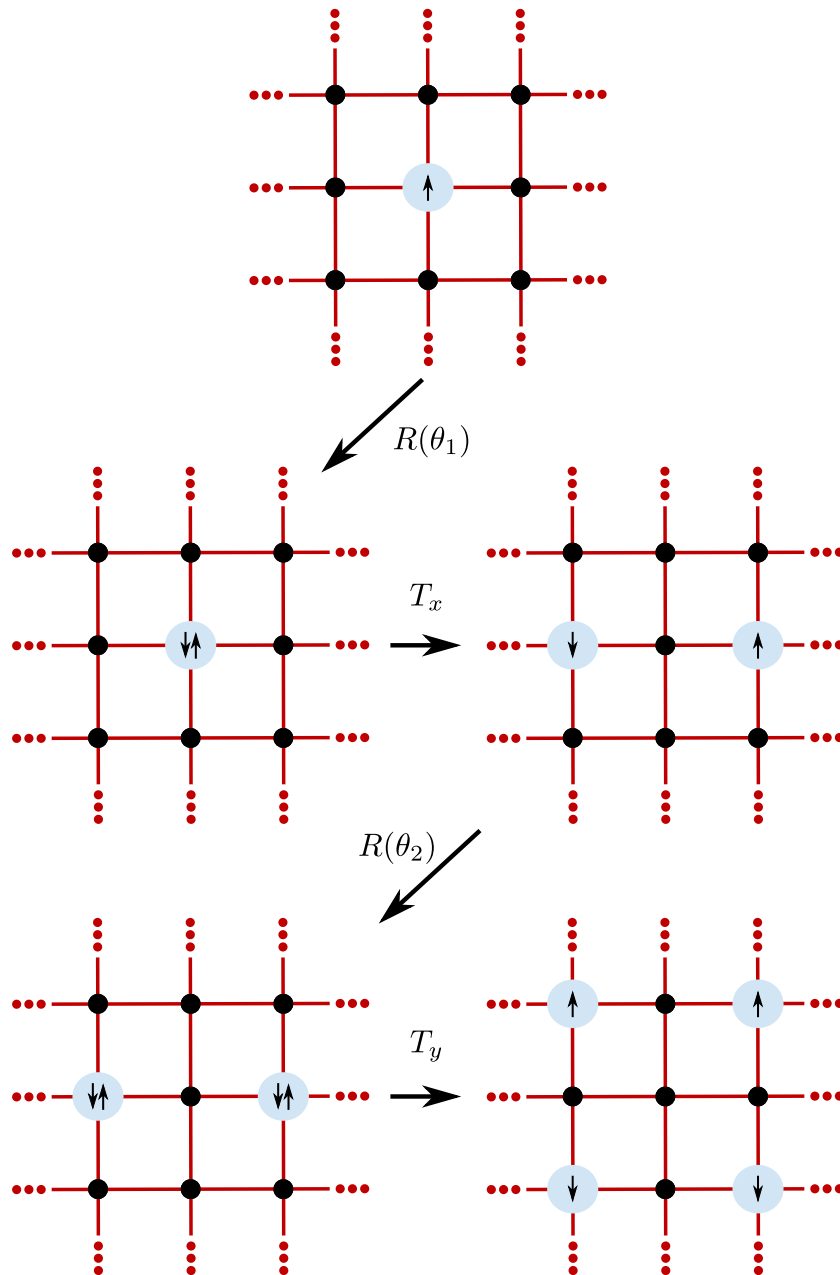


FIGURE 3.7: Schematic of the protocol of 2D DTQW. The system consists of 2D lattice and site index runs from $-n$ to $+n$ in both the directions.

We can extend the idea of a quantum walk to higher dimensions as well. There are several ways of defining a 2D DTQW in a lattice. First, we start with a simple one as shown in Fig. 3.7. It consists of the following operations

1. Rotations of the spin around y with an angle θ_1 which is written as $R(\theta_1) = e^{-i\sigma_y\theta_1/2}$,

2. Translation operator T_x in x direction which shifts the up spin to the right and spin down to the left. It is written as

$$T_x = \sum_{x,y} |\uparrow\rangle \langle\uparrow| \otimes |x+1, y\rangle \langle x, y| + |\downarrow\rangle \langle\downarrow| \otimes |x-1, y\rangle \langle x, y|, \quad (3.36)$$

3. Rotations of the spin around y with an angle θ_2 which is written as $R(\theta_2) = e^{-i\sigma_y\theta_2/2}$,
4. Translation operator T_y in y direction which shifts the up and down spin to up and down vertically respectively. It is written as

$$T_y = \sum_{x,y} |\uparrow\rangle \langle\uparrow| \otimes |x, y+1\rangle \langle x, y| + |\downarrow\rangle \langle\downarrow| \otimes |x, y-1\rangle \langle x, y|, \quad (3.37)$$

such that the time evolution operator for one step reads

$$U_{2D}(\theta_1, \theta_2) = T_y R(\theta_2) T_x R(\theta_1), \quad (3.38)$$

Note that there are other ways too to define higher-dimensional quantum which consists of more internal degrees of freedom (for example, with a 4 dimensional coin). We restrict ourselves to the one where we use only two internal degrees of freedom. Now, we define an extended version of 2D DTQW on a triangular lattice, which consists of three spin-dependent translations separated by coin-flip operations. In that case, the unitary operator which governs the time evolution is written as [15]

$$\tilde{U}_{2D}(\theta_1, \theta_2) = T_{xy} R(\theta_1) T_y R(\theta_2) T_x R(\theta_1), \quad (3.39)$$

where $T_i (i = x, y, xy)$ are the translations along the s_i directions with $T_{xy} = T_x T_y$, as shown in the Fig. 3.8. We can further derive another two-dimensional quantum walk that is unitarily equivalent to $\tilde{U}_{2D}(\theta_1, \theta_2)$ as $\tilde{U}_{2D} \rightarrow U_{2D} = T_x^\dagger \tilde{U}_{2D} T_x$. The resulting time-evolution unitary operator can be written as

$$U_{2D}(\theta_1, \theta_2) = T_y R(\theta_1) T_y R(\theta_2) T_x R(\theta_1) T_x. \quad (3.40)$$

The underlying Hamiltonian for this quantum walk (in quasi-momentum space) reads

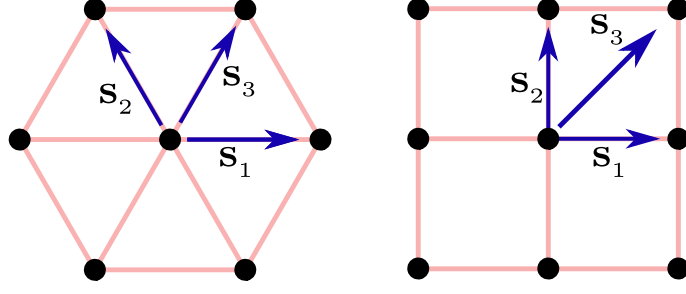


FIGURE 3.8: (Color online) 2D DTQW with nontrivial topology on a triangular lattice and its equivalent square lattice.

$$H_{2D}(\theta_1, \theta_2) = \sum_{k_x, k_y} E(k_x, k_y) \hat{\mathbf{n}}(k_x, k_y) \cdot \boldsymbol{\sigma} \otimes |k_x, k_y\rangle\langle k_x, k_y|, \quad (3.41)$$

where the expression of quasi-energy [see Fig. 3.9] reads

$$\begin{aligned} \cos E(k_x, k_y) &= \cos \theta_1 \cos(\theta_2/2) \cos^2(k_x + k_y) - \cos(\theta_2/2) \sin^2(k_x + k_y) \\ &\quad - \sin \theta_1 \sin(\theta_2/2) \cos(k_x + k_y) \cos(k_x - k_y), \end{aligned} \quad (3.42)$$

and the Bloch vector reads [14]

$$\hat{\mathbf{n}}(k_x, k_y) = \frac{n_x(k_x, k_y) \hat{\mathbf{i}} + n_y(k_x, k_y) \hat{\mathbf{j}} + n_z(k_x, k_y) \hat{\mathbf{k}}}{\sin E(k_x, k_y)},$$

with

$$\begin{aligned} n_x(k_x, k_y) &= -\sin \theta_1 \cos(\theta_2/2) \cos(k_x + k_y) \sin(k_x - k_y) \\ &\quad - \cos^2 \theta_1 \sin(\theta_2/2) \sin 2(k_x - k_y), \\ n_y(k_x, k_y) &= \sin \theta_1 \cos(\theta_2/2) \cos(k_x + k_y) \cos(k_x - k_y) \\ &\quad + \cos \theta_1 \cos^2(k_x - k_y) \sin(\theta_2/2) \\ &\quad - \sin^2(k_x - k_y) \sin(\theta_2/2), \\ n_z(k_x, k_y) &= -\cos^2(\theta_1/2) \cos(\theta_2/2) \sin 2(k_x + k_y) \\ &\quad + \sin \theta_1 \sin(\theta_2/2) \sin(k_x + k_y) \cos(k_x - k_y). \end{aligned}$$

In this case, each step of the quantum walk moves the walker from the even (odd) site to the even (odd) site, so the lattice constant of the effective Hamiltonian is 2. Thus, the first Brillouin zone is defined as $-\pi/2 \leq k_x \leq \pi/2$ and $-\pi/2 \leq k_y \leq \pi/2$. We plot the probability distribution of a particle initially localized at the origin $(0, 0)$ in Fig. 3.10 for different settings of θ_1 and θ_2 .

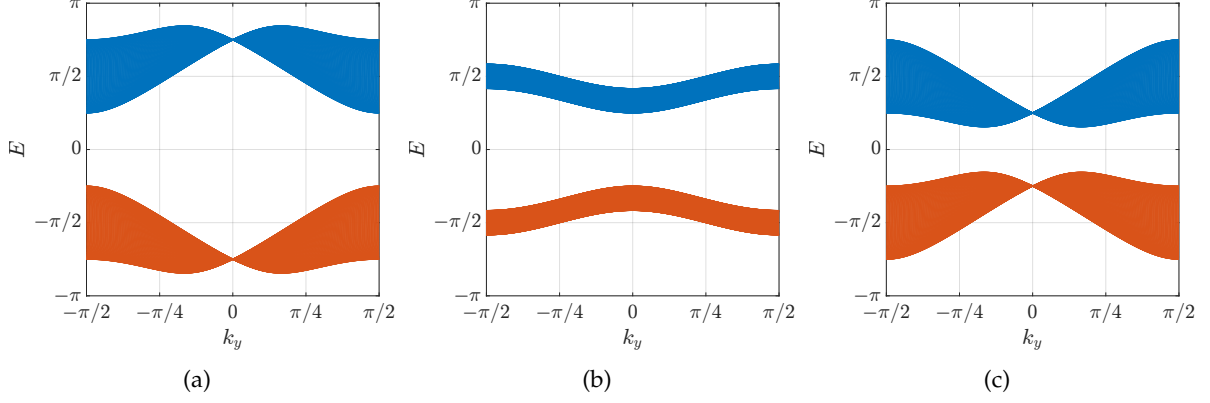


FIGURE 3.9: The quasi-energy band structure of the effective Hamiltonian $H_{2D}(\theta_1, \theta_2)$ for (a) $\theta_1 = \pi/2 = \theta_2$, (b) $\theta_1 = 7\pi/6 = \theta_2$ and (c) $\theta_1 = 3\pi/2 = \theta_2$.

The coin starts in the symmetric state and the system size is taken to be 201×201 . We get a symmetric probability distribution as a consequence of the initial symmetric state of the coin.

3.3.1 2D DTQW with 4D Coin

For our purpose, to study the persistence of topological order in quantum walks, we will consider 2D DTQW with 2D coin only. However, there are protocols in the literature [163–165] where one can have a 4D coin. For the sake of completeness, we briefly discuss a simple protocol of 2D DTQW using a 4D coin. For such quantum walks, the time evolution operator for one step is given by

$$U = T(C \otimes \mathbf{1}) \quad (3.43)$$

with

$$T = \sum_{x,y} |\uparrow\rangle\langle\uparrow| \otimes |x+1, y+1\rangle\langle x, y| + |\uparrow\rangle\langle\downarrow| \otimes |x+1, y-1\rangle\langle x, y| \\ + |\downarrow\rangle\langle\uparrow| \otimes |x-1, y+1\rangle\langle x, y| + |\downarrow\rangle\langle\downarrow| \otimes |x-1, y-1\rangle\langle x, y| \quad (3.44)$$

and the C operator can be one of the following:

1. Hadamard coin: This is one of the most general extensions of the 1D Hadamard transfor-

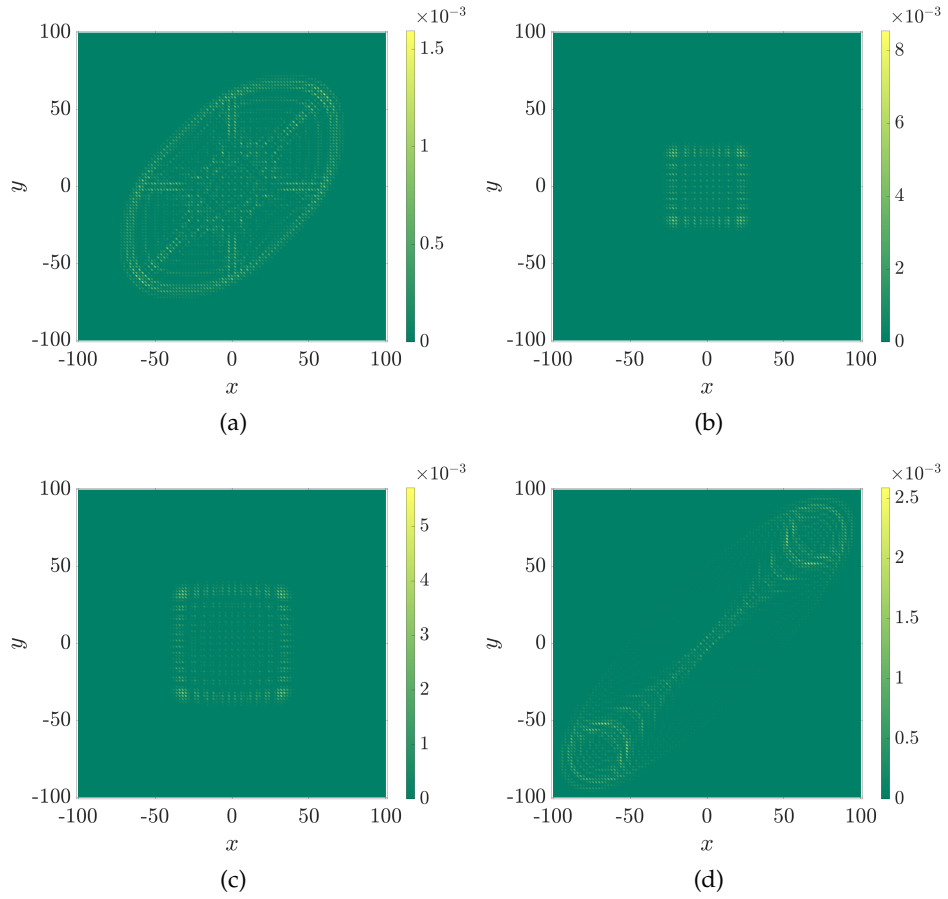


FIGURE 3.10: The probability distribution of the 2D DTQW given in Eq. (3.40) after 100 number of time steps for different values of θ_1 and θ_2 . In (a) $\theta_1 = \pi/2 = \theta_2$, (b) $\theta_1 = 7\pi/6 = \theta_2$, (c) $\theta_1 = 3\pi/4 = \theta_2$ and (d) $\theta_1 = -\pi/5, \theta_2 = 3\pi/7$. The system size is taken to be 201×201 .

mation given as

$$C = H_2 = H \otimes H = \frac{1}{\sqrt{2}} \begin{bmatrix} 1 & 1 \\ 1 & -1 \end{bmatrix} \otimes \frac{1}{\sqrt{2}} \begin{bmatrix} 1 & 1 \\ 1 & -1 \end{bmatrix} = \frac{1}{2} \begin{bmatrix} 1 & 1 & 1 & 1 \\ 1 & -1 & 1 & -1 \\ 1 & 1 & -1 & -1 \\ 1 & -1 & -1 & 1 \end{bmatrix} \quad (3.45)$$

and in d -dimensional quantum walks, it takes a very simple separable form, which reads $H_d = H \otimes H \otimes \dots \otimes H$.

2. Fourier coin: Another generalization is the 2^d -dimensional discrete Fourier transform F_d . Given the basis states $\{|u\rangle, i = 0, 1, 2, \dots, 2^d - 1\}$, the action of F_d on the bases states reads [163]

$$F_d |i\rangle = \frac{1}{\sqrt{2^d}} \sum_{v=0}^{2^d-1} e^{2\pi i uv/2^d} |v\rangle. \quad (3.46)$$

For $d = 1$, the discrete Fourier transform F_1 is just Hadamard. For $d = 2$, it reads

$$C = F_2 = \frac{1}{2} \begin{bmatrix} 1 & 1 & 1 & 1 \\ 1 & i & -1 & -i \\ 1 & -1 & 1 & -1 \\ 1 & -i & -1 & i \end{bmatrix} \quad (3.47)$$

3. Grover coin: Lastly, we talk about the Grover operator, which is given for d -dimensional systems as [163]

$$G_d |u\rangle = \frac{1}{\sqrt{2^d}} \left(-2 |u\rangle + \sum_{v=0}^{2^d-1} |v\rangle \right) \quad (3.48)$$

and in $d = 2$, it reads

$$C = G_2 = \frac{1}{2} \begin{bmatrix} -1 & 1 & 1 & 1 \\ 1 & -1 & 1 & 1 \\ 1 & 1 & -1 & 1 \\ 1 & 1 & 1 & -1 \end{bmatrix} \quad (3.49)$$

With the initial state of the composite system of the 2D lattice and the coin given by

$$|\Psi(0)\rangle = \sum_{x,y} \sum_{j,k} \Psi_{j,k}(x,y,0) |j,k\rangle \otimes |x,y\rangle \quad (3.50)$$

the wave function after t time step is written as

$$|\Psi(t)\rangle = U^t |\Psi(0)\rangle = \sum_{x,y} \sum_{j,k} \Psi_{j,k}(x,y,t) |j,k\rangle \otimes |x,y\rangle \quad (3.51)$$

and the probability of finding the walker at site (x,y) after t steps is

$$P(x,y,t) = \sum_{j,k} |\Psi_{j,k}(x,y,t)|^2. \quad (3.52)$$

We have plotted the probability distribution in Fig. 3.11 for various coins. In Figs. 3.11(a), 3.11(b) we have chosen the Hadamard coin, H_2 (3.45) with the initial state given by

$$|\Psi(0)\rangle = \frac{1}{2} (|0\rangle - i|1\rangle) (|0\rangle - i|1\rangle) |0,0\rangle. \quad (3.53)$$

Since we have considered the symmetric state for the coin, it produces a symmetric probability distribution after $t = 100$ time steps. It is the same as the one we get in 1D DTQW in both the x as well as y directions because the coin operator does not create any entanglement between two directions. Second, we plot the probability distribution with Grover coin G_2 (3.49) in Figs. 3.11(c), 3.11(d) with the initial state

$$|\Psi(0)\rangle = \frac{1}{2} (|0\rangle - |1\rangle) (|0\rangle - |1\rangle) |0,0\rangle. \quad (3.54)$$

In this case, the probability distribution is highly symmetric about the origin and has 4-fold symmetry. Lastly, we use the Fourier coin F_2 (3.47) and use

$$|\Psi(0)\rangle = \frac{1}{2} \left(|0,0\rangle + \frac{1-i}{\sqrt{2}} |0,1\rangle + |1,0\rangle - \frac{1-i}{\sqrt{2}} |1,1\rangle \right) |0,0\rangle \quad (3.55)$$

this as the initial state. The probability distribution is plotted in Figs. 3.11(e), 3.11(f). In this case, if we observe carefully, we see a 2-fold symmetry.

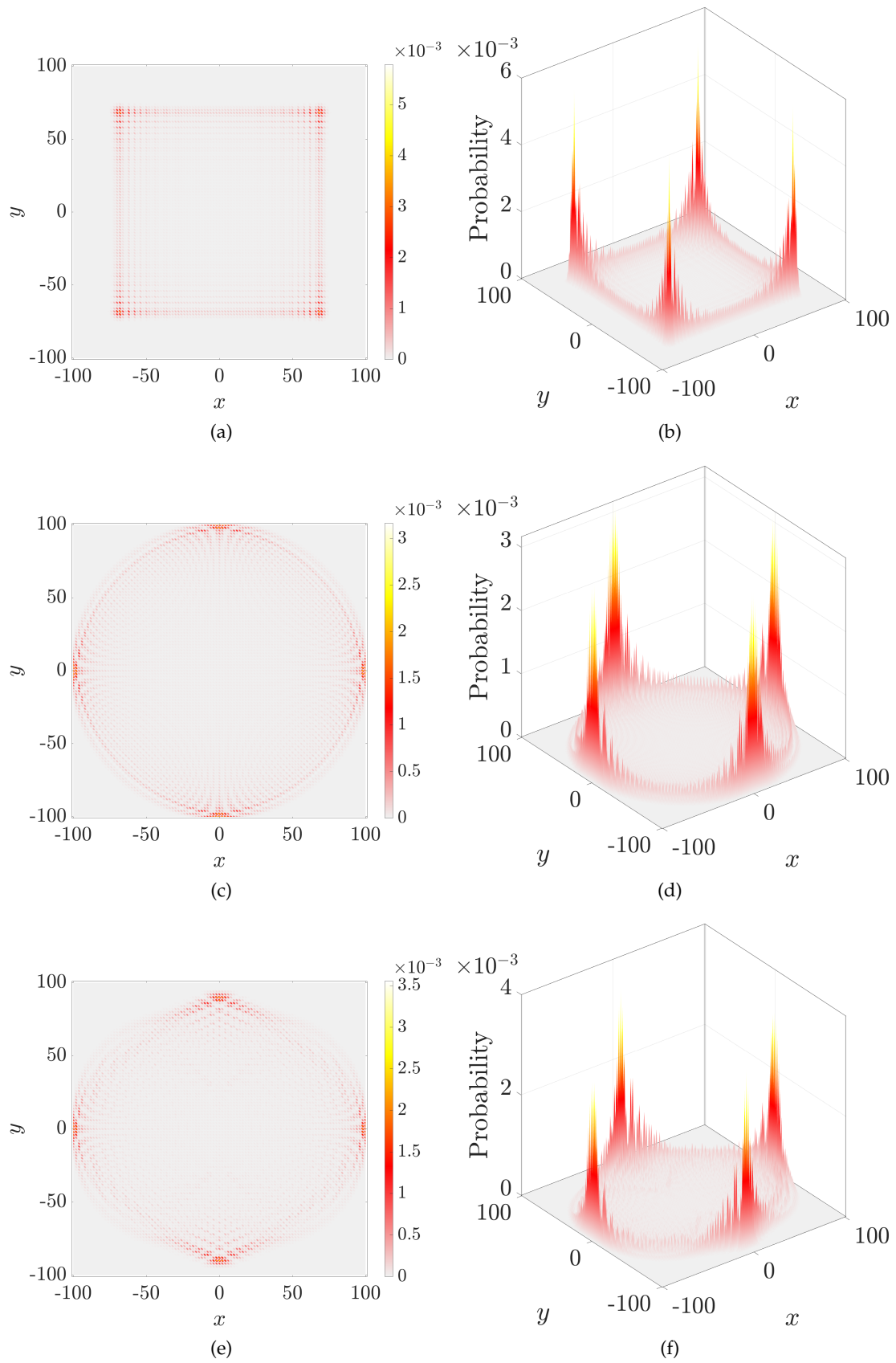


FIGURE 3.11: Probability distribution for (a) Hadamard, (c) Grover, and (e) Fourier coin. The lattice size is taken to be 201×201 for all the plots.

3.3.2 Decomposition of SSQW

In this section, we present a hierarchical structure to decompose a 1D SSQW and 2D DTQW into 1D DTQWs [166]. We start with the time evolution operator, $U_{\text{ss}}(\theta_1, \theta_2)$ of a 1D SSQW given in Eq. (3.32) and replace T_{\downarrow} and T_{\uparrow} with T_{\downarrow}^2 and T_{\uparrow}^2 respectively such that

$$U_{\text{ss}}(\theta_1, \theta_2) = T_{\downarrow}^2 R(\theta_2) T_{\uparrow}^2 R(\theta_1). \quad (3.56)$$

where

$$T_{\uparrow}^2 = \sum_n |\uparrow\rangle \langle \uparrow| \otimes |n+2\rangle \langle n+1| + |\downarrow\rangle \langle \downarrow| \otimes \mathbb{1}_{2j+1}, \quad (3.57)$$

$$T_{\downarrow}^2 = \sum_n |\uparrow\rangle \langle \uparrow| \otimes \mathbb{1}_{2j+1} + |\downarrow\rangle \langle \downarrow| \otimes |n-2\rangle \langle n|. \quad (3.58)$$

Qualitatively, there is no difference between (3.32) and (3.56). In the former, the walker moves on the neighboring sites, whereas in the latter one, the walker skips one lattice site in each jump. So, in the latter case, the probability of finding the particle at odd sites is always zero irrespective of the number of steps. We can also choose lattice with even or odd numbered sites, which would result in an identical probability distribution (as shown in Fig. 3.12). Now, using the fact that SSQW is translation invariant, we can write

$$U_{\text{ss}}(\theta_1, \theta_2) = T_+ T_{\downarrow}^2 R(\theta_2) T_{\uparrow}^2 R(\theta_1) T_- \quad (3.59)$$

with

$$T_+ = \sum_n \mathbb{1} \otimes |n+1\rangle \langle n| = T_-^\dagger. \quad (3.60)$$

Since T_{\pm} acts only on the lattice part, we can rewrite it as

$$U_{\text{ss}}(\theta_1, \theta_2) = T_+ T_{\downarrow}^2 R(\theta_2) T_{\uparrow}^2 T_- R(\theta_1) = T_+ T_{\downarrow}^2 R(\theta_2) T_- T_{\uparrow}^2 R(\theta_1) \quad (3.61)$$

and we can easily show

$$T_+ T_{\downarrow}^2 = T = T_- T_{\uparrow}^2. \quad (3.62)$$

where

$$T = \sum_n |\uparrow\rangle \langle \uparrow| \otimes |n+1\rangle \langle n| + |\downarrow\rangle \langle \downarrow| \otimes |n-1\rangle \langle n|. \quad (3.63)$$

is the translation operator from 1D DTQW. Hence,

$$U_{\text{SS}}(\theta_1, \theta_2) = (TR(\theta_2))(TR(\theta_1)) = U(\theta_2)U(\theta_1). \quad (3.64)$$

So, even though 1D SSQW seems complicated when it comes to implementation, it is not much different from ordinary 1D DTQW. From (3.64) it is clear that the 1D SSQW is equivalent to a quantum walker performing the ordinary 1D DTQW, with alternate coin operations at each step. Therefore, each step of a 1D SSQW can be decomposed into two steps of the 1D DTQW with alternating spin-flip operations. Furthermore, this decomposition connects the Hamiltonian of the 1D DTQW to the Hamiltonian for the 1D SSQW. We plotted the probability distribution of the walker after 200 steps in Fig. (3.12). We observe that both plots are nearly identical and only differ in their spread on the x -axis.

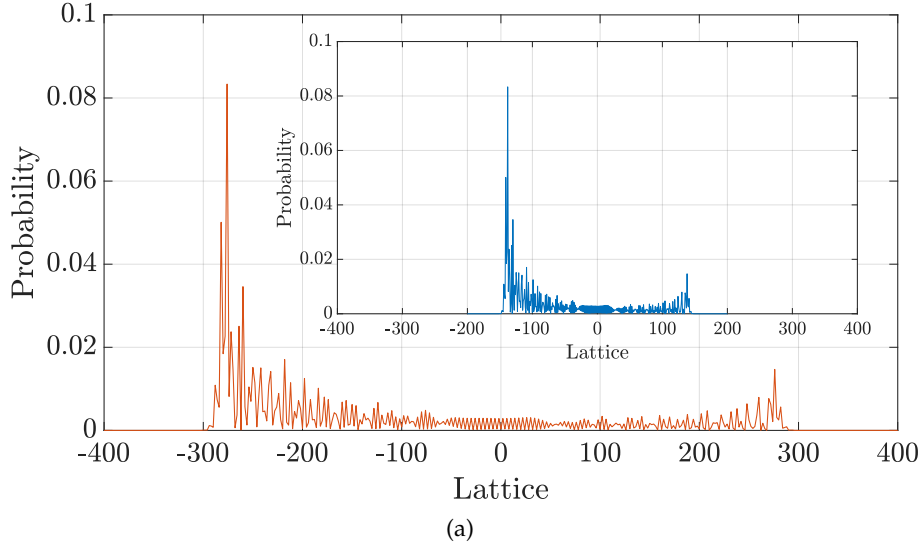


FIGURE 3.12: Probability distribution of the walker initially localized at the origin and with the symmetric state of the coin for $\theta_1 = \pi/4, \theta_2 = \pi/7$ after 200 steps. We took the system size to be $N = 400$. with unitary given by (3.32) and in the inset with unitary given by (3.59).

We extend this structure to decompose the 2D DTQW given in Eq. (3.40) into two 1D SSQW performed in two independent degrees of freedom (for example, directions) with the same coin [166]. We can rewrite the time evolution operator in $U_{2D}(\theta_1, \theta_2)$ given in Eq. (3.40) as

$$U_{2D}(\theta_1, \theta_2) = U_{\text{SS}}^y(\theta_1, 0)U_{\text{SS}}^x(\theta_1, \theta_2), \quad (3.65)$$

where $U_{\text{SS}}^i (i = x, y)$ is the time evolution operator of the 1D SSQW (3.32) in the i th direction.

3.3.3 Electric Quantum Walk

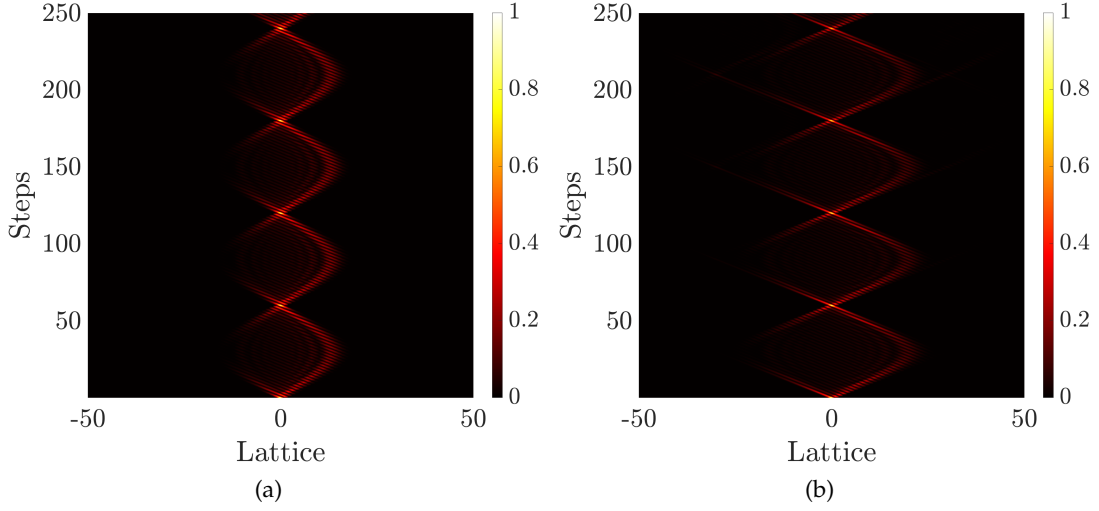


FIGURE 3.13: The evolution of probability density on the lattice with number of time steps with lattice size, $N = 101$. (a) $\theta_2 = \pi/2$, and (b) $\theta_2 = \pi/4$. Here we chose $\phi = 2\pi/60$.

We have introduced a phase factor, given by

$$E_\phi = \sum_n e^{i\phi n} \otimes |n\rangle\langle n| \quad (3.66)$$

during the discussion on unitary equivalence of quantum walks. This extra phase results in a modified time evolution for 1D DTQW which reads

$$U = E_\phi TR(\theta). \quad (3.67)$$

This modified quantum walk is referred to as ‘‘Electric Quantum Walk’’ [124, 135, 167–170]. We plot the variation of probability distribution with the number of steps in Fig. (3.13) for the initial state given by

$$|\psi(t = 0)\rangle = \frac{1}{\sqrt{2}} (|0\rangle + i|1\rangle) \otimes |0\rangle. \quad (3.68)$$

and observe the Bloch oscillations [171] which are the results of quantum particle superimposed with electric field. This is one of the main feature of these quantum walks. We also plot the probability of the return of the walker to the initial state and the variance as a function of time steps in Fig. 3.14.

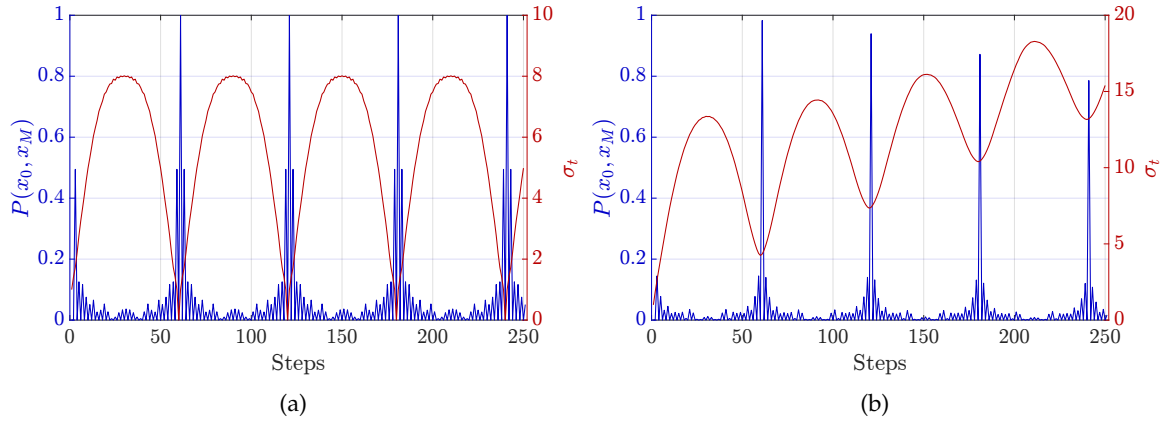


FIGURE 3.14: The plot of the returning probability $P(x_0, x_M)$ after M number of steps and the variance as a function of time steps for (a) $\theta_2 = \pi/2$, (b) $\theta_2 = \pi/4$.

To summarize, in this chapter, we have discussed general protocols for 1D and 2D DTQW and other related concepts. In Chapter 4 and 6, we will describe the topological phases exhibit by quantum walks and discuss the persistence of topological behaviour in such systems with more general setting.

Chapter 4

Symmetries and Topology

One of the central aims in condensed matter physics is to classify different states (or phases) of matter and study the behavior of a system in the vicinity of a phase transition. A state or phase of matter is defined as a particular order in which the constituent particles are organized in the system, leading to a distinct set of physical properties. This is referred to as the '*principle of emergence*', which states that the arrangement of the constituent particles, not the constituent particles themselves, determines the physical properties of the material [13, 172]. Different settings of the constituent particles lead to different phases of matter, which result in distinct properties. An immediate question one can ask here is that "Is there a way to tell whether the two phases of a system are same or equivalent?" The answer to the question which has been posed is that, the phases or states of a system are identical if they are connected to each other without any *phase transition*. And by connecting the two states, we mean that we start with one state of the system and start deforming it by changing the local parameters such as temperature, pressure, external fields, etc. until we reach the desired phase. A *phase transition* in the system is indicated by a discontinuity in one of the local quantities, known as *order parameter*.

The first step to classify the distinct phases of matter was taken by one of the great physicists of all time, Lev Landau, in the first half of the twentieth century by introducing the theory of phase transitions [173–176]. These phase transitions, known as "Landau-like phase transitions", are characterized by symmetry breaking. Landau proposed that different phases correspond to the existence of contrasting symmetries in a system, and a phase transition is

simply a transition that changes the symmetry of the system. In a phase transition, a higher symmetry group is broken into a lower symmetry subgroup or vice versa. When a fluid which has rotational and translational symmetries turns into a crystal, where these symmetries are broken, it is an example of a phase transition. Another example of the same kind of phase transition is when the temperature of a magnet is raised past a critical value, it goes from the ferromagnetic state to the paramagnetic state. The ferromagnetic state has a nonzero magnetization (because the spins are aligned in a particular direction), which breaks the rotation symmetry, which is reinstated in the paramagnetic state. In a phase transition in the ferromagnet, the net magnetization is the order parameter, whereas the shear modulus is the order parameter in the liquid-solid phase transition.

Landau's theory of phase transition was successful in classifying 230 different kinds of crystal that can exist in three dimensions. It managed to make people believe that the quest to understand the different phases of matter has come to an end. However, our understanding of phases took a sharp turn with the discovery of integer [4] and fractional quantum Hall effect [5] and the high-temperature superconductivity [177]. In these systems, for example, in the quantum Hall effect, the system supports different states with same symmetries. The discovery of these phases led physicists to take a break from Landau's theory of phase transitions and resort to topological concepts to understand these phases [178–182]. The order in such systems is beyond the laws of symmetries, and a new term was given to them, "topological order" [172].

The topological phases of matter have started to gain popularity very quickly due to their unique characteristics. The ground wavefunction of the system in such phases cannot be described by localized orbitals and exhibits entanglement (short-range or long-range) [183]. Further, the topological phases are defined globally, for example, to calculate a topological invariant, we need to integrate over the whole parameter space in order to get the information of the phase. This global behavior makes these phases robust against local noise, such as defects and impurities. In addition to this, the topological phases have a quantized response against the control parameter (like the external field), which only depends on fundamental constants such as h, c, e [4, 184]. For example, the Hall conductivity in a two-dimensional electron gas is given by an integer multiple of e^2/h [4, 179]. Topological properties are found in many systems, such as electrons in insulators [185, 186], metals [187], photonics [188], strongly interacting systems [189] and in amorphous matter [190].

As we discussed earlier, in ferromagnets the local magnetization is the order parameter which accounts for the spontaneous symmetry breaking and hence the phase transition. However, topological phases, being global in nature, cannot be described by local order parameters. The topological phases in a material can be described by *topological invariants*, which takes different quantized values in different phases, depending on the dimensions of the system. Topological invariants are deeply connected with a theorem from differential geometry known as *Gauss-Bonnet theorem* [185, 191]

$$\frac{1}{2\pi} \int_S K dA = \chi. \quad (4.1)$$

It states that the integral of the Gaussian curvature K on a surface of the manifold divided by 2π is always an integer χ (also known as the Euler characteristic). The integer χ is related to the genus as $\chi = 1 - g$ which represents the number of holes in the surface. For example, the surface of a sphere has $g = 0$ and the surface of a doughnut has $g = 1$, making them two topologically different objects. We encounter integrals, as one appearing in the Gauss-Bonnet theorem, while dealing with topological phases (we will see this in preceding sections) and χ is directly related to the topological invariants. Note that the small perturbations affect the curvature of the surface only locally and the integration over the new surface yields the same value on the right hand side of the Eq. (4.1) and hence the same topological invariants. This is the fundamental idea behind the robustness of topological phases.

In this chapter, we will discuss unitary and anti-unitary symmetries and how these symmetries define topological classes. We then discuss the SSH model model to understand the concepts of topological phases, topological invariants, and bulk-boundary correspondence.

4.1 Classification of topological phases

We start by looking for the following information about the system: a) the statistics of the constituents particles: bosons, fermions, and even anyons (particles that acquire an arbitrary phase $e^{i\phi}$ on exchange, rather than just ± 1 [192]), b) whether the system under consideration is gapped or gapless, and c) the entanglement (short-range or long-range) in the system. Once we have this information, the topological phases are characterized by the dimensionality and symmetries of the systems [193–197]. Here, by classifying, we mean finding the topological invariants of the system. These topological invariants can be a Chern number, a winding num-

ber, or some other mathematical index [13, 198, 199].

In topological materials, topological insulators are of particular interest [200]. An ordinary insulator has a bulk with a band gap and lacks states that can support electrical conductivity. On the other hand, topological insulators are materials that also have a gapped bulk but are characterized by some topological invariant. This bulk invariant allows and predicts a number of low-energy eigenstates, which are robust against perturbations, at the edges, which is known as *bulk-boundary correspondence* [6, 201, 202]. In some materials, these topological phases and, hence, low-energy eigenstates are protected against perturbations due to discrete symmetries of the system [203, 204].

4.2 Symmetries

Symmetry [195, 201, 205–207] is an operation that leaves the properties of the system unaffected. The concept of symmetry has always been useful in understanding physical systems. Although systems without any symmetries can also exhibit topological phases, understanding the symmetries allows us to classify the topological phases and the topological invariants that define their characteristics. In this section, we will go through the unitary and non-unitary symmetries and how they are useful in the context of classifying topological phases of matter.

4.2.1 Unitary symmetries

Before beginning the discussion on symmetries, let us first write a general (non-superconducting) Hamiltonian written in the second quantization [208] as

$$\hat{H} = \sum_{ij} \hat{b}_i^\dagger H_{ij} \hat{b}_j = \hat{b}^\dagger H \hat{b} \quad (4.2)$$

where H is the first quantized Hamiltonian, and $\{\hat{b}_i^\dagger\}$ and $\{\hat{b}_j\}$ are the creation and annihilation operators, respectively. Note that all statistics of the particle and operator properties of the Hamiltonian are contained in the creation and destruction operators \hat{b}^\dagger and \hat{b} . In the subsequent section, we will understand this structure with the SSH model. A system exhibits unitary

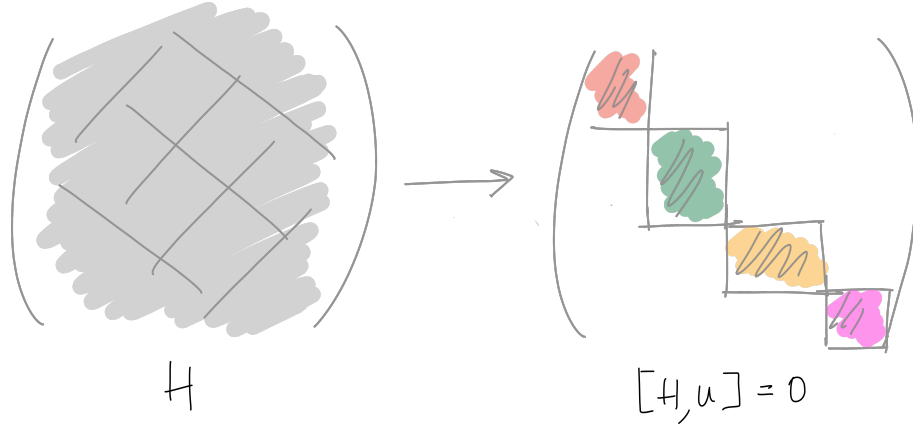


FIGURE 4.1: Block diagonalization of \hat{H} as the consequence of a unitary symmetry.

symmetry if the first-quantized Hamiltonian H of the system commutes with U such that

$$UHU^\dagger = H. \quad (4.3)$$

In terms of second quantization, this symmetry corresponds to a linear operator \mathcal{U} that acts on fermionic operators as [197]

$$\hat{b}_i \rightarrow \hat{b}'_i = \sum_j U_{ij} \hat{b}_j = \mathcal{U} \hat{b}_i \mathcal{U}^{-1}, \quad \hat{b}_i^\dagger \rightarrow (\hat{b}'_i)^\dagger = \sum_j \hat{b}_j^\dagger U_{ji}^* = \mathcal{U} \hat{b}_i^\dagger \mathcal{U}^{-1}. \quad (4.4)$$

and commutes with the Hamiltonian as

$$\mathcal{U} \hat{H} \mathcal{U}^{-1} = \hat{H}. \quad (4.5)$$

From here on-wards we will consider first-quantized Hamiltonian H only. Furthermore, in such scenarios, we can find a basis in which H and U both take a block diagonal form and each block is referred to as an irreducible representation of the symmetry [207] as shown in Fig. 4.1. Note that the individual blocks do not need to be of the same dimension. An example of unitary symmetries is *Translational symmetry*, which we will use in studying the SSH model in the next section. Another example is *Inversion/Parity symmetry*, \mathcal{P} under the action of which the position and the momentum transform as

$$\mathcal{P} \hat{x} \mathcal{P}^{-1} = -\hat{x}, \quad \mathcal{P} \hat{p} \mathcal{P}^{-1} = -\hat{p}, \quad \mathcal{P} [\hat{x}, \hat{p}] \mathcal{P}^{-1} = \mathcal{P} i\hbar \mathcal{P}^{-1} = i\hbar. \quad (4.6)$$

The third identity explicitly shows that the inversion symmetry is a unitary symmetry. Let us consider a simple example to understand the inversion symmetry: a molecule having two atoms with an electron hopping between them with amplitude t . The Hamiltonian for this system is written as

$$H = \begin{pmatrix} 0 & t \\ t & 0 \end{pmatrix} = t\sigma_x. \quad (4.7)$$

The eigenvalues and the eigenvectors are

$$E_{\pm} = \pm t, \quad |\psi_{\pm}\rangle = \frac{1}{\sqrt{2}} \begin{pmatrix} \pm 1 \\ 1 \end{pmatrix}. \quad (4.8)$$

In this case, the inversion interchanges two atoms and hence $\mathcal{P} = \sigma_x$ such that $[H, \mathcal{P}] = 0$. Furthermore, we can construct a matrix U_D using $|\psi_{\pm}\rangle$ as its column, which will take H to a diagonal basis as

$$H = U_D H' U_D^{\dagger} \implies H' = U_D^{\dagger} H U_D = \frac{1}{2} \begin{pmatrix} 1 & 1 \\ -1 & 1 \end{pmatrix} \begin{pmatrix} 0 & t \\ t & 0 \end{pmatrix} \begin{pmatrix} 1 & -1 \\ 1 & 1 \end{pmatrix} = t\sigma_z. \quad (4.9)$$

4.2.2 Non-unitary/Anti-unitary symmetries

As we have seen in the previous section, the symmetry operation U commutes with the Hamiltonian H (i.e. $U H U^{\dagger} = H$) allows us to write H in block diagonalized form in the irreducible representation of the symmetry group. However, such block diagonalization is not possible with anti-unitary symmetries. Hence, it is assumed that all of the unitary symmetries that commute with the Hamiltonian can be eliminated by writing the Hamiltonian in block form and by focusing attention on a block of the Hamiltonian. So, we are left with only the anti-unitary symmetries that need to be further analyzed for each block. The *time-reversal* and *particle-hole* symmetries are the anti-unitary symmetries that commutes with the Hamiltonian H . We can combine these two to get a unitary symmetry, called the *chiral* or *sublattice* symmetry, but that anticommutes with H . These possibilities have been shown to be exhaustive [201] and lead to 10 different classes of topological phases [193, 194, 196, 197].

4.2.2.1 Time-reversal symmetry (TRS)

Time reversal symmetry [209, 210] is one of the fundamental symmetry of a system. This symmetry leaves the Hamiltonian of the system unchanged under the time reversal transformation of the form $\mathcal{T} : t \rightarrow t' = -t$. Mathematically, time-reversal invariance is written as

$$\mathcal{T}H\mathcal{T}^{-1} = H. \quad (4.10)$$

It implies that the time-reversal operator commutes with the Hamiltonian and H and \mathcal{T} share the same set of eigenstates. If $|\psi\rangle$ is an eigenstate of H with energy E , then $\mathcal{T}|\psi\rangle$ will also be an eigenstate of H with the same energy. We will come back to this discussion later in the section. Furthermore, the effect of the time-reversal operator on the position, momentum, and spin operators, respectively, is as follows

$$\begin{aligned} \mathcal{T}\hat{x}\mathcal{T}^{-1} &= \hat{x}, \\ \mathcal{T}\hat{p}\mathcal{T}^{-1} &= -\hat{p}, \\ \mathcal{T}\hat{\sigma}\mathcal{T}^{-1} &= -\hat{\sigma}. \end{aligned} \quad (4.11)$$

Consequently, we have

$$\begin{aligned} \mathcal{T}[\hat{x}, \hat{p}]\mathcal{T}^{-1} &= \mathcal{T}\hat{x}\hat{p}\mathcal{T}^{-1} - \mathcal{T}\hat{p}\hat{x}\mathcal{T}^{-1} \\ &= \mathcal{T}\hat{x}\mathcal{T}^{-1}\mathcal{T}\hat{p}\mathcal{T}^{-1} - \mathcal{T}\hat{p}\mathcal{T}^{-1}\mathcal{T}\hat{x}\mathcal{T}^{-1} \\ &= -[\hat{x}, \hat{p}] \end{aligned} \quad (4.12)$$

which implies

$$\mathcal{T}i\mathcal{T}^{-1} = -i. \quad (4.13)$$

From all of the above properties, we can conclude that \mathcal{T} must include the operator \mathcal{K} that takes any complex number z into its complex conjugate

$$\mathcal{K}z\mathcal{K}^{-1} = z^*, \quad \mathcal{K}^{-1} = \mathcal{K}. \quad (4.14)$$

and \mathcal{T} is an *anti-unitary* operator that can be written, in general, as the product of a unitary operator and the complex conjugation operator

$$\mathcal{T} = U\mathcal{K} \quad (4.15)$$

with $U^{-1} = U^\dagger$. As far as \mathcal{K} is concerned, we have

$$\mathcal{K}|\psi\rangle = |\psi^*\rangle \implies \mathcal{K}^2 = \mathbb{1}. \quad (4.16)$$

For a time-reversal operator \mathcal{T} , we have

$$\begin{aligned} \mathcal{T}(\alpha|\psi\rangle + \beta|\phi\rangle) &= U\mathcal{K}(\alpha|\psi\rangle + \beta|\phi\rangle) \\ &= U(\alpha^*\mathcal{K}|\psi\rangle + \beta^*\mathcal{K}|\phi\rangle) \\ &= \alpha^*U\mathcal{K}|\psi\rangle + \beta^*U\mathcal{K}|\phi\rangle \\ &= \alpha^*\mathcal{T}|\psi\rangle + \beta^*\mathcal{T}|\phi\rangle. \end{aligned}$$

These are the properties of an anti-linear operator. Apart from these \mathcal{T} has one more property

$$\begin{aligned} \langle \mathcal{T}\psi | \mathcal{T}\phi \rangle &= \langle U\mathcal{K}\psi | U\mathcal{K}\phi \rangle \\ &= \langle U\psi^* | U\phi^* \rangle = \langle \psi^* | U^\dagger U \phi^* \rangle = \langle \psi^* | \phi^* \rangle \\ &= \langle \psi | \phi \rangle^* = \langle \phi | \psi \rangle. \end{aligned} \quad (4.17)$$

An operator which satisfies Eq. (4.17) is called the *anti-unitary* operator [211]. Now, if we apply the time-reversal operator twice, it should leave the system unchanged, i.e.

$$\mathcal{T}^2 = UKUK = UU^*\mathcal{K}\mathcal{K} = UU^* \quad (4.18)$$

NOTE: From this we can show that UU^ is equivalent (related by a unitary transformation) to its complex conjugate*

$$UU^* = UU^*UU^{-1} = U(UU^*)^*U^{-1}. \quad (4.19)$$

Since \mathcal{T}^2 leaves the system unchanged, i.e.

$$\begin{aligned} UU^* &= U(U^{-1})^T = e^{i\phi} \\ U(U^{-1})^T U^T &= U(UU^{-1})^T = U = e^{i\phi} U^T \\ \implies U &= e^{i\phi} (e^{i\phi} U^T)^T = e^{2i\phi} U \end{aligned}$$

which implies $e^{i\phi} = \pm 1$ and consequently

$$\mathcal{T}^2 = UU^* = e^{i\phi} = \pm \mathbb{1}. \quad (4.20)$$

Using the action of the complex conjugation operator \mathcal{K} on the position eigenvector which is $\mathcal{K}|\psi\rangle = |\psi\rangle$, we obtain the action of the complex conjugation operator \mathcal{K} on the position operator as

$$\mathcal{K}\hat{x}\mathcal{K}^{-1} = \hat{x} \quad (4.21)$$

and the action on the momentum operator can be obtained as

$$\mathcal{K}\hat{p}\mathcal{K}^{-1}|x\rangle = \mathcal{K}\hat{p}|x\rangle = \mathcal{K}\left(-i\hbar\frac{\partial}{\partial x}\right)|x\rangle = i\hbar\frac{\partial}{\partial x}|x\rangle = -p|x\rangle. \quad (4.22)$$

which gives us

$$\mathcal{K}\hat{p}\mathcal{K}^{-1} = -\hat{p}. \quad (4.23)$$

Now, for a spinless particle, we have only \hat{x} and \hat{p} and the action of \mathcal{T} on \hat{x} and \hat{p} is given by

$$\mathcal{T}\hat{x}\mathcal{T}^{-1} = \hat{x}, \quad \mathcal{T}\hat{p}\mathcal{T}^{-1} = -\hat{p} \quad (4.24)$$

which implies $U = \mathbb{1}$ and $\mathcal{T} = \mathcal{K}$. Consequently, we have

$$\mathcal{T}^2 = \mathcal{K}^2 = +\mathbb{1}. \quad (4.25)$$

On the other hand, if we consider a particle with a spin (say spin-1/2). Then, there is one more job that \mathcal{T} has to do. The time reversal operation flips the spin, i.e.

$$\mathcal{T}\boldsymbol{\sigma}\mathcal{T}^{-1} = -\boldsymbol{\sigma}. \quad (4.26)$$

where the components of σ are given by

$$\sigma_x = \begin{pmatrix} 0 & 1 \\ 1 & 0 \end{pmatrix}, \quad \sigma_y = \begin{pmatrix} 0 & -i \\ i & 0 \end{pmatrix}, \quad \sigma_z = \begin{pmatrix} 1 & 0 \\ 0 & -1 \end{pmatrix} \quad (4.27)$$

$$\implies \mathcal{K}\sigma_x\mathcal{K}^{-1} = \sigma_x, \quad \mathcal{K}\sigma_y\mathcal{K}^{-1} = -\sigma_y, \quad \mathcal{K}\sigma_z\mathcal{K}^{-1} = \sigma_z \quad (4.28)$$

Furthermore, using $\mathcal{T}\sigma\mathcal{T}^{-1} = -\sigma$ and $\mathcal{T} = U\mathcal{K}$ we can derive the following

$$U\sigma_xU^{-1} = -\sigma_x, \quad U\sigma_yU^{-1} = \sigma_y, \quad U\sigma_zU^{-1} = -\sigma_z \quad (4.29)$$

which implies $U = c_0\sigma_y$, where c_0 is some constant. We can choose $c_0 = 1$, using the unitarity of U , which results in

$$\mathcal{T} = \sigma_y\mathcal{K} \quad (4.30)$$

such that $\mathcal{T}^2 = \sigma_y\mathcal{K}\sigma_y\mathcal{K} = \sigma_y\sigma_y^*\mathcal{K}^2 = -\mathbb{1}$. In conclusion, for a quantum system with **half-integer** spin, the operator \mathcal{T} squares to negative of the identity, i.e. $\mathcal{T}^2 = -\mathbb{1}$. Similarly, one can show that for a quantum system without spin or **integer** spin, the time reversal operator squares to $\mathcal{T}^2 = \mathcal{K}^2 = \mathbb{1}$.

A quantum particle moving in a periodic potential exhibits translation symmetry. In that case, the eigenvalues of the position and momentum are the same, and the Hamiltonian will be block-diagonalized in momentum basis and written in second-quantization as

$$\hat{H} = \sum_{\mathbf{k}} b_{\mathbf{k}}^\dagger H(\mathbf{k}) b_{\mathbf{k}} \quad (4.31)$$

The time-reversal invariance for $H(\mathbf{k})$ for quasi-momentum \mathbf{k} is expressed as

$$\mathcal{T}H(\mathbf{k})\mathcal{T}^{-1} = U\mathcal{K}H(\mathbf{k})\mathcal{K}^{-1}U^{-1} = UH^*(\mathbf{k})U^{-1} = H(-\mathbf{k}). \quad (4.32)$$

In continuation, we observe that if $|\psi(\mathbf{k})\rangle$ is an eigenstate of $H(\mathbf{k})$ with energy $E(\mathbf{k})$ then $\mathcal{T}|\psi(\mathbf{k})\rangle$ is an eigenstate of $H(-\mathbf{k})$ with energy $E(-\mathbf{k})$ which is the same as $E(\mathbf{k})$. Further, we can show

$$\begin{aligned} \langle \mathcal{T}\psi(\mathbf{k}) | \psi(\mathbf{k}) \rangle &= \langle \mathcal{T}\psi(\mathbf{k}) | \mathcal{T}^2\psi(\mathbf{k}) \rangle = -\langle \mathcal{T}\psi(\mathbf{k}) | \psi(\mathbf{k}) \rangle \\ \implies \langle \mathcal{T}\psi(\mathbf{k}) | \psi(\mathbf{k}) \rangle &= 0 \end{aligned} \quad (4.33)$$

where we used the fact that \mathcal{T} preserves the norm (or probability) and $\mathcal{T}^2 = -\mathbb{1}$. Thus, $|\psi(\mathbf{k})\rangle$ and $\mathcal{T}|\psi(\mathbf{k})\rangle$ are two different states with the same energy $E(\mathbf{k})$. This is called *Kramer's degeneracy*. Note that only the system with time-reversal symmetry and $\mathcal{T}^2 = -\mathbb{1}$ exhibits this kind of degeneracy.

4.2.3 Particle-hole or Charge conjugation symmetry (PHS)

The next symmetry that plays an integral role in the classification of single particle Hamiltonians is the particle-hole (\mathcal{C}). In the context of high-energy physics, charge conjugation refers to a transformation of a particle into its antiparticle. However, in a condensed matter system, this symmetry turns creating particles into creating holes [199]. The invariance of the Hamiltonian under charge conjugation results the following condition

$$\mathcal{C}H\mathcal{C}^{-1} = -H \implies U_{\mathcal{C}}HU_{\mathcal{C}}^{-1} = -H \quad (4.34)$$

Therefore, the particle-hole operator $\mathcal{C} = U_{\mathcal{C}}\mathcal{K}$ is an anti-unitary operator that anti-commutes with the Hamiltonian. Like in the case of time-reversal, we can show that the action of the particle-hole operator on the single-particle Hamiltonian, in momentum space, reads

$$\mathcal{C}H(\mathbf{k})\mathcal{C}^{-1} = -H(-\mathbf{k}) \implies U_{\mathcal{C}}H^*(\mathbf{k})U_{\mathcal{C}}^{-1} = -H(-\mathbf{k}) \quad (4.35)$$

The operator \mathcal{C} also squares to ± 1 . In this case, given $|\psi(\mathbf{k})\rangle$ is an eigenstate of $H(\mathbf{k})$ with energy $E_+(\mathbf{k})$, it has a correspondent $\mathcal{C}|\psi(\mathbf{k})\rangle$, with energy $E_-(-\mathbf{k}) = -E_+(\mathbf{k})$. The PHS is responsible for a symmetric energy band structure about $k = 0$ as shown in Fig. 4.2.

4.2.4 Chiral or Sub-lattice symmetry (CS)

Having talked about TRS and PHS, we can construct another symmetry by combining the previous two symmetries (time-reversal and charge-conjugation) as $\Gamma = \mathcal{T} \cdot \mathcal{C}$. (Note that we can also take $\Gamma = \mathcal{C} \cdot \mathcal{T}$, which only corresponds to the change of the basis.) This new symmetry Γ is a unitary symmetry that does not commute but anti-commutes with the Hamiltonian [201] and hence $\mathcal{T} \cdot \mathcal{C}$ does not correspond to an 'ordinary' Hamiltonian symmetry. This is the reason why we consider chiral symmetry Γ as an additional essential ingredient for the classification of the

blocks of the irreducible representation, other than time-reversal \mathcal{T} and charge-conjugation (particle–hole) symmetries \mathcal{C} . Mathematically, it satisfies the following relation

$$\Gamma H \Gamma^{-1} = -H. \quad (4.36)$$

It is interesting to note here that this unitary symmetry does not represent a conventional symmetry in quantum mechanics because it anti-commutes with the Hamiltonian, whereas conventionally we talk about symmetries which commute with the Hamiltonian. In the momentum space, it acts as

$$\Gamma H(\mathbf{k}) \Gamma^{-1} = -\Gamma(\mathbf{k}). \quad (4.37)$$

Since Γ is unitary, it always squares to $+\mathbb{1}$. The spectrum of a system exhibiting chiral symmetry has eigenstates $|\psi(\mathbf{k})\rangle$ and $\Gamma|\psi(\mathbf{k})\rangle$ as shown in Fig. 4.2. This is the last ingredient in order to talk about topological classes based on the existence of the symmetries in the system.

4.3 Tenfold Way by AZ

Having all the symmetries that a system can possess at our disposal, we can talk about symmetry classes. Depending on the type of the symmetry our system possess among TRS, PHS and CS we have symmetry classification. The system can have TRS in three possible ways: i) absence of time-reversal ($\mathcal{T} = 0$), ii) presence of time-reversal with $\mathcal{T}^2 = +1$, iii) presence of time-reversal with $\mathcal{T}^2 = -1$. Similarly, we have such distinct possibilities with PHS and CS. Consequently, we have precisely ten symmetry classes given in Table (4.1) which are due to Altland and Zirnbauer [212–214]. which have completed the earlier classification due to Wigner and Dyson [215].

	Cartan label	TRS	PHS	CS
Standard Classes	A	0	0	0
	AI	+1	0	0
	AII	-1	0	0
Chiral Classes	AIII	0	0	1
	BDI	+1	+1	1
	CII	-1	-1	1
BdG classes	D	0	+1	0
	C	0	-1	0
	DII	-1	+1	1
	CI	+1	-1	1

TABLE 4.1: 10-fold way.

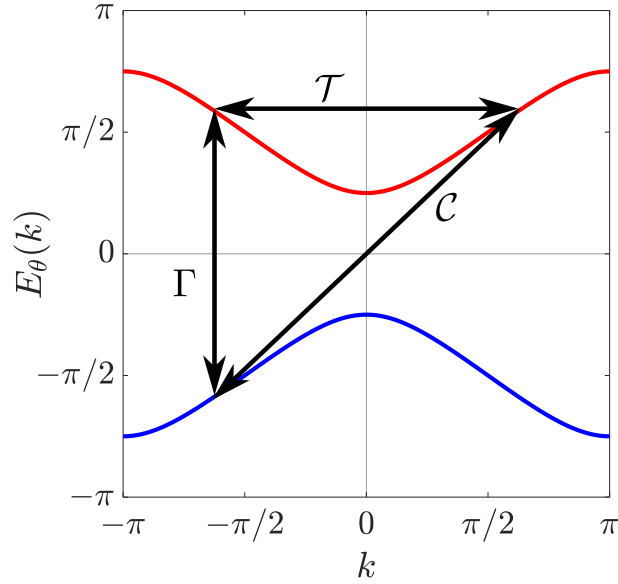


FIGURE 4.2: Dispersion relation of a system that exhibits all three, time-reversal, charge-conjugation and chiral symmetry. The arrows represent the relation between the states $|\psi(\mathbf{k})\rangle$ and $\mathcal{T}|\psi(\mathbf{k})\rangle, \mathcal{C}|\psi(\mathbf{k})\rangle, \Gamma|\psi(\mathbf{k})\rangle$ which is discussed in the text.

4.4 1D Tight-Binding Model

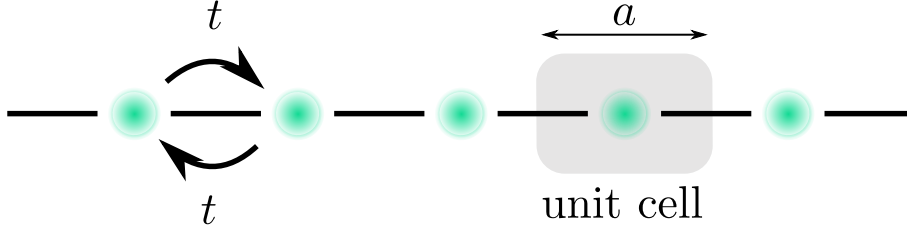


FIGURE 4.3: 1D lattice with lattice spacing a and the hopping amplitude between nearest neighbors t .

In this section, consider an infinite 1D chain having N sites with only nearest-neighbor interaction denoted by t as shown in Fig. 4.3. We will illustrate how unitary symmetries result in block diagonalization with this very simple model and extend it to the SSH model in the next section. For electrons (spinless) hopping on this 1D chain with amplitude t , we can write the Hamiltonian in second-quantized basis as

$$\hat{H} = \sum_i^N t \hat{b}_{i+1}^\dagger \hat{b}_i + t \hat{b}_i^\dagger \hat{b}_{i+1} + \mu \hat{n}_i \quad (4.38)$$

where \hat{b}_i^\dagger and \hat{b}_i are the fermionic (because of electrons) creation and annihilation operators, respectively, and $\hat{n}_i \equiv \hat{b}_i^\dagger \hat{b}_i$ is the number or density operator. The creation and annihilation operators satisfy the commutation relations

$$\{\hat{b}_i, \hat{b}_j^\dagger\} = \delta_{ij}, \quad \{\hat{b}_i, \hat{b}_j\} = 0 = \{\hat{b}_i^\dagger, \hat{b}_j^\dagger\}. \quad (4.39)$$

These operators act on a state written in occupation number representation that looks like $|n_1, n_2, \dots, n_N\rangle$ where n_i is the occupation number of the i th site [208, 216, 217]. For fermions, these occupation numbers can only take a value of either zero or one, in accordance with Pauli's exclusion principle. For spinless electrons, we have

$$\begin{aligned} \hat{b}_i^\dagger |0, 0, \dots, 0\rangle &= |0, \dots, 1_i, \dots, 0\rangle, \quad \hat{b}_i |0\rangle = 0 \quad \hat{b}_i |0, 0, \dots, 1_i, \dots, 0\rangle = 0 \\ \hat{b}_i^\dagger \hat{b}_i |n_1, n_2, \dots, n_i, \dots, n_N\rangle &= \hat{n}_i |n_1, n_2, \dots, n_i, \dots, n_N\rangle = n_i |n_1, n_2, \dots, n_i, \dots, n_N\rangle, \quad n_i \in [0, 1]. \end{aligned} \quad (4.40)$$

The last term in Eq. (4.38) corresponds to the chemical potential μ . Now, we make use of the translational symmetry of the chain and write

$$\hat{b}_i^\dagger = \frac{1}{\sqrt{N}} \sum_k e^{ikx_i} \hat{b}_k^\dagger, \quad \hat{b}_i = \frac{1}{\sqrt{N}} \sum_k e^{-ikx_i} \hat{b}_k \quad (4.41)$$

where $x_i = ia$ and $k = 2\pi n/N$ are the allowed momenta. Using the above relations, we can have

$$\begin{aligned} \sum_i \hat{b}_{i+n}^\dagger \hat{b}_i &= \sum_i \left(\frac{1}{\sqrt{N}} \sum_k e^{ikx_{i+n}} \hat{b}_k^\dagger \right) \left(\frac{1}{\sqrt{N}} \sum_{k'} e^{-ik'x_i} \hat{b}_{k'} \right) \\ &= \frac{1}{N} \sum_{k,k'} \sum_i e^{ik(x_i+na)} e^{-ik'x_i} \hat{b}_k^\dagger \hat{b}_{k'} \\ &= \sum_{k,k'} e^{ikna} \hat{b}_k^\dagger \hat{b}_{k'} \left(\frac{1}{N} \sum_i e^{i(k-k')x_i} \right) \\ &= \sum_{k,k'} e^{ikna} \hat{b}_k^\dagger \hat{b}_{k'} \delta_{kk'} \\ &= \sum_k e^{ikna} \hat{b}_k^\dagger \hat{b}_k. \end{aligned} \quad (4.42)$$

Therefore, utilizing Eq. (4.42), the Hamiltonian in Eq. (4.38) can be written in momentum space as

$$\hat{H} = \sum_k \left[te^{ika} + te^{-ika} + \mu \right] \hat{b}_k^\dagger \hat{b}_k = \sum_k E(k) \hat{b}_k^\dagger \hat{b}_k \quad (4.43)$$

where

$$E(k) = 2t \cos(ka) + \mu \quad (4.44)$$

which we plotted in Fig. 4.4. In this example, it was straightforward to find a dispersion relation because we had only one degree of freedom. We will now extend the same analysis to a model in which we have two degrees of freedom in the next section.

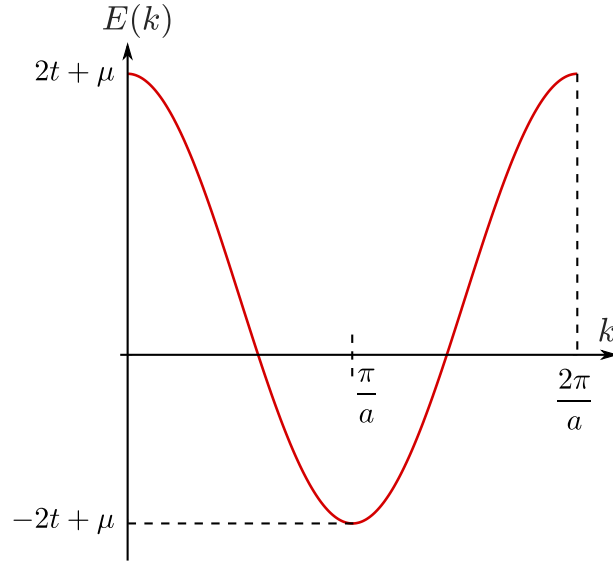


FIGURE 4.4: The plot of the dispersion relation derived in Eq. (4.44).

4.5 Su-Schrieffer-Heeger (SSH) model

The SSH was introduced to model polyacetylene, which is a 1D carbon chain [218, 219]. The model consists of a one-dimensional lattice (chain) in which each lattice site consists of a unit cell that also hosts two sites A and B . The electrons jump on this one-dimensional chain with amplitudes v and w as shown in Fig. 4.5. Using this model, which has been implemented experimentally using ultracold atoms [220–224], we illustrate the concepts of the single-particle Hamiltonian, symmetries of the Hamiltonian (unitary and anti-unitary), topological invariance, and bulk-boundary correspondence.

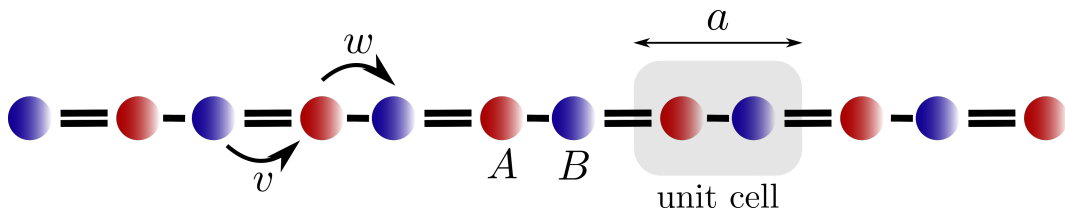


FIGURE 4.5: The geometry of SSH with lattice spacing a . One unit cell consists of two sites A and B , which is shown with shaded part. A chain consists of N unit cells.

We consider here non-interacting particles, hence the dynamics of the system is governed by a

single particle Hamiltonian which is written as [202, 225]

$$\hat{H} = \sum_{n=1}^N [v |n, B\rangle\langle n, A| + h.c.] + \sum_{n=1}^{N-1} [w |n+1, A\rangle\langle n, B| + h.c.] \quad (4.45)$$

where $h.c.$ is the Hermitian conjugate. For the case where we have $N = 3$ lattice sites, the Hamiltonian takes the form

$$H = \begin{pmatrix} 0 & v & 0 & 0 & 0 & 0 \\ v & 0 & w & 0 & 0 & 0 \\ 0 & w & 0 & v & 0 & 0 \\ 0 & 0 & v & 0 & w & 0 \\ 0 & 0 & 0 & w & 0 & v \\ 0 & 0 & 0 & 0 & v & 0 \end{pmatrix} \quad (4.46)$$

We separate the two degrees of freedom in external (unit cell) and internal (orbital/site index) as $|n, \sigma\rangle = |n\rangle \otimes |\sigma\rangle$ which belongs to a composite Hilbert space $\mathcal{H} = \mathcal{H}_{\text{external}} \otimes \mathcal{H}_{\text{internal}}$ where $n = 1, 2, \dots, N$ and $\sigma = A, B$. Using this tensor product basis and choosing the computational basis $\{|0\rangle, |1\rangle\}$ for $\{A, B\}$, we can write Hamiltonian as

$$\begin{aligned} \hat{H} &= \sum_{n=1}^N v [|n\rangle\langle n| \otimes (|1\rangle\langle 0| + |0\rangle\langle 1|)] + \sum_{n=1}^{N-1} w [|n+1\rangle\langle n| \otimes |0\rangle\langle 1| + |n\rangle\langle n+1| \otimes |1\rangle\langle 0|] \\ &= v \sum_{n=1}^N [|n\rangle\langle n| \otimes \sigma_x] + w \sum_{n=1}^{N-1} [|n+1\rangle\langle n| \otimes \sigma_+ + |n\rangle\langle n+1| \otimes \sigma_-] \end{aligned} \quad (4.47)$$

where σ_x is the Pauli x matrix and $\sigma_+ = \sigma_-^\dagger$ is the step-up operator in computational basis. First, we will concentrate on the bulk part of the chain by connecting the edges, leading to periodic boundary conditions. This corresponds to a closed ring with the slight different Hamiltonian which reads

$$\hat{H}_{\text{bulk}} = \sum_{n=1}^N [v |n, B\rangle\langle n, A| + w |(n \bmod N) + 1, A\rangle\langle n, B|] + h.c. \quad (4.48)$$

By further exploiting the translational invariance of the system, we can go to quasi-momentum space by defining

$$|n, \sigma\rangle = \frac{1}{\sqrt{N}} \sum_k e^{ikx_n} |k, \sigma\rangle; \sigma = A, B. \quad (4.49)$$

where $x_n = an$, and let us take $a = 1$ for the sake of simplicity. The bulk Hamiltonian in

momentum basis reads

$$\begin{aligned}
\hat{H}_{\text{bulk}} &= \frac{1}{N} \sum_{n=1}^N \left[v \sum_{k,l} e^{ikn} e^{-iln} |k, A\rangle\langle l, B| + w \sum_{s,t} e^{is(n+1)} e^{-itn} |s, B\rangle\langle t, A| + h.c. \right] \\
&= \sum_k \left[v |k, A\rangle\langle k, B| + w e^{ik} |k, B\rangle\langle k, A| + v |k, B\rangle\langle k, A| + w e^{-ik} |k, A\rangle\langle k, B| \right] \\
&= \sum_k \left[\left(v + w e^{-ik} \right) |k, A\rangle\langle k, B| + \left(v + w e^{ik} \right) |k, B\rangle\langle k, A| \right].
\end{aligned}$$

where we used

$$\frac{1}{N} \sum_{n=1}^N e^{i(k-l)n} = \delta_{kl}. \quad (4.50)$$

We can further write it as

$$\hat{H}_{\text{bulk}} = \sum_k |k\rangle\langle k| \otimes \begin{bmatrix} 0 & v + w e^{ik} \\ v + w e^{-ik} & 0 \end{bmatrix} = \bigoplus_k H(k) \quad (4.51)$$

where

$$H(k) = \mathbf{d}(k) \cdot \boldsymbol{\sigma} \quad (4.52)$$

with the vector $\mathbf{d}(k)$ given by

$$\mathbf{d}(k) = (d_x, d_y, d_z) = (v + w \cos k, w \sin k, 0) \quad (4.53)$$

and the dispersion relation;

$$E_{\pm}(k) = \pm \sqrt{d_x^2 + d_y^2} = \pm \sqrt{v^2 + w^2 + 2vw \cos k}. \quad (4.54)$$

We now plot the dispersion relation and the vector $\hat{\mathbf{d}}(k)$ for different settings of v and w . We can write the Hamiltonian in the second-quantization basis also as

$$\hat{H} = \sum_n \left[v \hat{b}_{B,n}^\dagger \hat{b}_{A,n} + w \hat{b}_{A,n+1}^\dagger \hat{b}_{B,n} + h.c. \right] \quad (4.55)$$

and again going to momentum basis using

$$\hat{b}_{i,\alpha} = \frac{1}{\sqrt{N}} \sum_k e^{ikx_i} \hat{b}_{k,\alpha}, \quad \alpha = A, B \quad (4.56)$$

we get

$$\hat{H} = \sum_{k,\alpha\beta} \hat{b}_{k,\alpha}^\dagger H_{\alpha\beta}(k) \hat{b}_{\beta,k} \quad (4.57)$$

with $H_{\alpha\beta}(k)$ same as $H(k)$ from Eq. (4.52). We plot the dispersion relation for different settings of the amplitudes v and w in Fig. 4.6.

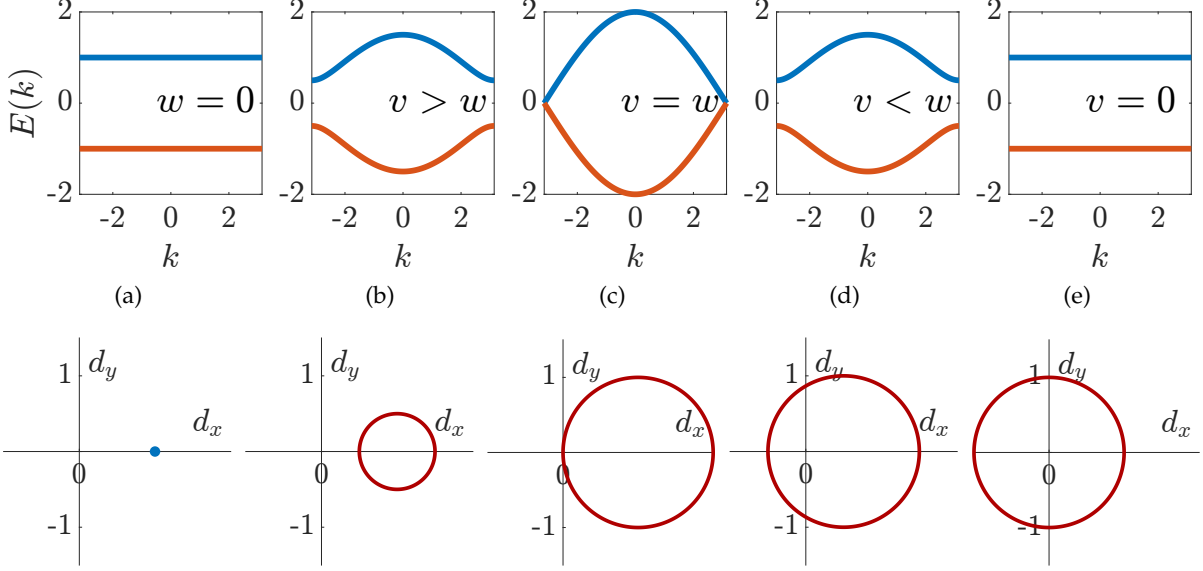


FIGURE 4.6: Dispersion relation of the SSH model $E_{\pm}(k)$ given in Eq. (4.54) for different settings of v and w . (a) $v = 1, w = 0$, (b) $v = 1, w = 0.5$, (c) $v = 1, w = 1$, (d) $v = 0.5, w = 1$, (e) $v = 0, w = 1$. In the bottom row, the endpoints of the vectors $\mathbf{d}(k)$ [given in Eq. (4.53)] in the d_x - d_y plane as k takes values from 0 to 2π in first Brillouin zone.

We observe that, as long as the hopping amplitudes are staggered, $v \neq w$, the two bands are separated by a band gap $\sim |v - w|$ as shown in Fig. 4.6a,b,d,e. When the two amplitudes are the same, we see the closing of the band gap [see Fig. 4.6c] and the chain behaved as a conductor. We naturally come across this type of staggering in systems like polyacetylene, which is the result of Peierls' instability [226–228].

So far, we have studied the dispersion relation to study the characteristics of the SSH model. Looking at Fig. 4.6, we see that the dispersion looks exactly the same in the two regimes, namely $v > w$ and $v < w$ and does not provide any interesting information in more detail. However, we can still further investigate the system using information about eigenstates, encoded in the vector $\mathbf{d}(k)$. As k takes values from 0 to 2π in the Brillouin zone, the tip of the

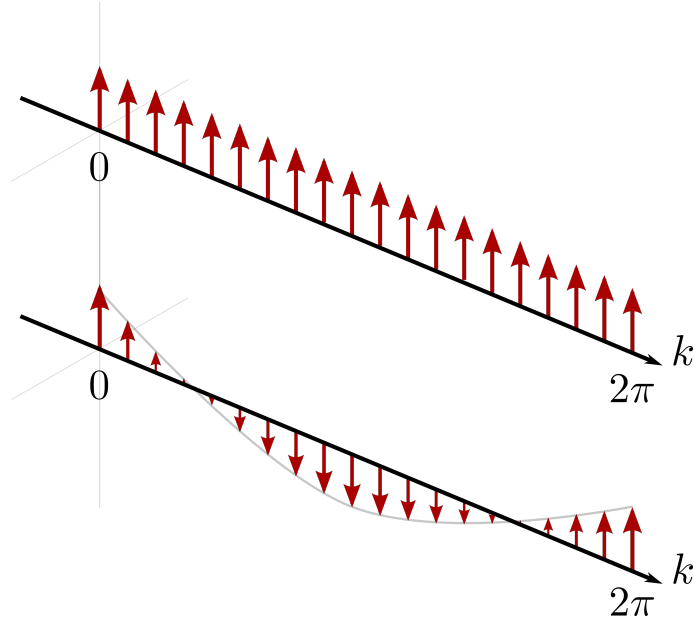


FIGURE 4.7: A schematic to illustrate the winding of the wavefunction $|\psi(k)\rangle$, as k goes around in the Brillouin zone, for the trivial (top) and the topological phase (bottom). Note, that the two phases shown above cannot be smoothly connected due to the presence of a twist in the topologically non-trivial phase (bottom).

vector $\mathbf{d}(k)$ traces out a closed curve due to periodic boundary conditions and

$$d_x = v + w \cos k, \quad d_y = w \sin k \implies (d_x - v)^2 + d_y^2 = w^2 \quad (4.58)$$

i.e. it traces out a circle of radius w , centered at $(v, 0)$. Note that in general, it does not need to be a circle. Here, we can define the topology of the loop by an integer called the bulk winding number W . The winding number refers to the number of times the loop winds around the origin of the d_x - d_y plane. Therefore, it is evident from the bottom row of Fig. 4.6, that the two insulating phases (gapped phases) in the two regions, namely $v > w$ and $v < w$ are different. For example, the winding number, $W = 0$ for $v > w$ [Fig. 4.6a,b] and $W = 1$ for $v < w$ [Fig. 4.6d,e], whereas, for $v = w$, the circle just touched the origin and therefore the winding number is not defined for this parameter setting. As plotted in Fig. 4.7, we can imagine a two-dimensional vector corresponding to each value of k and see that the rotation of it as k goes from 0 to 2π . We will refer to the insulating phase with $W = 0$ as *trivial* and with $W = 1$ as *topological*. In the next section, we will come out of the bulk and explore the edges.

4.5.1 Edge states

Till now, we have looked at the dispersion of the Hamiltonian under periodic boundary conditions. We also define the bulk winding number, which decides whether we have trivial ($W = 0$) or non-trivial topology ($W = 1$) in the system depending on the hopping amplitudes. In most practical situations, we have finite-size lattices, where we cannot use translational invariance and study bulk characteristics, as we did in the last section. In such cases, we need to consider open chains and solve the Hamiltonian for the dispersion in the real space. Here, an interesting question to ask is “What are the physical consequences of the non-zero winding number in the bulk we see on the edges or boundaries?”

We start by looking at the two extreme cases, known as the dimerized limit [202]: a) when we allow only intracell hopping and intercell hopping to vanish, i.e. $v \neq 0$ (set 1 for simplicity), $w = 0$, b) when we have the reverse situation, i.e. $w \neq 0$ (set 1 for simplicity), $v = 0$. In both cases, the SSH chain breaks down into dimers, as shown in Fig. 4.8.

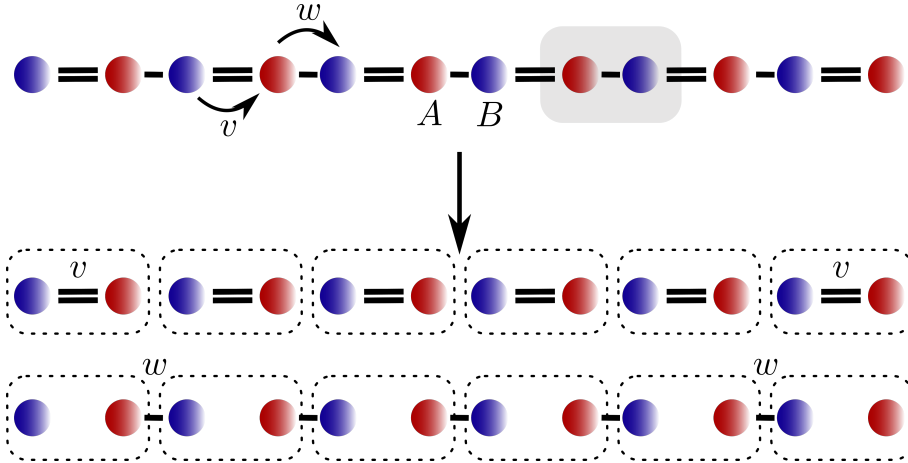


FIGURE 4.8: The two extremes cases of open chain of SSH in the dimerized limit.

Since, we do not have periodicity anymore, we cannot find a dispersion relation as the function of momentum k , but we can still calculate it numerically by diagonalizing the Hamiltonian written in Eq. (4.52). The bulk has flat bands in the dimerized limits. In the *trivial* case of $v = 1, w = 0$, we have $H(k) = \sigma_x$ and the energy eigenstates would simply be a superposition of the A and B sites for each dimer, i.e.

$$H(|n, A\rangle \pm |n, B\rangle) = \pm(|n, A\rangle \pm |n, B\rangle). \quad (4.59)$$

Similarly, in the *non-trivial* or *topological* case of $v = 0, w = 1$, we have $H(k) = \sigma_x \cos k + \sigma_y \sin k$ and the energy eigenstates would be a superposition of the A and B sites of neighboring sites, i.e.

$$H(|n, A\rangle \pm |n + 1, B\rangle) = \pm(|n, A\rangle \pm |n + 1, B\rangle). \quad (4.60)$$

However, in addition to these states, we have two additional states which come from the two single sites at the end of the chain [as shown at the bottom in Fig. 4.8]. Each of these sites hosts a single eigenstate with zero energy because of the absence of onsite potentials in SSH.

In Fig. 4.9(a), 4.9(b), we have plotted the spectrum of eigenvalues of the Hamiltonian corresponding to the open chain, having $N = 100$ unit cells, by varying the intra-cell hopping amplitude v and fixed $w = 1$ and vice versa. For the *topological* case, we see the two states with zero energy, *edge states*, in the band gap at $v = 0$ in Fig. 4.9(a) and in *trivial* case, we do not observe any zero mode states for $w = 0$ and $v = 1$ as shown in Fig. 4.9(b). Interestingly, we see that the system exhibits energy eigenstates that are very close to zero when we move away from the dimerized limit by switching on the intracell hopping parameter v . If these are really edge states, then the wavefunctions of these states have to be localized exponentially at both edges. When we plot the wavefunction, corresponding to these states in Figs. 4.10(a) and 4.10(b), we observe that the zero energy states are exponentially localized at the two edges of the chain. For reference, we have also plotted the wavefunction corresponding to a non-zero state in Fig. 4.10(c) and we see that this state is delocalized throughout the chain. We note another interesting thing in the plots of the zero-energy eigenstates, the left (right) edge state has a nonvanishing contribution only on sublattice A (B). These edge states exist as long as $v < w$, which makes this regime different from the regime $v > w$, where we do not see any edge states. Lastly, in Fig. 4.9(a), we plot the spectrum of eigenvalues for the trivial $v > w$ and topological $v < w$ region.

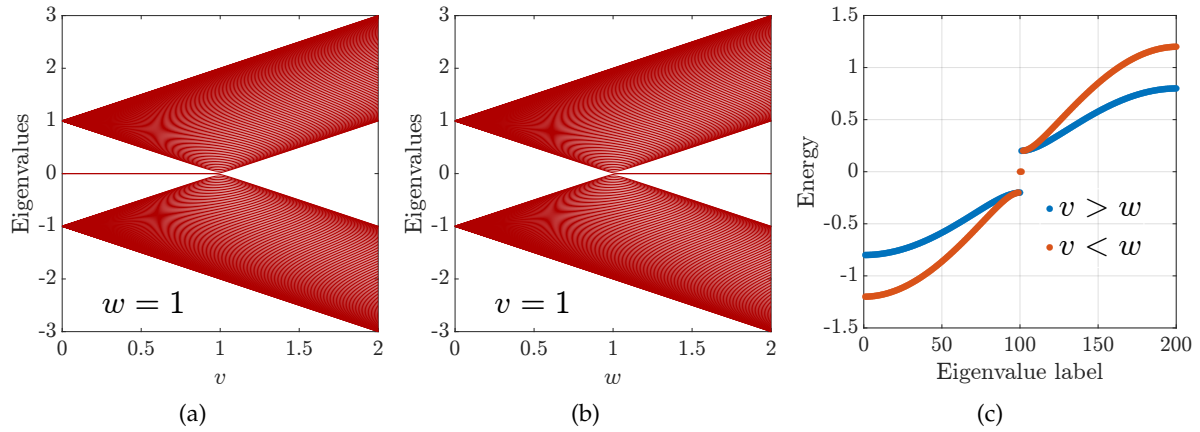


FIGURE 4.9: (Energy spectrum of the finite chain with $N = 100$ unit cells and for (a) fixed $w = 1$ and varying v , (b) fixed $v = 1$ and varying w . (a) shows that $v > w$ and $v < w$ corresponds to trivial and topological phases respectively.

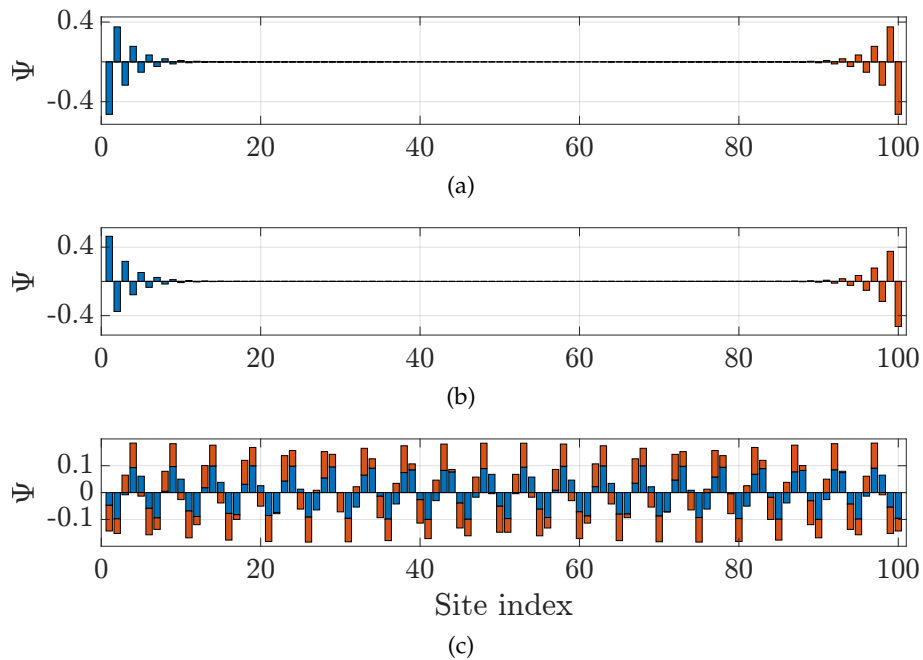


FIGURE 4.10: (a), (b) The plot of the wavefunction corresponding to zero-energy edge states. The blue and orange bars represent the components on the sublattice A and B respectively. (c) shown any bulk state for the reference which is delocalized all over the chain.

4.5.2 Symmetries of SSH model

The Hamiltonian of the SSH model exhibits sublattice or chiral symmetry (discussed in Sec. (4.2.4)) and hence belongs to AIII class. The chiral symmetry is represented by the operator

$$\Gamma = \sigma_z. \quad (4.61)$$

The existence of chiral symmetry confines the vector $\mathbf{d}(k)$ to the d_x - d_y plane

$$\sigma_z H(k) \sigma_z = -H(k) \implies d_z = 0. \quad (4.62)$$

Furthermore, with the given chiral symmetry operator, we can define the projectors that act on the sublattices A and B as

$$\begin{aligned} \mathcal{P}_A &= \frac{1}{2} (\mathbb{1} + \Gamma) = \mathbb{1}_{\text{lattice}} \otimes |A\rangle\langle A| \\ \mathcal{P}_B &= \frac{1}{2} (\mathbb{1} - \Gamma) = \mathbb{1}_{\text{lattice}} \otimes |B\rangle\langle B| \end{aligned} \quad (4.63)$$

and can rewrite the Hamiltonian as

$$H = \mathcal{P}_A H \mathcal{P}_B + \mathcal{P}_B H \mathcal{P}_A. \quad (4.64)$$

4.5.3 Winding number

Formally, for a given Hamiltonian $H(k)$, the winding number W_m for the m th band (we have two bands in the SSH model) is defined as

$$W_m = \frac{1}{\pi} \int_{-\pi}^{\pi} i \langle \Gamma \psi_m(k) | \frac{\partial}{\partial k} | \psi_m(k) \rangle, \quad (4.65)$$

where Γ is the chiral symmetric operator and $|\psi_m(k)\rangle$ is the eigenstate that belongs to the m th band of $H(k)$ for the parameter value k . Note that the expression of the winding number is very familiar with the Gauss-Bonnet theorem. In SSH, we have the Hamiltonian in momentum

space which reads

$$H(k) = \begin{bmatrix} 0 & v + we^{ik} \\ v + we^{-ik} & 0 \end{bmatrix} \equiv \begin{bmatrix} 0 & re^{i\theta(k)} \\ re^{-i\theta(k)} & 0 \end{bmatrix} \quad (4.66)$$

with eigenvalues $\lambda_{\pm} = \pm r$ and eigenvectors

$$|\psi_+(k)\rangle = \frac{1}{\sqrt{2}} \begin{bmatrix} e^{i\theta(k)} \\ 1 \end{bmatrix}, \quad |\psi_-(k)\rangle = \frac{1}{\sqrt{2}} \begin{bmatrix} -1 \\ e^{-i\theta(k)} \end{bmatrix} \quad (4.67)$$

such that

$$\det \left(\frac{1}{\sqrt{2}} \begin{bmatrix} e^{i\theta(k)} & -1 \\ 1 & e^{-i\theta(k)} \end{bmatrix} \right) = +1. \quad (4.68)$$

and now we calculate the Zak phase [12] for the ground state $|\psi(k)\rangle$ of the Hamiltonian as

$$\gamma = i \oint_k \langle \Gamma \psi(k) | \partial_k \psi(k) \rangle dk = \frac{1}{2} \oint_k \frac{\partial}{\partial k} \theta(k) dk. \quad (4.69)$$

Hence

$$\gamma = \frac{1}{2} \oint_k \frac{\partial \theta(k)}{\partial k} dk = \frac{\pi}{2} \left(1 - \frac{1}{\text{sign}(v-w)} \right). \quad (4.70)$$

Therefore

$$\gamma = \begin{cases} 0, & \text{if } v > w \\ \pi, & \text{if } v < w \\ \text{undefined,} & \text{if } v = w \end{cases} \implies W_{\pm} = \begin{cases} 0, & \text{if } v > w \\ 1, & \text{if } v < w \\ \text{undefined,} & \text{if } v = w \end{cases} \quad (4.71)$$

There exist other ways to calculate the winding number also. We define a unit vector $\hat{\mathbf{d}}(k)$ as $\hat{\mathbf{d}}(k) = \mathbf{d}(k)/|\mathbf{d}(k)|$ and the winding number is written as [202]

$$W = \frac{1}{2\pi} \int_{-\pi}^{\pi} \left(\hat{\mathbf{d}}(k) \times \frac{d}{dk} \hat{\mathbf{d}}(k) \right)_z dk. \quad (4.72)$$

4.5.4 Bulk-edge correspondence

We have shown the existence of edge states in the dimer limit $w = 1, v = 0$. These appear at the edges of the open chain and are robust even after turning on the intracell hopping amplitude v and remain the same in number. The total number of zero-energy states is finite, and they

are restricted to a single sublattice site (either A or B) as shown in Fig. 4.10(a), 4.10(b). If we denote the edge states on the sublattice A and B by N_A and N_B , respectively, then

$$N_A - N_B = \text{invariant} \quad (4.73)$$

i.e., the net number of edge states on the sublattice A (B) on the left (right) edge is a topological invariant [202, 229]. So, we have two topological invariants, one from the bulk part of the system, and one from the information on the edges. We have shown that both topological invariants are 0 in the trivial case $v > w$ and both are 1 in the topological case $v < w$. This is referred to as *bulk-edge correspondence*. The bulk-boundary correspondence is a physical concept that relates the topological properties of the bulk with the number of gapless edge modes. The bulk-edge correspondence for higher-dimensional systems has also been studied [230, 231].

4.6 Topological characterization in 2D systems

In 2D systems, for example in the integer quantum Hall effect, quantized Hall conductances are related to the Chern number [2, 40, 179, 232]. The Chern number is defined for two-dimensional quantum systems with periodic parameters, for example two-dimensional momentum $\mathbf{k} = (k_x, k_y)$ and is given by the integral

$$C_n = \frac{1}{2\pi} \oint_S \mathcal{F}_{12}(k) d^2k, \quad (4.74)$$

where the Berry connection $A_\mu(k)$; $\mu = 1, 2$ (for example $\mu = x, y$) and the field strength \mathcal{F}_{12} are defined as [2, 40, 179]

$$A_\mu(k) = -i \langle \psi_n(k) | \partial_\mu \psi_n(k) \rangle, \quad \mathcal{F}_{12}(k) = \partial_1 A_2(k) - \partial_2 A_1(k) \quad (4.75)$$

where $|\psi_n(k)\rangle$ is the normalized wavefunction of the n th band such that

$$H(k) |\psi_n(k)\rangle = E_n(k) |\psi_n(k)\rangle. \quad (4.76)$$

Since in a 2D system, the Hamiltonian is periodic in both directions, i.e.

$$H(k_1, k_2) = H(k_1 + 2\pi/q_1, k_2) = H(k_1, k_2 + 2\pi/q_2) \quad (4.77)$$

where q_1, q_2 are some integers (lattice constants), the Brillouin zone can be imagined as a two-dimensional torus T^2 . Now, we discuss an efficient method to calculate the Chern number for a discretized Brillouin zone using a $U(1)$ link variable [233]. The $U(1)$ link variable is defined as

$$U_n^{\hat{e}}(\mathbf{k}) \equiv \frac{\langle \psi_n(\mathbf{k}) | \psi_n(\mathbf{k} + \hat{e}) \rangle}{|\langle \psi_n(\mathbf{k}) | \psi_n(\mathbf{k} + \hat{e}) \rangle|} \quad (4.78)$$

where \hat{e} is the unit vector in the direction of either k_x or k_y and such that

$$(k_x, k_y) + \hat{e}_x = (k_x + \delta k_x, k_y), \quad (k_x, k_y) + \hat{e}_y = (k_x, k_y + \delta k_y) \quad (4.79)$$

and as shown in Fig. 4.11. Using the link variable, we can now define the field strength which would give us the Berry curvature as

$$\mathcal{F}_n(\mathbf{k}) = \frac{1}{i} \ln U_n^{\hat{e}_x}(k_x, k_y) U_n^{\hat{e}_y}(k_x + \delta k_x, k_y) U_n^{-\hat{e}_x}(k_x + \delta k_x, k_y + \delta k_y) U_n^{-\hat{e}_y}(k_x, k_y + \delta k_y). \quad (4.80)$$

The summation of all $\mathcal{F}_n(\mathbf{k})$ over the Brillouin zone will result in

$$\sum_{BZ} \mathcal{F}_n(\mathbf{k}) = 2\pi C_n \quad (4.81)$$

where C_n is the Chern number of the n th band. We use these methods to calculate the topological invariants in 1D and 2D quantum walks in the preceding chapters.

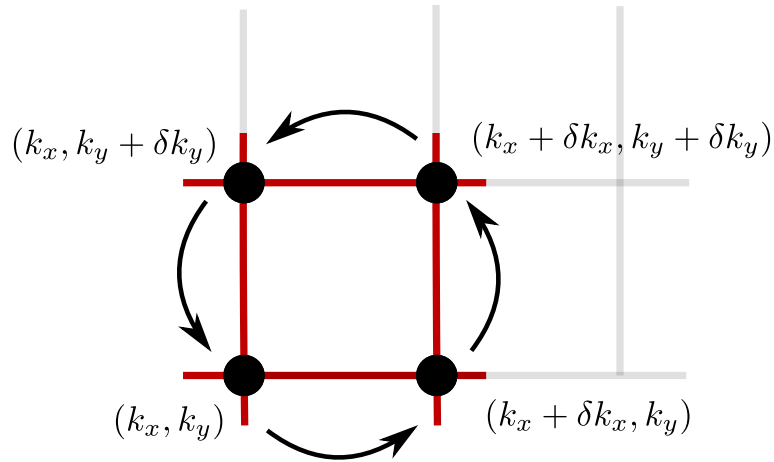


FIGURE 4.11: The calculation of the Berry curvature using the $U(1)$ -link on a discretized two-dimensional Brillouin zone. The two momenta k_x, k_y goes from 0 to $2\pi/q_x$ and 0 to $2\pi/q_y$ in a discrete step of $2\pi/q_x N_x$ and $2\pi/q_y N_y$ respectively. N_x, N_y being the total number of points in respective directions.

4.7 Topological Phases in Quantum Walk

Quantum walk Hamiltonian possesses a rich topological structure. For example, 1D SSQW with an effective Hamiltonian $H_{\text{SS}}(\theta_1, \theta_2)$ with parameters θ_1 and θ_2 [discussed in Chapter 3 in Eq. 3.33] exhibits two different topological phases characterized by the winding number $W = 0$ and $W = 1$, as shown in Fig. 4.12(a) [14, 234]. The 1D SSQW possess TRS and PHS with the choice of

$$\mathcal{T} = \sigma_x \mathcal{K}, \quad \mathcal{C} = \sigma_z \mathcal{K} \quad (4.82)$$

respectively. The presence of both TRS and PHS results in the existence of chiral symmetry, which is represented by the operator

$$\Gamma = \mathcal{C} \cdot \mathcal{T} = i\sigma_y. \quad (4.83)$$

Interestingly, the presence of two out of three (PHS, TRS, CS) symmetries in the system ensures the existence of the remaining [193, 196], which is also evident from the Table (4.1).

In order to see the existence chiral symmetry, we redefine the time evolution operator for SSQW (written in quasi-momentum space) by performing a unitary transformation which reads [235] as

$$\tilde{U}(\theta_1, \theta_2, k) \rightarrow \tilde{U}'(\theta_1, \theta_2, k) = R(\theta_1/2)T_{\downarrow}(k)R(\theta_2)T_{\uparrow}(k)R(\theta_1/2), \quad (4.84)$$

where by tilde we meant the part which acts only on the coin space. The $\tilde{U}'(\theta_1, \theta_2, k)$ is related to $\tilde{U}(\theta_1, \theta_2, k)$ as $\tilde{U}'(k) = R(\theta_1/2)\tilde{U}(\theta_1, \theta_2, k)R^{-1}(\theta_1/2)$. We shifted the origin of time so that the time-evolution operator has symmetric order of individual operators in the time direction. This is referred as time-symmetric representation [235]. The motivation behind this transformation is to show the existence of CS in 1D SSQW explicitly. In addition to that, there exists another CS time-frame in which the redefined time-evolution reads

$$\tilde{U}''(k) = R(\theta_2/2)T_{\downarrow}(k)R(\theta_1)T_{\uparrow}(k)R(\theta_2/2). \quad (4.85)$$

Using these two evolution operators, together, one can identify the two topological invariants, which are needed to completely characterize the chiral symmetric quantum walks.

The effective Hamiltonian corresponding to 2D DTQW exhibits only PHS with

$$C = \mathcal{K} \quad (4.86)$$

In Fig. 4.12(b), we plot the topological phases with Chern number $C = 0, \pm 1$ exhibited by the Hamiltonian $H_{2D}(\theta_1, \theta_2)$ for 2D DTQW [14].

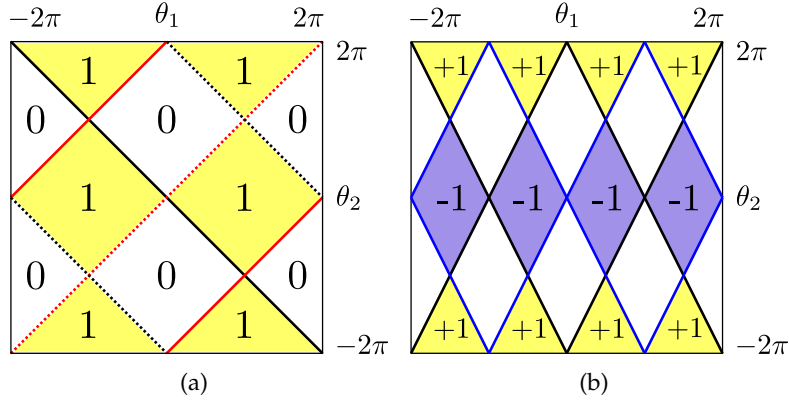


FIGURE 4.12: (Color online) (a) Different topological phases realized in 1D SSQW as a function of θ_1 and θ_2 . We observe two topological phases here corresponding to $W = 0$ and 1. Here, black and red lines represent closing of energy band at $k = 0$ and $k = \pi$, respectively, and solid and dotted lines demonstrate the closing at $E = 0$ and $E = \pi$, respectively. (b) Topological phases which exist in 2D DTQW for different values of θ_1 and θ_2 . Here, blue and black lines show the closing of energy gap at $E = 0$ and $E = \pi$, respectively. The yellow, violet and white regions correspond to $C = +1, -1$ and 0, respectively.

4.8 Real-space representation of Winding number

In an extended SSH model where losses are added at every second sublattice site (A or B), it has been shown that the average distance traveled by a particle, which was initialized at a site without losses, is quantized and is directly related to the winding number [236]. This correspondence holds for all 1D systems that exhibit chiral symmetry. This addition of the losses leads to non-Hermiticity (we will discuss it in detail in the next chapter) in systems that have already been studied in the SSH model [237, 238]. The idea to have a real space representation of winding number that serves as a topological invariant for one-dimensional systems [239]. The idea was further generalized to the systems in the presence of disorders that break translation symmetry [240]. These approaches are instrumental in experimental studies of the topological phases in various systems. In this section, we will elucidate the connection

between the average displacement and the bulk winding number. We will end the discussion by considering 1D SSQW.

We take the SSH model except that each lattice site can host $2N$ internal sites or sublattice sites. The basis in this case would be $\{|x, \sigma\rangle\}$ where $n = 1, 2, \dots, L$ lattice site, $\sigma = 1, 2, \dots, 2N$ internal state. We group internal sites into two sublattices A & B and

$$\hat{P}_A = \sum_{n \in \mathbb{Z}} \sum_{a=1}^N |n, a\rangle \langle n, a| = \mathbb{1} \otimes \sum_{a=1}^N |a\rangle \langle a| \quad (4.87)$$

with

$$\hat{P}_B = \mathbb{1} - \hat{P}_A$$

and the corresponding chiral symmetry operator is given as

$$\hat{\Gamma} = \hat{P}_A - \hat{P}_B \implies \hat{\Gamma} \hat{H} \hat{\Gamma}^{-1} = -\hat{H}.$$

As a consequence of chiral symmetry, the eigenstates come in pair $\{|n\rangle, \hat{\Gamma}|n\rangle\}$ with energy $\{-\varepsilon_n, \varepsilon_n\}$ respectively. We can correspondingly define the projectors for the lower and upper spectrum as

$$\hat{Q}_- = \sum_{n^-} |n^-\rangle \langle n^-|, \quad \hat{Q}_+ = \hat{\Gamma} \hat{Q}_- \hat{\Gamma}$$

with

$$\hat{Q} = \hat{Q}_+ - \hat{Q}_- \quad (4.88)$$

The presence of chiral symmetry allows the system to have non-trivial topology which is characterized by the winding number in real space representation given by [239, 240]

$$W = -\frac{1}{L} \text{tr} \{ \hat{P}_B \hat{Q} \hat{P}_A [\hat{X}, \hat{P}_A \hat{Q} \hat{P}_B] \}$$

where $\hat{X} \equiv \sum_x \sum_{c=1}^{2N} x |x, c\rangle \langle x, c|$ is the position operator. Now to detect the winding number, we localize the particle at sublattice A and introduce weak partial measurement after each time step to measure the position of the particle at sublattice B only (which is why partial measurement). Mathematically, such a weak measurement can be modeled with a non-unitary operator M_1 given by

$$\hat{M}_1 = \hat{P}_A + \sqrt{1 - p_M} \hat{P}_B. \quad (4.89)$$

where p_M is the measurement strength such that $0 \leq p_M \leq 1$. Here, the second operator is given by $\hat{M}_2 = \sqrt{p_M} \hat{P}_B$ such that

$$M_1^\dagger M_1 + M_2^\dagger M_2 = \mathbb{1}. \quad (4.90)$$

When this measurement yields a positive result, i.e., when the particle is detected at the site B with conditional probability p_M , we stop the evolution. However, if the measurement yields a negative result when the particle is not detected, we will have the time evolution followed by the next measurement. The wave function after the j steps reads as follows

$$|\psi(t = jT)\rangle = \hat{U}[\hat{M}_1 \hat{X}]^{j-1} |\psi(0)\rangle.$$

The probability of finding the particle at $|y, b\rangle$ after j steps, initially localized at $|x, a\rangle$ is given by

$$s_{(x,a) \rightarrow (y,b)}(j) = p_M |\langle y, b | \psi(t = jT)\rangle|^2 \quad (4.91)$$

Basically, we have \hat{M}_2 at the j th step, due to which we get a factor p_M and it projects the state in the B sublattice, which is responsible for the inner product with $|y, b\rangle$ in the expression above. The average displacement is then defined as

$$\langle \Delta x \rangle_{(x,a)} \equiv \sum_{j=\mathbb{N}} \sum_{y=1}^L (y-x) \sum_{b=2N+1}^{2N} s_{(x,a) \rightarrow (y,b)}(j) \quad (4.92)$$

and to get a more general expression valid for any arbitrary N we sum over all the initial states $|x, a\rangle$ and write

$$\langle \langle \Delta x \rangle \rangle \equiv \frac{\sum_{x,a} \langle \Delta x \rangle_{(x,a)}}{NL} = \frac{1}{NL} \sum_{x,a} \sum_{j=\mathbb{N}} \sum_{y=1}^L (y-x) \sum_{b=2N+1}^{2N} s_{(x,a) \rightarrow (y,b)}(j) \quad (4.93)$$

It can be solved further to write it in a compact form as [236]

$$\langle \langle \Delta x \rangle \rangle = -\frac{2}{NL} \text{tr}(\hat{X} \hat{\Gamma} \hat{Q}_-) \quad (4.94)$$

with

$$\hat{\Gamma} = \hat{P}_A - \hat{P}_B = \sum_{x=1}^L \left[\sum_a |x, a\rangle \langle x, a| - \sum_b |x, b\rangle \langle x, b| \right].$$

and after simplifying it further, we arrive at the very interesting connection between the aver-

age displacement and the topological invariant, winding number in this case, which reads

$$\langle\langle\Delta x\rangle\rangle = \frac{W}{N}. \quad (4.95)$$

As an example, we consider the SSQW quantum walk where $N = 1$ as described in the previous chapter. The time evolution is governed by the following unitary operator

$$U(\theta_1, \theta_2) = R(\theta_1/2)T_\downarrow R(\theta_2)T_\uparrow R(\theta_1/2) \quad (4.96)$$

The chiral symmetry operator is given by

$$\Gamma = \sigma_x \otimes \mathbf{1} \quad (4.97)$$

which decides the sublattices corresponding to the internal states

$$|\pm\rangle = \frac{|\uparrow\rangle \pm |\downarrow\rangle}{\sqrt{2}}. \quad (4.98)$$

Initially the particle is localized at $|\psi_0\rangle = |-\rangle \otimes |0\rangle$ and we remove the particle if it is detected at $|+\rangle$. This is realized by the operator

$$\hat{M} = |-\rangle\langle -| \otimes \mathbf{1}. \quad (4.99)$$

We plot the average displacement of the walker after $M = 200$ number of steps in Fig. 4.13 for two different settings of θ_2 . We can clearly observe the quantized behavior of the average displacement, which exactly coincides with the winding number. This approach has already been used to measure the winding number in experimental settings [241–244].

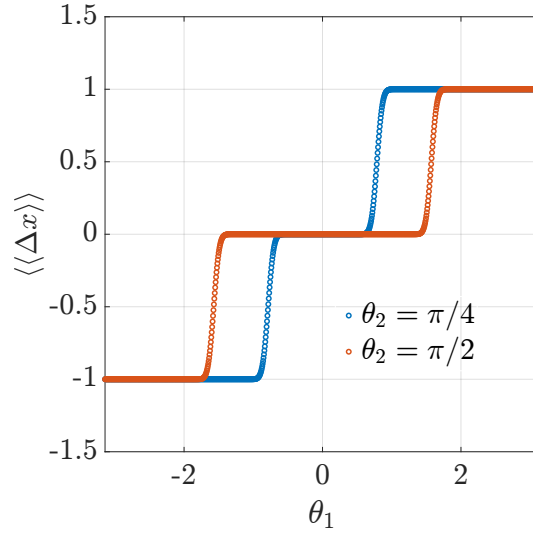


FIGURE 4.13: Plot of the average displacement of the walker, initially localized at $|-\rangle \otimes |0\rangle$, as a function of θ_1 after $M = 200$ steps for two different values of θ_2 . The number of sites L are taken to be 51.

4.9 Gauss-Bonnet theorem

As we discussed in the beginning of this chapter, the Gauss-Bonnet theorem reads

$$\int_S \kappa dA = 4\pi(1 - g) \quad (4.100)$$

where

$$\kappa = \frac{1}{r_1 r_2} = \text{Gaussian curvature,}$$

$g = \text{genus (\# of holes).}$

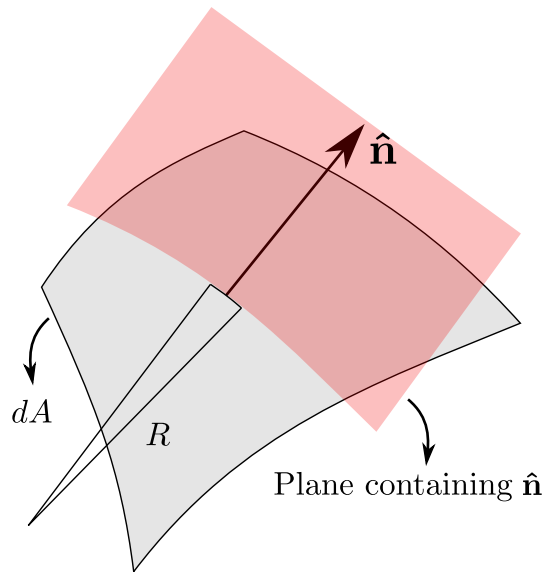


FIGURE 4.14: Gaussian curvature.

If we consider a surface element dA and a unit vector \hat{n} . The intersection of a plane containing the unit vector and dA gives a 1D curve that can be approximated by a circle of radius R (as shown in Fig. 4.14). r_1 and r_2 are the principal curvatures and are defined as

$$r_1 = \min(R), r_2 = \max(R) \quad (4.101)$$

This particular form of the Gauss-Bonnet theorem is applicable for "closed" surfaces. We can also write a more generic form of it, which can be used for open surfaces, too.

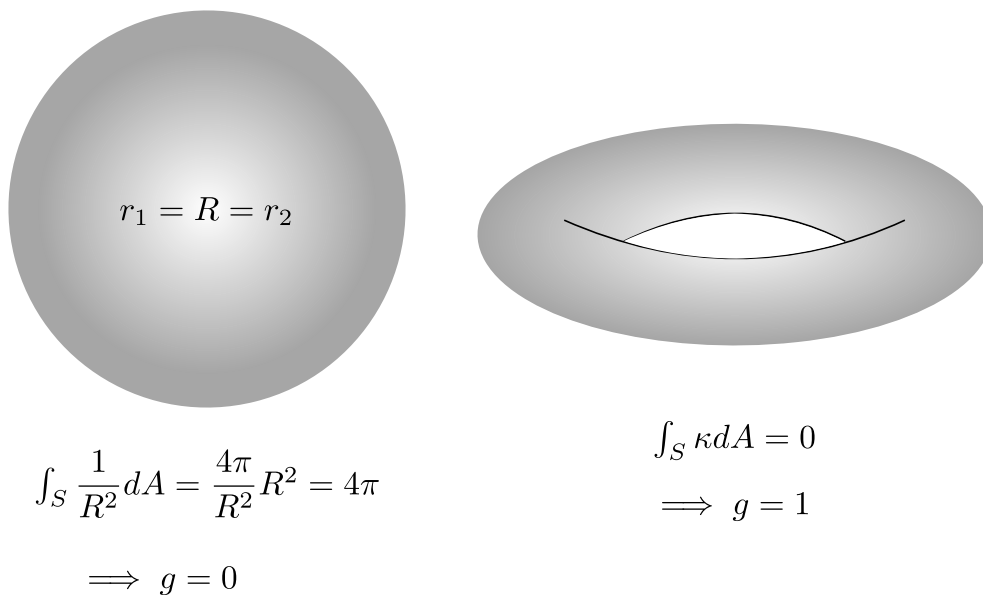


FIGURE 4.15: Explaining Gaussian curvature.

In case of torus (T^2), we have positive and negative that will add up to zero. The integral is invariant under any smooth transformations or disorder in the system.

Chapter 5

Non-Hermitian Systems

In conventional quantum mechanics, in order to have a real spectrum (eigenvalues) and unitary evolution (probability conservation), we demand that the physical observables of a closed quantum system should be represented by hermitian operators [35]. However, in practical situations, our system is coupled to an environment, or at least with a measuring device, which leads to non-unitary dynamics and non-Hermitian observables, especially Hamiltonian. In such systems, we resort to the master equation of formalism [245, 246]. In 1998, Bender *et al.* proposed a class of Hamiltonians that exhibit real spectrum despite the fact that they are non-Hermitian [247, 248]. This novel class of Hamiltonians has an additional property which is that they respect the combined time-reversal (\mathcal{T}) and parity (\mathcal{P}) symmetry and are called \mathcal{PT} symmetric Hamiltonian. The parity \mathcal{P} is a unitary operator that reverses the position as $x \rightarrow -x$. On the other hand, the time reversal operator \mathcal{T} is an anti-unitary operator that reverses the arrow of time, i.e., $t \rightarrow -t$ (we discussed it in detail in Chapter 4). Therefore, a Hamiltonian H is said to be \mathcal{PT} -symmetric if

$$(\mathcal{PT})H(\mathcal{PT})^{-1} = H. \quad (5.1)$$

Basically, when \mathcal{PT} operator commutes with the Hamiltonian H . Due to the anti-linear nature of the \mathcal{PT} operator, even if the Hamiltonian H commutes with the operator \mathcal{PT} , they need not necessarily share the same set of eigenvectors. Note that the Hamiltonian can satisfy Eq. (5.1) even when it does not possess these symmetries individually. In addition to the existence of an anti-unitary operator \mathcal{PT} , we demand that the \mathcal{PT} operator and the non-Hermitian Hamiltonian must have the same set of eigenvectors. Together, these two conditions are suf-

efficient to ensure the real spectrum of the Hamiltonian [249–253]. Furthermore, the notion of pseudo-hermiticity was introduced to show that all the Hamiltonian with a real spectrum are pseudo-hermitian [254–257]. A given Hamiltonian is pseudo-hermitian with respect to a metric η if [254]

$$H^\dagger = \eta H \eta^{-1}. \quad (5.2)$$

It has also been argued that \mathcal{PT} -symmetry is a necessary and sufficient condition for unitary time evolution [258]. Since then, there have been numerous studies, theoretical and experimental both, where \mathcal{PT} symmetric systems have been realized [259–268]. Recently, non-Hermitian systems have been used in quantum information masking [269]. Motivated by these studies, the notion of topological phases has been extended to non-Hermitian systems [270–278] and a bulk-boundary correspondence has also been proposed with the presence of a non-Hermitian skin effect [271, 279–282] and exceptional points [283, 284]. The exceptional points are sort of degeneracies of a non-Hermitian system, where the real parts and the corresponding imaginary parts of certain eigenvalues coincide and the eigenvectors coalesce [285]. The most fundamental model, the SSH model (which we discussed in the last chapter in detail), has been extended to include non-hermiticity [286–289]. The topological features of the periodically driven non-Hermitian SSH model was also introduced [290]. Further, a geometrical interpretation of topological invariant is provided for non-hermitian systems [291]. In this chapter we will discuss how non-hermiticity results in symmetry ramification, then we discuss non-Hermitian 1D SSQW and conclude with a discussion on exceptional points.

5.1 Symmetry ramification and unification in non-Hermitian systems

In the last chapter we discussed that particle-hole symmetry for the Hermitian systems is represented by an anti-unitary operator, \mathcal{C} which satisfies

$$\mathcal{C}H\mathcal{C}^{-1} = -H \implies U_{\mathcal{C}}H^*U_{\mathcal{C}}^{-1} = -H \quad (5.3)$$

where we have used the fact that any anti-unitary operator can be written as $\mathcal{C} = U_{\mathcal{C}}\mathcal{K}$. Here, $U_{\mathcal{C}}$ is a unitary matrix and \mathcal{K} is the complex conjugation operator. Since H is hermitian, we have

$$H = H^\dagger \implies H^T = H^*$$

and the relation in Eq. (5.3) is equivalent to

$$CH^TC^{-1} = -H. \quad (5.4)$$

However, Eqs. (5.3) and (5.4) are not equivalent for a non-Hermitian system. We see similar kind of symmetry ramification in other symmetries as well. For example, chiral symmetry is represented by a unitary operator Γ and for Hermitian systems it is defined as

$$\Gamma H \Gamma^{-1} = -H. \quad (5.5)$$

For Hermitian system, Eq. (5.5) is equivalent to

$$\Gamma H \Gamma^{-1} = -H^\dagger \quad (5.6)$$

however, Eqs. (5.5) and (5.6) are not same for non-Hermitian systems. Due to the distinction between the complex conjugation and the transposition in non-Hermitian systems, we see such ramifications and unification in symmetries which decides the topological classes as discussed in the last Chapter 4. As a consequence, 10-fold classification is no longer valid and we will have 38-fold classification [274]. For our purpose, we are only interested on Chiral symmetry and we will show our system exhibits CS and satisfies Eq. (5.6) even in the non-Hermitian regime.

5.2 Non-unitary/Non-hermitian Quantum Walk

Generally, quantum walk dynamics is given by a unitary time evolution operator. However, limitations in physical implementation and the environmental effects can cause losses which can cause the dynamics to deviate from unitary nature. In general, one can extend 1D SSQW to a non-unitary quantum walk by introducing a scaling (or gain/loss) operator, G_i and a phase operator, Φ_i [292], with tunable parameters in the dynamics. The resulting time evolution operator for a non-unitary quantum walk can be written as

$$U = T_\downarrow G_2 \Phi_2 R(\theta_2) T_\uparrow G_1 \Phi_1 R(\theta_1) \quad (5.7)$$

with

$$G_i = \sum_n \tilde{G}_{i,n} \otimes |n\rangle\langle n| ; \quad \tilde{G}_{i,n} = \begin{pmatrix} g_{i,\uparrow}(n) & 0 \\ 0 & g_{i,\downarrow}(n) \end{pmatrix} \quad (5.8)$$

$$\Phi_i = \sum_n \tilde{\Phi}_{i,n} \otimes |n\rangle\langle n| ; \quad \tilde{\Phi}_{i,n} = \begin{pmatrix} \phi_{i,\uparrow}(n) & 0 \\ 0 & \phi_{i,\downarrow}(n) \end{pmatrix}. \quad (5.9)$$

5.2.1 Homogeneous system

For the homogeneous system, all the operators are n independent i.e. $\{\tilde{R}(\theta_{i,n}), \tilde{G}_{i,n}, \tilde{\Phi}_{i,n}\}$ become $\{\tilde{R}(\theta_i), \tilde{G}_i, \tilde{\Phi}_i\}$ and are given by

$$\tilde{G}_2 = \tilde{G}_1^{-1} = \tilde{G} = \begin{pmatrix} e^\gamma & 0 \\ 0 & e^{-\gamma} \end{pmatrix} = e^{\gamma\sigma_z} \quad (5.10)$$

$$\tilde{\Phi}_2 = \tilde{\Phi}_1 = \tilde{\Phi} = \begin{pmatrix} e^{i\phi} & 0 \\ 0 & e^{-i\phi} \end{pmatrix} = e^{i\phi\sigma_z} \quad (5.11)$$

where σ_z is the Pauli z matrix in computational basis. The time evolution operator in Eq. (5.7) reads

$$U = T_\downarrow G \Phi R(\theta_2) T_\uparrow G^{-1} \Phi R(\theta_1) \quad (5.12)$$

With the initial state $|\psi(0)\rangle$, the state after t time step will be [293]

$$|\psi(t)\rangle = U^t |\psi(0)\rangle = \sum_{n,s=\uparrow,\downarrow} C_{n,s}(t) |n\rangle \otimes |s\rangle \quad (5.13)$$

where $C_{n,s}(t)$'s are the normalized probability amplitudes. We can now write the eigenvalue equation to define the quasienergy as

$$U |\psi_\lambda\rangle = \lambda |\psi_\lambda\rangle ; \quad \lambda = e^{i\varepsilon}. \quad (5.14)$$

For a unitary quantum walk $|\lambda| = 1$ and ε is real. For the case $\phi = 0$, we have

$$U_{\text{SS}}^{\text{NU}} = T_\downarrow G_2 R(\theta_2) T_\uparrow G_1 R(\theta_1), \quad (5.15)$$

with

$$G_2 = G_1^{-1} = G_\gamma = \begin{pmatrix} e^\gamma & 0 \\ 0 & e^{-\gamma} \end{pmatrix} \otimes \mathbb{1}. \quad (5.16)$$

The above choice of operators is motivated by the experimental setup used in [264]. The factor γ is known as the loss and gain factor as the operator G results in increasing (decreasing) the amplitude of spin-up (down). The time evolution operator for the non-unitary 1D SSQW becomes

$$U_{\text{SS}}^{\text{NU}} = T_\downarrow G_\gamma R(\theta_2) T_\uparrow G_\gamma^{-1} R(\theta_1). \quad (5.17)$$

This particular choice of the scaling operator leaves the translational symmetry of the quantum walk intact. Hence, the dynamical operator can be block diagonalized in the momentum basis as

$$U_{\text{SS}}^{\text{NU}} = \sum_k \tilde{U}_{\text{SS}}^{\text{NU}}(k) \otimes |k\rangle\langle k|, \quad (5.18)$$

where

$$\tilde{U}_{\text{SS}}^{\text{NU}}(k) = T_\downarrow(k) G_\gamma R(\theta_2) T_\uparrow(k) G_\gamma^{-1} R(\theta_1), \quad (5.19)$$

with $T_\downarrow(k) = e^{ik(\sigma_z - \mathbb{1})/2}$, $T_\uparrow(k) = e^{ik(\sigma_z + \mathbb{1})/2}$ and it acts only on the coin part. The corresponding generator or an effective Hamiltonian $H_{\text{NU}}(\theta_1, \theta_2, \gamma)$ reads

$$H_{\text{NU}}(\theta_1, \theta_2, \gamma) = \bigoplus_k E(k) \hat{\mathbf{n}}(k) \cdot \sigma, \quad (5.20)$$

with quasi-energy

$$\cos E(k) = \cos(\theta_1/2) \cos(\theta_2/2) \cos k - \sin(\theta_1/2) \sin(\theta_2/2) \cosh 2\gamma, \quad (5.21)$$

and $\hat{\mathbf{n}} = n_x(k)\hat{\mathbf{i}} + n_y(k)\hat{\mathbf{j}} + n_z(k)\hat{\mathbf{k}}$ with

$$\begin{aligned} n_x(k) &= \frac{\sin(\theta_1/2) \cos(\theta_2/2) \sin k - i \cos(\theta_1/2) \sin(\theta_2/2) \sinh 2\gamma}{\sin E(k)}, \\ n_y(k) &= \frac{\sin(\theta_1/2) \cos(\theta_2/2) \cos k + \cos(\theta_1/2) \sin(\theta_2/2) \cosh 2\gamma}{\sin E(k)}, \\ n_z(k) &= \frac{-\cos(\theta_1/2) \cos(\theta_2/2) \sin k - i \sin(\theta_1/2) \sin(\theta_2/2) \sinh 2\gamma}{\sin E(k)}. \end{aligned} \quad (5.22)$$

Note that for $\gamma \neq 0$, G and $U_{\text{ss}}^{\text{NU}}$ are no longer unitary operators and the norm of the state in evolution may not be preserved. Consequently, $H_{\text{NU}}(\theta_1, \theta_2, \gamma)$ is not Hermitian, but we still have a real spectrum up to a certain critical value of $\gamma = \gamma_c$. Given the fact that the energy band closes at $k = 0, E = 0$ and from Eq. (5.21) we have an expression for γ_c which reads

$$\gamma_c = \frac{1}{2} \cosh^{-1} \left[\frac{\cos(\theta_1/2) \cos(\theta_2/2) - 1}{\sin(\theta_1/2) \sin(\theta_2/2)} \right]. \quad (5.23)$$

The argument of \cosh^{-1} in the above equation is positive (or negative) when θ_1 and θ_2 have the opposite (or same) sign. The negative argument results in a complex value of γ_c . Therefore, γ can be complex in general and it would be convenient to use the form given by $\gamma = a + ib$. We observe that the negative argument of \cosh^{-1} results in a critical value of $b, \pi/2$. It amounts to shifting $k \rightarrow k + \pi/2$, leaving all the results unaffected. Therefore, we restrict ourselves to the case when γ_c is real, i.e., opposite signs for θ_1 and θ_2 and refer γ as the scaling factor. The γ_c is the point where the exact \mathcal{PT} -symmetry of the system breaks spontaneously (also known as the exceptional point [283]), and we will have complex energies for $\gamma > \gamma_c$. We plotted quasi-energy Eq. (5.21) and the eigenvalues of the unitary operator Eq. (5.19) as a function of k and for several values of γ in Fig. (5.1). We can clearly see that the spectrum of quasi-energy becomes imaginary for values of $\gamma > \gamma_c$ and the eigenvalues of the unitary operator do not constrain to the circle of unit radius. We plot the time evolution of sum of probability distribution $P(t)$ (norm)

$$P(t) = \sum_n |C_n(t)|^2 \quad (5.24)$$

and the probability distribution

$$|C_n(t)|^2 = |C_{n,\uparrow}(t)|^2 + |C_{n,\downarrow}(t)|^2 \quad (5.25)$$

in Fig. (5.2) for different values of the scaling parameter γ . Till the critical point γ_c we see that the time evolution is not very different from that of unitary quantum walk and we observe that the norm of the wavefunction oscillates around as shown in Fig. 5.2(b). However, at the critical or exceptional point γ_c , the situation changes very drastically and we see linear growth and beyond the point γ_c we observe exponential growth as shown in Fig. 5.2(c) and 5.2(d), respectively. Also, the time evolution beyond the exceptional point can be approximated by the Gaussian distribution centered around the initial position [Fig. 5.2(d)].

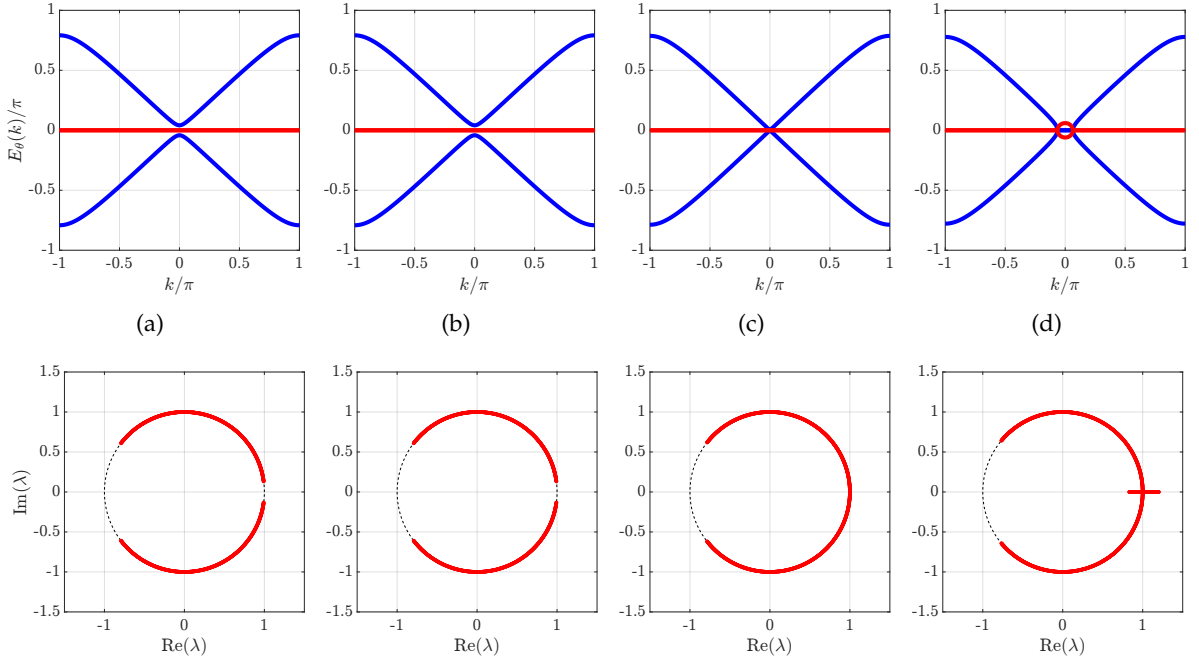


FIGURE 5.1: The quasienergy for $\theta_1 = \pi/4, \theta_2 = -\pi/6$, and $\phi = 0$. In top row, the blue (red) corresponds to real (imaginary) part of the quasienergy, whereas in the bottom row we have eigenvalues of the unitary operator Eq. (5.19) on a unit circle. (a) $e^\gamma = 1$, (b) $e^\gamma = 1.1$, (c) $e^\gamma = e^{\gamma_c}$, (d) $e^\gamma = 1.4$.

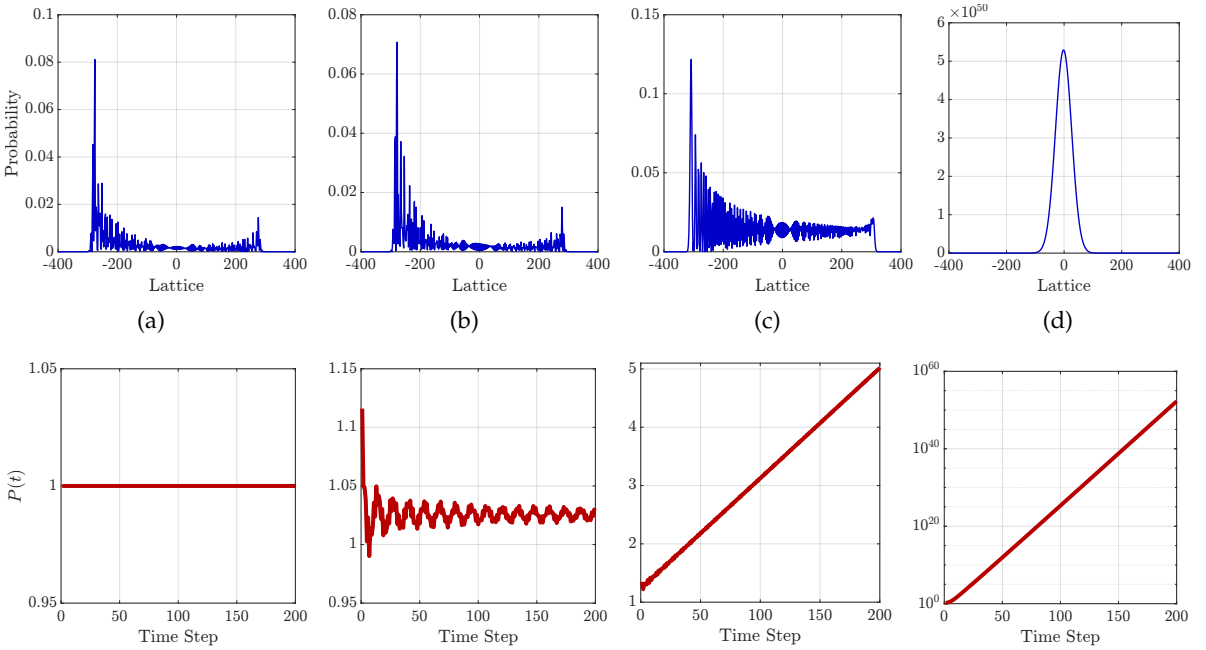


FIGURE 5.2: Probability distribution of the walker initially localized at the origin and with the symmetric state of the coin for $\theta_1 = \pi/4, \theta_2 = -\pi/6$ after 200 steps in top row. In bottom row we plot the time evolution of the norm for different settings of γ . (a) $e^\gamma = 1$, (c), $e^\gamma = 1.1$ $e^\gamma = e^{\gamma_c}$, (d) $e^\gamma = 1.4$. The system size is taken to be $N = 400$.

5.3 Physics of degenerate and exceptional points

Here, we illustrate the difference between degenerate points and exceptional points by considering an explicit example. Let us take a non-symmetric matrix [294]

$$H(\beta) = \begin{pmatrix} 0 & 1 & 1 \\ 1 & 0 & 1 \\ \beta & 1 & 0 \end{pmatrix} \quad (5.26)$$

which has the following eigenvalues

$$E_1 = -1, E_{\pm} = \frac{1}{2} \left(1 \pm \sqrt{5 + 4\beta} \right). \quad (5.27)$$

Here we observe that E_1 and E_- become degenerate for $\beta = 1$ and the corresponding orthonormal vectors will be

$$E_- = -1, \quad |E_-\rangle = \frac{1}{\sqrt{2}} \begin{pmatrix} -1 \\ 0 \\ 1 \end{pmatrix}, \quad E_1 = -1, \quad |E_1\rangle = \frac{1}{\sqrt{2}} \begin{pmatrix} -1 \\ 1 \\ 0 \end{pmatrix},$$

$$E_+ = 2, \quad |E_+\rangle = \frac{1}{\sqrt{3}} \begin{pmatrix} 1 \\ 1 \\ 1 \end{pmatrix}. \quad (5.28)$$

The symmetric matrix $H(1)$ exhibits 3 linearly independent eigenvectors and can be diagonalized by a matrix S formed by the three eigenvectors such that

$$S^{-1}H(1)S = \begin{pmatrix} 2 & 0 & 0 \\ 0 & -1 & 0 \\ 0 & 0 & -1 \end{pmatrix}, \quad S = \{|E_+\rangle, |E_-\rangle, |E_1\rangle\}. \quad (5.29)$$

This degeneracy is what we generally come across in quantum mechanics.

However, the eigenvalues E_+ and E_- coalesce at $\beta = -5/4$. The real and imaginary parts of the eigenvalues are plotted in Fig. (5.3). The eigenvalues become complex for $\beta < -5/4$ as

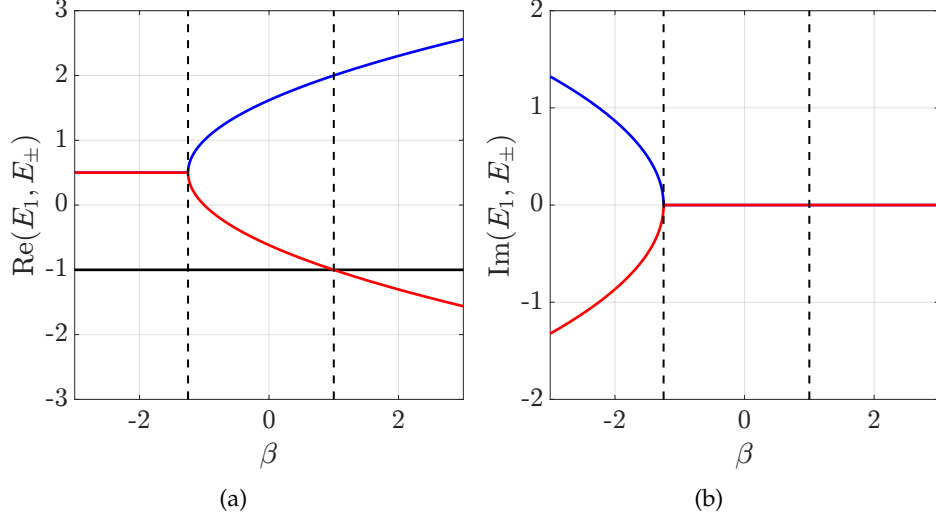


FIGURE 5.3: Real (a) and imaginary (b) part of the eigenvalues are plotted with the parameter β . The blue and red corresponds to E_+ and E_- respectively.

shown in Fig. (5.3). The Hamiltonian $H(-5/4)$ has the eigensystem given by

$$\begin{aligned}
 E_- = E_+ = 1/2, \quad |E_{\pm}\rangle &= \frac{1}{3} \begin{pmatrix} -2 \\ -2 \\ 1 \end{pmatrix}, \\
 E_1 = -1, \quad |E_1\rangle &= \frac{1}{\sqrt{2}} \begin{pmatrix} 0 \\ -1 \\ 1 \end{pmatrix}.
 \end{aligned} \tag{5.30}$$

We note here that $H(-5/4)$ exhibit only two linearly independent vectors and $H(-5/4)$ is no longer diagonalizable because S^{-1} does not exist. Therefore, coalescence is different from degeneracy because at the exceptional point there is only one linearly independent eigenvector. It is sometimes referred to as non-Hermitian degeneracy as opposed to Hermitian degeneracy.

Chapter 6

Persistence of Topological Phases in Non-Hermitian Quantum Walk

In this work we introduce non-Hermiticity and establish the *persistent* nature of topological phases in non-Hermitian quantum walks [295]. We show that the topological nature of the underlying Hamiltonian does not change in the lossy environment within certain limits. We show that in 1D SSQW the topological phase persists as long the system possess exact \mathcal{PT} -symmetry. In the case of a 2D quantum walk, such correspondence between the topological order and the \mathcal{PT} -symmetry is missing. In this systems, an interesting observation is the loss-induced topological phase transition, which is absent in the 1D case.

6.1 Symmetries of the Hamiltonian

The system under consideration is quantum walk which is performed on position space with the aid of coin states. Since, the time evolution operator $U(k)$ is block diagonal in the momentum space i.e. $U(k) = \sum_k \tilde{U}(k) \otimes |k\rangle\langle k|$ and $U(k) = e^{-iH(k)}$, we write the condition for $\tilde{U}(k)$ in order to have \mathcal{PT} symmetry as

$$(\tilde{\mathcal{P}}\tilde{\mathcal{T}})\tilde{U}(k)(\tilde{\mathcal{P}}\tilde{\mathcal{T}})^{-1} = \tilde{U}^{-1}(k), \quad (6.1)$$

where the operators $\tilde{\mathcal{P}}, \tilde{\mathcal{T}}$ act only on the coin Hilbert space.

In the case of non-Hermitian 1D SSQW, $\tilde{U}(k)$ given in Eq. (5.19) satisfies the above mentioned conditions with the choice of $\tilde{\mathcal{P}} = \sigma_y$ and $\tilde{\mathcal{T}} = \sigma_x \mathcal{K}$ such that the combined operator becomes $\tilde{\mathcal{P}}\tilde{\mathcal{T}} = i\sigma_z \mathcal{K}$ and we have

$$\sigma_z \tilde{U}^* \sigma_z^{-1} = \tilde{U}^{-1}(k), \quad (6.2)$$

where \mathcal{K} is the complex conjugation operator. Therefore, the 1D SSQW is \mathcal{PT} -symmetric for all the values of δ (and γ). However, at the exceptional point [283] γ_c , the eigenstates and eigenvectors become degenerate. Beyond this point, the eigenvectors of the Hamiltonian and the \mathcal{PT} operator are not the same [292]; hence the system no longer possesses exact- \mathcal{PT} -symmetry, which results in a complex spectrum, as shown in the previous section.

Next we discuss the particle hole symmetry (PHS) represented by an antiunitary operator Ξ , and the chiral symmetry (CS) represented by a unitary operator Γ for the time evolution operator and they read [296]

$$\Xi U(k) \Xi^{-1} = U(-k), \quad (6.3)$$

$$\Gamma U(k) \Gamma^{-1} = U^\dagger(k). \quad (6.4)$$

We redefine the time evolution operator given in Eq. (5.19) by performing a unitary transformation which reads [235]

$$\tilde{U}'(k) = R(\theta_1/2) T_\downarrow(k) G_\delta R(\theta_2) T_\uparrow(k) G_\delta^{-1} R(\theta_1/2), \quad (6.5)$$

which is related to $\tilde{U}_{\text{SS}}^{\text{NU}}(k)$ as $\tilde{U}'(k) = R(\theta_1/2) \tilde{U}_{\text{SS}}^{\text{NU}}(k) R^{-1}(\theta_1/2)$. This is done to make the evolution operator symmetric in time and known as time-symmetric representation. The motivation behind this transformation is to show the existence of CS and PHS in non-Hermitian 1D SSQW explicitly. We can clearly see that $\tilde{U}'(k)$ satisfies Eq. (6.3) and Eq. (6.4) with the choice of $\Gamma = \sigma_x$ and $\Xi = \mathcal{K}$. Hence, with the existence of these symmetries, $\tilde{U}_{\text{SS}}^{\text{NU}}(k)$ belongs to a symmetry class (BDI[†] [296]) which supports \mathbb{Z} topological invariant. Note, we can also define another time-symmetric that reads [241]

$$\tilde{U}''(k) = R(\theta_2/2) T_\downarrow(k) G_\delta R(\theta_1) T_\uparrow(k) G_\delta^{-1} R(\theta_2/2). \quad (6.6)$$

For the current purpose, we consider only the $\tilde{U}'(k)$ to define the topological invariants and

see the persistence of with the introduction of gain and loss.

6.2 Results

In this section, we study the behavior of the topological phases in 1D SSQW and 2D DTQW by introducing a nonzero scaling factor γ which, essentially, makes the system non-Hermitian. In 1D SSQW, we find that the topological phases are unaffected even when the system is non-Hermitian (i.e., $\gamma \neq 0$), as far as the system possesses a real spectrum following the exact \mathcal{PT} -symmetry. However, the topological nature of the system vanishes as we cross the exceptional point γ_c , which means the quantity W becomes a non-integer number which decays asymptotically to zero for $\gamma > \gamma_c$. We observe the persistence of the Chern number C in 2D DTQW as well until the scaling factor γ reaches a critical value. However, unlike the 1D case, we cannot associate exact \mathcal{PT} -symmetry breaking with the point where the topological phase transition happens due to the absence of the \mathcal{PT} -symmetry in 2D DTQW. Since the \mathcal{PT} -symmetry is absent in 2D DTQW even in the unitary region, we can not associate the persistence of the topological phase with this particular symmetry. Furthermore, we observe a loss-induced topological phase transition in 2D DTQW.

6.2.1 Topological phases in 1D non-unitary quantum walk

We start our analysis with non-unitary 1D SSQW, with the associated non-Hermitian Hamiltonian $H_{\text{NU}}(\theta_1, \theta_2, \gamma)$ being given in (5.20). Since the Hamiltonian is traceless for all values of γ , the corresponding eigenvalues will always be of the form of $\pm E(k)$. For each momentum k , we compute the energy eigenstates $|\psi_{\pm}(k)\rangle$ corresponding to energies $\pm E(k)$ and, we call the set $\{|\psi_{-}(k)\rangle\}$ and $\{|\psi_{+}(k)\rangle\}$ as the lower and upper energy bands, respectively. Using the expression for the winding number W from (4.65), we calculate the winding numbers for the lower and upper bands and we name them as W_{-} and W_{+} , respectively.

Since the eigenstates and eigenvalues depend on γ , θ_1 and θ_2 , the winding numbers are also expected to depend upon these parameters. In Fig. 6.2, we plot the winding number for the lower band W_{-} as a function of γ and θ_2 for different values of θ_1 . In all figures, we notice that for $\gamma = 0$, the winding number can take two different values, zero and one, depending

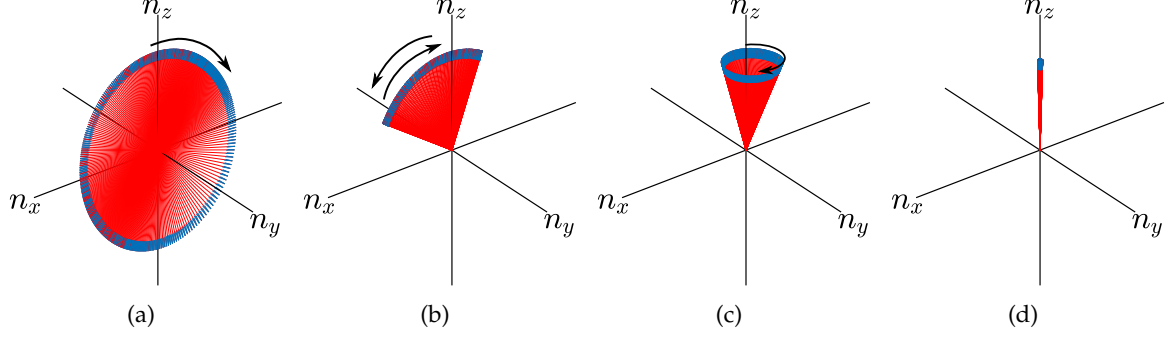


FIGURE 6.1: (Color online) Winding of the Bloch vector around the origin with the lattice size, $N = 201$ (a) $\theta_1 = -3\pi/8$, $\theta_2 = \pi/8$, $\gamma = 0.25$ (b) $\theta_1 = -3\pi/8$, $\theta_2 = 5\pi/8$, $\gamma = 0.25$ (c) $\theta_1 = -3\pi/8$, $\theta_2 = \pi/8$, $\gamma = 1.8$ (d) $\theta_1 = -3\pi/8$, $\theta_2 = \pi/8$, $\gamma = 3.0$.

on the choice of θ_1 and θ_2 . Focusing on the case of $W_- = 1$ for a vanishing γ , we observe that for a given (θ_1, θ_2) if we increase the value of γ , the winding number remains unaffected until we approach the critical value of γ , i.e., γ_c (5.23). Crossing the γ_c causes a phase transition and the value of W starts decreasing and approaches zero asymptotically. Whereas, if initially the winding number $W_- = 0$, it remains zero until we approach γ_c , and then it starts to increase momentarily approaching some maximum value and then deteriorates to zero asymptotically.

By definition, the winding number is an integer quantity. In other words, the geometric phase acquired by the eigenstates of the Hamiltonian in the k -space is quantized and is a multiple of π , which is possible only when all the states in an energy band lie in a plane on the Bloch sphere. The winding number must always be an integer for all the Hermitian Hamiltonians. However, beyond the exceptional points, W acquires non-integer values, hence it does not qualify as the winding number. This non-integer value of W can be explained by observing the behaviour of the eigenstates of the non-Hermitian Hamiltonian. In Fig. 6.1, we plot the Bloch vectors corresponding to the eigenstates $|\psi_-(k)\rangle$ of the Hamiltonian $H_{\text{NU}}(\theta_1, \theta_2, \gamma)$ on the Bloch sphere. In Fig. 6.1(a), the Bloch Vector moves in the clockwise direction and comes back to the same point, winding around the origin once resulting in $W = 1$. However, in Fig. 6.1(b), it first goes clockwise and reverses its direction, and; therefore, $W = 0$. Figs. 6.1(a) and 6.1(b) are for $\gamma \leq \gamma_c$ whereas Figs. 6.1(c) and 6.1(d) are for $\gamma > \gamma_c$. The animation of Bloch vectors can be found in the Supplementary Material online. We can clearly see that in the exact \mathcal{PT} -symmetric region, the eigenstates lie in a plane and results in an integer value of W , whereas in the exact \mathcal{PT} -symmetry broken region the eigenvectors trace a path which lies outside the plane. Hence geometric phase is not a multiple of π resulting in a non-integer value of W .

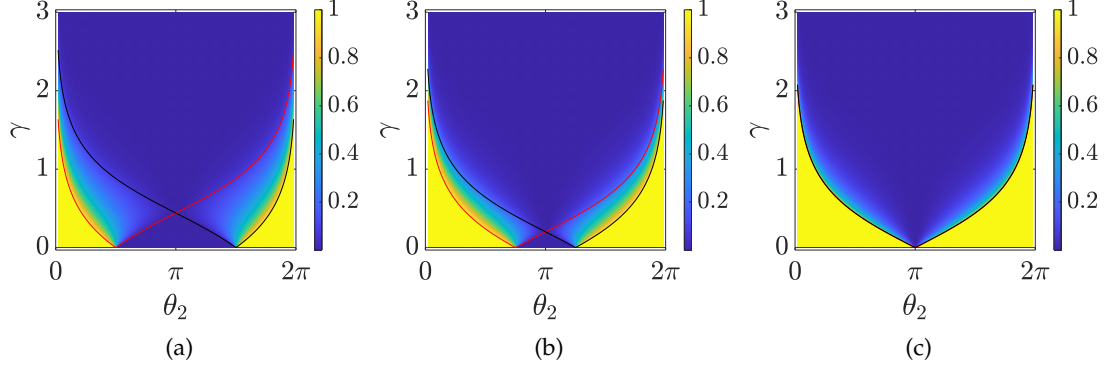


FIGURE 6.2: (Color online) Plot for W_- for lower energy band as a function of γ and θ_2 , and (a) $\theta_1 = -\pi/2$ (b) $\theta_1 = -3\pi/4$ (c) $\theta_1 = -\pi$. The system size is taken to be $N = 201$. The red and black lines in all of the panels represent γ_c for $(k, E) = (0, 0)$ and $(k, E) = (\pi, 0)$, respectively.

In summary, we have shown that the topological phase in 1D SSQW remains invariant as long as the energy eigenvalues are real, even though the Hamiltonian is not Hermitian, i.e., the topological order persists as long as the Hamiltonian respects exact \mathcal{PT} symmetry. Next, we extend our study to the case of 2D DTQW.

6.2.2 Topological phases in 2D non-unitary quantum walk

Since 2D DTQW can be decomposed as a product of two 1D SSQW, we can easily extend 2D DTQW to non-unitary limits by introducing the scaling operator G along the x - as well as the y -axis. The time evolution operator can be written as

$$U_{2D}^{\text{NU}}(\theta_1, \theta_2, \gamma_x, \gamma_y) = G_{\gamma_y} T_y R(\theta_1) G_{\gamma_y}^{-1} T_y R(\theta_2) G_{\gamma_x} T_x R(\theta_1) G_{\gamma_x}^{-1} T_x. \quad (6.7)$$

The corresponding non-Hermitian Hamiltonian of this system reads

$$H_{2D}^{\text{NU}}(\theta_1, \theta_2, \gamma_x, \gamma_y) = \bigoplus_{k_x, k_y} E(k_x, k_y, \gamma_x, \gamma_y) \mathbf{n}(k_x, k_y, \gamma_x, \gamma_y) \cdot \boldsymbol{\sigma}, \quad (6.8)$$

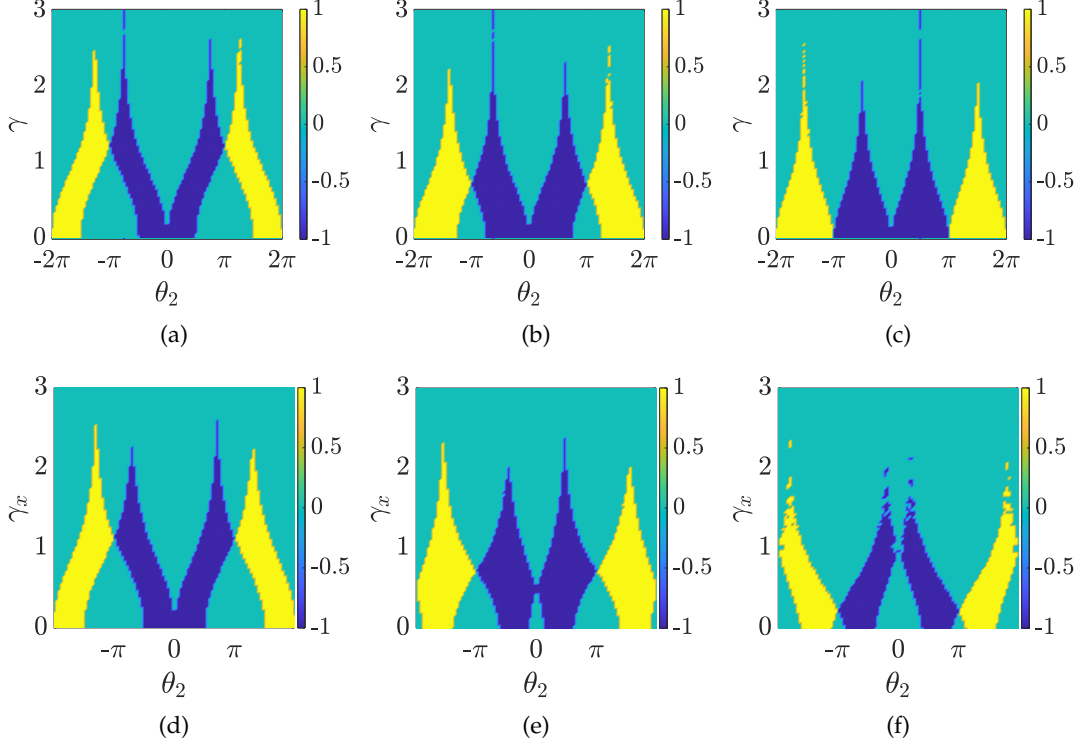


FIGURE 6.3: (Color online) Effect of γ_x on Chern number is plotted with varying θ_2 for $\gamma_y = 0$ (a) $\theta_1 = \pi/4$ (b) $\theta_1 = 3\pi/8$ (c) $\theta_1 = 3\pi/2$. In the bottom row, (d) $\gamma_y = 0.1$, (e) $\gamma_y = 0.5$, (f) $\gamma_y = 1.0$, respectively. The lattice size is taken to be 201×201 .

where

$$\begin{aligned}
& \cos E(k_x, k_y, \gamma_x, \gamma_y) \\
&= \cos \theta_1 \cos(\theta_2/2) \cos(k_x + k_y - i\gamma_x + i\gamma_y) \cos(k_x + k_y + i\gamma_x - i\gamma_y) \\
&\quad - \cos(\theta_2/2) \sin(k_x + k_y - i\gamma_x + i\gamma_y) \sin(k_x + k_y + i\gamma_x - i\gamma_y) \\
&\quad - \sin \theta_1 \sin(\theta_2/2) \cos(k_x - k_y - i\gamma_x - i\gamma_y) \cos(k_x + k_y + i\gamma_x - i\gamma_y), \tag{6.9}
\end{aligned}$$

and

$$\hat{\mathbf{n}}(k_x, k_y, \gamma_x, \gamma_y) = \frac{n_x(k_x, k_y, \gamma_x, \gamma_y)\hat{\mathbf{i}} + n_y(k_x, k_y, \gamma_x, \gamma_y)\hat{\mathbf{j}} + n_z(k_x, k_y, \gamma_x, \gamma_y)\hat{\mathbf{k}}}{\sin E(k_x, k_y, \gamma_x, \gamma_y)}, \tag{6.10}$$

with

$$\begin{aligned}
n_x(k_x, k_y, \gamma_x, \gamma_y) &= -\sin \theta_1 \cos(\theta_2/2) \cos(k_x + k_y - i\gamma_x + i\gamma_y) \sin(k_x - k_y + i\gamma_x + i\gamma_y) \\
&\quad - \cos \theta_1 \sin(\theta_2/2) \cos(k_x - k_y - i\gamma_x - i\gamma_y) \sin(k_x - k_y + i\gamma_x + i\gamma_y) \\
&\quad - \sin(\theta_2/2) \sin(k_x - k_y - i\gamma_x - i\gamma_y) \cos(k_x - k_y + i\gamma_x + i\gamma_y), \\
n_y(k_x, k_y, \gamma_x, \gamma_y) &= \sin \theta_1 \cos(\theta_2/2) \cos(k_x + k_y - i\gamma_x + i\gamma_y) \cos(k_x - k_y + i\gamma_x + i\gamma_y) \\
&\quad + \cos \theta_1 \sin(\theta_2/2) \cos(k_x - k_y - i\gamma_x - i\gamma_y) \cos(k_x - k_y + i\gamma_x + i\gamma_y) \\
&\quad - \sin(\theta_2/2) \sin(k_x - k_y - i\gamma_x - i\gamma_y) \sin(k_x - k_y + i\gamma_x + i\gamma_y), \\
n_z(k_x, k_y, \gamma_x, \gamma_y) &= -\cos \theta_1 \cos(\theta_2/2) \cos(k_x + k_y - i\gamma_x + i\gamma_y) \sin(k_x + k_y + i\gamma_x - i\gamma_y) \\
&\quad - \cos(\theta_2/2) \sin(k_x + k_y - i\gamma_x + i\gamma_y) \cos(k_x + k_y + i\gamma_x - i\gamma_y) \\
&\quad + \sin \theta_1 \sin(\theta_2/2) \cos(k_x - k_y - i\gamma_x - i\gamma_y) \sin(k_x + k_y + i\gamma_x - i\gamma_y).
\end{aligned}$$

The 2D DTQW is different from the 1D SSQW as the former case does not support \mathcal{PT} -symmetry even in the unitary region. The energy eigenvalues become complex even for very small values of the scaling factor. If we take $\gamma_x \ll 1$ and $\gamma_y = 0$, the expression for the energy reads

$$\cos E(\gamma_x) = \cos E(\gamma_x = 0) + i\gamma_x \sin \theta_1 \sin(\theta_2/2) \sin(2k_y), \quad (6.11)$$

which makes the quasi-energy complex for infinitesimal scaling parameter γ_x .

For 2D DTQW we will have $\mathbf{k} = (k_x, k_y)$ and the time evolution operator in Eq. (3.40) in momentum space must satisfy $\Xi U(\mathbf{k})\Xi^{-1} = U(-\mathbf{k})$ in order to possess PHS [14, 292], which is satisfied by choosing $\Xi = \mathcal{K}$ for all the values of scaling factor G_{γ_x} and G_{γ_y} . Their exist PHS in 2D DTQW and the topological phases in the class with \mathbb{Z} topological invariant can be realized [14, 193, 196].

Similar to the case of 1D SSQW, in 2D quantum walks also the energy eigenvalues appear in pairs $\pm E(k_x, k_y, \gamma_x, \gamma_y)$ resulting in two energy bands. Introducing loss and gain (scaling factor γ) in x and y -direction results in complex pairs of energy eigenvalues. We can choose the lower energy state by looking at the sign of the real part of the energy eigenstate and calculate the Chern number.

We use (4.74) to calculate the Chern number for the lower energy band and plot it against

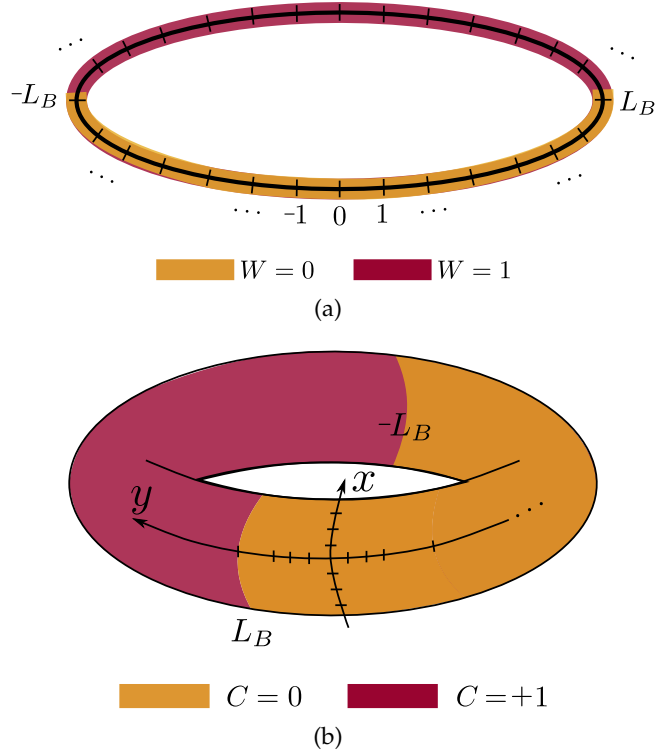


FIGURE 6.4: (Color online) The bulk boundary correspondence is studied by dividing the lattice in two parts which are characterized by distinct topological phases locally. (a) 1D lattice is divided in two equal parts with two boundaries at $\pm L_B$ with $L_B = 50$ and system size $N = 201$. (b) A two dimensional periodic lattice is divided into two equal parts where the partition is made in the y -direction while retaining the periodicity in the x -direction. The boundary on the y -axis is chosen at $\pm L_B$ with a lattice size 201×201 .

γ_x and θ_2 for some fixed values of θ_1 and γ_y (Fig. 6.3). Despite the absence of a real spectrum, we see the persistence of the topological phase as we turn on the scaling. In other words, the system remains in the same topological phase as we introduce loss and gain factors. In 2D DTQW we observe another interesting feature, namely, for some particular values of θ_1 and θ_2 , the Chern number can change abruptly from one integer value to another as γ_x increases, resulting in a topological phase transition. This is a loss-induced topological phase transition. Furthermore, unlike the 1D SSQW, the Chern number in 2D DTQW changes abruptly and for sufficiently large values of γ_x and γ_y the Chern number for all the parameters becomes zero.

6.2.3 Bulk-boundary correspondence

In the case of infinite lattice or with periodic boundary condition, we characterize our system with topological invariants such as Winding number and Chern number, however, when we have finite lattice with open boundary conditions, we observe topologically protected states

on the boundary [202, 297]. In the bulk of topological insulators, the system behaves like an ordinary insulator but on the edges, we find conducting edge states. This is referred to as bulk-boundary correspondence. In this section, we study the edge states in the 1D SSQW and the 2D DTQW systems to ensure the persistence of the topological states and hence topological order.

The 1D SSQW is generally performed on an infinite lattice or a closed chain. In order to create a boundary in this system, we still consider the quantum walk on a closed chain, but divide the lattice into two regions with different rotation angles (θ_1, θ_2) , thus making the lattice inhomogeneous. The parameters for the two parts are chosen such that the two parts locally have different topological phases, as shown in Fig. 6.4(a). At the boundary of these two phases, we should see edge states which establish the topological nature of 1D SSQW.

In Fig. 6.5, we plot the complex eigenvalues λ of the non-unitary evolution operator U given by (5.17). Here the closed chain of length 201 is divided into two parts of length $L = 100$ and $L = 101$ lattice sites. The boundaries are denoted by points $L_B = \pm 50$. We have chosen $(\theta_1^1, \theta_2^1) = (-3\pi/8, \pi/4)$ for $n > |L_B|$ and $(\theta_1^0, \theta_2^0) = (-3\pi/8, 5\pi/8)$ for $n \leq |L_B|$ corresponding to winding numbers $W = 1$ and $W = 0$, respectively.

In Fig. 6.5(a), we observe that two of the eigenvalues of the operator U lying on the real axis, signifying the states with energy 0 or π for $\gamma = 0$. These states were absent in the homogeneous case; therefore, they are the edge states. As we introduce scaling factor i.e. $\gamma \neq 0$, the same behaviour persists until we reach the critical value of γ . Since we have two sets of θ_1, θ_2 which correspond to two different energy landscapes, we will have different exceptional points. Using Eq. (5.23), these exceptional points come out to be $\gamma_c^1 = 0.2110$ and $\gamma_c^0 = 0.2832$ for the given choice of rotation parameters θ 's. We find that the edge states persist till the point given by $\min(\gamma_c^0, \gamma_c^1)$ after which we will have a complex spectrum for the Hamiltonian and we get many states with pure real λ which have a contribution from broken exact \mathcal{PT} -symmetry.

In the case of non-Hermitian 2D DTQW, it is more difficult to establish the bulk-edge correspondence. This is mainly due to the fact that 2D DTQW does not support \mathcal{PT} -symmetry. The spectrum becomes complex as soon as we introduce the scaling which is evident from Eq. (6.11). In order to see the persistence of edge states, we only plot the real part of the eigenvalues of the Hamiltonian. In the case of 2D DTQW, we introduce the boundary by considering position-dependent coin operator only along the y -axis while keeping the x -direction periodic,

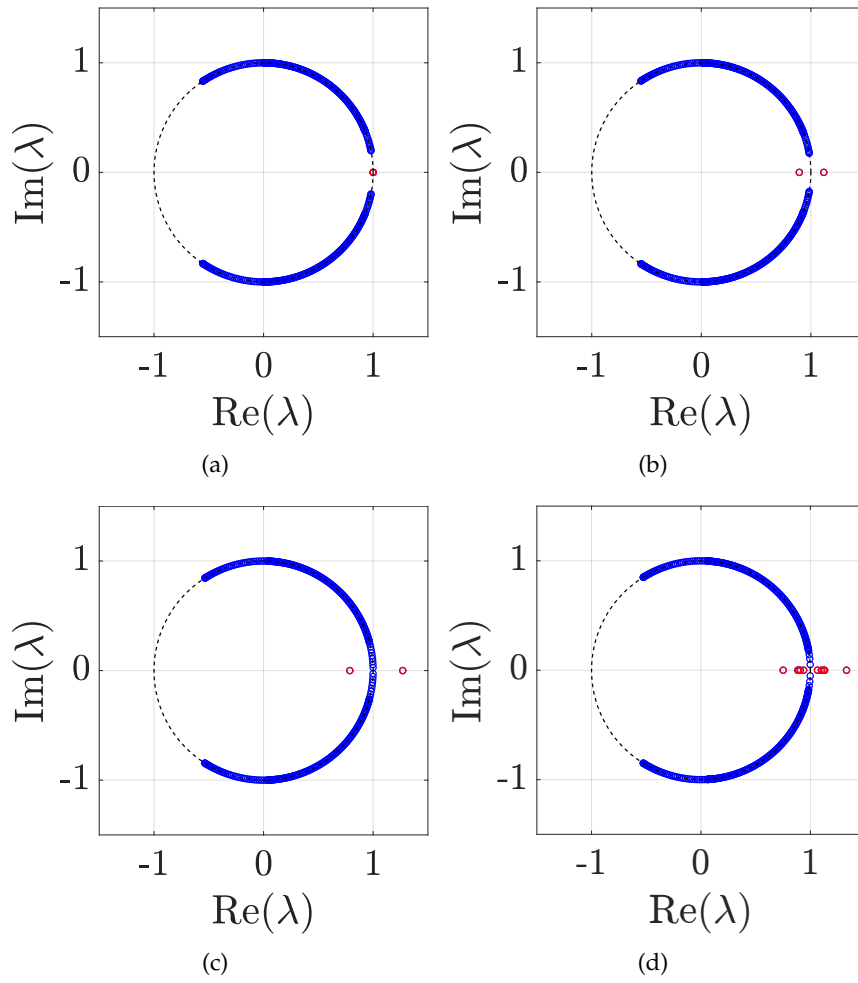


FIGURE 6.5: (Color online) The eigenvalues, λ of the time evolution operator in Eq. (5.17) are plotted for $(\theta_1^1, \theta_2^1) = (-3\pi/8, \pi/4)$ and $(\theta_1^0, \theta_2^0) = (-3\pi/8, 5\pi/8)$ and different values of γ . In (a) $\gamma = 0$, (b) $\gamma = 0.2$, (c) $\gamma = \min(\gamma^1, \gamma^2) = 0.2110$, and (d) $\gamma = 0.25$.

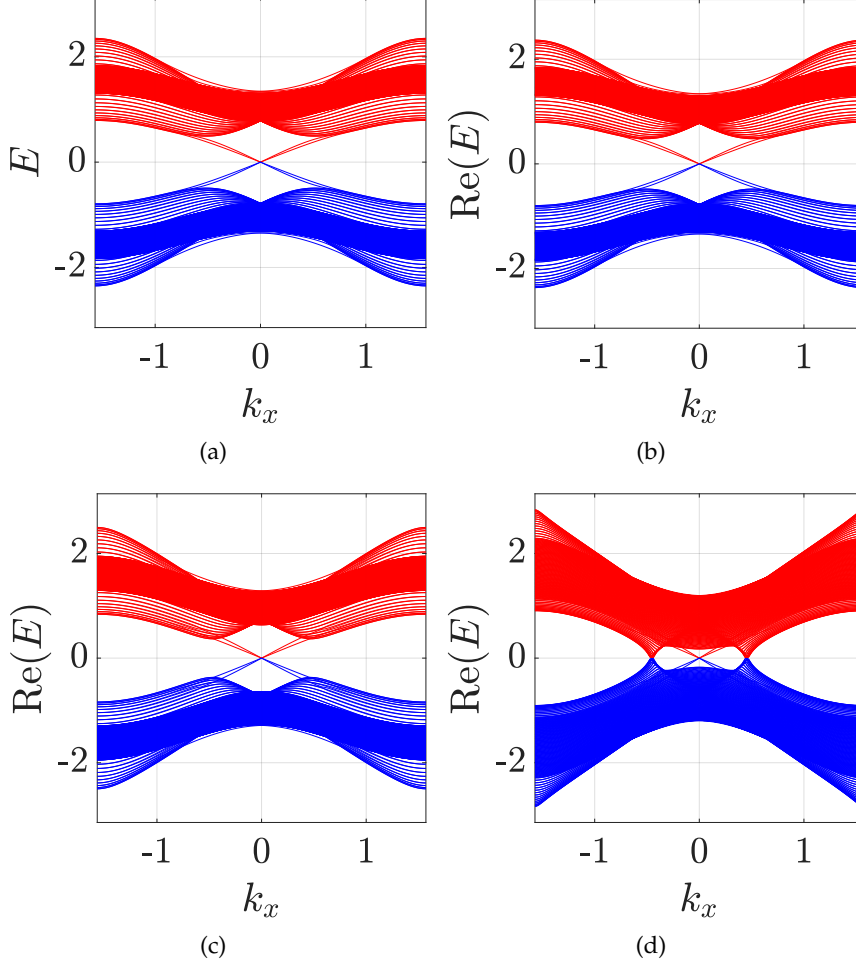


FIGURE 6.6: (Color online) Energy bands for the 2D DTQW are plotted for inhomogeneous lattice with lattice size 201×201 . We have chosen $(\theta_1^0, \theta_2^0) = (3\pi/2, 2\pi/2)$ and $(\theta_1^{+1}, \theta_2^{+1}) = (7\pi/6, 7\pi/6)$ which correspond to $C = 0$ and $C = +1$, respectively, for the two parts of the lattice. The scaling parameters are chosen to be $\gamma_x = \gamma_y = 0, 0.2, 0.3$ for (a), (b) and (c), respectively. In all these figures we can see the edge states appearing on the boundaries of the two parts of the lattice. For larger values of the scaling parameter, i.e., $\gamma_x = \gamma_y = 0.47$ in Fig. (d) we see a large number of states between the two bands, which is due to the losses.

as shown in Fig. 6.4(b). For one part of the lattice, we choose $(\theta_1^{+1}, \theta_2^{+1}) = (7\pi/6, 7\pi/6)$ and for the other, we choose $(\theta_1^0, \theta_2^0) = (3\pi/2, 2\pi/2)$; hence, the Chern numbers are $C = +1$ and 0 for the two parts.

In Fig. 6.6, we plot the real part of the spectrum as a function of the quasi-momentum in the x -direction. From these plots, we can see the persistence of the edge states even after introducing the scaling factor γ . For the large value of the scaling factors, we see the gap vanishes which is predominately due to the losses. Thus, it becomes very difficult to study the bulk-edge correspondence.

To conclude, we have studied the effect of a balanced gain and loss environment on the topological properties of discrete-time quantum walks. Specifically, we have studied the 1D SSQW and 2D DTQW and observed the persistence of topological phases against losses in these systems. The loss is incorporated using the non-Hermitian Hamiltonian approach, where we include a scaling parameter γ which characterizes the non-Hermiticity. We find a strong correspondence between the spontaneous exact \mathcal{PT} -symmetry breaking and the loss of topological order in 1D SSQW, i.e, the system retains its topological order for any value of γ , as long as the system respects the exact \mathcal{PT} -symmetry. Due to the absence of \mathcal{PT} -symmetry in 2D DTQW, we do not observe such correspondence in these systems. However, we observe loss-induced topological phase transition where we see that increasing the scaling parameter γ may transfer the system from one non-trivial topological phase to another. We studied the bulk-boundary correspondence in 1D and 2D DTQW and observe the robustness of edge states against the losses. Our results confirm the robustness of topological properties of DTQWs and the role of losses in a topological phase transition.

Chapter 7

Bloch decomposition of geodesics and null phase curves (NPCs)

The shortest path between two (non-antipodal or non-orthogonal) points on a given surface is a minimal geodesic¹ [42, 43]. In the state space of a quantum system, the geodesics are also the curves along which the acquired geometric phase is zero [9, 26] as discussed in detail in Chapter 2. Hence, they play a crucial role in the theory of geometric phases. Further, they are also used in designing optimal quantum circuits, which turned out to be equivalent to finding the shortest path between two points in a certain curved geometry [298, 299]. Geodesics can be generalized to a larger class of curves, known as null phase curves (NPCs) [10]. An NPC is defined as a curve between two pure quantum states on the state space along which the acquired geometric phase is zero [57, 300]. Unlike geodesics, the NPCs need not be the shortest path between the two states. The role of the geometric phase in characterizing topological phases of matter [12], in precision measurements [301–303], and in robust quantum information processing [7, 22] highlights the importance of understanding NPCs and geodesics. In this chapter, we present a geometric decomposition of the geodesics and NPCs for the higher-dimensional quantum systems to a set of curves on the Bloch sphere. This decomposition reveals the hidden symmetries of higher-dimensional geodesics and NPCs and may facilitate a deeper understanding of the state space structure for such systems.

To find the geometric decomposition of the geodesics and NPCs, we use the Majorana star

¹In the rest of the chapter, when we refer to geodesic, we shall mean the minimal geodesic.

(MS) representation, which enables the representation of a state of an n -level quantum system by a symmetric combination of $(n - 1)$ states of a two-level systems [11, 304]. This representation has found applications in quantum information [305, 306], quantum entanglement [307–312], geometric phases [311, 313–315] and topological phases of matter [316, 317]. Recently, the bulk topology and the bulk-boundary correspondence have been studied in the non-hermitian tight-binding model using the MS representation [318].

Since in the MS representation, a state $|\Psi\rangle$ of an n -level quantum system can be mapped to a symmetric state of $n - 1$ number of two-level systems, it can be represented by a set of $n - 1$ points on the Bloch sphere. Hence, a curve on the state space of n -level system can be mapped to $n - 1$ curves on the Bloch sphere. The $n - 1$ points corresponding to the state $|\Psi\rangle$ are often called MSs, and the collection of the points is referred to as a constellation.

In this chapter, we decompose the geodesics and NPCs of higher-dimensional quantum systems into curves on the Bloch sphere using MS representation [303]. The key findings of this paper are the following: (i) geodesics of the n -level quantum system decompose to $n - 1$ circular segments on the Bloch sphere when the end states are represented by $(n - 1)$ -fold degenerate MSs. When n is odd, the $n - 1$ curves occur in pairs that are reflection of each other about the great circle on the Bloch sphere connecting the end states. For n even, one curve is along the great circle connecting the end states, and the remaining $n - 2$ curves occur in pairs reflective about the same great circle. (ii) for odd n , a class of NPCs can be constructed using $(n - 1)/2$ pairs of curves which are reflective about a great circle, whereas, for even n , $(n - 2)/2$ pairs of curves are reflective, and the remaining curve can be chosen along the great circle connecting the two states.

Our treatment provides a deeper understanding and inherent symmetries of geodesics in higher-dimensional state space. For example, geodesics in three-dimensional state space, where the end states are chosen such that each one of them is represented by degenerate MSs, decomposes into two curves. We found that these two curves together form a unique circle on the Bloch sphere, where the end states are the diagonally opposite points on the circle. The radius of the circle depends solely on the inner product between the end states. Therefore, we can generate a geodesic between two states in three-dimensional state space by constructing a circle on the Bloch sphere between the corresponding end points. Since any pair of three-dimensional states can be mapped to states represented by a degenerate MSs using a unitary

transformation, we can construct a geodesic between any arbitrary states.

Using our geometric decomposition, we construct a prominent class of NPCs for $(n > 2)$ -dimensional state space [319]. These NPCs can be constructed by choosing curves in pairs such that the curves within a pair are reflections of each other. If the total number of curves is odd, then one curve can be chosen along the great circle connecting the end states on the Bloch sphere. Since there exists an infinite number of such pairs between any two end states, we can construct infinitely many NPCs. A special subset of these NPCs is where the curves are reflections of themselves, i.e., all the curves are along the great circle connecting the end points. This subset can be of experimental importance while designing quantum circuits.

7.1 MS representation

Symmetric subspace of $n - 1$ number of two-level quantum systems is n -dimensional which is isomorphic to n -level quantum system. Hence, the state of an n -level system can be geometrically represented as a collection of $n - 1$ number of points on the Bloch sphere, which is known as MS representation [11, 304]. In this section, we briefly outline the details of MS representation.

Consider a general n -level state $|\Psi\rangle$ written as

$$|\Psi\rangle = \sum_{r=0}^{n-1} c_r |r\rangle, \quad (7.1)$$

where c_r are the expansion coefficients such that $\sum_r |c_r|^2 = 1$ and $\{|r\rangle\}$ is the computational basis. The same state $|\Psi\rangle$ can also be written as a symmetric superposition of $n - 1$ number of two-level systems as

$$|\tilde{\Psi}\rangle = \mathcal{N} \sum_P [|\psi_1\rangle \otimes |\psi_2\rangle \otimes \cdots \otimes |\psi_{n-1}\rangle]. \quad (7.2)$$

Here \sum_P corresponds to the sum over all $(n - 1)!$ permutations of the qubits and \mathcal{N} is the normalization factor. From here onwards, we denote the state in the MS representation with a 'tilde' sign on the state, i.e., a state $|\Psi\rangle$ in the normal representation will read $|\tilde{\Psi}\rangle$ in MS representation.

The state $|\psi_k\rangle = \alpha_k |0\rangle + \beta_k |1\rangle$ represents a state of a two-level system. In order to arrive

at the MS representation, $|\psi_k\rangle$ is expressed in dual-rail representation [320] i.e. $|\psi_k\rangle \equiv (\alpha_k a_1^\dagger + \beta_k a_2^\dagger) |0, 0\rangle$ where a_1^\dagger, a_2^\dagger are the bosonic creation operators for two independent modes and $|0, 0\rangle$ is the two-mode vacuum state. The symmetrized state of $n - 1$ two-level systems in this representation can simply be written as $\prod_{k=1}^{n-1} (\alpha_k a_1^\dagger + \beta_k a_2^\dagger) |0, 0\rangle$ due to the indistinguishable nature of $n - 1$ bosons. Hence,

$$|\tilde{\Psi}\rangle \equiv \prod_{k=1}^{n-1} (\alpha_k a_1^\dagger + \beta_k a_2^\dagger) |0, 0\rangle, \quad (7.3)$$

$$\equiv \sum_{r=0}^{n-1} c_r \frac{(a_1^\dagger)^{n-1-r} (a_2^\dagger)^r}{\sqrt{r!(n-1-r)!}} |0, 0\rangle. \quad (7.4)$$

Comparing Eqs. (7.1) and (7.3), we get

$$|r\rangle = \frac{(a_1^\dagger)^{n-1-r} (a_2^\dagger)^r}{\sqrt{r!(n-1-r)!}} |0, 0\rangle \quad (7.5)$$

and coefficients c_r are functions of α_k 's and β_k 's. Now the task is to evaluate the α_k and β_k from given c_r 's. This can be achieved by constructing a polynomial of the form:

$$\prod_{k=1}^{n-1} (\alpha_k x - \beta_k) \equiv \sum_{r=0}^{n-1} f_r x^{n-1-r} = 0 \quad (7.6)$$

where

$$f_r = (-1)^r \frac{c_r}{\sqrt{r!(n-1-r)!}}. \quad (7.7)$$

Hence, solving the polynomial equation (7.6) yields the α_k 's and β_k 's. For example, the vector space corresponding to two-qubit system is 4 dimensional, however, it's symmetric subspace is 3 dimensional. Whenever, we say symmetric, it is symmetric under particle exchange. The 4D space is spanned by $\{|\uparrow\uparrow\rangle, |\uparrow\downarrow\rangle, |\downarrow\uparrow\rangle, |\downarrow\downarrow\rangle\}$ and the corresponding symmetric subspace will be spanned by

$$|1, +1\rangle = |\uparrow\uparrow\rangle$$

$$|1, 0\rangle = \frac{1}{\sqrt{2}} (|\uparrow\downarrow\rangle + |\downarrow\uparrow\rangle)$$

$$|1, -1\rangle = |\downarrow\downarrow\rangle$$

and, anti-symmetric subspace

$$|0, 0\rangle = \frac{1}{\sqrt{2}} (|\uparrow\downarrow\rangle - |\downarrow\uparrow\rangle).$$

It is exactly same as addition of angular momentum. When we add the spin angular momentum of two spin-half particles we write

$$2 \otimes 2 = 3 \oplus 1 \tag{7.8}$$

where 3 and 1 are the dimensions of the symmetric and anti-symmetric subspace respectively.

7.1.1 Bargmann invariant (BI) and geometric phase

In this subsection, we define the BI and its relation with the geometric phase. Given three non-orthogonal states $\{|\Psi_1\rangle, |\Psi_2\rangle, |\Psi_3\rangle\}$ from the Hilbert space \mathcal{H} , i.e., $\langle\Psi_i|\Psi_j\rangle \neq 0; \forall i \neq j$, the BI of third order is defined as

$$\Delta_3(\Psi_1, \Psi_2, \Psi_3) = \langle\Psi_1|\Psi_2\rangle \langle\Psi_2|\Psi_3\rangle \langle\Psi_3|\Psi_1\rangle. \tag{7.9}$$

The BI is invariant under unitary transformation $|\Psi_i\rangle \rightarrow U|\Psi_i\rangle$. It plays a crucial role in the theory of geometric phase. Consider a closed curve \mathcal{C} constructed by connecting the three non-orthogonal states $\{|\Psi_i\rangle\}$ by geodesics, then the geometric phases Φ_g associated with this closed curve is given by [9]

$$\Phi_g[\mathcal{C}] = -\arg \Delta_3(\Psi_1, \Psi_2, \Psi_3). \tag{7.10}$$

It is straightforward to generalize Eq. (7.9) to define n th order BI as

$$\Delta_n(\Psi_1, \dots, \Psi_n) = \langle\Psi_1|\Psi_2\rangle \langle\Psi_2|\Psi_3\rangle \dots \langle\Psi_n|\Psi_1\rangle. \tag{7.11}$$

Further, any higher order BIs can be reduced to third order BIs [9] and correspondingly the geometric phase for a closed curve constructed by connecting n number of states via geodesics can be expressed as the sum of geometric phases for $n - 2$ third order BIs.

7.1.2 Geodesic curves

Geodesic is the path of shortest distance between two points on a surface. In this subsection, we introduce a differential equation for the geodesic in the state space of a quantum system. To define geodesic curves, we need a continuously parametrized smooth curve \mathcal{C} in the Hilbert space \mathcal{H} given by

$$\mathcal{C} = \{|\Psi(s)\rangle \in \mathcal{H} \mid s_1 \leq s \leq s_2\}, \quad (7.12)$$

where s is the real parameter varies over $[s_1, s_2]$. The quantity called ‘length’ associated with \mathcal{C} is defined as [9]

$$\mathcal{L} = \int_{s_1}^{s_2} ds \langle u_{\perp}(s) | u_{\perp}(s) \rangle^{1/2}, \quad (7.13)$$

where

$$|u_{\perp}(s)\rangle = |u(s)\rangle - \langle \Psi(s) | u(s) \rangle |\Psi(s)\rangle,$$

and $|u(s)\rangle$ is the tangent to $|\Psi(s)\rangle$ which reads

$$|u(s)\rangle = \frac{d}{ds} |\Psi(s)\rangle \equiv |\dot{\Psi}(s)\rangle.$$

By requiring $\delta\mathcal{L} = 0$, we obtain a differential equation obeyed by \mathcal{C} to be a geodesic:

$$\left(\frac{d}{ds} - \langle \Psi(s) | u(s) \rangle \right) \frac{|u_{\perp}(s)\rangle}{\|u_{\perp}(s)\|} = f(s) |\Psi(s)\rangle, \quad (7.14)$$

where $f(s)$ is a real function of s which is yet to be determined.

The geodesics are invariant under the $U(1)$ transformation of the form $|\Psi(s)\rangle \rightarrow e^{i\alpha(s)} |\Psi(s)\rangle$. By exploiting this freedom and the freedom of reparameterization, we can make $\langle \Psi(s) | u(s) \rangle = 0$ and $\|u\| = \text{constant}$, respectively, which yields [9, 57]

$$\frac{d^2}{ds^2} |\Psi(s)\rangle = f(s) |\Psi(s)\rangle. \quad (7.15)$$

It is important to note that such reparametrisations, referred to as *affine* reparametrisations, are unique only up to linear transformations i.e.,

$$s \rightarrow s' = as + b \quad (7.16)$$

where a and b are constants. Further, the above equation can be shown equivalent to a differential equation of the form [9]:

$$\frac{d^2}{ds^2} |\Psi(s)\rangle = -\langle \dot{\Psi}(s) | \dot{\Psi}(s) \rangle |\Psi(s)\rangle. \quad (7.17)$$

A formal solution of Eq. (7.17), for the given two end states $|\Psi(s_1)\rangle$ and $|\Psi(s_2)\rangle$ with

$$\langle \Psi(s_1) | \Psi(s_2) \rangle \equiv \xi \text{ real and positive}, \quad (7.18)$$

is given by

$$|\Psi(s)\rangle = \cos(s) |\Psi(s_1)\rangle + \frac{|\Psi(s_2)\rangle - \xi |\Psi(s_1)\rangle}{(1 - \xi^2)^{1/2}} \sin(s). \quad (7.19)$$

Hence, using Eq. (7.19) we can generate the geodesic between any two points in the state space.

7.1.3 NPCs

NPCs are the curves between two points on the quantum state space along which the acquired geometric phase is zero [10, 57, 300]. Mathematically, these curves can be defined as follows: consider a differentiable curve $\{|\Psi(s)\rangle\}$ for the real parameter $s \in (s_1, s_2)$ such that $\langle \Psi(s) | \Psi(s') \rangle \neq 0$ for all $s, s' \in (s_1, s_2)$. The curve $\{|\Psi(s)\rangle\}$ is an NPC if for any three points on the curve, the BI is real and positive, i.e.,

$$\Delta_3(\Psi(s), \Psi(s'), \Psi(s'')) > 0, \quad s, s', s'' \in [s_1, s_2]. \quad (7.20)$$

From the above definition it is clear that if the curve $\{|\Psi(s)\rangle\}$ is an NPC, then $\{e^{i\beta} |\Psi(s)\rangle\}$ will also be an NPC. Exploiting this condition, we can always choose a curve in the \mathcal{H} such that

$$\langle \Psi(s) | \Psi(s') \rangle > 0 \quad (7.21)$$

for any $s, s' \in (s_1, s_2)$ [57]. Hence, there exist infinitely many NPCs between any two points in the state space.

7.2 Bloch sphere decomposition of geodesics

The geodesic between any two states of a two-level quantum system is the segment of the great circle connecting these states on the Bloch sphere. This is the consequence of the spherical geometry of the state space of a two-level system. However, the geodesics in three or higher dimensional state spaces are notoriously difficult to understand, even though the expression to calculate these geodesics is given in Eq. (7.19). In this section, we present the Bloch sphere decomposition of higher dimensional geodesics using MS representation. This Bloch sphere decomposition reveals intrinsic symmetries of geodesics which may help to understand the geometric structure of higher dimensional state space. We start with geodesics in three-dimensional state space and extend these results to higher dimensions.

7.2.1 Geodesics in three-dimensional state space

Consider two states $\{|\Psi_1\rangle, |\Psi_2\rangle\}$ in the three-dimensional state space. For simplicity, we choose states of the following form

$$|\Psi_1\rangle = \begin{pmatrix} 1 \\ 0 \\ 0 \end{pmatrix}, \quad |\Psi_2\rangle = \begin{pmatrix} \alpha^2 \\ \sqrt{2}\alpha\beta \\ \beta^2 \end{pmatrix}, \quad (7.22)$$

such that each one of them individually are represented by degenerate MSs. Here α and β are real, with $\langle\Psi_1|\Psi_2\rangle = \alpha^2 \equiv \cos\theta$; $0 \leq \theta < \pi/2$ and $\alpha^2 + \beta^2 = 1$.

In the MS representation, the states considered in Eq. (7.22) takes the form

$$\begin{aligned} |\tilde{\Psi}_1\rangle &= |0\rangle \otimes |0\rangle, \\ |\tilde{\Psi}_2\rangle &= |\phi\rangle \otimes |\phi\rangle, \end{aligned} \quad (7.23)$$

where $|0\rangle = \begin{pmatrix} 1 & 0 \end{pmatrix}^T$ and $|\phi\rangle = \begin{pmatrix} \alpha & \beta \end{pmatrix}^T$.

From Eq.(7.19) we can find a geodesic $\{|\Psi(s)\rangle \mid 0 \leq s \leq \theta\}$ connecting $|\Psi_1\rangle$ and $|\Psi_2\rangle$ which

reads

$$|\Psi(s)\rangle = \begin{pmatrix} \cos(s) \\ a \sin(s) \\ b \sin(s) \end{pmatrix} \equiv \frac{1}{\mathcal{N}(s)} [|\psi_+(s)\rangle |\psi_-(s)\rangle + |\psi_-(s)\rangle |\psi_+(s)\rangle]. \quad (7.24)$$

Here $a = \sqrt{2}\alpha\beta/\sin\theta$, $b = \beta^2/\sin\theta$ and $\mathcal{N}(s)$ is the normalisation constant. The states $|\psi_{\pm}\rangle$ in the MS representation of $|\Psi(s)\rangle$ are given by

$$|\psi_{\pm}(s)\rangle = \frac{1}{\sqrt{1 + |x_{\pm}(s)|^2}} \begin{pmatrix} 1 \\ x_{\pm}(s) \end{pmatrix}, \quad (7.25)$$

where

$$x_{\pm}(s) = \frac{a \sin(s) \pm i \sqrt{b \sin(2s) - a^2 \sin^2(s)}}{\sqrt{2} \cos(s)}. \quad (7.26)$$

Here $x_{\pm}(s)$ are the solutions of the Majorana polynomial Eq. (7.6) corresponding to the $|\Psi(s)\rangle$ in Eq. (7.24). So, the geodesic curve $\{|\Psi(s)\rangle\}$ decomposes into two curves $\{|\psi_+(s)\rangle \mid 0 \leq s \leq \theta\}$ and $\{|\psi_-(s)\rangle \mid 0 \leq s \leq \theta\}$ belonging to two-dimensional space. Note that the curves $\{|\psi_{\pm}(s)\rangle \mid 0 \leq s \leq \theta\}$ themselves do not satisfy the differential equation for a geodesic (7.14). Therefore, they are not geodesics in two-dimensional space.

The Bloch vectors corresponding to $\{|\psi_{\pm}(s)\rangle\}$ are denoted as $\{\mathbf{n}_{\pm}(s)\}$ and obtained by

$$\mathbf{n}_{\pm}(s) = \langle \psi_{\pm}(s) | \boldsymbol{\sigma} | \psi_{\pm}(s) \rangle, \quad (7.27)$$

where $\boldsymbol{\sigma} = \{\sigma_x, \sigma_y, \sigma_z\}$ is the vector of Pauli matrices [321]. The components of the curves $\{\mathbf{n}_{\pm}(s)\}$ along x, y, z read

$$\begin{aligned} (\mathbf{n}_+)_{x} &= (\mathbf{n}_-)_{x} = \frac{\sqrt{2}a \sin(s)}{\cos(s) + b \sin(s)}, \\ (\mathbf{n}_+)_{y} &= -(\mathbf{n}_-)_{y} = \frac{\sqrt{b \sin(2s) - a^2 \sin^2(s)}}{\cos(s) + b \sin(s)}, \\ (\mathbf{n}_+)_{z} &= (\mathbf{n}_-)_{z} = \frac{\cos(s) - b \sin(s)}{\cos(s) + b \sin(s)}. \end{aligned} \quad (7.28)$$

Since, the end states $|0\rangle$ and $|\phi\rangle$ in Eq. (7.23) lie on the xz -plane on the Bloch sphere and the solutions $\{x_{\pm}(s)\}$ (7.26) form a complex conjugate pair, the components of the curves $\{\mathbf{n}_{\pm}(s)\}$ differ only along y -axis by a negative sign. Therefore, the two curves are reflective about the

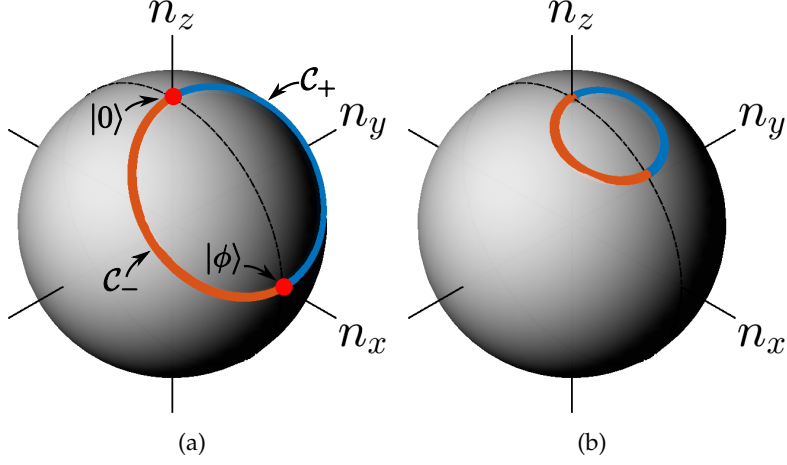


FIGURE 7.1: (Color online) Here we plot the geometric decomposition of a geodesic between two states given in Eq. (7.23) where we have chosen (a) $\theta = \pi/3$, (b) $\theta = \pi/5$. The blue and orange curve correspond to $\{\mathbf{n}_+\}$ and $\{\mathbf{n}_-\}$ respectively, given in Eq. (7.28).

xz -plane. We will call these curves as ‘dual’ of each other.

On a careful observation, we can see that the components of the pair of dual curves along x, y, z axes satisfy an equation of the form

$$\left((\mathbf{n}_\pm)_x - \alpha\beta \right)^2 + (\mathbf{n}_\pm)_y^2 + \left((\mathbf{n}_\pm)_z - \alpha^2 \right)^2 = \beta^2, \quad (7.29)$$

which is an equation of a circle with center at $(\alpha\beta, 0, \alpha^2)$, the midpoint of the line joining the end states on the Bloch sphere. Hence, the two curves are segments of a circle, and share the same center and the same radius β . Therefore, the geodesic curve connecting two states in the three-dimensional state space can be identified by a complete circle of radius $\beta = \sqrt{1 - \langle \Psi_1 | \Psi_2 \rangle}$ on the Bloch sphere constructed by joining two semi-circular arcs $\{\mathbf{n}_\pm(s)\}$. The pair of dual curves $\mathcal{C}_\pm \equiv \{\mathbf{n}_\pm(s)\}$ traced by the two states in Eq. (7.25) are shown in Fig. 7.1 for different values of θ .

So far we have considered the geodesics between the end states which are represented by degenerate MSs given in Eq. (7.22). Interestingly, this formalism can be applied to the geodesics between two arbitrary three-dimensional states.

We note that any two states $\{|\Psi_1\rangle, |\Psi_2\rangle\}$ in three-dimensional Hilbert space can be transformed to degenerate MSs by a common unitary transformation U . We can show it explicitly by considering two arbitrary states $\{|\Psi_1\rangle, |\Psi_2\rangle\}$ in three-dimensional state space with the inner

product given by $\langle \Psi_1 | \Psi_2 \rangle = \cos \theta$, i.e., real and positive. We can write $|\Psi_2\rangle$ as

$$|\Psi_2\rangle = \cos \theta |\Psi_1\rangle + \gamma |\bar{\Psi}_1\rangle \quad (7.30)$$

where $\gamma = \sin \theta e^{i\phi}$, $\phi \in \mathbb{R}$ and $|\bar{\Psi}_1\rangle$ is orthogonal to $|\Psi_1\rangle$. Now, we take unitary of the form

$$U = |0\rangle\langle\Psi_1| + e^{-i\phi} |1\rangle\langle\bar{\Psi}_1| + |2\rangle\langle\tilde{\Psi}_1| \quad (7.31)$$

where $\{|0\rangle, |1\rangle, |2\rangle\}$ and $\{|\Psi_1\rangle, |\bar{\Psi}_1\rangle, |\tilde{\Psi}_1\rangle\}$ form the orthonormal bases. On application of this unitary on the two states $\{|\Psi_1\rangle, |\Psi_2\rangle\}$ results in the states of the form

$$U |\Psi_1\rangle \equiv |\Psi'_1\rangle = \begin{pmatrix} 1 \\ 0 \\ 0 \end{pmatrix}, \quad U |\Psi_2\rangle \equiv |\Psi'_2\rangle = \begin{pmatrix} \cos \theta \\ \sin \theta \\ 0 \end{pmatrix}. \quad (7.32)$$

One can see that $|\Psi'_2\rangle$ cannot be represented by a degenerate MSs. For that one need to apply one more unitary transformation in order to bring $|\Psi'_2\rangle$ to a state represented by degenerate MSs. An appropriate unitary for that is given by

$$U = \begin{pmatrix} 1 & 0 & 0 \\ 0 & a & b \\ 0 & -b & a \end{pmatrix} \quad (7.33)$$

where $a = \sqrt{2}\alpha\beta / \sin \theta$, $b = \beta^2 / \sin \theta$, $\alpha^2 = \cos \theta$ and $\alpha^2 + \beta^2 = 1$. After applying the following unitary, we will get

$$|\Psi_2\rangle = \begin{pmatrix} \alpha^2 \\ \sqrt{2}\alpha\beta \\ \beta^2 \end{pmatrix} \quad (7.34)$$

which is written as

$$|\tilde{\Psi}_2\rangle = \begin{pmatrix} \alpha \\ \beta \end{pmatrix} \otimes \begin{pmatrix} \alpha \\ \beta \end{pmatrix}. \quad (7.35)$$

Therefore, any two arbitrary states with real inner product can be brought to the degenerate MSs states and we can study the structure of the geodesics between these states by first

mapping them to degenerate MSs and constructing the geodesic using the semicircular curves \mathcal{C}_\pm . Applying U^\dagger on these curves will result the actual curves corresponding to the geodesic between $\{|\Psi_1\rangle, |\Psi_2\rangle\}$.

To summarize the results obtained in this section: (i) A geodesic connecting the three-dimensional states $|\Psi_1\rangle$ and $|\Psi_2\rangle$, which are represented by degenerate MSs on the Bloch sphere, decomposes into two unique curves on the Bloch sphere. (ii) These two curves are reflective about the great circle connecting the two end points on the Bloch sphere, and constitute a circle of radius $\sqrt{1 - \langle\Psi_1|\Psi_2\rangle}$. (iii) One can obtain the geodesic connecting any two arbitrary states in three-dimensional space by first converting the two end states to degenerate MSs states by using a unitary transformation and then constructing the unique circle between the end states on the Bloch sphere.

7.2.2 Geodesics in higher-dimensional state space

We extend our analysis to study the structure of geodesics in higher-dimensional state space. Let us start by considering non-orthogonal end states $\{|\Psi_1\rangle, |\Psi_2\rangle\}$ in an n -dimensional state space which map to $(n - 1)$ -fold degenerate MSs individually on the Bloch sphere. In the MS representation, the end states can be written as

$$\begin{aligned} |\tilde{\Psi}_1\rangle &= |0\rangle_0 \otimes |0\rangle_1 \otimes \cdots \otimes |0\rangle_{n-2}, \\ |\tilde{\Psi}_2\rangle &= |\phi\rangle_0 \otimes |\phi\rangle_1 \otimes \cdots \otimes |\phi\rangle_{n-2}, \end{aligned} \quad (7.36)$$

where $|0\rangle = \begin{pmatrix} 1 & 0 \end{pmatrix}^T$ and $|\phi\rangle = \begin{pmatrix} \alpha & \beta \end{pmatrix}^T$. Here α and β are real, with $\langle\Psi_1|\Psi_2\rangle = \alpha^{n-1} \equiv \cos\theta$; $0 \leq \theta < \pi/2$ and $\alpha^2 + \beta^2 = 1$. From Eq. (7.19), the geodesic curve $\{|\Psi(s)\rangle; 0 \leq s \leq \theta\}$ connecting the end states in the MS representation turns out to be

$$|\tilde{\Psi}(s)\rangle = |0\rangle^{\otimes n-1} + A^{(n-1)}(s) |\phi\rangle^{\otimes n-1}, \quad (7.37)$$

$$\equiv \mathcal{N} \sum_P [|\chi_1(s)\rangle \otimes |\chi_2(s)\rangle \otimes \cdots \otimes |\chi_{n-1}(s)\rangle] \quad (7.38)$$

where \sum_P corresponds to the sum over all symmetric permutations of the $n - 1$ number of states $|\chi_k(s)\rangle$ of two-level systems. \mathcal{N} is the normalization constant, and

$$A^{(n-1)}(s) = \frac{\sin s}{\cos s(1 - \alpha^{n-1})^{1/2} - \alpha^{n-1} \sin s}. \quad (7.39)$$

Since the end states considered in Eq. (7.36) are real, the Majorana polynomial [Eq. (7.6)] is also real. Therefore, the roots occur as complex conjugate pairs along with a real root depending on the dimension of the state space. By solving the Majorana polynomial Eq. (7.6), one can find the curves $\{|\chi_k(s)\rangle\}$, $i = 1, \dots, n - 1$ as

$$|\chi_k(s)\rangle = |0\rangle + \Delta \omega_k A(s) |\phi\rangle. \quad (7.40)$$

Here, ω_k 's are the $(n - 1)$ th roots of unity given by $\omega_k = e^{2\pi ik/n-1}$ with $k = 0, 1, \dots, n - 2$ and $\Delta = \left(\prod_{k=0}^{n-2} \omega_k\right)^{1/(n-1)}$. This shows that a geodesic curve in an n -dimensional state space decomposes to $n - 1$ curves on the Bloch sphere.

The Bloch vector corresponding to the state $\{|\chi_k(s)\rangle\}$ can be written as $\{\mathbf{n}_k(s) = \langle \chi_k(s) | \boldsymbol{\sigma} | \chi_k(s) \rangle\}$. Next we show that the curve $\{|\chi_k(s)\rangle\}$ traced by the states $|\chi_k(s)\rangle$ for all the values of k constitute circular segments on the Bloch sphere.

Consider three Bloch vectors \mathbf{p}_1 , \mathbf{p}_2 , \mathbf{p}_3 corresponding to three states on the curve $\{|\chi_k(s)\rangle\}$. The unit vector \mathbf{m} orthogonal to the plane containing these three Bloch vectors can be written as

$$\mathbf{m} = \frac{(\mathbf{p}_2 - \mathbf{p}_1) \times (\mathbf{p}_3 - \mathbf{p}_1)}{\|(\mathbf{p}_2 - \mathbf{p}_1) \times (\mathbf{p}_3 - \mathbf{p}_1)\|}. \quad (7.41)$$

The intersection of the plane containing the three vectors \mathbf{p}_1 , \mathbf{p}_2 , \mathbf{p}_3 and the Bloch sphere constitute a circle. The three Bloch vectors \mathbf{p}_1 , \mathbf{p}_2 , \mathbf{p}_3 also lie on the circle whereas the unit vector \mathbf{m} passes through the center of this circle. Therefore, the projection of any of these three Bloch vectors will be the same on the vector \mathbf{m} .

We find that the \mathbf{m} is the same for any choice of the three Bloch vectors on the curve $\{|\chi_k(s)\rangle\}$. Moreover, the projection of all the Bloch vectors $\mathbf{p}(s)$ on the curve $\{|\chi_k(s)\rangle\}$ with \mathbf{m} remains constant. This indicates that the curve traced by $|\chi_k(s)\rangle$ is circular segment for all

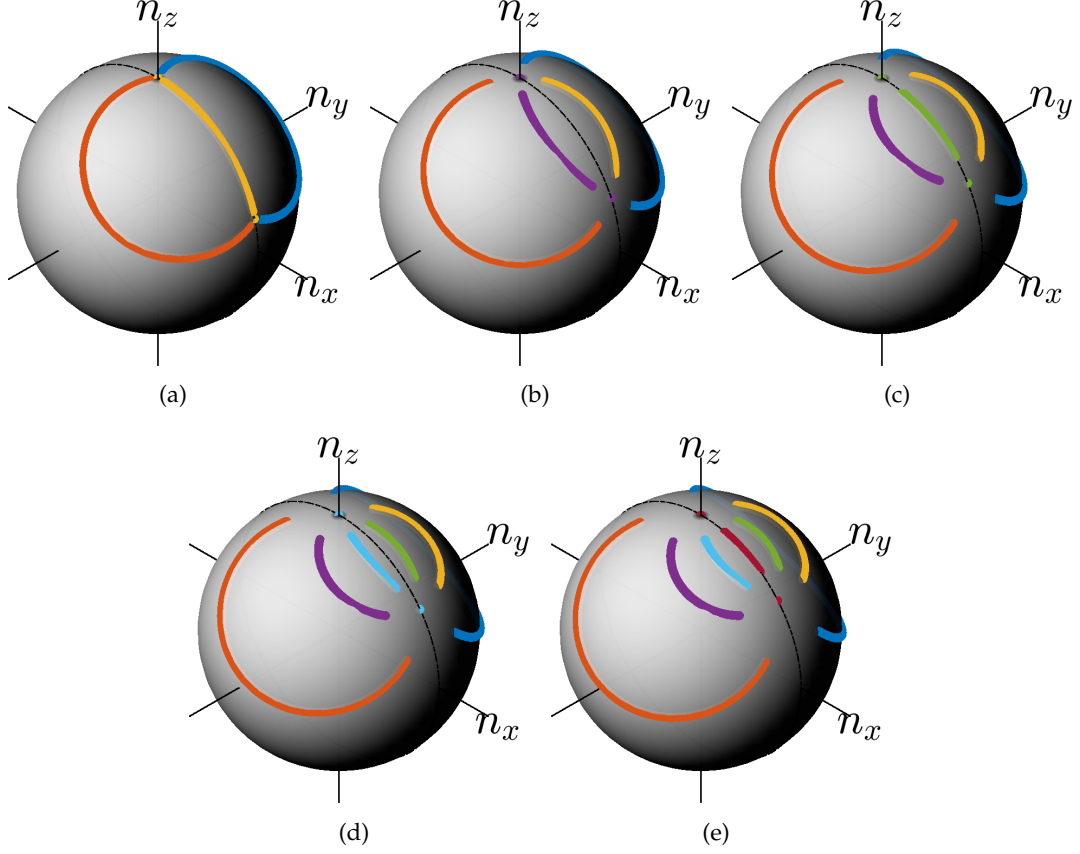


FIGURE 7.2: (Color online) Geometric decomposition of geodesics in (a) 4- (b) 5- (c) 6- (d) 7- (e) 8-dimensional state space for $\theta = \pi/3$. We can see that we obtain $n - 1$ number of curves for n -dimensional system which is consistent with our decomposition.

the values of k . The radius corresponding to the k -th circular segment is

$$R_k = \frac{2\beta}{\sqrt{4\beta^2 - \alpha^2(\Delta^* \omega_k^* - \Delta \omega_k)^2}}. \quad (7.42)$$

From the above expression, we see that the radii depends only on the inner product between the end states and not explicitly on the states. Furthermore, the circular segments are unique for the geodesic between a given set of end states. Therefore, once the end states are uniquely identified on the Bloch sphere, one can construct the desired geodesic by using Eq. (7.42) alone. In Fig. 7.2, we have plotted the structure of geodesic curve on the Bloch sphere for $n = 4$ - and 5-dimensional state space.

There are certain intrinsic symmetries in the MS representation of a higher dimensional geodesic. These symmetries reflect differently for even and odd dimensions. For example, if the dimension n is odd, we get even number of curves which appear in dual pairs, i.e., the pair

of curves which are reflections of each other. The two curves $\{|\chi_i(s)\rangle\}, \{|\chi_j(s)\rangle\}$, which are dual of each other, satisfy the condition $i + j = 0 \pmod{n-1}$, where $i, j = 0, 1, 2, \dots, n-2$ and $i \neq j$. However, in the case of even n , one curve occurs along the great circle connecting the end states and the remaining $n-2$ curves occur in dual pairs. For even n , the two dual curves $\{|\chi_i(s)\rangle\}, \{|\chi_j(s)\rangle\}$ satisfy the condition $i + j = n-2 \pmod{n-1}$. From Eq. (7.41) and Eq. (7.42), it is evident that the dual curves give the same value of radius with different centers.

Now, we have a way of constructing a unique geodesic between any two states $\{|\Psi_1\rangle, |\Psi_2\rangle\}$ in the n -dimensional state space. Given $|\Psi_1\rangle, |\Psi_2\rangle$ we first map them to $(n-1)$ -fold degenerate MSs states $|\tilde{\Psi}_1\rangle, |\tilde{\Psi}_2\rangle$ in the MS representation using a unitary transformation U . Thereafter, we construct circular segments on the Bloch sphere which are defined by Eqs. (7.41) and (7.42) yielding the geodesic in n -dimensional state space, connecting the states $|\tilde{\Psi}_1\rangle$ and $|\tilde{\Psi}_2\rangle$. Finally, we apply the U^\dagger to get the desired geodesic between the original states.

7.3 Bloch Sphere decomposition of NPCs

So far we have seen that the geometric decomposition of the geodesic has revealed an interesting underlying symmetry. This not only have given us better understanding of the geodesics but also have provided us geometric ways of constructing one. In this section, we investigate the geometric structure of NPCs in higher-dimensional state space. We mostly deal with the three-dimensional case but the analysis can easily be extended to n -dimensional state space. Here we propose a way to construct NPCs by choosing suitable set of curves on the Bloch sphere.

Once again, we consider the end states $|\tilde{\Psi}_1\rangle = |0\rangle \otimes |0\rangle$, and $|\tilde{\Psi}_2\rangle = |\phi\rangle \otimes |\phi\rangle$ as defined earlier. In order to construct an NPC between $|\Psi_1\rangle$ and $|\Psi_2\rangle$ we propose the following:

Proposition : An arbitrary curve \mathcal{C} connecting the states $\{|\tilde{\Psi}_1\rangle, |\tilde{\Psi}_2\rangle\}$, and its dual curve \mathcal{C}^* together form an NPC in the three-dimensional state space.

Proof: The most general curve $\mathcal{C} \equiv \{|\psi(s)\rangle | s_1 \leq s \leq s_2\}$ connecting the states $\{|\tilde{\Psi}_1\rangle, |\tilde{\Psi}_2\rangle\}$, is given by

$$|\psi(s)\rangle = \begin{pmatrix} \cos(\eta(s)/2) \\ e^{i\Gamma(s)} \sin(\eta(s)/2) \end{pmatrix}, \quad (7.43)$$

where $\eta(s)$ and $\Gamma(s)$ are arbitrary real functions of s . The functions $\eta(s)$ and $\Gamma(s)$ satisfy the relations $\eta(s_1) = 0, \eta(s_2) = 2 \cos^{-1}(\alpha)$ and $\Gamma(s_1) = \Gamma(s_2) = 0$. The dual curve $\mathcal{C}^* \equiv \{|\psi(s)\rangle | s_1 \leq s \leq s_2\}$ can then be defined as

$$|\psi'(s)\rangle = \begin{pmatrix} \cos(\eta(s)/2) \\ e^{-i\Gamma(s)} \sin(\eta(s)/2) \end{pmatrix} \quad (7.44)$$

Using the curves \mathcal{C} and \mathcal{C}^* the states on the curve in the three-dimensional state space can be written as

$$|\tilde{\Psi}(s)\rangle = \frac{1}{\mathcal{N}(s)} [|\psi(s)\rangle |\psi'(s)\rangle + |\psi'(s)\rangle |\psi(s)\rangle], \quad (7.45)$$

where $\mathcal{N}(s)$ is the normalization constant. Now, we will find the third order BI between any three states on the curve given in Eq. (7.45). The BI of third order Δ_3 for any given three mutually non-orthogonal states $\{|\Psi_1\rangle, |\Psi_2\rangle, |\Psi_3\rangle\}$ is written as

$$\Delta_3(\Psi_1, \Psi_2, \Psi_3) = \langle \Psi_1 | \Psi_2 \rangle \langle \Psi_2 | \Psi_3 \rangle \langle \Psi_3 | \Psi_1 \rangle. \quad (7.46)$$

In the MS representation, these states are written as

$$\begin{aligned} |\Psi_1\rangle &= \frac{1}{\mathcal{N}_1} [|\psi_1\rangle |\psi'_1\rangle + |\psi'_1\rangle |\psi_1\rangle] \\ |\Psi_2\rangle &= \frac{1}{\mathcal{N}_2} [|\psi_2\rangle |\psi'_2\rangle + |\psi'_2\rangle |\psi_2\rangle] \\ |\Psi_3\rangle &= \frac{1}{\mathcal{N}_3} [|\psi_3\rangle |\psi'_3\rangle + |\psi'_3\rangle |\psi_3\rangle] \end{aligned} \quad (7.47)$$

where \mathcal{N}_i are the normalization constants. Using this representation, we can expand $\Delta_3(\Psi_1, \Psi_2, \Psi_3)$

as follows

$$\begin{aligned}
& \langle \Psi_1 | \Psi_2 \rangle \langle \Psi_2 | \Psi_3 \rangle \langle \Psi_3 | \Psi_1 \rangle \\
&= \langle \psi_1 | \psi_2 \rangle \langle \psi_2 | \psi_3 \rangle \langle \psi_3 | \psi_1 \rangle \langle \psi'_1 | \psi'_2 \rangle \langle \psi'_2 | \psi'_3 \rangle \langle \psi'_3 | \psi'_1 \rangle \\
&+ \langle \psi_1 | \psi_2 \rangle \langle \psi_2 | \psi'_3 \rangle \langle \psi'_3 | \psi'_1 \rangle \langle \psi'_1 | \psi'_2 \rangle \langle \psi'_2 | \psi_3 \rangle \langle \psi_3 | \psi_1 \rangle \\
&+ \langle \psi_1 | \psi'_2 \rangle \langle \psi'_2 | \psi'_3 \rangle \langle \psi'_3 | \psi'_1 \rangle \langle \psi'_1 | \psi_2 \rangle \langle \psi_2 | \psi_3 \rangle \langle \psi_3 | \psi_1 \rangle \\
&+ \langle \psi_1 | \psi'_2 \rangle \langle \psi'_2 | \psi_3 \rangle \langle \psi_3 | \psi_1 \rangle \langle \psi'_1 | \psi_2 \rangle \langle \psi_2 | \psi'_3 \rangle \langle \psi'_3 | \psi'_1 \rangle \\
&+ \langle \psi_1 | \psi_2 \rangle \langle \psi_2 | \psi_3 \rangle \langle \psi_3 | \psi'_1 \rangle \langle \psi'_1 | \psi'_2 \rangle \langle \psi'_2 | \psi'_3 \rangle \langle \psi'_3 | \psi_1 \rangle \\
&+ \langle \psi_1 | \psi_2 \rangle \langle \psi_2 | \psi'_3 \rangle \langle \psi'_3 | \psi_1 \rangle \langle \psi'_1 | \psi'_2 \rangle \langle \psi'_2 | \psi_3 \rangle \langle \psi_3 | \psi'_1 \rangle \\
&+ \langle \psi_1 | \psi'_2 \rangle \langle \psi'_2 | \psi'_3 \rangle \langle \psi'_3 | \psi_1 \rangle \langle \psi'_1 | \psi_2 \rangle \langle \psi_2 | \psi_3 \rangle \langle \psi_3 | \psi'_1 \rangle \\
&+ \langle \psi_1 | \psi'_2 \rangle \langle \psi'_2 | \psi_3 \rangle \langle \psi_3 | \psi'_1 \rangle \langle \psi'_1 | \psi_2 \rangle \langle \psi_2 | \psi'_3 \rangle \langle \psi'_3 | \psi_1 \rangle
\end{aligned}$$

Now we choose,

$$|\psi(s)\rangle = \begin{pmatrix} \cos(\eta(s)/2) \\ e^{i\Gamma(s)} \sin(\eta(s)/2) \end{pmatrix}, \quad (7.48)$$

and

$$|\psi'(s)\rangle = \begin{pmatrix} \cos(\eta(s)/2) \\ e^{-i\Gamma(s)} \sin(\eta(s)/2) \end{pmatrix}. \quad (7.49)$$

It is very clear from the above choice, that a pairs of inner products $\langle \psi_i | \psi_j \rangle$ and $\langle \psi'_i | \psi'_j \rangle$ or $\langle \psi_i | \psi'_j \rangle$ and $\langle \psi'_i | \psi_j \rangle$ or $\langle \psi_i | \psi'_j \rangle$ and $\langle \psi'_i | \psi_j \rangle$ are complex conjugate of each other. The $\Delta_3(\Psi_1, \Psi_2, \Psi_3)$ has eight terms where each term contains three such pairs. Hence, it is very straightforward to show that $\Delta_3(\Psi_1, \Psi_2, \Psi_3)$ is real and positive for the above choice of $|\psi(s)\rangle$ and $|\psi'(s)\rangle$. Hence the curve $\{|\tilde{\Psi}(s)\rangle\}$ is an NPC. For the given inner product between the end states, by choosing $\eta(s)$ and $\Gamma(s)$, one can generate NPCs. Since, one can construct infinitely many curves \mathcal{C} connecting the states $\{|\tilde{\Psi}_1\rangle, |\tilde{\Psi}_2\rangle\}$, we can construct infinitely many NPCs between these two states.

There is a particularly interesting subclass of NPC which can be useful. An arc of a great circle passing through the initial and final states is dual to itself and referred as “self-dual”.

This kind of curve on the Bloch sphere is given by (up to a unitary transformation)

$$|\psi(s)\rangle = \begin{pmatrix} \cos(\eta(s)/2) \\ \sin(\eta(s)/2) \end{pmatrix}; \quad s_1 \leq s \leq s_2 \quad (7.50)$$

with $\eta(s_1) = 0$, $\eta(s_2) = 2 \cos^{-1}(\alpha)$. A curve $\{|\tilde{\Psi}(s)\rangle = |\psi(s)\rangle \otimes |\psi(s)\rangle\}$ is also an NPC, which we shall call a self dual curve.

Although, we have presented the construction of NPCs for the end states which can be represented by degenerate MSs, same technique can be used to construct NPCs for arbitrary end states. As an example, let us construct an NPC connecting the two non-orthogonal states $|\Psi_1\rangle = (1 \ 0 \ 0)^T$ and $|\Psi_2\rangle = (\cos \theta \ \sin \theta \ 0)^T$ in three-dimensional state space. Since the state $|\Psi_2\rangle$ cannot be represented by degenerate MSs, we first apply a common unitary transformation U to bring this to the state represented by degenerate MSs. The appropriate unitary transformation U is of the form

$$U = \begin{pmatrix} 1 & 0 & 0 \\ 0 & a & b \\ 0 & -b & a \end{pmatrix}, \quad (7.51)$$

where $a = \sqrt{2}\alpha\beta/\sin \theta$, $b = \beta^2/\sin \theta$, $\alpha^2 = \cos \theta$ and $\alpha^2 + \beta^2 = 1$. The states after applying U reads

$$|\Psi'_1\rangle = \begin{pmatrix} 1 \\ 0 \\ 0 \end{pmatrix}, \quad |\Psi'_2\rangle = \begin{pmatrix} \cos \theta \\ a \sin \theta \\ -b \sin \theta \end{pmatrix} \quad (7.52)$$

which can further be written as

$$\begin{aligned} |\tilde{\Psi}_1\rangle &= |0\rangle \otimes |0\rangle \\ |\tilde{\Psi}_2\rangle &= |\phi\rangle \otimes |\phi\rangle \end{aligned}$$

where $|0\rangle$ and $|\phi\rangle$ are the same as defined earlier. We now take a pair of dual curves given in

Eq. (7.43) and Eq. (7.44) with appropriate boundary conditions on $\eta(s)$ and $\Gamma(s)$. Consequently, the state in three-dimensional state is written as

$$|\Psi'\rangle = \mathcal{N} \begin{pmatrix} 2 \cos^2(\eta(s)/2) \\ \sqrt{2} \cos(\eta(s)/2) \sin(\eta(s)/2) \cos(\Gamma(s)) \\ 2 \sin^2(\eta(s)/2) \end{pmatrix}$$

Now we apply U^\dagger on $|\Psi'\rangle$ to get the state $|\Psi\rangle$ back. With the appropriate choice of η and Γ we can bring it to the form which is already given in [57] as an example of an NPC. If we choose the functions $\eta(s)$ and $\Gamma(s)$ with $0 \leq s \leq \theta$ as

$$\begin{aligned} \eta(s) &= \cos^{-1} \left[\frac{A(s) - C(s)}{A(s) + C(s)} \right], \\ \Gamma(s) &= \tan^{-1} \left[\frac{\sqrt{4A(s)C(s) - B^2(s)}}{B(s)} \right], \end{aligned} \quad (7.53)$$

where

$$\begin{aligned} A(s) &= g(s) \cos s, \\ B(s) &= b(1 - g(s)^2)^{1/2} - ag(s) \sin s \\ C(s) &= a(1 - g(s)^2)^{1/2} + bg(s) \sin s \end{aligned} \quad (7.54)$$

with $0 \leq g(s) \leq 1$, and $g(0) = g(\theta) = 1$. This particular choice of the functions, results in an NPC given by

$$|\Psi(s)\rangle = \begin{pmatrix} g(s) \cos s \\ g(s) \sin s \\ (1 - g(s)^2)^{1/2} \end{pmatrix}; \quad 0 \leq s \leq \theta. \quad (7.55)$$

that is exactly the same derived in [57] between the states $|\Psi_1\rangle = (1 \ 0 \ 0)^T$ and $|\Psi_2\rangle = (\cos \theta \ \sin \theta \ 0)^T$. In Figs. 7.3(a), 7.3(b) we plot the geometric construction of NPCs on the Bloch sphere where we have chosen $g(s) = \cos[s(s - \theta)]$.

We have provided methods to generate NPCs in three-dimensional state space using pairs of dual curves on the Bloch sphere. Our method of constructing NPCs can be easily extended to n -dimensional state space. For example, for odd n , we can construct $(n - 1)/2$ number of pairs of dual curves to get an NPC. For the case when n is even, we take $(n - 2)/2$ number of

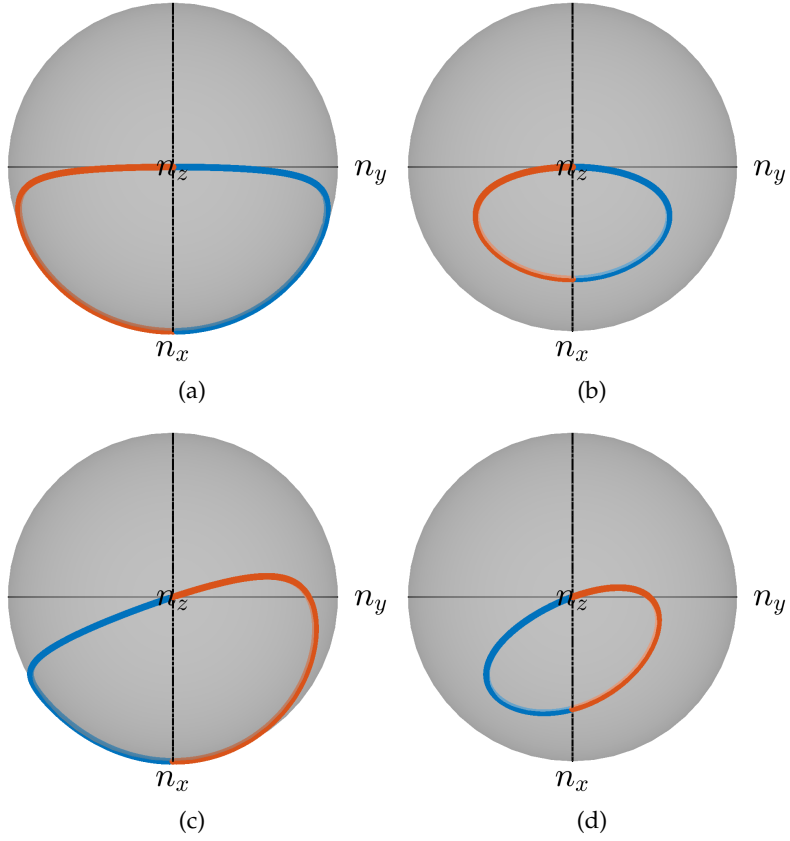


FIGURE 7.3: (Color online) Here we plot the Bloch geometric decomposition of NPCs in three-dimensional state space between the two states given in Eq. (7.52). In (a) $\theta = \pi/3$, (b) $\theta = \pi/6$ we plot the NPCs which are constructed by considering dual pairs of curves. Whereas, in (c) and (d) we plot the NPCs which are constructed by geometric decomposition of the curve in Eq. (7.57). We have chosen $\chi = \pi/3$ and the same values of θ as in (a) and (b).

pairs of dual curves and one curve along the great circle connecting the end states, to construct the NPC.

Example of NPCs which do not come under this category: Interestingly, there exist NPCs connecting the considered end states $|\Psi_1\rangle$ and $|\Psi_2\rangle$ which cannot be constructed either by a pair of dual curves or by self-dual curves. These NPCs are obtained from Eq. (7.55) by applying a unitary transformation which reads

$$V = \begin{pmatrix} 1 & 0 & 0 \\ 0 & 1 & 0 \\ 0 & 0 & e^{i\chi} \end{pmatrix}. \quad (7.56)$$

The BI is invariant under such unitary transformations and results in another NPC. The new NPC reads

$$|\Psi(s)\rangle \mapsto V |\Psi(s)\rangle = \begin{pmatrix} g(s) \cos s \\ g(s) \sin s \\ e^{i\chi} (1 - g(s)^2)^{1/2} \end{pmatrix}, \quad (7.57)$$

where the parameter $0 \leq s \leq \theta$, $\chi \in \mathbb{R}$ is a constant phase factor, $0 \leq g(s) \leq 1$ and $g(0) = g(\theta) = 1$. After a common unitary transformation, these NPCs decompose to a pair of curves which are not reflective about the great circle connecting the degenerate MSs on the Bloch sphere as shown in Fig. 7.3(c), 7.3(d). Therefore, this kind of NPCs cannot be constructed by choosing $\eta(s)$ and $\Gamma(s)$.

In conclusion, we have developed a Bloch sphere geometric decomposition for geodesics and NPCs in higher-dimensional state space. We have shown that geodesics connecting the two $(n - 1)$ -fold degenerate MS states in n -dimensional state space decompose to $n - 1$ number of circular segments on the Bloch sphere. The circular segments, which are uniquely determined by the radius and the end states, can be completely characterized by the MSs corresponding to the end states and the inner product between them. Therefore, once the MSs for the end states is known, we can construct the geodesic between any given states in n -dimensional state space. We have also shown that NPCs can be constructed between any given end states by constructing arbitrary pairs of dual curves between the end states. A particularly interesting class of NPCs is the one where all the curves are dual of themselves, i.e., self dual curves. The geometric decomposition presented in this paper reveals intrinsic symmetries in the geodesics and NPCs and improve our understanding of the geometric structure

of the higher-dimensional state space.

Chapter 8

Geometric Phase and non-inertial Effect

The experimental detection of the non-inertial effects in quantum field theory, e.g., the Unruh effect [322–325], the Hawking radiation [326, 327], has remained elusive till date because of the requirement of extreme conditions. For example, in the Unruh effect, to perceive a thermal effect of 1 K, typically an acceleration of the order of 10^{21} m/s² is required [325]. Numerous attempts have been made to relax extreme conditions using sophisticated techniques and precise measurements, but only to a limited success [328–339].

It has been further advocated that quantum features such as geometric phase (GP) may be of much usage in bringing down the scales involved. Moreover, due to its accumulative and sensitive nature, the GP can be helpful in capturing weak effects such as the non-inertial effects in quantum field theory.

It has been proposed [301] that using the GP the Unruh effect can be detected for accelerations as low as 10^{17} m/s², which, though a significant reduction in the acceleration typically required, is still extremely challenging to achieve. In [340], the GP acquired by a circularly rotating detector in free space was studied, but the detector's non-inertial response remains too feeble to be detectable at physically realizable accelerations.

Interestingly, the usage of an electromagnetic cavity has been argued to further relax the acceleration requirement by a few orders [331, 332, 341]. For example, by studying the spontaneous emission rate of an atom circularly rotating inside an electromagnetic cavity, it has been shown that the non-inertial effects can be detected at accelerations as low as 10^{12} m/s² [341].

In this work, we study the GP acquired by a circularly rotating two-level atom inside an electromagnetic cavity [303]. Since the GP is sensitive to transition rates and we already know that the transition rates become significantly modified inside the cavity [342], we expect the non-inertial component of the GP to be correspondingly modified. The accumulative nature of the GP [2, 32] facilitates the detection of weak effects such as the non-inertial modifications to the field correlators, whereas using the electromagnetic cavity the atom's non-inertial response can be isolated from, or strengthened relative to, the inertial response [341].

By studying the GP response of the atom inside an electromagnetic cavity, we show that the acceleration-induced modifications to the field correlators can be detected at much lower accelerations and with much relaxed parameters for the experimental setup. Specifically, we show that the atom acquires an experimentally detectable GP at accelerations of the order of 10^7 m/s^2 which is experimentally feasible. Therefore, an efficient GP measurement inside a cavity is supposed to manifest the non-inertial quantum field theoretic effects more robustly as compared to any other setup proposed so far.

8.1 Open quantum system description of the rotating atom and the Geometric phase

The state of a closed quantum system is represented, up to an overall phase, by a state vector $|\psi\rangle \in \mathcal{H}$, where \mathcal{H} is the Hilbert space of the system and $|\psi\rangle$ is said to be a pure state of the system. The evolution of a closed system is governed by Schroedinger equation [35]. In general, a system is found to be interacting with an external environment and pure states are not adequate for the description of such systems. The most general state of such a composite quantum system, called a mixed state, is represented by a density operator ρ such that

$$\rho = \rho^\dagger, \quad \text{Tr } \rho = 1, \quad \langle \phi | \rho | \phi \rangle > 0 \quad \forall |\phi\rangle \in \mathcal{H}_{\text{SE}}, \quad (8.1)$$

where \mathcal{H}_{SE} is the Hilbert space of the composite system. This will be helpful in the upcoming calculations where we consider an open system, state of which is described by a density operator.

We start by considering a two-level atom interacting with an electromagnetic field. The

atomic ground and excited states are denoted, respectively, by $|g\rangle$ and $|e\rangle$. The proper frequency gap between the two atomic levels is Ω_0 and the atom carries an electric dipole moment four-vector \hat{d}'^μ . Throughout this paper, primed quantities refer to the atom's co-moving frame. In the interaction picture, the dipole moment operator $\hat{\mathbf{d}}'(\tau)$ is given in terms of its matrix elements (as they will appear in later expressions) by

$$\hat{\mathbf{d}}'(\tau) = \mathbf{d}'\sigma_- \exp(-i\Omega_0\tau) + \mathbf{d}'^*\sigma_+ \exp(i\Omega_0\tau), \quad (8.2)$$

where $\mathbf{d}' \equiv \langle g | \hat{\mathbf{d}}'(\tau=0) | e \rangle$ and $\sigma_+ = \sigma_-^\dagger = |e\rangle\langle g|$ is the step-up operator for the atomic states. For simplicity, we assume that $\mathbf{d}' = (0, d', 0)$. The electromagnetic field is assumed to be in vacuum state $|0\rangle$. The interaction Hamiltonian between the atom and the electromagnetic field is given by $\hat{H}_I = -\hat{d}'^\mu E_\mu$ [343], where $E_\mu \equiv F_{\mu\nu}u^\nu$, $F_{\mu\nu}$ is the electromagnetic field strength tensor and u^ν is the four-velocity of the atom. The interaction Hamiltonian takes the form $\hat{H}_I = -\hat{\mathbf{d}}' \cdot \mathbf{E}'$ in the rest frame of the atom, where \mathbf{E}' is the electric field 3-vector as seen by the atom. The electric field operator inside a quantization volume V is given by [344]

$$\mathbf{E}[x(\tau)] = i \sum_{\mathbf{k}, \lambda} \mathcal{E}_k \epsilon_{\mathbf{k}, \lambda} \left(a_{\mathbf{k}, \lambda} e^{-i(\omega_k t(\tau) - \mathbf{k} \cdot \mathbf{x}(\tau))} - \text{h.c.} \right), \quad (8.3)$$

where $\mathcal{E}_k \equiv \sqrt{\hbar\omega_k/(2\epsilon_0 V)}$, $\epsilon_{\mathbf{k}, \lambda}$ with $\lambda = 1, 2$ are the two orthogonal polarization vectors, and h.c. denotes Hermitian conjugate.

In the rest frame of the atom, the evolution of the atom-field composite system is governed by [245]

$$\frac{d\rho_{\text{AF}}(\tau)}{d\tau} = -\frac{i}{\hbar}[H, \rho_{\text{AF}}(\tau)], \quad (8.4)$$

where ρ_{AF} is the density operator of the composite system and τ is the proper time of the atom. From (8.4), we can obtain the Lindblad evolution of the reduced density operator for the atom $\rho(\tau) \equiv \text{Tr}_F(\rho_{\text{AF}})$, which is given by [246]

$$\frac{d\rho(\tau)}{d\tau} = -\frac{i}{\hbar}[H_{\text{eff}}, \rho(\tau)] + \mathcal{L}[\rho(\tau)], \quad (8.5)$$

where

$$\mathcal{L}[\rho] = \frac{1}{2} \sum_{i,j=1}^3 a_{ij} (2\sigma_j \rho \sigma_i - \sigma_i \sigma_j \rho - \rho \sigma_i \sigma_j), \quad (8.6)$$

captures the dissipation and decoherence of the atom induced by its interaction with the elec-

tromagnetic field. The H_{eff} represents the Hamiltonian of the two-level atom with the renormalized atomic level spacing, Ω , which consists of the Lamb shift [245]. The σ_i 's are the standard Pauli matrices [345] and the coefficients a_{ij} are given by [346]

$$a_{ij} = A\delta_{ij} - iB\epsilon_{ijk}\delta_{k3} - A\delta_{i3}\delta_{j3}, \quad (8.7)$$

with A and B defined as

$$A = \frac{1}{4} [\Gamma_{\downarrow} + \Gamma_{\uparrow}], \quad B = \frac{1}{4} [\Gamma_{\downarrow} - \Gamma_{\uparrow}], \quad (8.8)$$

whereas,

$$\Gamma_{\downarrow\uparrow} = \left| \langle \psi_f | \hat{\mathbf{d}}'(0) | \psi_i \rangle \right|^2 \int_{-\infty}^{\infty} d\tau_{-} e^{\pm i\Omega_0\tau_{-}} G'^{\pm}(x(\tau_{-})), \quad (8.9)$$

with '+' and '-' corresponding to Γ_{\downarrow} and Γ_{\uparrow} , i.e., the emission and the absorption rates, respectively. Here, $\tau_{-} \equiv \tau_2 - \tau_1$; $|\psi_i\rangle, |\psi_f\rangle \in \{|g\rangle, |e\rangle\}$; and $G'^{\pm}(x(\tau_{-})) \equiv \langle 0 | E'^y(\tau_1) E'^y(\tau_2) | 0 \rangle$ is the two-point vacuum Wightman function. By taking the initial state of the atom to be

$$|\psi(0)\rangle = \cos(\theta/2) |e\rangle + \sin(\theta/2) |g\rangle, \quad (8.10)$$

and solving Eq. (8.5), we get the reduced density operator to be

$$\rho(\tau) = \begin{pmatrix} e^{-4A\tau} \cos^2(\theta/2) + \frac{B-A}{2A} (e^{-4A\tau} - 1) & \frac{1}{2} e^{-2A\tau - i\Omega\tau} \sin \theta \\ \frac{1}{2} e^{-2A\tau + i\Omega\tau} \sin \theta & 1 - e^{-4A\tau} \cos^2(\theta/2) - \frac{B-A}{2A} (e^{-4A\tau} - 1) \end{pmatrix}, \quad (8.11)$$

in which the effect of the environment is contained in A and B . The GP for an N -level quantum system in a mixed state and evolving non-unitarily is given by [32]

$$\gamma_g = \arg \left(\sum_{k=1}^N \sqrt{p_k(0)p_k(T)} \langle \phi_k(0) | \phi_k(T) \rangle e^{-\int_0^T \langle \phi_k(\tau) | \dot{\phi}_k(\tau) \rangle d\tau} \right), \quad (8.12)$$

where $p_k(\tau)$ and $|\phi_k(\tau)\rangle$ are instantaneous eigenvalues and eigenvectors of the system's den-

sity operator $\rho(\tau)$. The eigenvalues of $\rho(\tau)$ are

$$p_{\pm}(\tau) = \frac{1}{2}(1 \pm \lambda), \quad (8.13)$$

where $\lambda = \sqrt{r_3^2 + e^{-4A} \sin^2 \theta}$ and $r_3 = e^{-4A\tau} \cos \theta + \frac{B}{A}(e^{-4A\tau} - 1)$. Since $p_-(0) = 0$, the only eigenvector that contributes to γ_g is the one corresponding to p_+ which reads

$$|\phi_+(\tau)\rangle = \sin(\theta_\tau/2) |+\rangle + e^{i\Omega_0\tau} \cos(\theta_\tau/2) |-\rangle, \quad (8.14)$$

with

$$\tan(\theta_\tau/2) = \sqrt{\frac{\lambda + r_3}{\lambda - r_3}}. \quad (8.15)$$

By substituting Eq. (8.13) and Eq. (8.14) in the expression of the GP in Eq. (8.12), we get [302]

$$\gamma_g = -\frac{\Omega}{2} \int_0^T d\tau \left(1 - \frac{\mathcal{R} - \mathcal{R}e^{4A\tau} + \cos \theta}{\sqrt{e^{4A\tau} \sin^2 \theta + (\mathcal{R} - \mathcal{R}e^{4A\tau} + \cos \theta)^2}} \right), \quad (8.16)$$

where $\mathcal{R} \equiv B/A$. The above expression is valid for all time T . Now, if we take $T = 2\pi n/\Omega_0$, where n is the number of quasi-cycles, and if $A/\Omega_0 \ll 1$, we can further simplify the expression for γ_g and obtain [302]

$$\gamma_g = -\pi n(1 - \cos \theta) - \frac{2\pi^2 n^2}{\Omega_0} (2B + A \cos \theta) \sin^2 \theta, \quad (8.17)$$

where n is restricted by the demand $\pi n A/\Omega_0 \ll 1$, because to obtain (8.17) from (8.16), we need $4A\phi/\Omega_0 \ll 1$ and for n cycles $\phi = 2\pi n$. The GP has two contributions: the first term in Eq. (8.17) is due to the unitary evolution of the atom and the second term is coming from the non-unitary evolution of the atom which results from the atom's interaction with the environment. We will shortly see that in case of non-inertial motion of the atom, the non-unitary contribution can be further separated into an inertial and a non-inertial part. Further, using the cavity's resonance structure, the non-inertial contribution to the GP can be significantly enhanced.

8.2 GP response of the circularly rotating detector

In this section, we study the GP acquired by an atom moving on a circular trajectory of radius R and angular frequency ω , inside an electromagnetic cavity. We have seen in Eq. (8.17) that

the GP depends directly on the quantities A and B which, in turn, depend on the atomic transition rates. The non-inertial motion of the atom only affects the transition rates and leaves the form of Lindblad master equation [Eq. (8.5)] unchanged. Therefore, the expression of GP in Eq. (8.16) can be used in the case of a rotating atom with the modified transition rates. It is natural to start, therefore, by computing the transition rates and then obtain the GP.

We study the GP in two different regimes distinguished by the relative magnitudes of the rotational frequency of the atom (ω) and the atomic frequency gap (Ω_0). Specifically, we study the $\omega \gg \bar{\Omega}_0$ and $\omega \ll \bar{\Omega}_0$ regimes, where $\bar{\Omega}_0 \equiv \Omega_0 \sqrt{1 - \omega^2 R^2 / c^2}$. As we shall see, in the $\omega \gg \bar{\Omega}_0$ regime, the non-inertial contribution in the spontaneous decay rate dominates over the inertial one when the normal frequency of the cavity is tuned at $\omega + \bar{\Omega}_0$. In the $\omega \ll \bar{\Omega}_0$ regime, on the other hand, the inertial contribution to the GP overshadows the non-inertial component. However, with a suitable choice of parameters, the non-inertial contribution can be made comparable to the inertial component. Therefore, in both regimes, we can analyze the non-inertial contribution to the GP effectively.

8.2.1 Transition rates in the atom's frame

We get the transition rates in the lab frame for small $\zeta(\omega) \equiv \omega^2 R^2 / c^2$, and to the first order in $\zeta(\omega)$ as [303]

$$\Gamma_{\downarrow\uparrow}^{\text{lab}} = \eta \int_0^\infty dk \rho(k) \omega_k \left[\delta(\pm\bar{\Omega}_0 - \omega_k) + \frac{R^2 \omega^2}{2c^2} \frac{1}{2} [\delta(\pm\bar{\Omega}_0 - \omega_k + \omega) + \delta(\pm\bar{\Omega}_0 - \omega_k - \omega)] - \frac{\omega_k^2 R^2}{c^2} \frac{2}{5} \left\{ \delta(\pm\bar{\Omega}_0 - \omega_k) - \frac{1}{2} (\delta(\pm\bar{\Omega}_0 + \omega - \omega_k) + \delta(\pm\bar{\Omega}_0 - \omega - \omega_k)) \right\} \right], \quad (8.18)$$

where $\eta \equiv |\mathbf{d}|^2 / (3\pi\hbar\epsilon_0 V)$; '+' and '-' correspond, respectively, to the spontaneous decay rate (Γ_\downarrow) and the excitation rate (Γ_\uparrow) with $\rho(k)$ being the density of the field states. The transition rates in the co-moving frame can be obtained as $\Gamma_{\downarrow\uparrow} = \gamma \Gamma_{\downarrow\uparrow}^{\text{lab}}$. Inside a cavity, the density of states can be taken to be of Lorentzian form [347, 348]

$$\rho(\omega_k) \sim \frac{(\omega_c/Q)}{(\omega_c/Q)^2 + (\omega_k - \omega_c)^2}, \quad (8.19)$$

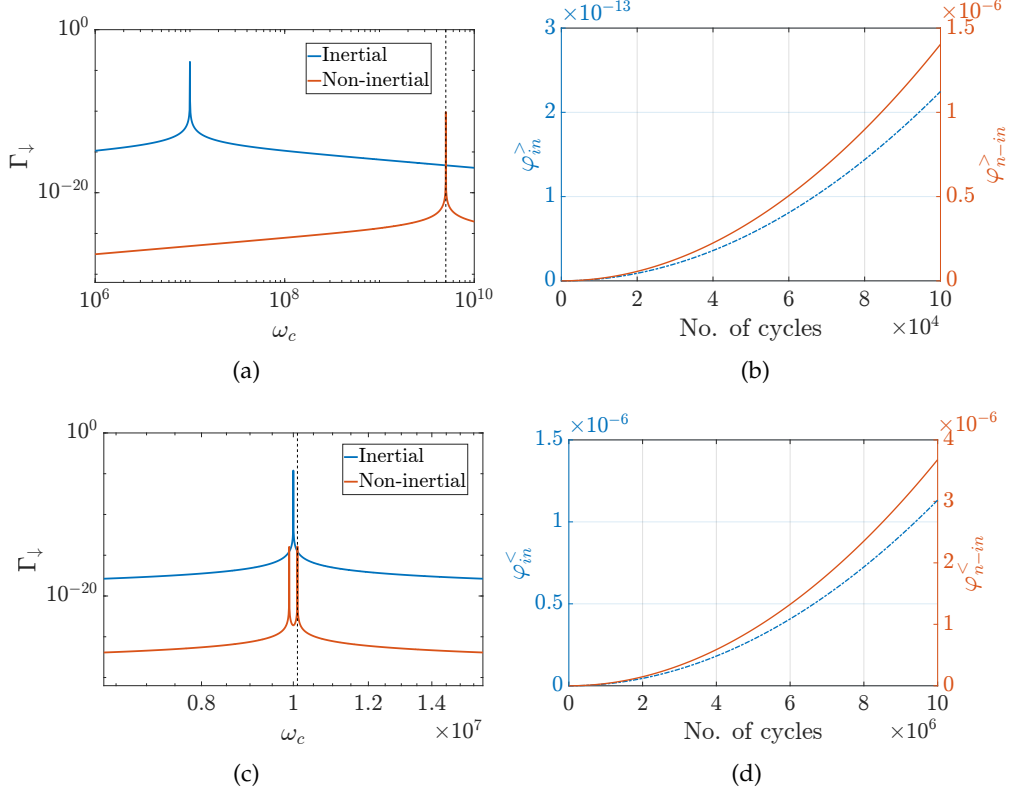


FIGURE 8.1: (Color online) The plot for Γ_{\downarrow} vs. ω_c and the non-unitary GP versus the number of quasi-cycles (n) in the two regimes discussed in the paper. We plot the inertial (φ_{in}) and the non-inertial contributions (φ_{n-in}) to the non-unitary GP here. (a),(b) $\omega \gg \bar{\Omega}_0$ with $\omega = 5$ GHz, $\Omega_0 = 10$ MHz, $V = 10^{-7}$ m³, and $R = 10^{-6}$ m which correspond to an average acceleration $a = \omega^2 R \sim 2.5 \times 10^{13}$ m/s². For this set of parameters, $\pi n A / \Omega_0 \sim 10^{-16} n$. (c),(d) $\omega \ll \bar{\Omega}_0$ with $\omega = 0.1$ MHz, $\Omega_0 = 10$ MHz, $V = 10^{-3}$ m³, and $R = 10^{-3}$ m which correspond to an average acceleration $a = \omega^2 R \sim 10^7$ m/s². The plots are for $\theta = \pi/2$ in Eq. (8.10). The vertical black dashed lines in Figs. (a), (c) mark the normal frequencies at which the cavity is tuned to obtain the GP versus n plots in Figs. (b),(d).

where ω_c is the normal frequency and Q is the quality factor of the cavity. The expression for the transition rates takes a simpler form in the two regimes, namely $\omega \gg \bar{\Omega}_0$ and $\omega \ll \bar{\Omega}_0$. Now, we shall explore the transition rates and the GP response of the atom in these two regimes.

Case 1: $\omega \gg \bar{\Omega}_0$

From Eq. (8.8), we know that A is the sum of the spontaneous emission and absorption rates and, therefore, up to the first order in $\zeta(\omega)$, using Eq. (8.18) is given by

$$A = \frac{\eta}{4} \left[\rho(\Omega_0) \Omega_0 - \frac{\zeta(\omega)}{2} \Omega_0^2 \rho'(\Omega_0) + \frac{9}{20} \zeta(\omega) \{ \omega_+ \rho(\omega_+) + \rho(\omega_-) \omega_- \} \right]. \quad (8.20)$$

where $\rho'(\omega) = \partial\rho/\partial\omega$ and $\omega_{\pm} \equiv \omega \pm \bar{\Omega}_0$. Similarly, B is obtained by replacing the term in curly brackets in Eq. (8.20) by $\omega_+\rho(\omega_+) - \rho(\omega_-)\omega_-$. Using (8.17), we obtain the non-unitary GP acquired by the atom in n number of quasi-cycles to be

$$\varphi^> = -\frac{2\pi^2 n^2 \eta}{\Omega_0} \frac{1}{4} \left[\left(\rho(\Omega_0)\Omega_0 - \frac{\zeta(\omega)}{2}\Omega_0^2\rho'(\Omega_0) \right) (2 + \cos\theta) + \frac{9}{20}\zeta(\omega) \left\{ \omega_+\rho(\omega_+)(2 + \cos\theta) - \omega_-\rho(\omega_-)(2 - \cos\theta) \right\} \right] \sin^2\theta, \quad (8.21)$$

where a quasi-cycle consists of a time period of $T = 2\pi/\Omega_0$. Note that we are using the symbol $\varphi^>$ to denote the non-unitary GP in the $\omega \gg \bar{\Omega}_0$ regime. Next, we discuss some numerical estimates of GP for realistic settings [341, 349, 350].

When we use A and B obtained by tuning the cavity to ω_+ , the non-unitary GP [see Eq. (8.21)] acquired by the atom is predominantly non-inertial [see Fig. 8.1(b)]. In Fig. 8.1(b) we plot the inertial and the non-inertial contributions to the GP acquired by the atom as a function of the number of quasi-cycles for $V = 10^{-7} \text{ m}^3$ and $R = 10^{-6} \text{ m}$. With these values for the parameters, $\pi An/\Omega_0 \sim 10^{-16}n$ which decides the allowed number of quasi-cycles consistent with the approximation made to obtain Eq. (8.17). We note from Fig. 8.1(b) that the system acquires an experimentally observable [351] non-inertial GP $\sim 10^{-6}$ radian (1 second radian) in roughly 10^5 quasi-cycles, whereas the inertial contribution to the GP is $\sim 10^{-13}$ radian in the same number of quasi-cycles.

Case 2: $\omega \ll \bar{\Omega}_0$

If $\omega \ll \bar{\Omega}_0$, the spontaneous emission rate can be approximated, to the first order in $\zeta(\omega)$, to be

$$\Gamma_{\downarrow} = \eta \left[\rho(\Omega_0)\Omega_0 - \frac{\zeta(\omega)}{2}\Omega_0^2\rho'(\Omega_0) + \frac{\zeta(\omega)}{4} (\rho(\bar{\Omega}_0^+)\bar{\Omega}_0^+ + \rho(\bar{\Omega}_0^-)\bar{\Omega}_0^-) - \frac{2}{5} \left\{ \zeta(\Omega_0)\rho(\Omega_0)\Omega_0 - \frac{1}{2} (\zeta(\bar{\Omega}_0^+)\rho(\bar{\Omega}_0^+)\bar{\Omega}_0^+ + \zeta(\bar{\Omega}_0^-)\rho(\bar{\Omega}_0^-)\bar{\Omega}_0^-) \right\} \right], \quad (8.22)$$

where $\bar{\Omega}_0^{\pm} = \bar{\Omega}_0 \pm \omega > 0$. The absorption rate to the first order in $\zeta(\omega)$ vanishes. Therefore, we have

$$A = B = \Gamma_{\downarrow}/4, \quad (8.23)$$

which leads to a non-unitary GP given by

$$\varphi^< = -\frac{\pi^2 n^2}{2\Omega_0} \Gamma_{\downarrow} (2 + \cos \theta) \sin^2 \theta, \quad (8.24)$$

where we have used the symbol $\varphi^<$ to denote the non-unitary GP in the $\omega \ll \bar{\Omega}_0$ regime. By choosing the parameters of the cavity carefully, we can make the inertial and the non-inertial contributions to the transition rate become comparable as shown in Fig. 8.1(c). Fig. 8.1(d) gives the plot of the inertial and the non-inertial contributions to the GP as a function of the number of quasi-cycles. With the parameters taken in Fig. 8.1(d), the allowed number of quasi-cycles consistent with Eq. (8.17) is determined by $\pi A n / \Omega_0 \ll 1$, that is, $10^{-21} n \ll 1$.

Here, we have studied the GP acquired by a circularly rotating two-level atom, inside an electromagnetic cavity, interacting with the electromagnetic field in the inertial vacuum. The acceleration-induced modifications to the field correlators perceived by the atom depend on the angular frequency of the rotating atom. We have studied GP in two distinct regimes characterized by $\omega \gg \bar{\Omega}_0$ and $\omega \ll \bar{\Omega}_0$. The $\omega \ll \bar{\Omega}_0$ regime is of particular experimental interest because one of the main hindrances to the detection of acceleration-induced modifications to field correlators is that such detection requires very high accelerations.

In the $\omega \gg \bar{\Omega}_0$ regime, for $\omega \sim 10^9$ Hz and $\Omega_0 \sim 10^7$ Hz, we have shown that the atom acquires a non-inertial GP $\sim 10^{-6}$ radian in 10^5 quasi-cycles, i.e., $\sim 10^{-2}$ s, while the inertial contribution remains insignificant, thereby successfully isolating the non-inertial response to the GP from the inertial one.

In general, in the $\omega \ll \bar{\Omega}_0$ regime the non-inertial GP comes out be much weaker than the inertial GP. However, we show that it is possible to make the two contributions comparable by tuning the cavity to $\bar{\Omega}_0 + \omega$ and taking a larger radius (R). Specifically, we achieve this by weakening the inertial response by tuning the cavity away from the atomic resonance. Note that we cannot indiscriminately increase R because an atom rotating on a larger radius requires a bigger cavity to encase it and a larger cavity volume suppresses the overall detector response. By allowing the atom to evolve for $\sim 10^7$ quasi-cycles, a non-inertial GP $\sim 10^{-6}$ radian can be acquired, which is comparable to the inertial GP acquired by the atom. This will enable the possibility of the detection of acceleration-induced modifications to field correlators with much more relaxed parameters compared to previous studies [301, 341].

Specifically, we have shown, in the $\omega \ll \bar{\Omega}_0$ regime, that it is possible to detect the acceleration-induced modifications to the field correlators at an acceleration $\sim 10^7$ m/s². Compare this with the accelerations required for the non-inertial effects to be substantial in other proposals. For example, the Unruh effect demands acceleration of the order of 10^{21} m/s² if the detector transition rates are used as an observable [324], and 10^{17} m/s² if GP is used as an observable [301]. Similarly, detecting non-inertial effects using a circularly rotating atom inside an electromagnetic cavity, by observing the atomic spontaneous decay rate, requires an acceleration of the order of 10^{12} m/s² [341]. Thus we demonstrate that, aided by the cavity, usage of the GP response for observing weak, but nontrivial, non-inertial effects in quantum field theory is a much sensitive and powerful tool.

Chapter 9

Conclusion and Future Outlook

The geometric phase is one of the fundamental aspects of quantum mechanics as it accounts for a wide range of phenomena. It provides a way to classify distinct phases (topological) of matter in condensed matter physics which is a central theme. It further facilitates the precise measurement and capturing of the weak effects. In this thesis, we reviewed the fundamental structure of the geometric phase and studied a number of its applications.

The geometrical representation of the state space of an n -level quantum system is essential in characterizing the system. One possible way to achieve that is to understand the structure of geodesics and null phase curves in the state space. In this thesis, we proposed a fresh geometrical perspective of geodesics and null phase curves in higher-dimensional state spaces. This geometrical decomposition provides a consistent way to construct geodesics and a class of null phase curves in d -level systems. We used Majorana star representation which maps a pure quantum state of an n -level system to the symmetric subspace of $(n-1)$ two-level systems. This work can be instrumental in studying the topological phases in the systems with three or more band structures. Also, geodesics can be used to design optimal quantum circuits, which is equivalent to finding the shortest path between two points in a certain curved geometry.

The geometric phase is an integral component in characterizing the topological phases. Quantum walks are the quantum analog of classical random walks. They have started gaining popularity among condensed matter physicists in the last decade because one can simulate these topological phases in one (1D) and two-dimensional (2D) discrete-time quantum walks (DTQW). We studied the topological order in 1D and 2D quantum walks. We investigated

the behavior of topological phases in the presence of a lossy environment that leads to non-Hermiticity. The non-Hermitian systems exhibit rich topological structure due to the complex-valued spectrum and the presence of exceptional points. We take the non-Hermitian Hamiltonian approach to include the environmental effects and find that the topological phases in quantum walks are robust against moderate losses. We unveiled a persistence of topological order for one-dimensional quantum walks as long as the system respects the parity-time \mathcal{PT} -symmetry. We also find the persistent nature of topological phases in two-dimensional quantum walks. However, \mathcal{PT} -symmetry does not play a role there. We further showed the bulk-boundary correspondence to support our results.

We further used the geometric phase to encapsulate the weak effect of the non-inertial motion of a quantum system. We studied the non-inertial effects in a rotating two-level atom placed inside an electromagnetic cavity. The electromagnetic cavity allows us to isolate and strengthen the non-inertial effects, over inertial ones, by appropriately tuning the resonance frequency. The sensitive nature of the geometric phase is instrumental in capturing the impact of the rotation through transition rates. Further, the accumulative nature of the geometric phase facilitates the experimental observation of the weak effects at very low accelerations. We demonstrated that aided by the cavity, usage of the GP response for observing weak but nontrivial, non-inertial effects in quantum field theory is a much more sensitive and powerful tool.

The existing definitions of geometric phases are primarily mathematical. In the future, we plan to introduce an operational definition of the geometric phase, which does not require explicit information about the state. It will lead to a more profound understanding of the subject. Continuing our work on geometric phase-assisted observation of non-inertial cavity-QED effects, we plan to use the geometric phase to observe the weak response in other phenomenons, for example, to observe the gravitational waves.

List of Publications

1. **Vikash Mittal**, Aswathy Raj, Sanjib Dey & Sandeep K. Goyal, “Persistence of topological phases in non-Hermitian quantum walks” *Scientific Reports* **11**, 10262, (2021),
2. **Vikash Mittal**, Akhilesh K.S. & Sandeep K. Goyal, “Geometric decomposition of geodesics and null phase curves using Majorana star representation” *Phys. Rev. A* **105**, 052219 (2022),
3. [†] Navdeep Arya, **Vikash Mittal**, Kinjalk Lochan and Sandeep K. Goyal, “Geometric phase assisted observation of non-inertial cavity-QED effects” *Phys. Rev. D* **106**, 045011, Aug (2022).

[†]Partially included in the thesis

Bibliography

- [1] Marie Ericsson, Daryl Achilles, Julio T. Barreiro, David Branning, Nicholas A. Peters, and Paul G. Kwiat. Measurement of geometric phase for mixed states using single photon interferometry. *Phys. Rev. Lett.*, 94:050401, Feb 2005.
- [2] Michael Victor Berry. Quantal phase factors accompanying adiabatic changes. *Proceedings of the Royal Society of London. A. Mathematical and Physical Sciences*, 392(1802):45–57, 1984.
- [3] Y. Aharonov and D. Bohm. Significance of electromagnetic potentials in the quantum theory. *Phys. Rev.*, 115:485–491, Aug 1959.
- [4] K. v. Klitzing, G. Dorda, and M. Pepper. New method for high-accuracy determination of the fine-structure constant based on quantized hall resistance. *Phys. Rev. Lett.*, 45:494–497, Aug 1980.
- [5] D. C. Tsui, H. L. Stormer, and A. C. Gossard. Two-dimensional magnetotransport in the extreme quantum limit. *Phys. Rev. Lett.*, 48:1559–1562, May 1982.
- [6] Jeffrey C. Y. Teo and C. L. Kane. Topological defects and gapless modes in insulators and superconductors. *Phys. Rev. B*, 82:115120, Sep 2010.
- [7] Jonathan A. Jones, Vlatko Vedral, Artur Ekert, and Giuseppe Castagnoli. Geometric quantum computation using nuclear magnetic resonance. *Nature*, 403(6772):869–871, Feb 2000.
- [8] Jason Alicea, Yuval Oreg, Gil Refael, Felix von Oppen, and Matthew P. A. Fisher. Non-abelian statistics and topological quantum information processing in 1d wire networks. *Nature Physics*, 7(5):412–417, May 2011.

- [9] N. Mukunda and R. Simon. Quantum kinematic approach to the geometric phase. I. general formalism. *Annals of Physics*, 228(2):205–268, 1993.
- [10] Eqab M. Rabei, Arvind, N. Mukunda, and R. Simon. Bargmann invariants and geometric phases: A generalized connection. *Phys. Rev. A*, 60:3397–3409, Nov 1999.
- [11] Ettore Majorana. Atomi orientati in campo magnetico variabile. *Il Nuovo Cimento (1924-1942)*, 9(2):43–50, Feb 1932.
- [12] J. Zak. Berry’s phase for energy bands in solids. *Phys. Rev. Lett.*, 62:2747–2750, Jun 1989.
- [13] Tudor D Stanescu. *Introduction to topological quantum matter & quantum computation*. CRC Press, 2016.
- [14] Takuya Kitagawa, Mark S. Rudner, Erez Berg, and Eugene Demler. Exploring topological phases with quantum walks. *Phys. Rev. A*, 82:033429, Sep 2010.
- [15] Takuya Kitagawa. Topological phenomena in quantum walks: elementary introduction to the physics of topological phases. *Quantum Information Processing*, 11(5):1107–1148, Oct 2012.
- [16] F Wilczek and A Shapere. *Geometric Phases in Physics*. WORLD SCIENTIFIC, 1989.
- [17] D. Chruscinski and A. Jamiolkowski. *Geometric Phases in Classical and Quantum Mechanics*. Progress in Mathematical Physics. Birkhäuser Boston, 2012.
- [18] A. Bohm, A. Mostafazadeh, H. Koizumi, Q. Niu, and J. Zwanziger. *The Geometric Phase in Quantum Systems: Foundations, Mathematical Concepts, and Applications in Molecular and Condensed Matter Physics*. Theoretical and Mathematical Physics. Springer Berlin Heidelberg, 2013.
- [19] Qian Niu, Ming-Che Chang, Biao Wu, Di Xiao, and Ran Cheng. *Physical Effects of Geometric Phases*. WORLD SCIENTIFIC, 2017.
- [20] S. Pancharatnam. Generalized theory of interference and its applications. *Proceedings of the Indian Academy of Sciences - Section A*, 44(6):398–417, Dec 1956.
- [21] Barry Simon. Holonomy, the quantum adiabatic theorem, and berry’s phase. *Phys. Rev. Lett.*, 51:2167–2170, Dec 1983.

- [22] Vlatko Vedral. Geometric phases and topological quantum computation. *International Journal of Quantum Information*, 01(01):1–23, 2003.
- [23] Rajendra Bhandari. Polarization of light and topological phases. *Phys. Rep.*, 281(1):1–64, 1997.
- [24] Hidenori Sonoda. Berry’s phase in chiral gauge theories. *Nucl. Phys. B*, 266(2):410–422, 1986.
- [25] Y. Aharonov and J. Anandan. Phase change during a cyclic quantum evolution. *Phys. Rev. Lett.*, 58:1593–1596, Apr 1987.
- [26] Joseph Samuel and Rajendra Bhandari. General setting for berry’s phase. *Phys. Rev. Lett.*, 60:2339–2342, Jun 1988.
- [27] V. Bargmann. Note on wigner’s theorem on symmetry operations. *Journal of Mathematical Physics*, 5(7):862–868, 1964.
- [28] Joseph Samuel and Rajendra Bhandari. General setting for berry’s phase. *Phys. Rev. Lett.*, 60:2339–2342, Jun 1988.
- [29] N. Mukunda and R. Simon. Quantum kinematic approach to the geometric phase. i. general formalism. *Annals of Physics*, 228(2):205 – 268, 1993.
- [30] Armin Uhlmann. Parallel transport and quantum holonomy along density operators. *Reports on Mathematical Physics*, 24(2):229 – 240, 1986.
- [31] Erik Sjöqvist, Arun K. Pati, Artur Ekert, Jeeva S. Anandan, Marie Ericsson, Daniel K. L. Oi, and Vlatko Vedral. Geometric phases for mixed states in interferometry. *Phys. Rev. Lett.*, 85:2845–2849, Oct 2000.
- [32] D. M. Tong, E. Sjöqvist, L. C. Kwek, and C. H. Oh. Kinematic approach to the mixed state geometric phase in nonunitary evolution. *Phys. Rev. Lett.*, 93:080405, Aug 2004.
- [33] Tosio Kato. On the adiabatic theorem of quantum mechanics. *Journal of the Physical Society of Japan*, 5(6):435–439, 1950.
- [34] A. Messiah. *Quantum Mechanics*. Dover Books on Physics. Dover Publications, 2014.
- [35] J.J. Sakurai and S.F. Tuan. *Modern Quantum Mechanics*. Benjamin/Cummings Pub., California, 1985.

- [36] Don N. Page. Geometrical description of berry's phase. *Phys. Rev. A*, 36:3479–3481, Oct 1987.
- [37] K. Vogtmann, A. Weinstein, and V.I. Arnol'd. *Mathematical Methods of Classical Mechanics*. Graduate Texts in Mathematics. Springer New York, NY, 1997.
- [38] S. Pancharatnam. Generalized theory of interference and its applications. *Proceedings of the Indian Academy of Sciences - Section A*, 44(6):398–417, Dec 1956.
- [39] S. Ramaseshan and Rajaram Nityananda. The interference of polarized light as an early example of berry's phase. *Current Science*, 55(24):1225–1226, 1986.
- [40] Barry Simon. Holonomy, the quantum adiabatic theorem, and berry's phase. *Phys. Rev. Lett.*, 51:2167–2170, Dec 1983.
- [41] Zhifan Zhou, Yair Margalit, Samuel Moukouri, Yigal Meir, and Ron Folman. An experimental test of the geodesic rule proposition for the noncyclic geometric phase. *Science Advances*, 6(9):eaay8345, 2020.
- [42] Manfredo P Do Carmo. *Differential geometry of curves and surfaces: revised and updated second edition*. Courier Dover Publications, 2016.
- [43] R. Kimmel, A. Amir, and A.M. Bruckstein. Finding shortest paths on surfaces using level sets propagation. *IEEE Transactions on Pattern Analysis and Machine Intelligence*, 17(6):635–640, 1995.
- [44] Angelo Carollo, Davide Valenti, and Bernardo Spagnolo. Geometry of quantum phase transitions. *Physics Reports*, 838:1–72, 2020. Geometry of quantum phase transitions.
- [45] Young-Wook Cho, Yosep Kim, Yeon-Ho Choi, Yong-Su Kim, Sang-Wook Han, Sang-Yun Lee, Sung Moon, and Yoon-Ho Kim. Emergence of the geometric phase from quantum measurement back-action. *Nature Physics*, 15(7):665–670, Jul 2019.
- [46] Valentin Gebhart, Kyrylo Snizhko, Thomas Wellens, Andreas Buchleitner, Alessandro Romito, and Yuval Gefen. Topological transition in measurement-induced geometric phases. *Proceedings of the National Academy of Sciences*, 117(11):5706–5713, 2020.
- [47] P. Facchi, A.G. Klein, S. Pascazio, and L.S. Schulman. Berry phase from a quantum zeno effect. *Physics Letters A*, 257(5):232 – 240, 1999.

- [48] Akira Tomita and Raymond Y. Chiao. Observation of berry's topological phase by use of an optical fiber. *Phys. Rev. Lett.*, 57:937–940, Aug 1986.
- [49] Dieter Suter, Gerard C. Chingas, Robert A. Harris, and Alexander Pines. Berry's phase in magnetic resonance. *Molecular Physics*, 61(6):1327–1340, 1987.
- [50] T. Bitter and D. Dubbers. Manifestation of berry's topological phase in neutron spin rotation. *Phys. Rev. Lett.*, 59:251–254, Jul 1987.
- [51] H. von Busch, Vas Dev, H.-A. Eckel, S. Kasahara, J. Wang, W. Demtröder, P. Sebald, and W. Meyer. Unambiguous proof for berry's phase in the sodium trimer: Analysis of the transition A^2E'' . *Phys. Rev. Lett.*, 81:4584–4587, Nov 1998.
- [52] Yuanbo Zhang, Yan-Wen Tan, Horst L. Stormer, and Philip Kim. Experimental observation of the quantum hall effect and berry's phase in graphene. *Nature*, 438(7065):201–204, Nov 2005.
- [53] J. C. Loredó, O. Ortíz, R. Weingärtner, and F. De Zela. Measurement of pancharatnam's phase by robust interferometric and polarimetric methods. *Phys. Rev. A*, 80:012113, Jul 2009.
- [54] Apoorva G. Wagh and Veer Chand Rakhecha. On measuring the pancharatnam phase. i. interferometry. *Physics Letters A*, 197(2):107–111, 1995.
- [55] Apoorva G. Wagh and Veer Chand Rakhecha. On measuring the pancharatnam phase. ii. su(2) polarimetry. *Physics Letters A*, 197(2):112–115, 1995.
- [56] T. Malhotra, R. Gutiérrez-Cuevas, J. Hassett, M. R. Dennis, A. N. Vamivakas, and M. A. Alonso. Measuring geometric phase without interferometry. *Phys. Rev. Lett.*, 120:233602, Jun 2018.
- [57] N. Mukunda, Arvind, E. Ercolessi, G. Marmo, G. Morandi, and R. Simon. Bargmann invariants, null phase curves, and a theory of the geometric phase. *Phys. Rev. A*, 67:042114, Apr 2003.
- [58] K. Singh, D. M. Tong, K. Basu, J. L. Chen, and J. F. Du. Geometric phases for nondegenerate and degenerate mixed states. *Phys. Rev. A*, 67:032106, Mar 2003.
- [59] D. M. Tong, E. Sjöqvist, L. C. Kwek, and C. H. Oh. Kinematic approach to the mixed state geometric phase in nonunitary evolution. *Phys. Rev. Lett.*, 93:080405, Aug 2004.

- [60] Angelo Bassi and Emiliano Ippoliti. Geometric phase for open quantum systems and stochastic unravelings. *Phys. Rev. A*, 73:062104, Jun 2006.
- [61] A. Carollo, I. Fuentes-Guridi, M. França Santos, and V. Vedral. Geometric phase in open systems. *Phys. Rev. Lett.*, 90:160402, Apr 2003.
- [62] F. M. Cucchietti, J.-F. Zhang, F. C. Lombardo, P. I. Villar, and R. Laflamme. Geometric phase with nonunitary evolution in the presence of a quantum critical bath. *Phys. Rev. Lett.*, 105:240406, Dec 2010.
- [63] X X Yi, D P Liu, and W Wang. Quantum trajectory approach to the geometric phase: open bipartite systems. *New Journal of Physics*, 7:222–222, oct 2005.
- [64] T. S. Yakovleva, A. M. Rostom, V. A. Tomilin, and L. V. Il'ichov. Geometric phase in open quantum system as a function of its history. *Quantum Studies: Mathematics and Foundations*, 6(2):217–224, Jun 2019.
- [65] A. Carollo, I. Fuentes-Guridi, M. França Santos, and V. Vedral. Spin-1/2 geometric phase driven by decohering quantum fields. *Phys. Rev. Lett.*, 92:020402, Jan 2004.
- [66] Marie Ericsson, Daryl Achilles, Julio T. Barreiro, David Branning, Nicholas A. Peters, and Paul G. Kwiat. Measurement of geometric phase for mixed states using single photon interferometry. *Phys. Rev. Lett.*, 94:050401, Feb 2005.
- [67] Armin Uhlmann. A gauge field governing parallel transport along mixed states. *Letters in Mathematical Physics*, 21(3):229–236, Mar 1991.
- [68] Marie Ericsson, Arun K. Pati, Erik Sjöqvist, Johan Brännlund, and Daniel K. L. Oi. Mixed state geometric phases, entangled systems, and local unitary transformations. *Phys. Rev. Lett.*, 91:090405, Aug 2003.
- [69] O. Viyuela, A. Rivas, and M. A. Martin-Delgado. Uhlmann phase as a topological measure for one-dimensional fermion systems. *Phys. Rev. Lett.*, 112:130401, Apr 2014.
- [70] O. Viyuela, A. Rivas, and M. A. Martin-Delgado. Two-dimensional density-matrix topological fermionic phases: Topological uhlmann numbers. *Phys. Rev. Lett.*, 113:076408, Aug 2014.
- [71] O Viyuela, A Rivas, and M A Martin-Delgado. Symmetry-protected topological phases at finite temperature. *2D Materials*, 2(3):034006, jun 2015.

- [72] Paul B. Slater. Mixed state holonomies. *Letters in Mathematical Physics*, 60(2):123–133, May 2002.
- [73] A. T. Rezakhani and P. Zanardi. General setting for a geometric phase of mixed states under an arbitrary nonunitary evolution. *Phys. Rev. A*, 73:012107, Jan 2006.
- [74] O Andersson and H Heydari. Operational geometric phase for mixed quantum states. *New Journal of Physics*, 15(5):053006, may 2013.
- [75] J. Zhu, M. Shi, V. Vedral, X. Peng, D. Suter, and J. Du. Experimental demonstration of a unified framework for mixed-state geometric phases. *EPL (Europhysics Letters)*, 94(2):20007, April 2011.
- [76] Da-Jian Zhang and Jiangbin Gong. Topological characterization of one-dimensional open fermionic systems. *Phys. Rev. A*, 98:052101, Nov 2018.
- [77] S. Chaturvedi, E. Ercolessi, G. Marmo, G. Morandi, N. Mukunda, and R. Simon. Geometric phase for mixed states: a differential geometric approach. *The European Physical Journal C - Particles and Fields*, 35(3):413–423, Jun 2004.
- [78] J. G. Peixoto de Faria, A. F. R. de Toledo Piza, and M. C Nemes. Phases of quantum states in completely positive non-unitary evolution. *Europhysics Letters (EPL)*, 62(6):782–788, jun 2003.
- [79] A. Carollo, I. Fuentes-Guridi, M. França Santos, and V. Vedral. Geometric phase in open systems. *Phys. Rev. Lett.*, 90:160402, Apr 2003.
- [80] A. Uhlmann. On berry phases along mixtures of states. *Annalen der Physik*, 501(1):63–69, 1989.
- [81] Armin Uhlmann. Geometric phases and related structures. *Reports on Mathematical Physics*, 36(2):461–481, 1995. Proceedings of the XXVI Symposium on Mathematical Physics.
- [82] Armin Uhlmann. Transition probability (fidelity) and its relatives. *Foundations of Physics*, 41(3):288–298, Mar 2011.
- [83] Michael A. Nielsen and Isaac L. Chuang. *Quantum Computation and Quantum Information: 10th Anniversary Edition*. Cambridge University Press, New York, NY, USA, 10th edition, 2011.

- [84] Richard Jozsa. Fidelity for mixed quantum states. *Journal of Modern Optics*, 41(12):2315–2323, 1994.
- [85] Matthias Hübner. Computation of uhlmann’s parallel transport for density matrices and the bures metric on three-dimensional hilbert space. *Physics Letters A*, 179(4):226 – 230, 1993.
- [86] Zhoushen Huang and Daniel P. Arovas. Topological indices for open and thermal systems via uhlmann’s phase. *Phys. Rev. Lett.*, 113:076407, Aug 2014.
- [87] Ole Andersson, Ingemar Bengtsson, Marie Ericsson, and Erik Sjöqvist. Geometric phases for mixed states of the kitaev chain. *Philosophical Transactions of the Royal Society A: Mathematical, Physical and Engineering Sciences*, 374(2068):20150231, 2016.
- [88] Bruno Mera, Chrysoula Vlachou, Nikola Paunković, and Vítor R. Vieira. Uhlmann connection in fermionic systems undergoing phase transitions. *Phys. Rev. Lett.*, 119:015702, Jul 2017.
- [89] Yan He, Hao Guo, and Chih-Chun Chien. Thermal uhlmann-chern number from the uhlmann connection for extracting topological properties of mixed states. *Phys. Rev. B*, 97:235141, Jun 2018.
- [90] O. Viyuela, A. Rivas, S. Gasparinetti, A. Wallraff, S. Filipp, and M. A. Martin-Delgado. Observation of topological uhlmann phases with superconducting qubits. *npj Quantum Information*, 4(1):10, Feb 2018.
- [91] Jan Carl Budich and Sebastian Diehl. Topology of density matrices. *Phys. Rev. B*, 91:165140, Apr 2015.
- [92] Charles-Edouard Bardyn, Lukas Wawer, Alexander Altland, Michael Fleischhauer, and Sebastian Diehl. Probing the topology of density matrices. *Phys. Rev. X*, 8:011035, Feb 2018.
- [93] Lukas Wawer and Michael Fleischhauer. Chern number and berry curvature for gaussian mixed states of fermions. *Phys. Rev. B*, 104:094104, Sep 2021.
- [94] Yakir Aharonov, David Z. Albert, and Lev Vaidman. How the result of a measurement of a component of the spin of a spin-1/2 particle can turn out to be 100. *Phys. Rev. Lett.*, 60:1351–1354, Apr 1988.

- [95] Y Aharonov and L Vaidman. Complete description of a quantum system at a given time. *Journal of Physics A: Mathematical and General*, 24(10):2315–2328, may 1991.
- [96] Justin Dressel, Mehul Malik, Filippo M. Miatto, Andrew N. Jordan, and Robert W. Boyd. Colloquium: Understanding quantum weak values: Basics and applications. *Rev. Mod. Phys.*, 86:307–316, Mar 2014.
- [97] Erik Sjöqvist. Geometric phase in weak measurements. *Physics Letters A*, 359(3):187 – 189, 2006.
- [98] J. von Neumann and R.T. Beyer. *Mathematical Foundations of Quantum Mechanics*. Goldstone Printed Materials. Princeton University Press, 1955.
- [99] Richard Jozsa. Complex weak values in quantum measurement. *Phys. Rev. A*, 76:044103, Oct 2007.
- [100] A. Van Oosterom and J. Strackee. The solid angle of a plane triangle. *IEEE Transactions on Biomedical Engineering*, BME-30(2):125–126, Feb 1983.
- [101] Shengjun Wu and Klaus Mølmer. Weak measurements with a qubit meter. *Physics Letters A*, 374(1):34 – 39, 2009.
- [102] D. Morachis Galindo, F. Rojas, and Jesús A. Maytorena. Topological uhlmann phase transitions for a spin- j particle in a magnetic field. *Phys. Rev. A*, 103:042221, Apr 2021.
- [103] Ye Zhang, Aixin Pi, Yan He, and Chih-Chun Chien. Comparison of finite-temperature topological indicators based on uhlmann connection. *Phys. Rev. B*, 104:165417, Oct 2021.
- [104] Y. Aharonov, L. Davidovich, and N. Zagury. Quantum random walks. *Phys. Rev. A*, 48:1687–1690, Aug 1993.
- [105] Andris Ambainis, Eric Bach, Ashwin Nayak, Ashvin Vishwanath, and John Watrous. One-dimensional quantum walks. In *Proceedings of the Thirty-Third Annual ACM Symposium on Theory of Computing*, STOC 01, pages 37 – 49, New York, NY, USA, 2001. Association for Computing Machinery.
- [106] J Kempe. Quantum random walks: An introductory overview. *Contemporary Physics*, 44(4):307–327, 2003.
- [107] Salvador Elías Venegas-Andraca. Quantum walks: a comprehensive review. *Quantum Information Processing*, 11(5):1015–1106, Oct 2012.

- [108] Ashwin Nayak and Ashvin Vishwanath. Quantum Walk on the Line. *arXiv e-prints*, pages quant-ph/0010117, October 2000.
- [109] Andrew M. Childs. Universal computation by quantum walk. *Phys. Rev. Lett.*, 102:180501, May 2009.
- [110] Andrew M. Childs, David Gosset, and Zak Webb. Universal computation by multipartite quantum walk. *Science*, 339(6121):791–794, 2013.
- [111] Neil B. Lovett, Sally Cooper, Matthew Everitt, Matthew Trevers, and Viv Kendon. Universal quantum computation using the discrete-time quantum walk. *Phys. Rev. A*, 81:042330, Apr 2010.
- [112] Andris Ambainis. Quantum walks and their algorithmic applications. *International Journal of Quantum Information*, 01(04):507–518, 2003.
- [113] Andrew M. Childs and Jeffrey Goldstone. Spatial search by quantum walk. *Phys. Rev. A*, 70:022314, Aug 2004.
- [114] Neil Shenvi, Julia Kempe, and K. Birgitta Whaley. Quantum random-walk search algorithm. *Phys. Rev. A*, 67:052307, May 2003.
- [115] E. Agliari, A. Blumen, and O. Mülken. Quantum-walk approach to searching on fractal structures. *Phys. Rev. A*, 82:012305, Jul 2010.
- [116] Dengke Qu, Samuel Marsh, Kunkun Wang, Lei Xiao, Jingbo Wang, and Peng Xue. Deterministic search on star graphs via quantum walks. *Phys. Rev. Lett.*, 128:050501, Feb 2022.
- [117] Francesco De Nicola, Linda Sansoni, Andrea Crespi, Roberta Ramponi, Roberto Oselame, Vittorio Giovannetti, Rosario Fazio, Paolo Mataloni, and Fabio Sciarrino. Quantum simulation of bosonic-fermionic noninteracting particles in disordered systems via a quantum walk. *Phys. Rev. A*, 89:032322, Mar 2014.
- [118] Paweł Kurzyński and Antoni Wójcik. Discrete-time quantum walk approach to state transfer. *Phys. Rev. A*, 83:062315, Jun 2011.
- [119] Andreas Schreiber, Aurél Gábris, Peter P. Rohde, Kaisa Laiho, Martin Štefaňák, Václav Potoček, Craig Hamilton, Igor Jex, and Christine Silberhorn. A 2d quantum walk simulation of two-particle dynamics. *Science*, 336(6077):55–58, 2012.

- [120] Linda Sansoni, Fabio Sciarrino, Giuseppe Vallone, Paolo Mataloni, Andrea Crespi, Roberta Ramponi, and Roberto Osellame. Two-particle bosonic-fermionic quantum walk via integrated photonics. *Phys. Rev. Lett.*, 108:010502, Jan 2012.
- [121] Alberto Peruzzo, Mirko Lobino, Jonathan C. F. Matthews, Nobuyuki Matsuda, Alberto Politi, Konstantinos Poulios, Xiao-Qi Zhou, Yoav Lahini, Nur Ismail, Kerstin Wörhoff, Yaron Bromberg, Yaron Silberberg, Mark G. Thompson, and Jeremy L. O'Brien. Quantum walks of correlated photons. *Science*, 329(5998):1500–1503, 2010.
- [122] Masoud Mohseni, Patrick Rebentrost, Seth Lloyd, and Alán Aspuru-Guzik. Environment-assisted quantum walks in photosynthetic energy transfer. *The Journal of Chemical Physics*, 129(17):174106, 2008.
- [123] Neill Lambert, Yueh-Nan Chen, Yuan-Chung Cheng, Che-Ming Li, Guang-Yin Chen, and Franco Nori. Quantum biology. *Nature Physics*, 9(1):10–18, Jan 2013.
- [124] A. Romanelli, A. Auyuanet, R. Siri, G. Abal, and R. Donangelo. Generalized quantum walk in momentum space. *Physica A: Statistical Mechanics and its Applications*, 352(2):409–418, 2005.
- [125] A. Romanelli, R. Siri, G. Abal, A. Auyuanet, and R. Donangelo. Decoherence in the quantum walk on the line. *Physica A: Statistical Mechanics and its Applications*, 347:137 – 152, 2005.
- [126] Viv Kendon. Decoherence in quantum walks - a review. *Mathematical Structures in Computer Science*, 17(6):1169 – 1220, 2007.
- [127] Paweł Kurzyński and Antoni Wójcik. Quantum walk as a generalized measuring device. *Phys. Rev. Lett.*, 110:200404, May 2013.
- [128] Yuan-yuan Zhao, Neng-kun Yu, Paweł Kurzyński, Guo-yong Xiang, Chuan-Feng Li, and Guang-Can Guo. Experimental realization of generalized qubit measurements based on quantum walks. *Phys. Rev. A*, 91:042101, Apr 2015.
- [129] C. A. Ryan, M. Laforest, J. C. Boileau, and R. Laflamme. Experimental implementation of a discrete-time quantum random walk on an nmr quantum-information processor. *Phys. Rev. A*, 72:062317, Dec 2005.

- [130] H. Schmitz, R. Matjeschk, Ch. Schneider, J. Glueckert, M. Enderlein, T. Huber, and T. Schaetz. Quantum walk of a trapped ion in phase space. *Phys. Rev. Lett.*, 103:090504, Aug 2009.
- [131] Robert Matjeschk, Ch Schneider, Martin Enderlein, Thomas Huber, Hector Schmitz, Jan Glueckert, and Tobias Schaetz. Experimental simulation and limitations of quantum walks with trapped ions. *New Journal of Physics*, 14(3):035012, 2012.
- [132] F. Zähringer, G. Kirchmair, R. Gerritsma, E. Solano, R. Blatt, and C. F. Roos. Realization of a quantum walk with one and two trapped ions. *Phys. Rev. Lett.*, 104:100503, Mar 2010.
- [133] Peter L. Knight, Eugenio Roldán, and J.E. Sipe. Optical cavity implementations of the quantum walk. *Optics Communications*, 227(1):147–157, 2003.
- [134] Peter L. Knight, Eugenio Roldán, and J. E. Sipe. Quantum walk on the line as an interference phenomenon. *Phys. Rev. A*, 68:020301, Aug 2003.
- [135] M. C. Bañuls, C. Navarrete, A. Pérez, Eugenio Roldán, and J. C. Soriano. Quantum walk with a time-dependent coin. *Phys. Rev. A*, 73:062304, Jun 2006.
- [136] A. Schreiber, K. N. Cassemiro, V. Potoček, A. Gábris, P. J. Mosley, E. Andersson, I. Jex, and Ch. Silberhorn. Photons walking the line: A quantum walk with adjustable coin operations. *Phys. Rev. Lett.*, 104:050502, Feb 2010.
- [137] A. Schreiber, K. N. Cassemiro, V. Potoček, A. Gábris, I. Jex, and Ch. Silberhorn. Decoherence and disorder in quantum walks: From ballistic spread to localization. *Phys. Rev. Lett.*, 106:180403, May 2011.
- [138] Deepak Pandey, Nandan Satapathy, M. S. Meena, and Hema Ramachandran. Quantum walk of light in frequency space and its controlled dephasing. *Phys. Rev. A*, 84:042322, Oct 2011.
- [139] Youn-Chang Jeong, Carlo Di Franco, Hyang-Tag Lim, M. S. Kim, and Yoon-Ho Kim. Experimental realization of a delayed-choice quantum walk. *Nature Communications*, 4(1):2471, Sep 2013.
- [140] Philipp M. Preiss, Ruichao Ma, M. Eric Tai, Alexander Lukin, Matthew Rispoli, Philip Zupancic, Yoav Lahini, Rajibul Islam, and Markus Greiner. Strongly correlated quantum walks in optical lattices. *Science*, 347(6227):1229–1233, 2015.

- [141] Chiara Esposito, Mariana R. Barros, Andrés Durán Hernández, Gonzalo Carvacho, Francesco Di Colandrea, Raouf Barboza, Filippo Cardano, Nicolò Spagnolo, Lorenzo Marrucci, and Fabio Sciarrino. Quantum walks of two correlated photons in a 2d synthetic lattice. *npj Quantum Information*, 8(1):34, Mar 2022.
- [142] Zhi Zhao, Jiangfeng Du, Hui Li, Tao Yang, Zeng-Bing Chen, and Jian-Wei Pan. Implement Quantum Random Walks with Linear Optics Elements. *arXiv e-prints*, pages quant-ph/0212149, December 2002.
- [143] H. Jeong, M. Paternostro, and M. S. Kim. Simulation of quantum random walks using the interference of a classical field. *Phys. Rev. A*, 69:012310, Jan 2004.
- [144] Binh Do, Michael L. Stohler, Sunder Balasubramanian, Daniel S. Elliott, Christopher Eash, Ephraim Fischbach, Michael A. Fischbach, Arthur Mills, and Benjamin Zwickl. Experimental realization of a quantum quincunx by use of linear optical elements. *J. Opt. Soc. Am. B*, 22(2):499–504, Feb 2005.
- [145] M. A. Broome, A. Fedrizzi, B. P. Lanyon, I. Kassal, A. Aspuru-Guzik, and A. G. White. Discrete single-photon quantum walks with tunable decoherence. *Phys. Rev. Lett.*, 104:153602, Apr 2010.
- [146] D. Francisco, C. Iemmi, J. P. Paz, and S. Ledesma. Simulating a quantum walk with classical optics. *Phys. Rev. A*, 74:052327, Nov 2006.
- [147] E. Flurin, V. V. Ramasesh, S. Hacoheh-Gourgy, L. S. Martin, N. Y. Yao, and I. Siddiqi. Observing topological invariants using quantum walks in superconducting circuits. *Phys. Rev. X*, 7:031023, Aug 2017.
- [148] Barry C. Sanders, Stephen D. Bartlett, Ben Tregenna, and Peter L. Knight. Quantum quincunx in cavity quantum electrodynamics. *Phys. Rev. A*, 67:042305, Apr 2003.
- [149] Xubo Zou, Yuli Dong, and Guangcan Guo. Optical implementation of one-dimensional quantum random walks using orbital angular momentum of a single photon. *New Journal of Physics*, 8(5):81, May 2006.
- [150] Pei Zhang, Xi-Feng Ren, Xu-Bo Zou, Bi-Heng Liu, Yun-Feng Huang, and Guang-Can Guo. Demonstration of one-dimensional quantum random walks using orbital angular momentum of photons. *Phys. Rev. A*, 75:052310, May 2007.

- [151] Pei Zhang, Bi-Heng Liu, Rui-Feng Liu, Hong-Rong Li, Fu-Li Li, and Guang-Can Guo. Implementation of one-dimensional quantum walks on spin-orbital angular momentum space of photons. *Phys. Rev. A*, 81:052322, May 2010.
- [152] Qi-Ping Su, Yu Zhang, Li Yu, Jia-Qi Zhou, Jin-Shuang Jin, Xiao-Qiang Xu, Shao-Jie Xiong, QingJun Xu, Zhe Sun, Kefei Chen, Franco Nori, and Chui-Ping Yang. Experimental demonstration of quantum walks with initial superposition states. *npj Quantum Information*, 5(1):40, May 2019.
- [153] F. Zähringer, G. Kirchmair, R. Gerritsma, E. Solano, R. Blatt, and C. F. Roos. Realization of a quantum walk with one and two trapped ions. *Phys. Rev. Lett.*, 104:100503, Mar 2010.
- [154] Michal Karski, Leonid Förster, Jai-Min Choi, Andreas Steffen, Wolfgang Alt, Dieter Meschede, and Artur Widera. Quantum walk in position space with single optically trapped atoms. *Science*, 325(5937):174–177, 2009.
- [155] Zhiguang Yan, Yu-Ran Zhang, Ming Gong, Yulin Wu, Yarui Zheng, Shaowei Li, Can Wang, Futian Liang, Jin Lin, Yu Xu, Cheng Guo, Lihua Sun, Cheng-Zhi Peng, Keyu Xia, Hui Deng, Hao Rong, J. Q. You, Franco Nori, Heng Fan, Xiaobo Zhu, and Jian-Wei Pan. Strongly correlated quantum walks with a 12-qubit superconducting processor. *Science*, 364(6442):753–756, 2019.
- [156] Ming Gong, Shiyu Wang, Chen Zha, Ming-Cheng Chen, He-Liang Huang, Yulin Wu, Qingling Zhu, Youwei Zhao, Shaowei Li, Shaojun Guo, Haoran Qian, Yangsen Ye, Fusheng Chen, Chong Ying, Jiale Yu, Daojin Fan, Dachao Wu, Hong Su, Hui Deng, Hao Rong, Kaili Zhang, Sirui Cao, Jin Lin, Yu Xu, Lihua Sun, Cheng Guo, Na Li, Futian Liang, V. M. Bastidas, Kae Nemoto, W. J. Munro, Yong-Heng Huo, Chao-Yang Lu, Cheng-Zhi Peng, Xiaobo Zhu, and Jian-Wei Pan. Quantum walks on a programmable two-dimensional 62-qubit superconducting processor. *Science*, 372(6545):948–952, 2021.
- [157] Filippo Cardano, Francesco Massa, Hammam Qassim, Ebrahim Karimi, Sergei Slusarenko, Domenico Paparo, Corrado de Lisio, Fabio Sciarrino, Enrico Santamato, Robert W. Boyd, and Lorenzo Marrucci. Quantum walks and wavepacket dynamics on a lattice with twisted photons. *Science Advances*, 1(2):e1500087, 2015.
- [158] Siamak Dadras, Alexander Gresch, Caspar Groiseau, Sandro Wimberger, and Gil S. Summy. Quantum walk in momentum space with a bose-einstein condensate. *Phys. Rev. Lett.*, 121:070402, Aug 2018.

- [159] Dizhou Xie, Tian-Shu Deng, Teng Xiao, Wei Gou, Tao Chen, Wei Yi, and Bo Yan. Topological quantum walks in momentum space with a bose-einstein condensate. *Phys. Rev. Lett.*, 124:050502, Feb 2020.
- [160] C. M. Chandrashekar, R. Srikanth, and Raymond Laflamme. Optimizing the discrete time quantum walk using a $su(2)$ coin. *Phys. Rev. A*, 77:032326, Mar 2008.
- [161] Sandeep K. Goyal, Thomas Konrad, and Lajos Diósi. Unitary equivalence of quantum walks. *Physics Letters A*, 379(3):100–104, 2015.
- [162] A. Kempf and R. Portugal. Group velocity of discrete-time quantum walks. *Phys. Rev. A*, 79:052317, May 2009.
- [163] T D Mackay, S D Bartlett, L T Stephenson, and B C Sanders. Quantum walks in higher dimensions. *Journal of Physics A: Mathematical and General*, 35(12):2745–2753, mar 2002.
- [164] Ben Tregenna, Will Flanagan, Rik Maile, and Viv Kendon. Controlling discrete quantum walks: coins and initial states. *New Journal of Physics*, 5:83–83, jul 2003.
- [165] A. C. Oliveira, R. Portugal, and R. Donangelo. Decoherence in two-dimensional quantum walks. *Phys. Rev. A*, 74:012312, Jul 2006.
- [166] Wei-Wei Zhang, Sandeep K. Goyal, Christoph Simon, and Barry C. Sanders. Decomposition of split-step quantum walks for simulating majorana modes and edge states. *Phys. Rev. A*, 95:052351, May 2017.
- [167] Antoni Wójcik, Tomasz Łuczak, Paweł Kurzyński, Andrzej Grudka, and Małgorzata Bednarska. Quasiperiodic dynamics of a quantum walk on the line. *Phys. Rev. Lett.*, 93:180601, Oct 2004.
- [168] Maximilian Genske, Wolfgang Alt, Andreas Steffen, Albert H. Werner, Reinhard F. Werner, Dieter Meschede, and Andrea Alberti. Electric quantum walks with individual atoms. *Phys. Rev. Lett.*, 110:190601, May 2013.
- [169] C. Cedzich, T. Rybár, A. H. Werner, A. Alberti, M. Genske, and R. F. Werner. Propagation of quantum walks in electric fields. *Phys. Rev. Lett.*, 111:160601, Oct 2013.
- [170] Luis A. Bru, Margarida Hinarejos, Fernando Silva, Germán J. de Valcárcel, and Eugenio Roldán. Electric quantum walks in two dimensions. *Phys. Rev. A*, 93:032333, Mar 2016.

- [171] Pablo Arnault, Benjamin Pepper, and A. Pérez. Quantum walks in weak electric fields and bloch oscillations. *Phys. Rev. A*, 101:062324, Jun 2020.
- [172] Xiao-Gang Wen. A theory of 2+1D bosonic topological orders. *National Science Review*, 3(1):68–106, 11 2015.
- [173] Lev Davidovich Landau and Dirk Ter-Haar. *Collected papers of L.D. Landau*. Pergamon, Oxford, 1965.
- [174] L.D. Landau and E.M. Lifshitz. *Statistical Physics*. Number v. 1 in A-W series in advanced physics. Pergamon Press, 1958.
- [175] V. L. Ginzburg and L. D. Landau. *On the Theory of Superconductivity*, pages 113–137. Springer Berlin Heidelberg, Berlin, Heidelberg, 2009.
- [176] Subir Sachdev. *Quantum Phase Transitions*. Cambridge University Press, 2 edition, 2011.
- [177] J. G. Bednorz and K. A. Müller. Possible high T_c superconductivity in the Ba-La-Cu-O system. *Zeitschrift für Physik B Condensed Matter*, 64(2):189–193, Jun 1986.
- [178] J M Kosterlitz and D J Thouless. Ordering, metastability and phase transitions in two-dimensional systems. *Journal of Physics C: Solid State Physics*, 6(7):1181–1203, apr 1973.
- [179] D. J. Thouless, M. Kohmoto, M. P. Nightingale, and M. den Nijs. Quantized hall conductance in a two-dimensional periodic potential. *Phys. Rev. Lett.*, 49:405–408, Aug 1982.
- [180] D. J. Thouless. Quantization of particle transport. *Phys. Rev. B*, 27:6083–6087, May 1983.
- [181] F.D.M. Haldane. Continuum dynamics of the 1-d heisenberg antiferromagnet: Identification with the o(3) nonlinear sigma model. *Physics Letters A*, 93(9):464–468, 1983.
- [182] F. D. M. Haldane. Model for a quantum hall effect without landau levels: Condensed-matter realization of the "parity anomaly". *Phys. Rev. Lett.*, 61:2015–2018, Oct 1988.
- [183] Xie Chen, Zheng-Cheng Gu, and Xiao-Gang Wen. Local unitary transformation, long-range quantum entanglement, wave function renormalization, and topological order. *Phys. Rev. B*, 82:155138, Oct 2010.
- [184] Liang Wu, M. Salehi, N. Koirala, J. Moon, S. Oh, and N. P. Armitage. Quantized faraday and kerr rotation and axion electrodynamics of a 3d topological insulator. *Science*, 354(6316):1124–1127, 2016.

- [185] M. Z. Hasan and C. L. Kane. Colloquium: Topological insulators. *Rev. Mod. Phys.*, 82:3045–3067, Nov 2010.
- [186] Xiao-Liang Qi and Shou-Cheng Zhang. Topological insulators and superconductors. *Rev. Mod. Phys.*, 83:1057–1110, Oct 2011.
- [187] N. P. Armitage, E. J. Mele, and Ashvin Vishwanath. Weyl and dirac semimetals in three-dimensional solids. *Rev. Mod. Phys.*, 90:015001, Jan 2018.
- [188] Tomoki Ozawa, Hannah M. Price, Alberto Amo, Nathan Goldman, Mohammad Hafezi, Ling Lu, Mikael C. Rechtsman, David Schuster, Jonathan Simon, Oded Zilberberg, and Iacopo Carusotto. Topological photonics. *Rev. Mod. Phys.*, 91:015006, Mar 2019.
- [189] Xiao-Gang Wen. Colloquium: Zoo of quantum-topological phases of matter. *Rev. Mod. Phys.*, 89:041004, Dec 2017.
- [190] Adolfo G. Grushin. Topological phases of amorphous matter. *arXiv e-prints*, page arXiv:2010.02851, October 2020.
- [191] Mikio Nakahara. *Geometry, topology and physics*. Graduate student series in physics. Hilger, Bristol, 1990.
- [192] Chetan Nayak, Steven H. Simon, Ady Stern, Michael Freedman, and Sankar Das Sarma. Non-abelian anyons and topological quantum computation. *Rev. Mod. Phys.*, 80:1083–1159, Sep 2008.
- [193] Andreas P. Schnyder, Shinsei Ryu, Akira Furusaki, and Andreas W. W. Ludwig. Classification of topological insulators and superconductors in three spatial dimensions. *Phys. Rev. B*, 78:195125, Nov 2008.
- [194] Andreas P. Schnyder, Shinsei Ryu, Akira Furusaki, and Andreas W. W. Ludwig. Classification of topological insulators and superconductors. *AIP Conference Proceedings*, 1134(1):10–21, 2009.
- [195] Shinsei Ryu, Andreas P. Schnyder, Akira Furusaki, and Andreas W. W. Ludwig. Topological insulators and superconductors: Tenfold way and dimensional hierarchy. *New J. Phys.*, 12:065010, 2010.
- [196] Alexei Kitaev. Periodic table for topological insulators and superconductors. *AIP Conference Proceedings*, 1134(1):22–30, 2009.

- [197] Andreas W W Ludwig. Topological phases: classification of topological insulators and superconductors of non-interacting fermions, and beyond. *Physica Scripta*, T168:014001, dec 2015.
- [198] Jan Carl Budich and Björn Trauzettel. From the adiabatic theorem of quantum mechanics to topological states of matter. *physica status solidi (RRL) – Rapid Research Letters*, 7(1-2):109–129, 2013.
- [199] Ching-Kai Chiu, Jeffrey C. Y. Teo, Andreas P. Schnyder, and Shinsei Ryu. Classification of topological quantum matter with symmetries. *Rev. Mod. Phys.*, 88:035005, Aug 2016.
- [200] Yoichi Ando. Topological insulator materials. *Journal of the Physical Society of Japan*, 82(10):102001, 2013.
- [201] Shinsei Ryu, Andreas P Schnyder, Akira Furusaki, and Andreas W W Ludwig. Topological insulators and superconductors: tenfold way and dimensional hierarchy. *New Journal of Physics*, 12(6):065010, jun 2010.
- [202] J.K. Asbóth, L. Oroszlány, and A.P. Pályi. *A Short Course on Topological Insulators: Band Structure and Edge States in One and Two Dimensions*. Lecture Notes in Physics. Springer International Publishing, 2016.
- [203] V. Mourik, K. Zuo, S. M. Frolov, S. R. Plissard, E. P. A. M. Bakkers, and L. P. Kouwenhoven. Signatures of majorana fermions in hybrid superconductor-semiconductor nanowire devices. *Science*, 336(6084):1003–1007, 2012.
- [204] Alan J. Heeger. Nobel lecture: Semiconducting and metallic polymers: The fourth generation of polymeric materials. *Rev. Mod. Phys.*, 73:681–700, Sep 2001.
- [205] Sujit Sarkar. Quantization of geometric phase with integer and fractional topological characterization in a quantum ising chain with long-range interaction. *Scientific Reports*, 8(1):5864, 2018.
- [206] Ching-Kai Chiu, Jeffrey C. Y. Teo, Andreas P. Schnyder, and Shinsei Ryu. Classification of topological quantum matter with symmetries. *Rev. Mod. Phys.*, 88:035005, Aug 2016.
- [207] T.D. Stanescu. *Introduction to Topological Quantum Matter & Quantum Computation*. CRC Press, 2016.

- [208] A.L. Fetter and J.D. Walecka. *Quantum Theory of Many-particle Systems*. Dover Books on Physics. Dover Publications, 2003.
- [209] R.G. Sachs. *The Physics of Time Reversal*. University of Chicago Press, Chicago, 1987.
- [210] Masatoshi Sato, Kazuki Hasebe, Kenta Esaki, and Mahito Kohmoto. Time-Reversal Symmetry in Non-Hermitian Systems. *Progress of Theoretical Physics*, 127(6):937–974, 06 2012.
- [211] Eugene P. Wigner. Normal form of antiunitary operators. *Journal of Mathematical Physics*, 1(5):409–413, 1960.
- [212] Martin R. Zirnbauer. Riemannian symmetric superspaces and their origin in random-matrix theory. *Journal of Mathematical Physics*, 37(10):4986–5018, 1996.
- [213] Alexander Altland and Martin R. Zirnbauer. Nonstandard symmetry classes in mesoscopic normal-superconducting hybrid structures. *Phys. Rev. B*, 55:1142–1161, Jan 1997.
- [214] P. Heinzner, A. Huckleberry, and M. R. Zirnbauer. Symmetry classes of disordered fermions. *Communications in Mathematical Physics*, 257(3):725–771, Aug 2005.
- [215] Freeman J. Dyson. The threefold way. algebraic structure of symmetry groups and ensembles in quantum mechanics. *Journal of Mathematical Physics*, 3(6):1199–1215, 1962.
- [216] H. Bruus and K. Flensberg. *Many-Body Quantum Theory in Condensed Matter Physics: An Introduction*. Oxford Graduate Texts. Oxford University Press, Oxford, 2004.
- [217] A. Altland and B.D. Simons. *Condensed Matter Field Theory*. Cambridge books online. Cambridge University Press, Cambridge, 2010.
- [218] W. P. Su, J. R. Schrieffer, and A. J. Heeger. Solitons in polyacetylene. *Phys. Rev. Lett.*, 42:1698–1701, Jun 1979.
- [219] W. P. Su, J. R. Schrieffer, and A. J. Heeger. Soliton excitations in polyacetylene. *Phys. Rev. B*, 22:2099–2111, Aug 1980.
- [220] Martin Leder, Christopher Grossert, Lukas Sitta, Maximilian Genske, Achim Rosch, and Martin Weitz. Real-space imaging of a topologically protected edge state with ultracold atoms in an amplitude-chirped optical lattice. *Nature Communications*, 7(1):13112, Oct 2016.

- [221] Shuta Nakajima, Takafumi Tomita, Shintaro Taie, Tomohiro Ichinose, Hideki Ozawa, Lei Wang, Matthias Troyer, and Yoshiro Takahashi. Topological Thouless pumping of ultracold fermions. *Nature Physics*, 12(4):296–300, Apr 2016.
- [222] M. Lohse, C. Schweizer, O. Zilberberg, M. Aidelsburger, and I. Bloch. A Thouless quantum pump with ultracold bosonic atoms in an optical superlattice. *Nature Physics*, 12(4):350–354, Apr 2016.
- [223] Lei Wang, Matthias Troyer, and Xi Dai. Topological charge pumping in a one-dimensional optical lattice. *Phys. Rev. Lett.*, 111:026802, Jul 2013.
- [224] Marcos Atala, Monika Aidelsburger, Julio T. Barreiro, Dmitry Abanin, Takuya Kitagawa, Eugene Demler, and Immanuel Bloch. Direct measurement of the Zak phase in topological Bloch bands. *Nature Physics*, 9(12):795–800, Dec 2013.
- [225] M. Franz and L. Molenkamp. *Topological Insulators*. ISSN. Elsevier Science, 2013.
- [226] R. Peierls. *More Surprises in Theoretical Physics*. Princeton Series in Physics. Princeton University Press, Princeton, 1991.
- [227] Robert E. Thorne. Charge-density-wave conductors. *Physics Today*, 49(5):42–47, 1996.
- [228] J. Sólyom. *Fundamentals of the Physics of Solids: Volume 3 - Normal, Broken-Symmetry, and Correlated Systems*. Theoretical Solid State Physics: Interaction Among Electrons. Springer, Berlin, Heidelberg, 2010.
- [229] B.A. Bernevig and T.L. Hughes. *Topological Insulators and Topological Superconductors*. Princeton University Press, Princeton, 2013.
- [230] Liang Fu and C. L. Kane. Topological insulators with inversion symmetry. *Phys. Rev. B*, 76:045302, Jul 2007.
- [231] L. Isaev, Y. H. Moon, and G. Ortiz. Bulk-boundary correspondence in three-dimensional topological insulators. *Phys. Rev. B*, 84:075444, Aug 2011.
- [232] Mahito Kohmoto. Topological invariant and the quantization of the Hall conductance. *Annals of Physics*, 160(2):343–354, 1985.
- [233] Takahiro Fukui, Yasuhiro Hatsugai, and Hiroshi Suzuki. Chern numbers in discretized Brillouin zone: Efficient method of computing (spin) Hall conductances. *Journal of the Physical Society of Japan*, 74(6):1674–1677, 2005.

- [234] Takuya Kitagawa, Matthew A. Broome, Alessandro Fedrizzi, Mark S. Rudner, Erez Berg, Ivan Kassal, Alán Aspuru-Guzik, Eugene Demler, and Andrew G. White. Observation of topologically protected bound states in photonic quantum walks. *Nature Communications*, 3:882 EP –, Jun 2012. Article.
- [235] János K. Asbóth and Hideaki Obuse. Bulk-boundary correspondence for chiral symmetric quantum walks. *Phys. Rev. B*, 88:121406, Sep 2013.
- [236] Tibor Rakovszky, János K. Asbóth, and Andrea Alberti. Detecting topological invariants in chiral symmetric insulators via losses. *Phys. Rev. B*, 95:201407, May 2017.
- [237] M. S. Rudner and L. S. Levitov. Topological transition in a non-hermitian quantum walk. *Phys. Rev. Lett.*, 102:065703, Feb 2009.
- [238] Julia M. Zeuner, Mikael C. Rechtsman, Yonatan Plotnik, Yaakov Lumer, Stefan Nolte, Mark S. Rudner, Mordechai Segev, and Alexander Szameit. Observation of a topological transition in the bulk of a non-hermitian system. *Phys. Rev. Lett.*, 115:040402, Jul 2015.
- [239] Ian Mondragon-Shem, Taylor L. Hughes, Juntao Song, and Emil Prodan. Topological criticality in the chiral-symmetric aiii class at strong disorder. *Phys. Rev. Lett.*, 113:046802, Jul 2014.
- [240] Ling Lin, Yongguan Ke, and Chaohong Lee. Real-space representation of the winding number for a one-dimensional chiral-symmetric topological insulator. *Phys. Rev. B*, 103:224208, Jun 2021.
- [241] Xiang Zhan, Lei Xiao, Zhihao Bian, Kunkun Wang, Xingze Qiu, Barry C. Sanders, Wei Yi, and Peng Xue. Detecting topological invariants in nonunitary discrete-time quantum walks. *Phys. Rev. Lett.*, 119:130501, Sep 2017.
- [242] Lei Xiao, Xingze Qiu, Kunkun Wang, Zhihao Bian, Xiang Zhan, Hideaki Obuse, Barry C. Sanders, Wei Yi, and Peng Xue. Higher winding number in a nonunitary photonic quantum walk. *Phys. Rev. A*, 98:063847, Dec 2018.
- [243] Xiao-Ye Xu, Qin-Qin Wang, Wei-Wei Pan, Kai Sun, Jin-Shi Xu, Geng Chen, Jian-Shun Tang, Ming Gong, Yong-Jian Han, Chuan-Feng Li, and Guang-Can Guo. Measuring the winding number in a large-scale chiral quantum walk. *Phys. Rev. Lett.*, 120:260501, Jun 2018.

- [244] Maria Maffei, Alexandre Dauphin, Filippo Cardano, Maciej Lewenstein, and Pietro Massignan. Topological characterization of chiral models through their long time dynamics. *New Journal of Physics*, 20(1):013023, jan 2018.
- [245] Heinz-Peter Breuer and Francesco Petruccione. *The Theory of Open Quantum Systems*. Oxford University Press, Oxford, 2007.
- [246] G. Lindblad. On the generators of quantum dynamical semigroups. *Commun. Math. Phys.*, 48(2):119–130, Jun 1976.
- [247] Carl M. Bender and Stefan Boettcher. Real spectra in non-hermitian hamiltonians having PT symmetry. *Phys. Rev. Lett.*, 80:5243–5246, Jun 1998.
- [248] Carl M. Bender, Stefan Boettcher, and Peter N. Meisinger. Pt -symmetric quantum mechanics. *Journal of Mathematical Physics*, 40(5):2201–2229, 1999.
- [249] Carl M Bender, M V Berry, and Aikaterini Mandilara. Generalized PT symmetry and real spectra. *Journal of Physics A: Mathematical and General*, 35(31):L467–L471, jul 2002.
- [250] Carl M. Bender, Dorje C. Brody, and Hugh F. Jones. Complex extension of quantum mechanics. *Phys. Rev. Lett.*, 89:270401, Dec 2002.
- [251] Carl M. Bender and Philip D. Mannheim. Pt symmetry and necessary and sufficient conditions for the reality of energy eigenvalues. *Physics Letters A*, 374(15):1616–1620, 2010.
- [252] Carl M Bender, Patrick E Dorey, Clare Dunning, Andreas Fring, Daniel W Hook, Hugh F Jones, Sergii Kuzhel, Géza Lévai, and Roberto Tateo. *PT Symmetry*. WORLD SCIENTIFIC (EUROPE), 2019.
- [253] Nimrod Moiseyev. *Non-Hermitian Quantum Mechanics*. Cambridge University Press, 2011.
- [254] Ali Mostafazadeh. Pseudo-hermiticity versus pt symmetry: The necessary condition for the reality of the spectrum of a non-hermitian hamiltonian. *Journal of Mathematical Physics*, 43(1):205–214, 2002.
- [255] Ali Mostafazadeh. Pseudo-hermiticity versus pt -symmetry. ii. a complete characterization of non-hermitian hamiltonians with a real spectrum. *Journal of Mathematical Physics*, 43(5):2814–2816, 2002.

- [256] Ali Mostafazadeh. Pseudo-hermiticity versus pt -symmetry iii: Equivalence of pseudo-hermiticity and the presence of antilinear symmetries. *Journal of Mathematical Physics*, 43(8):3944–3951, 2002.
- [257] Ali Mostafazadeh. Pseudo-hermiticity and generalized pt - and cpt -symmetries. *Journal of Mathematical Physics*, 44(3):974–989, 2003.
- [258] Philip D. Mannheim. PT symmetry as a necessary and sufficient condition for unitary time evolution. *Philosophical Transactions of the Royal Society A: Mathematical, Physical and Engineering Sciences*, 371(1989):20120060, 2013.
- [259] Joseph Schindler, Ang Li, Mei C. Zheng, F. M. Ellis, and Tsampikos Kottos. Experimental study of active lrc circuits with PT symmetries. *Phys. Rev. A*, 84:040101, Oct 2011.
- [260] S. Bittner, B. Dietz, U. Günther, H. L. Harney, M. Miski-Oglu, A. Richter, and F. Schäfer. PT symmetry and spontaneous symmetry breaking in a microwave billiard. *Phys. Rev. Lett.*, 108:024101, Jan 2012.
- [261] Romain Fleury, Dimitrios Sounas, and Andrea Alù. An invisible acoustic sensor based on parity-time symmetry. *Nature Communications*, 6(1):5905, Jan 2015.
- [262] Chao Hang, Guoxiang Huang, and Vladimir V. Konotop. PT symmetry with a system of three-level atoms. *Phys. Rev. Lett.*, 110:083604, Feb 2013.
- [263] Zhaoyang Zhang, Yiqi Zhang, Jiteng Sheng, Liu Yang, Mohammad-Ali Miri, Demetrios N. Christodoulides, Bing He, Yanpeng Zhang, and Min Xiao. Observation of parity-time symmetry in optically induced atomic lattices. *Phys. Rev. Lett.*, 117:123601, Sep 2016.
- [264] Alois Regensburger, Christoph Bersch, Mohammad-Ali Miri, Georgy Onishchukov, Demetrios N. Christodoulides, and Ulf Peschel. Parity–time synthetic photonic lattices. *Nature*, 488(7410):167–171, Aug 2012.
- [265] Carl M. Bender, Bjorn K. Berntson, David Parker, and E. Samuel. Observation of pt phase transition in a simple mechanical system. *American Journal of Physics*, 81(3):173–179, 2013.
- [266] Martin Wimmer, Alois Regensburger, Mohammad-Ali Miri, Christoph Bersch, Demetrios N. Christodoulides, and Ulf Peschel. Observation of optical solitons in pt -symmetric lattices. *Nature Communications*, 6(1):7782, Jul 2015.

- [267] Ramy El-Ganainy, Konstantinos G. Makris, Mercedeh Khajavikhan, Ziad H. Musslimani, Stefan Rotter, and Demetrios N. Christodoulides. Non-hermitian physics and pt symmetry. *Nature Physics*, 14(1):11–19, Jan 2018.
- [268] Liang Feng, Zi Jing Wong, Ren-Min Ma, Yuan Wang, and Xiang Zhang. Single-mode laser by parity-time symmetry breaking. *Science*, 346(6212):972–975, 2014.
- [269] Qiao-Qiao Lv, Jin-Min Liang, Zhi-Xi Wang, and Shao-Ming Fei. Quantum information masking in non-hermitian systems and robustness. *Laser Physics Letters*, 19(4):045203, feb 2022.
- [270] Zongping Gong, Yuto Ashida, Kohei Kawabata, Kazuaki Takasan, Sho Higashikawa, and Masahito Ueda. Topological phases of non-hermitian systems. *Phys. Rev. X*, 8:031079, Sep 2018.
- [271] Flore K. Kunst, Elisabet Edvardsson, Jan Carl Budich, and Emil J. Bergholtz. Biorthogonal bulk-boundary correspondence in non-hermitian systems. *Phys. Rev. Lett.*, 121:026808, Jul 2018.
- [272] Flore K. Kunst and Vatsal Dwivedi. Non-hermitian systems and topology: A transfer-matrix perspective. *Phys. Rev. B*, 99:245116, Jun 2019.
- [273] Shunyu Yao and Zhong Wang. Edge states and topological invariants of non-hermitian systems. *Phys. Rev. Lett.*, 121:086803, Aug 2018.
- [274] Kohei Kawabata, Ken Shiozaki, Masahito Ueda, and Masatoshi Sato. Symmetry and topology in non-hermitian physics. *Phys. Rev. X*, 9:041015, Oct 2019.
- [275] Hongfei Wang, Xiujuan Zhang, Jinguo Hua, Dangyuan Lei, Minghui Lu, and Yanfeng Chen. Topological physics of non-hermitian optics and photonics: a review. *Journal of Optics*, 23(12):123001, oct 2021.
- [276] Yuto Ashida, Zongping Gong, and Masahito Ueda. Non-hermitian physics. *Advances in Physics*, 69(3):249–435, 2020.
- [277] Kohei Kawabata, Sho Higashikawa, Zongping Gong, Yuto Ashida, and Masahito Ueda. Topological unification of time-reversal and particle-hole symmetries in non-hermitian physics. *Nature Communications*, 10(1):297, Jan 2019.

- [278] Kohei Kawabata, Ken Shiozaki, and Shinsei Ryu. Many-body topology of non-hermitian systems. *Phys. Rev. B*, 105:165137, Apr 2022.
- [279] V. M. Martinez Alvarez, J. E. Barrios Vargas, and L. E. F. Foa Torres. Non-hermitian robust edge states in one dimension: Anomalous localization and eigenspace condensation at exceptional points. *Phys. Rev. B*, 97:121401, Mar 2018.
- [280] Ye Xiong. Why does bulk boundary correspondence fail in some non-hermitian topological models. *Journal of Physics Communications*, 2(3):035043, mar 2018.
- [281] Tony E. Lee. Anomalous edge state in a non-hermitian lattice. *Phys. Rev. Lett.*, 116:133903, Apr 2016.
- [282] Nobuyuki Okuma, Kohei Kawabata, Ken Shiozaki, and Masatoshi Sato. Topological origin of non-hermitian skin effects. *Phys. Rev. Lett.*, 124:086801, Feb 2020.
- [283] Ş K. Özdemir, S. Rotter, F. Nori, and L. Yang. Parity–time symmetry and exceptional points in photonics. *Nature Materials*, 18(8):783–798, Aug 2019.
- [284] Emil J. Bergholtz, Jan Carl Budich, and Flore K. Kunst. Exceptional topology of non-hermitian systems. *Rev. Mod. Phys.*, 93:015005, Feb 2021.
- [285] W D Heiss. The physics of exceptional points. *Journal of Physics A: Mathematical and Theoretical*, 45(44):444016, oct 2012.
- [286] Baogang Zhu, Rong Lü, and Shu Chen. \mathcal{PT} symmetry in the non-hermitian su-schrieffer-heeger model with complex boundary potentials. *Phys. Rev. A*, 89:062102, Jun 2014.
- [287] Simon Lieu. Topological phases in the non-hermitian su-schrieffer-heeger model. *Phys. Rev. B*, 97:045106, Jan 2018.
- [288] Shunyu Yao and Zhong Wang. Edge states and topological invariants of non-hermitian systems. *Phys. Rev. Lett.*, 121:086803, Aug 2018.
- [289] Shuai Li, Min Liu, Fuli Li, and Bo Liu. Topological phase transition of the extended non-hermitian su-schrieffer-heeger model. *Physica Scripta*, 96(1):015402, nov 2020.
- [290] Vivek M. Vyas and Dibyendu Roy. Topological aspects of periodically driven non-hermitian su-schrieffer-heeger model. *Phys. Rev. B*, 103:075441, Feb 2021.

- [291] Chuanhao Yin, Hui Jiang, Linhu Li, Rong Lü, and Shu Chen. Geometrical meaning of winding number and its characterization of topological phases in one-dimensional chiral non-hermitian systems. *Phys. Rev. A*, 97:052115, May 2018.
- [292] Ken Mochizuki, Dakyeong Kim, and Hideaki Obuse. Explicit definition of \mathcal{PT} symmetry for nonunitary quantum walks with gain and loss. *Phys. Rev. A*, 93:062116, Jun 2016.
- [293] Michael A. Nielsen and Isaac L. Chuang. *Quantum Computation and Quantum Information: 10th Anniversary Edition*. Cambridge University Press, 2010.
- [294] Francisco M. Fernández. Symmetry and degeneracy, exceptional point and coalescence: a pedagogical approach. *arXiv e-prints*, page arXiv:2108.08287, August 2021.
- [295] Vikash Mittal, Aswathy Raj, Sanjib Dey, and Sandeep K. Goyal. Persistence of topological phases in non-hermitian quantum walks. *Scientific Reports*, 11(1):10262, May 2021.
- [296] Kohei Kawabata, Ken Shiozaki, Masahito Ueda, and Masatoshi Sato. Symmetry and topology in non-hermitian physics. *Phys. Rev. X*, 9:041015, Oct 2019.
- [297] C.L. Kane. Chapter 1 - topological band theory and the \mathbf{Z}_2 invariant. In Marcel Franz and Laurens Molenkamp, editors, *Topological Insulators*, volume 6 of *Contemporary Concepts of Condensed Matter Science*, pages 3–34. Elsevier, 2013.
- [298] Michael A. Nielsen, Mark R. Dowling, Mile Gu, and Andrew C. Doherty. Quantum computation as geometry. *Science*, 311(5764):1133–1135, 2006.
- [299] Mark R. Dowling and Michael A. Nielsen. The geometry of quantum computation. *Quantum Info. Comput.*, 8(10):861–899, nov 2008.
- [300] S. Chaturvedi, E. Ercolessi, G. Morandi, A. Ibert, G. Marmo, N. Mukunda, and R. Simon. Null phase curves and manifolds in geometric phase theory. *Journal of Mathematical Physics*, 54(6):062106, 2013.
- [301] Eduardo Martín-Martínez, Ivette Fuentes, and Robert B. Mann. Using berry’s phase to detect the unruh effect at lower accelerations. *Phys. Rev. Lett.*, 107:131301, Sep 2011.
- [302] Jiawei Hu and Hongwei Yu. Geometric phase for an accelerated two-level atom and the unruh effect. *Phys. Rev. A*, 85:032105, Mar 2012.
- [303] Navdeep Arya, Vikash Mittal, Kinjalk Lochan, and Sandeep K. Goyal. Geometric phase assisted observation of noninertial cavity-qed effects. *Phys. Rev. D*, 106:045011, Aug 2022.

- [304] F. Bloch and I. I. Rabi. Atoms in variable magnetic fields. *Rev. Mod. Phys.*, 17:237–244, Apr 1945.
- [305] T. Bastin, S. Krins, P. Mathonet, M. Godefroid, L. Lamata, and E. Solano. Operational families of entanglement classes for symmetric n -qubit states. *Phys. Rev. Lett.*, 103:070503, Aug 2009.
- [306] P. Mathonet, S. Krins, M. Godefroid, L. Lamata, E. Solano, and T. Bastin. Entanglement equivalence of n -qubit symmetric states. *Phys. Rev. A*, 81:052315, May 2010.
- [307] H. Mäkelä and A. Messina. Polynomial method to study the entanglement of pure n -qubit states. *Phys. Rev. A*, 81:012326, Jan 2010.
- [308] H Mäkelä and A Messina. N -qubit states as points on the bloch sphere. *Physica Scripta*, T140:014054, sep 2010.
- [309] Damian J. H. Markham. Entanglement and symmetry in permutation-symmetric states. *Phys. Rev. A*, 83:042332, Apr 2011.
- [310] A. R. Usha Devi, Sudha, and A. K. Rajagopal. Majorana representation of symmetric multiqubit states. *Quantum Information Processing*, 11(3):685–710, Jun 2012.
- [311] H. D. Liu and L. B. Fu. Berry phase and quantum entanglement in majorana’s stellar representation. *Phys. Rev. A*, 94:022123, Aug 2016.
- [312] Martin Aulbach, Damian Markham, and Mio Muraö. Geometric entanglement of symmetric states and the majorana representation. In Wim van Dam, Vivien M. Kendon, and Simone Severini, editors, *Theory of Quantum Computation, Communication, and Cryptography*, pages 141–158, Berlin, Heidelberg, 2011. Springer Berlin Heidelberg.
- [313] J H Hannay. The berry phase for spin in the majorana representation. *Journal of Physics A: Mathematical and General*, 31(2):L53–L59, jan 1998.
- [314] H. D. Liu and L. B. Fu. Representation of berry phase by the trajectories of majorana stars. *Phys. Rev. Lett.*, 113:240403, Dec 2014.
- [315] K. S. Akhilesh, Arvind, S. Chaturvedi, K. S. Mallesh, and N. Mukunda. Geometric phases for finite-dimensional systems—the roles of bargmann invariants, null phase curves, and the schwinger–majorana $SU(2)$ framework. *Journal of Mathematical Physics*, 61(7):072103, 2020.

- [316] Chao Yang, Huaiming Guo, Li-Bin Fu, and Shu Chen. Characterization of symmetry-protected topological phases in polymerized models by trajectories of majorana stars. *Phys. Rev. B*, 91:125132, Mar 2015.
- [317] Wei Xin Teo, Linhu Li, Xizheng Zhang, and Jiangbin Gong. Topological characterization of non-hermitian multiband systems using majorana's stellar representation. *Phys. Rev. B*, 101:205309, May 2020.
- [318] James Bartlett, Haiping Hu, and Erhai Zhao. Illuminating the bulk-boundary correspondence of a non-hermitian stub lattice with majorana stars. *Phys. Rev. B*, 104:195131, Nov 2021.
- [319] Vikash Mittal, Akhilesh K. S., and Sandeep K. Goyal. Geometric decomposition of geodesics and null-phase curves using majorana star representation. *Phys. Rev. A*, 105:052219, May 2022.
- [320] Pieter Kok, W. J. Munro, Kae Nemoto, T. C. Ralph, Jonathan P. Dowling, and G. J. Milburn. Linear optical quantum computing with photonic qubits. *Rev. Mod. Phys.*, 79:135–174, Jan 2007.
- [321] Michael A. Nielsen and Isaac L. Chuang. *Quantum Computation and Quantum Information: 10th Anniversary Edition*. Cambridge University Press, 2010.
- [322] Stephen A. Fulling. Nonuniqueness of canonical field quantization in riemannian space-time. *Phys. Rev. D*, 7:2850–2862, May 1973.
- [323] P C W Davies. Scalar production in schwarzschild and rindler metrics. *J. Phys. A: Math. Gen.*, 8(4):609–616, apr 1975.
- [324] W. G. Unruh. Notes on black-hole evaporation. *Phys. Rev. D*, 14:870–892, Aug 1976.
- [325] Luís C. B. Crispino, Atsushi Higuchi, and George E. A. Matsas. The unruh effect and its applications. *Rev. Mod. Phys.*, 80:787–838, Jul 2008.
- [326] S. W. Hawking. Black hole explosions? *Nature*, 248(5443):30–31, Mar 1974.
- [327] S. W. Hawking. Particle creation by black holes. *Communications in Mathematical Physics*, 43(3):199–220, Aug 1975.
- [328] J. Rogers. Detector for the temperaturelike effect of acceleration. *Phys. Rev. Lett.*, 61:2113–2116, Oct 1988.

- [329] Pisin Chen and Toshi Tajima. Testing unruh radiation with ultraintense lasers. *Phys. Rev. Lett.*, 83:256–259, Jul 1999.
- [330] Mariona Aspachs, Gerardo Adesso, and Ivette Fuentes. Optimal quantum estimation of the unruh-hawking effect. *Phys. Rev. Lett.*, 105:151301, Oct 2010.
- [331] Marlan O. Scully, Vitaly V. Kocharovskiy, Alexey Belyanin, Edward Fry, and Federico Capasso. Enhancing acceleration radiation from ground-state atoms via cavity quantum electrodynamics. *Phys. Rev. Lett.*, 91:243004, Dec 2003.
- [332] D. Jaffino Stargen and Kinjalk Lochan. Cavity optimization for Unruh effect at small accelerations. *arXiv e-prints*, page arXiv:2107.00049, June 2021.
- [333] Daniel A. T. Vanzella and George E. A. Matsas. Decay of accelerated protons and the existence of the fulling-davies-unruh effect. *Phys. Rev. Lett.*, 87:151301, Sep 2001.
- [334] S. Barshay and W. Troost. A possible origin for temperature in strong interactions. *Physics Letters B*, 73(4):437–439, 1978.
- [335] Saul Barshay, H. Braun, J. P. Gerber, and G. Maurer. Possible evidence for fluctuations in the hadronic temperature. *Phys. Rev. D*, 21:1849–1853, Apr 1980.
- [336] D. Kharzeev. Quantum black holes and thermalization in relativistic heavy ion collisions. *Nuclear Physics A*, 774:315–324, 2006.
- [337] J.S. Bell and J.M. Leinaas. Electrons as accelerated thermometers. *Nucl. Phys. B*, 212(1):131–150, 1983.
- [338] J.S. Bell and J.M. Leinaas. The unruh effect and quantum fluctuations of electrons in storage rings. *Nucl. Phys. B*, 284:488–508, 1987.
- [339] W.G. Unruh. Acceleration radiation for orbiting electrons. *Phys. Rep.*, 307(1):163–171, 1998.
- [340] Yao Jin, Jiawei Hu, and Hongwei Yu. Dynamical behavior and geometric phase for a circularly accelerated two-level atom. *Phys. Rev. A*, 89:064101, Jun 2014.
- [341] Kinjalk Lochan, Hendrik Ulbricht, Andrea Vinante, and Sandeep K. Goyal. Detecting acceleration-enhanced vacuum fluctuations with atoms inside a cavity. *Phys. Rev. Lett.*, 125:241301, Dec 2020.

- [342] Edward Mills Purcell. Spontaneous emission probabilities at radio frequencies. In *Confined Electrons and Photons: New Physics and Applications*, pages 839–839. Springer US, 1995.
- [343] Jeeva Anandan. Classical and quantum interaction of the dipole. *Phys. Rev. Lett.*, 85:1354–1357, Aug 2000.
- [344] Christopher Gerry and Peter Knight. *Introductory Quantum Optics*. Cambridge University Press, 2004.
- [345] J. J. Sakurai and Jim Napolitano. *Modern Quantum Mechanics*. Cambridge University Press, 2 edition, 2017.
- [346] Fabio Benatti and Floreanin Roberto. Open quantum dynamics: Complete positivity and entanglement. *Int. J. Mod. Phys. B*, 19(19):3063–3139, 2005.
- [347] Marlan O. Scully and M. Suhail Zubairy. *Quantum Optics*. Cambridge University Press, 1997.
- [348] Maciej Lewenstein and Luis Roso. Cooling of atoms in colored vacua. *Phys. Rev. A*, 47:3385–3389, Apr 1993.
- [349] Jonghoon Ahn, Zhujing Xu, Jaehoon Bang, Yu-Hao Deng, Thai M. Hoang, Qinkai Han, Ren-Min Ma, and Tongcang Li. Optically levitated nanodumbbell torsion balance and ghz nanomechanical rotor. *Phys. Rev. Lett.*, 121:033603, Jul 2018.
- [350] Henry G. Leduc, Bruce Bumble, Peter K. Day, Byeong Ho Eom, Jiansong Gao, Sunil Golwala, Benjamin A. Mazin, Sean McHugh, Andrew Merrill, David C. Moore, Omid Noroozian, Anthony D. Turner, and Jonas Zmuidzinas. Titanium nitride films for ultra-sensitive microresonator detectors. *Applied Physics Letters*, 97(10):102509, 2010.
- [351] Chenchen Wang, Xuwei Fan, You Guo, Huaqiao Gui, Huanqing Wang, Jianguo Liu, Benli Yu, and Liang Lu. Full-circle range and microradian resolution angle measurement using the orthogonal mirror self-mixing interferometry. *Opt. Express*, 26(8):10371–10381, Apr 2018.